The suction characteristics of power steering pumps

Jones, Brendan

Award date:
1999

Awarding institution:
University of Bath

THE SUCTION CHARACTERISTICS OF POWER STEERING PUMPS

Submitted by Brendan Jones
for the degree of PhD
of the University of Bath
1999

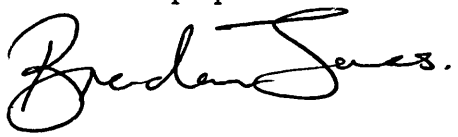

ProQuest LLC
789 East Eisenhower Parkway
P.O. Box 1346
Ann Arbor, MI 48106-1346

SUMMARY

Audible noise from power steering systems can be caused by fluctuations of pressure within the hydraulic system. An important location in the hydraulic circuit where fluid borne noise could be generated is the pump. The fluid borne noise emitted from the delivery port is well documented, however the suction port characteristics are less well understood. It is the aim of this thesis to examine the fluid borne noise characteristics of power steering pump suction ports and to evaluate their importance as a proportion of the pump noise.

Two computer models are developed in order to analyse the noise. One is an impedance model, which uses distributed parameter equations to predict the impedance of the passageways inside the pump's casing. The other is a dynamic simulation of flow ripple, which predicts the flow at the rotating group for different running conditions. Used in tandem, these two models can predict source, open-circuit and anechoic flow ripple.

Three types of pump are tested for both impedance and flow ripple characteristics. The results are used as validation aids for the computer models and also as a source of empirical data for an air-content function. The results show that in some cases, the flow ripple emitted from the suction port was of similar amplitude to that emitted from the delivery port. The high frequency harmonics of suction flow ripple are shown to be dominant and some design recommendations to reduce this effect are put forward.

ACKNOWLEDGEMENTS

Thanks are due to Allan Dickinson of Delphi Saginaw Steering Systems and the Engineering and Physical Sciences Research Council for supporting this project. I would also like to thank my supervisors and the staff and students in the department of mechanical engineering of the University of Bath.

Finally, I would like to thank my mother who taught me all I know. Honest!

CONTENTS

LIST OF TABLES

LIST OF FIGURES

NOMENCLATURE

c	Sonic speed
d	Diameter
d_h	Hydraulic diameter
f_t	Total friction force
f_1	Friction force on liquid phase
f_2	Friction force on gas phase
h	Height of leakage clearance
j	$\sqrt{-1}$
k	Time constant of evolution/solution of air
l	Length
n_c	Chamber number
n_v	Number of vanes in pump
p	Instantaneous pressure
q	Instantaneous flow rate
r	Radius
s	Laplace operator
t	Time
t_v	Vane thickness
u	Forward travelling wave, elemental fluid velocity in x direction
v	Backward travelling wave, elemental fluid velocity in y direction
w	Axial velocity, over relaxation factor
x	Cartesian co-ordinate at cam radius
y_{cam}	Radius of cam at angle θ
z	Axial co-ordinate
A	Cross-sectional area
B_e	Effective bulk modulus
B_1	Bulk modulus of oil
B_2	Bulk modulus of air
C	Capacitance
C_d	Orifice discharge coefficient
J_0	Zero order Bessel function
J_1	First order Bessel function
K	Value defined in Equation 3.2.1.2
L	Inductance
N_p	Pump speed
P	Laplace transform of pressure

Q	Laplace transform of flow
R	Universal gas constant, Component radius
S	Rate of phase change
T	Temperature
U	Tangential velocity of pump's rotating group
V_t	Total volume of air at a given time
V_1	Volume of oil
V_2	Volume of air
W	Laplace transform of axial velocity
X_A	X-co-ordinate of cam function breakpoint
X_B	X-co-ordinate of cam function breakpoint
X_C	X-co-ordinate of cam function breakpoint
X_D	X-co-ordinate of cam function breakpoint
X_E	X-co-ordinate of cam function breakpoint
X_F	X-co-ordinate of cam function breakpoint
Y	Admittance
Y_A	Y-co-ordinate of cam function breakpoint
Y_B	Y-co-ordinate of cam function breakpoint
Y_C	Y-co-ordinate of cam function breakpoint
Z	Impedance
Z_0	Characteristic impedance
α	Void fraction
ε	Convergence tolerance
γ	Wave propagation coefficient
μ	Absolute viscosity
ν	Kinematic viscosity
θ	Angle
ρ	Density
ω	Frequency

SUBSCRIPTS

0	Original value
1	Oil
2	Air
a	Measured in the axial direction
d	Downstream

del	Relating to the delivery port
e	Effective
i	Relating to internal flow ripple
in	Inlet to annulus
l	Leakage
p	Port
r	At a given radius
sc	Supercharge inlet
sp	Suction port entrance
t	Total
th	Theoretical
u	Upstream
A	Relating to anechoic flow ripple
C	Chamber
CA	Back of chamber
CB	Front of chamber
CC	Centre of chamber
E	Eccentricity, relating to open circuit flow ripple
R	Rotor
RES	Reservoir
S	Source
SP	Suction port orifice

SUPERSCRIPTS

n_c	Chamber number
*	New value

1 INTRODUCTION

Over the past decade, hydraulic power assisted steering has become a more and more common occurrence in lower cost family saloon cars. The increased ease of handling offered by such a system is nowadays a very powerful selling point in the market place. It is therefore necessary to ensure that the systems are as cheap and as easy to install as possible in order to maintain their availability in the lower price range. Another criterion is that power steering should cause as little noise and vibration as possible, which can be both a nuisance to the driver and be a possible cause of worn mountings. Unfortunately, noise, caused by pressure fluctuations in the fluid, is an intrinsic problem with hydraulics and is commonly noticeable to the driver in low speed manoeuvres such as parking. It is for this reason that much research is currently being carried out into the subject of power steering noise.

Audible noise is known as airborne noise (ABN), which is produced by poorly insulated vibrating structures. Vibration of solid materials such as hoses and pipes is known as structure borne noise (SBN) and can be caused by several different sources of excitation. For instance, the pump, which is attached to the piping, vibrates at a fundamental frequency equal to its rotational frequency which is due to imbalance of pressure or mass. Pressure fluctuation produced by the interaction between flow ripple and system impedance is known as fluid borne noise (FBN) and is another major source of excitation of SBN. The fundamental frequency of FBN is the multiple of the pump's shaft frequency and the number of pumping chambers. The two forms of noise interact to form a spectrum of very dominant harmonics at multiples of the pumping frequency and it is important that these should not coincide with a resonant frequency of the circuit or noise levels could become very high indeed.

The aim of this research is to study the fluid borne noise characteristics of the power steering pump with particular emphasis on the suction port. The condition of the oil that is drawn into a pump could have a major effect on the quality of system performance and therefore must be considered. At low pressure, cavitation and air-evolution become a cause for concern. Noise created by fluctuating pressure is present in both delivery and suction lines and the proportion of noise emitted from each side must be assessed. It will be seen that noise emitted from low-pressure lines can be comparable to that in the delivery line and that the design of the suction ports can be modified in order to reduce overall system noise. These factors may be explained through a series of dynamic simulation and experimental work, which is contained in this thesis.

1.1 A DESCRIPTION OF THE POWER STEERING SYSTEM

In a rack and pinion steering system the steering column has a pinion gear on its lower end that meshes with a toothed section on the rack (Figure 1-1). The lack of power assistance means that

low-speed manoeuvres such as parking require a lot of effort from the driver. The basic power assisted steering system works on the same principle as the rack and pinion except that a hydraulic actuator assists the mechanical gearing.

For safety reasons there must be a mechanical link between the steering column and the rack, which means that the way in which the actuator assists the driver is complicated. The base of the steering column is attached to a hydraulic valve and to the pinion gear via a small diameter bar called the torsion bar, which passes through the middle of the valve (Figure 1–2). As the steering column is turned it turns the valve such that fluid flows into the actuator, which in turn pushes the rack in the required direction. The pinion gear turns a short time after the valve due to torsion of the small diameter bar. If the hydraulics fail, the mechanical link is maintained via the torsion bar and via end stops limiting the relative angular movement of the valve.

The entire power steering system is shown in Figure 1–3. The power steering pump, which in this case is a vane pump although gear pumps are sometimes used, supplies pressure and flow to the hydraulic actuator via the valve. The delivery line is usually a combination of rigid piping and flexible hose. The hose acts as a noise attenuator and also facilitates routing around engine components. The return line links the valve to the reservoir, which can be mounted directly onto the pump or linked via a short suction line. The return line is also a combination of rigid pipe and flexible hose, which may be routed such that air passing over the rigid piping helps to cool the oil.

1.1.1 THE POWER STEERING PUMP

Vane pumps (1) are commonly used as power steering pumps because they are lightweight and are relatively inexpensive to manufacture. The type of vane pump used in power steering usually has two sets of suction ports set 180° apart and two sets of delivery ports also set 180° apart, shown in Figure 1–4. This arrangement ensures that the force due to the pressure in each pumping chamber acting on the bearings is balanced at all times, which means that bearing wear is at a minimum.

A pumping chamber is the volume trapped between two adjacent vanes. The vanes follow a cam on their outer radius and slide in and out of slots in the rotor as the pump rotates. The vanes are kept in contact with the cam by pressurisation of the slots with a bleed from the delivery of the pump. The effect of the vanes sliding on the cam is to adjust the volume of the chamber as it passes between suction and delivery. There are two major and two minor dwells on the cam ring, which lie between the ports. As a chamber opens to suction the cam rises and the volume of the chamber increases thus providing suction. Similarly, the cam falls towards the minor dwell as the chamber opens to delivery. Each chamber goes through this process twice per revolution in order to maintain the force balance.

If the pressure inside a chamber is not equal to the pressure in the suction port, every time a chamber opens to the port there will be a fluctuation in the flow. The change in volume of the chamber while it is open also produces a periodic flow fluctuation. The combination of successive chambers opening to the port creates a waveform that is periodic with a frequency equal to the number of chambers multiplied by the speed of the pump. This waveform is known as flow ripple and is the cause of the noise that is the subject of this thesis.

Vane pumps have a controlled delivery flow characteristic that gives an almost constant flow over a wide range of speeds. A typical flow characteristic is shown in Figure 1–5, which shows four flow-rates that can be achieved by changing the size of the flow control orifice on the delivery port of the pump. The flow increases with speed until the pump reaches the speed at which it can achieve the required flow. As the speed increases and the required flow-rate is reached the excess flow is diverted from the delivery line back to the suction line. The flow control valve through which the fluid passes is called the supercharge valve **(2)** because oil at high-pressure is de-compressed on its way through the valve but still enters the suction port passageways at a slightly elevated pressure. A schematic of the supercharge valve is shown in Figure 1–6. It is a pilot operated valve that is contained in the pump casing. High-pressure fluid from the rotating group flows into the system via the outlet orifice. The pressure of the fluid is transmitted via the pilot line to act on the first stage of the valve. As the flow becomes too great for the system requirement, the pressure increases and the first stage opens and the pressure behind the spool drops. The valve then opens and the excess flow passes via the flow control valve where it mixes with flow from the reservoir and enters the rotating group via the suction port.

A jet is created at the outlet of the supercharge valve because of the speed of the fluid that is dictated by the large pressure drop in a very small distance. This jet could cavitate thus causing damage to the internal surfaces of the housing and could also have an effect on the noise characteristics of the suction port.

Oil flows through a complicated system of passageways on its way from the reservoir to the rotating group (Figure 1–7). There are five main sections into which it may be broken down. Fluid enters the suction ports from two different sources: it travels through the pump entrance from the reservoir, and from the supercharge valve via the discharge section. These two flows mix at the entrance to the annulus, which surrounds the cam ring. Fluid in the annulus is drawn into the suction ports and thus through the pump to the delivery side. The effect of these passageways on the flow ripple waveform must be modelled if the noise characteristics of the suction port are to be understood.

1.2 NOISE EMITTED BY HYDRAULIC SYSTEMS

Noise emitted by hydraulic systems is caused by an interaction between flow ripple and the hydraulic impedance of the circuit, which is defined by the geometry and the oil properties. In a badly tuned system, the resulting standing waves can resonate causing unpleasant sound levels. These can be heard as low-pitched moaning and in some cases may become unstable and cause the flexible hoses to shudder violently. This is an extreme case that must be avoided as it increases the likelihood of failure of mountings and could precipitate leakage at pipe connections.

Other audible noise from power steering systems comes from high-speed jets when a large flow-rate passes through a small orifice. This occurs in the pump when the supercharge valve is open. It can also be found in the directional control valve that is mounted on the rack. These sounds are characterised by high-pitched random signals and can be reduced by using well-designed orifices **(3)**.

1.2.1 METHODS OF NOISE REDUCTION IN POWER STEERING

In order to reduce ABN, the problem is best tackled at its sources, one of which is the FBN level emitted by the pump. In power steering, methods of energy dissipation are employed to reduce the amplitude of FBN. The most fundamental means of dissipation is the flexible hose **(4)**, which is inserted between the pump and the valve. The hose expands and contracts as the fluid pressure fluctuates and the movement is damped by the attenuation properties of the rubber walls. More attenuation can be achieved if the hose walls are made of softer material but this has the effect of increasing the system capacitance and producing a lag between the steering input and the output at the front wheels.

Increased noise attenuation can be obtained by placing an insert into the flexible hose. These devices are known as tuners **(5)** and are usually placed in the upstream end of the hose. Tuners are usually made of metal and are tubular with spiral walls so that they can flex with the hose (Figure 1–8). The tuner therefore acts as a small diameter hose that leaks into the delivery hose. Leakage flow then runs along the annular section between the tuner and the hose until it mixes with the main flow from the middle of the tuner. The tuner attenuates due to resistive losses due to leakage through its wall and side-branch resonator effects between its outer wall and the hose.

In larger hydraulic systems, more emphasis is placed on attacking the problem of noise at its source, which is the pump. By altering the inner-casing passageways of the pump, the impedance can be changed in such a way as to decrease the pressure ripple that is emitted. The timing of the opening of a chamber to the suction or delivery port can be adjusted in order that the pressure is equal on either side of the orifice so that the flow ripple is reduced to a

minimum. The opening of the ports can be machined so that the acceleration of fluid is lower and fluctuations due to inertia are reduced, this is known as relief grooving.

None of these methods of noise reduction can be effective for the entire operating and frequency range of the FBN and so must be optimised for certain operating conditions. Optimisation can be done through trial-and-error testing or a cheaper method is to use simulation. By using simulation techniques, a large amount of configurations can be tested before prototypes are built. This cuts down on the amount of wasted time used in manufacturing and testing inadequate solutions.

1.3 RESEARCH OBJECTIVES

This project is an attempt to understand the mechanisms that lead to fluid borne noise propagation in the low-pressure side of a power steering vane pump. The noise characteristics will be modelled and validated using experimental results. Once a thorough knowledge of the system has been gained, design recommendations will be put forward, which will lead to research beyond the scope of this thesis.

1.3.1 SCOPE OF THE THESIS

Each chapter of this thesis is designed to be read on its own, however knowledge of the preceding chapters would be of use to thoroughly understand everything. The chapters all contain an introductory section, which where necessary includes reference to relevant literature on that subject. A brief summary of each chapter follows:

Chapter 2 concentrates on the effect of aeration in hydraulic oil. Aeration is present in oil at all times but at low-pressure it may have a great effect on system compliance and inertia. Bulk modulus, density and viscosity are discussed.

Chapter 3 looks at a model of the suction port impedance using a distributed parameter model. The fluid property expressions derived in Chapter 2 are incorporated into the model and their effect on impedance are observed.

In Chapter 4, a dynamic flow ripple simulation is discussed. Specialised functions for time-varying geometry are described. The simulation is used together with the impedance model of Chapter 3 to give flow ripple results both inside and outside of the pump housing.

Chapter 5 is the beginning of the experimental side of the research. An existing test method is modified to give impedance measurements at low pressure.

The test results measured on the test stand, described in Chapter 5, are discussed in Chapter 6. Impedance and flow ripple are compared for three types of vane pump at various operating conditions.

Chapter 7 uses the test results to validate the simulation work. An empirical function to describe air evolution in the pump is developed.

Chapter 8 contains recommendations for modifications to pump design that could reduce fluid borne noise levels. These simulation results have not been validated and leave the opportunity for further research to be carried out.

FIGURES FOR CHAPTER 1

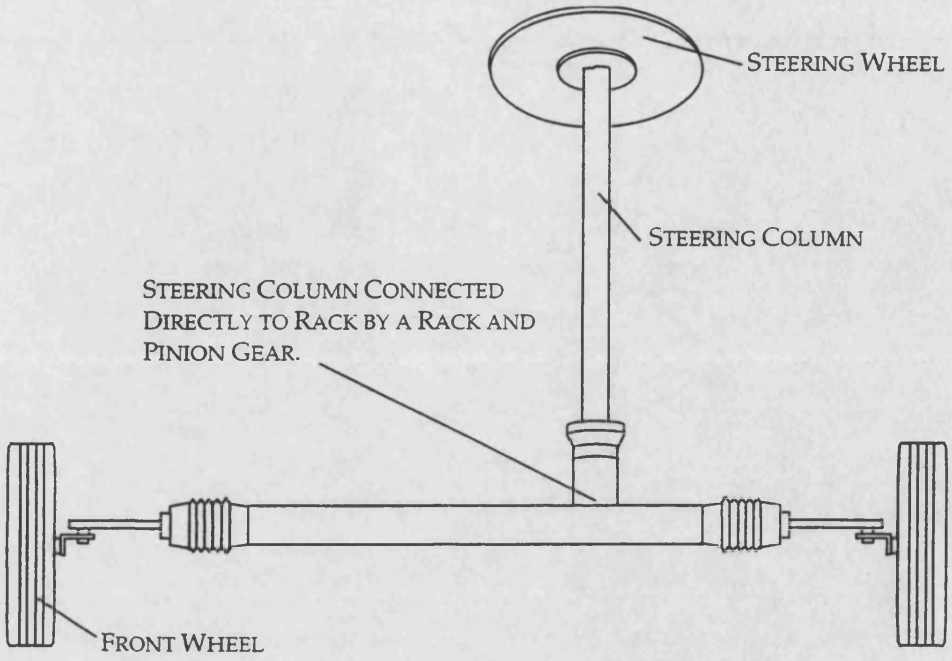

Figure 1–1: The Rack and Pinion Steering System

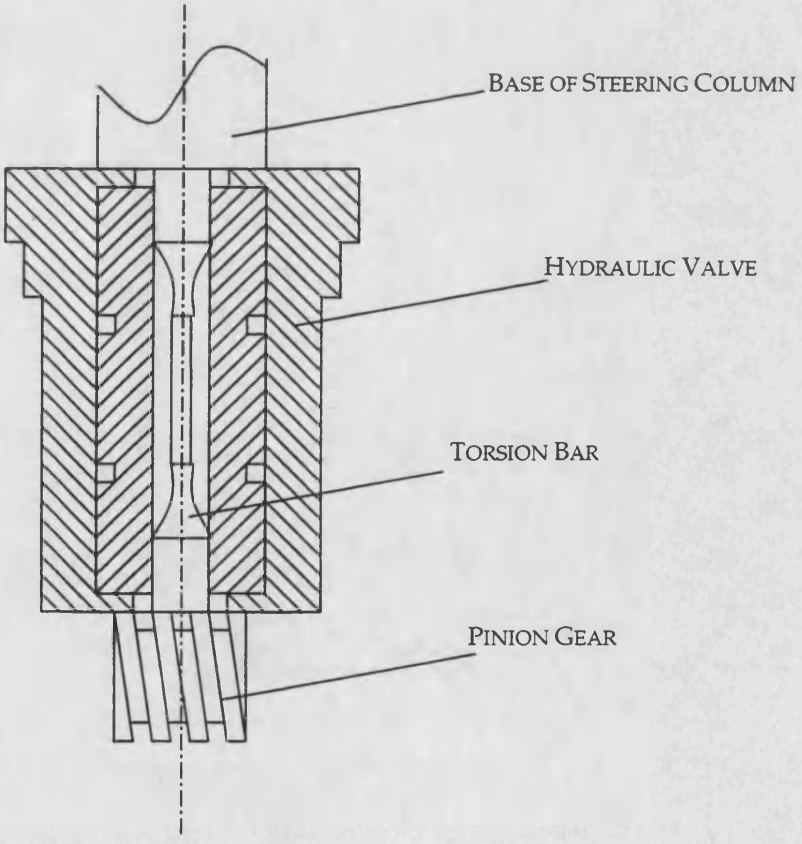

Figure 1–2: Schematic of Torsion Bar – Hydraulic Valve Assembly

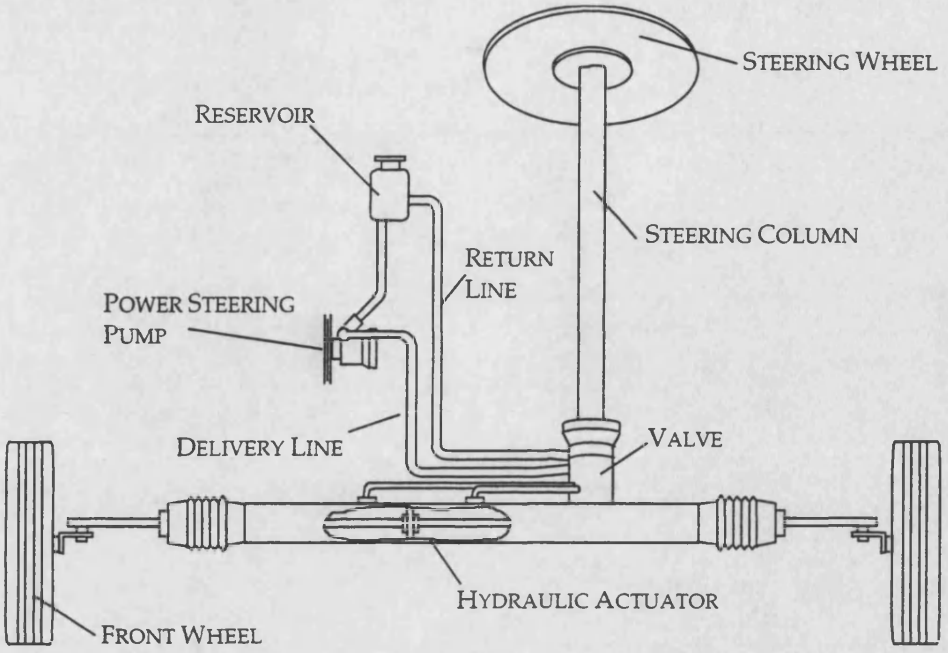

Figure 1–3: Schematic of a Power Steering System

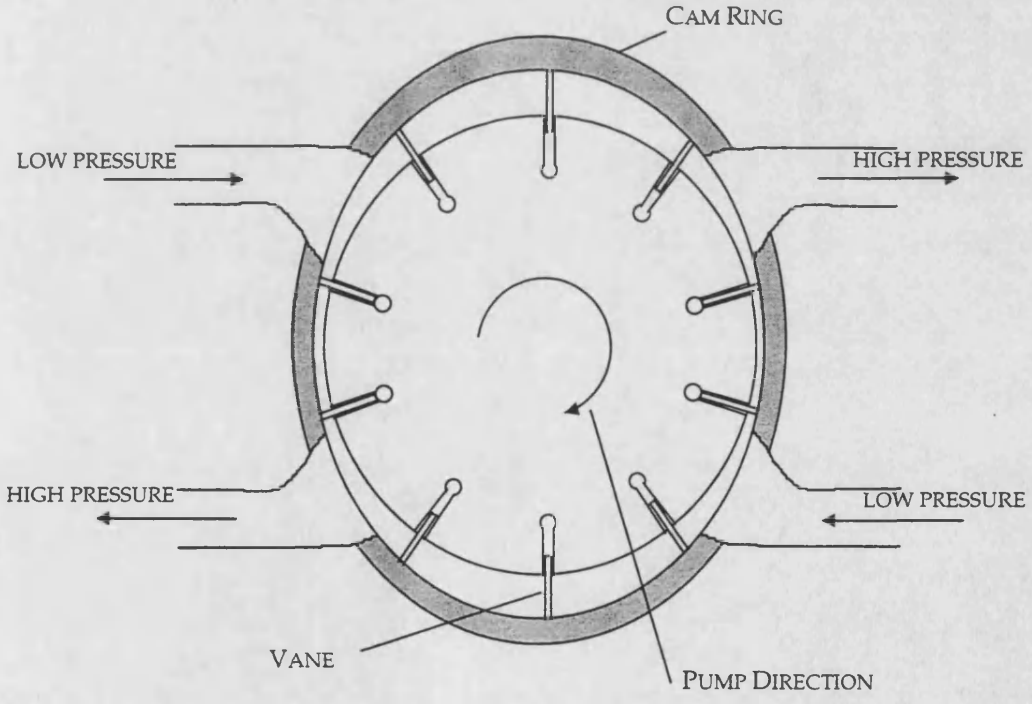

Figure 1–4: Schematic of a Balanced Vane Pump

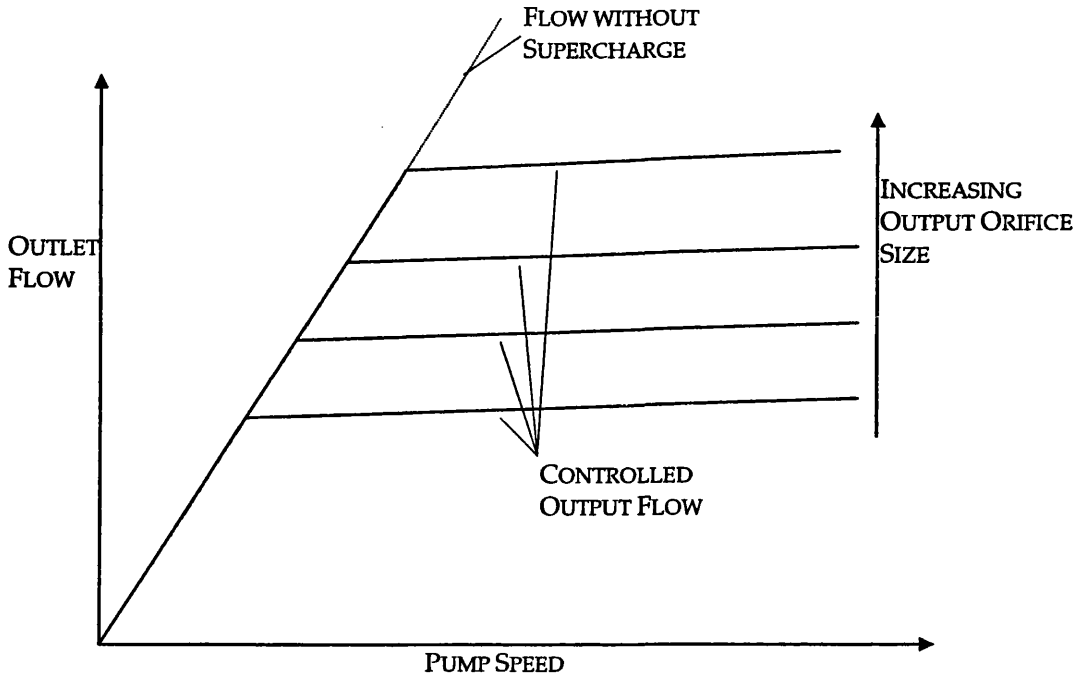

Figure 1–5: Power Steering Delivery Flow Characteristics

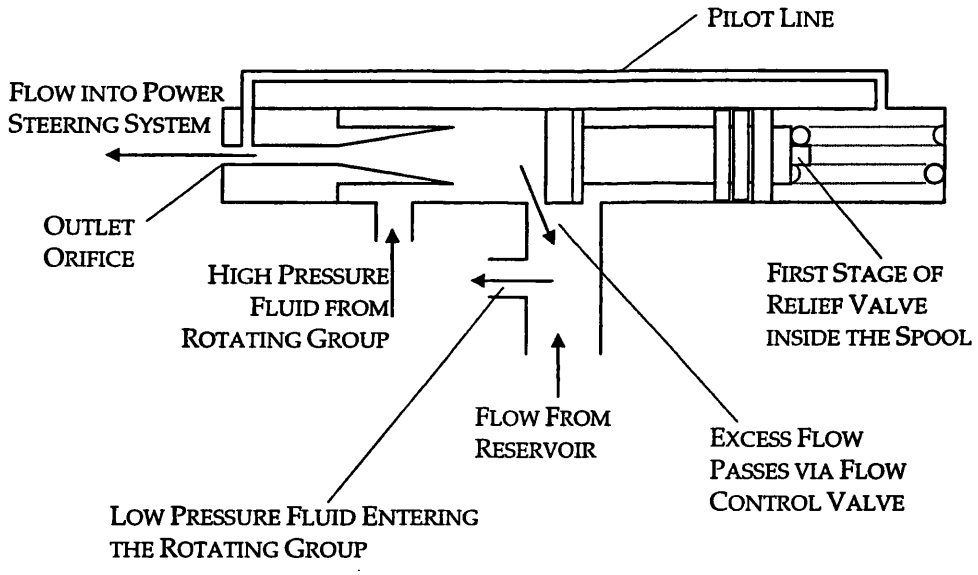

Figure 1–6: Supercharge Valve

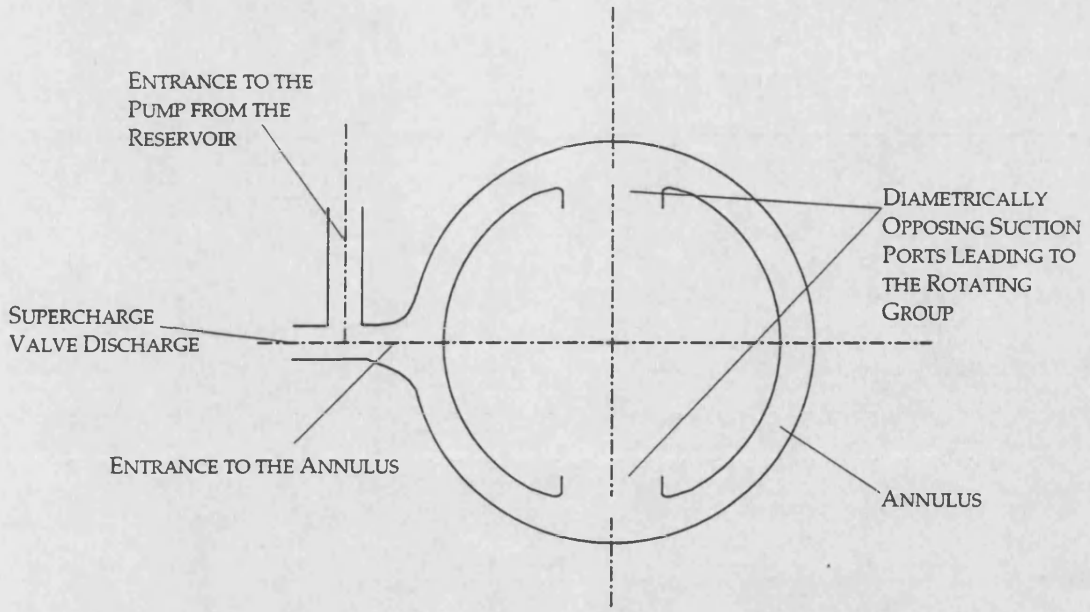

Figure 1–7: Passageways between Reservoir and Rotating Group

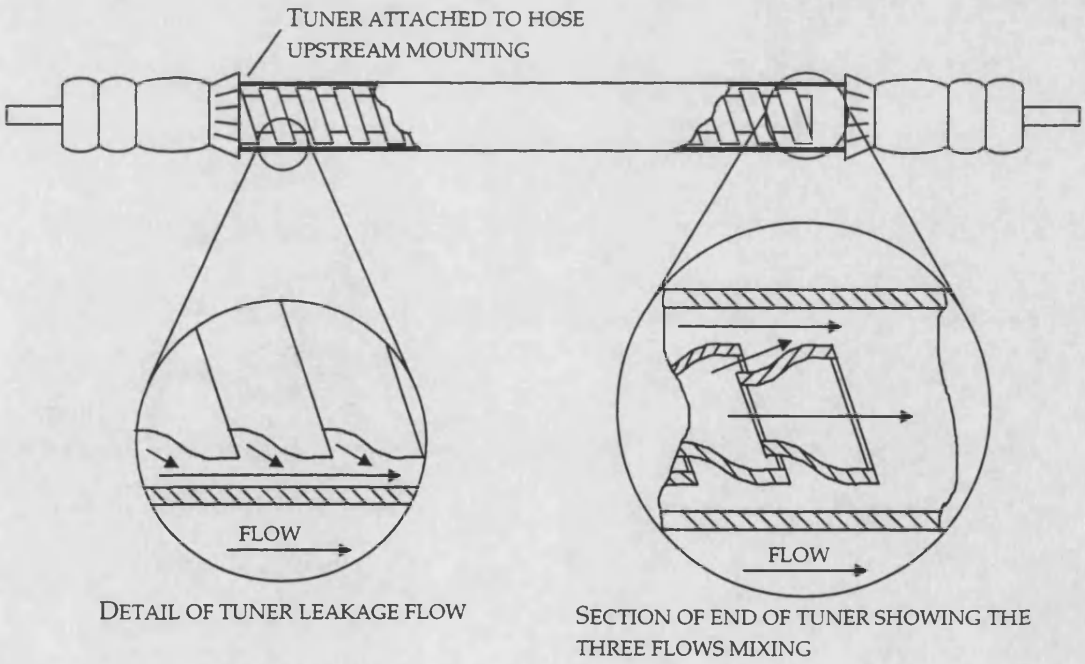

Figure 1–8: Flexible Hose with Tuner

2 THE EFFECT OF AERATION ON HYDRAULIC OIL

2.1 INTRODUCTION

The compliance of a hydraulic system can be greatly affected by the amount of air that is present in the oil. A reduction in the stiffness of a hydraulic system can cause stability problems, which in some cases can put the operator in danger. In power steering, a reduced bulk modulus may cause instability of the system or a slower dynamic response between the turning of the steering wheel and the front wheels of the car. Much research has been carried out on the effect of air in hydraulic oil and the effect on system performance due to increased compliance or heat loss. Aeration occurs in two different forms - either as bubbles or as air dissolved in the oil.

2.1.1 ENTRAINED AIR

Entrained air in a fluid can exhibit many different patterns ranging from uniformly distributed bubbles in the fluid to liquid droplets suspended in a stream of gas. In power steering, air is usually present in small quantities, which are assumed to be in the form of small bubbles.

Air may be entrained into a system from the reservoir, where if the surface of the oil is agitated, small pockets of air may be trapped in the fluid and carried into the pump suction line **(6, 7)**. Another source of air is from leakage at fittings, where the oil may not leak out of the system but air may be allowed to leak in. This situation could occur in an old system whose fittings have been worn by structural vibration. High-speed flow, such as in valves **(2, 8)** and other small orifices, creates localised low-pressure regions which may cause dissolved air to come out of solution. This can lead to an alteration of the discharge coefficient **(9)**, which may affect system response and cause unpredicted instability.

The effect of these air bubbles is to increase system compliance, which is analogous to a reduction in bulk modulus. The bulk modulus of air at atmospheric pressure is more than 10 000 times smaller than that of hydraulic oil and it can be shown that even a small percentage of air bubbles can considerably reduce the stiffness of the system. To show this effect, consider the following equation for effective bulk modulus, which takes oil and air properties into account (assuming a rigid container):

$$\frac{1}{B_e} = \frac{1}{B_1} + \frac{\alpha}{B_2} \qquad 2.1.1.1$$

Assuming that the bulk modulus of air, B_2, is so much smaller than that of the oil, B_1, that the oil stiffness can be neglected (i.e. $B_1 >> B_2/\alpha$) the effective bulk modulus can be approximated as a function of air content and stiffness alone:

$$B_e \approx \frac{B_2}{\alpha} \qquad 2.1.1.2$$

This shows that, when there is a significant amount of air present, the effective bulk modulus relies more on the individual bulk modulus of the air than that of the oil. For example, at atmospheric pressure for a typical oil with bulk modulus of $1.60\text{x}10^{9}\text{Nm}^{-2}$, equations 2.1.1.1 and 2.1.1.2 give the following for a 1% void fraction.

$$\frac{1}{B_e} = \frac{1}{1.6\times10^{9}} + \frac{0.01}{1\times10^{5}} = 9.938\times10^{6}\,\text{Nm}^{-2} \qquad 2.1.1.3$$

$$B_e \approx \frac{1\times10^{5}}{0.01} = 1\times10^{7}\,\text{Nm}^{-2} \qquad 2.1.1.4$$

Experiments have shown that the fluid viscosity is also affected by entrained air **(10)**. This is an empirical relationship defined as:

$$\frac{\mu_e}{\mu_0} = 1 + 1.5\alpha \qquad 2.1.1.5$$

This implies increased friction in the system and therefore more heating which could decrease the life of the oil. This is probably not significant in power steering systems, where the fluid lines are short and friction is therefore low. The small rise in viscosity, indicated in equation 2.1.1.5, may be beneficial in that it increases the damping of pressure transients.

Research has shown that although at low frequency bubble collapse is an isothermal process, at high frequency it becomes adiabatic **(11)**. This theory could therefore account for localised temperature rise where bubbles are collapsing inside pumps. However, this heating is only found to occur for large slugs of air and not for the size of bubbles which are normally found in hydraulic systems **(12)**.

Another consequence of entrained air is that it provides nuclei in which gaseous cavitation can take place. Small air bubbles are the seeds where vapour escapes to when system pressure drops **(12)** although Holl *et al.* suggest that surface rather than free stream nuclei may be more influential **(13)** because of the high surface tension of spherical bubbles.

Methods used to prevent entrained bubbles include placing fine gauze across the reservoir outlet, which traps the bubbles so that they are not carried into the system **(10)**. This however does not prevent air that is dissolved in the oil from coming out of solution after the oil has passed through the gauze into the system. A very large reservoir would also be a good means of reducing air bubbles because oil that enters from the return line would, in theory, have more settling time when air could rise to the surface before it re-enters the system.

2.1.2 DISSOLVED AIR

Henry's Law states that the solubility of a gas in a liquid is directly proportional to the partial pressure of the gas. Experiments have shown that, in the case of hydraulic oil at atmospheric pressure, approximately 10% air by volume is dissolved **(10, 14)**. If the pressure drops, the oil becomes supersaturated and air is released. Similarly, if the pressure rises, the under-saturated fluid dissolves air.

Although 10% seems like a large proportion, dissolved air has no appreciable effect on the compressibility or the viscosity of the oil. Study into air solubility in a single bubble or droplet system has been used to examine air solubility **(15, 16, 17, 18)**. The change in size of the bubble is looked at due to changes in pressure, temperature and other parameters. These studies show that Henry's Law is valid under laboratory conditions but in real terms can only be used as a rule of thumb.

Air is not released instantaneously from solution and the rate of evolution depends on many factors. The main criterion for air release is that there is a free surface for the air to escape to. This can be in the form of a surface in a reservoir **(14)** or the perimeter of an air bubble entrained in the fluid **(19)**. These surfaces are considered as weak points in the fluid analogous to cracks in a solid **(20)**. Hence, the tensile strength of the fluid is greatly reduced by these so-called cavitation nuclei and cavities can grow at pressures far below the tensile strength of the liquid. The void fraction, α, is commonly used to indicate the proportion of entrained air to oil in a given volume of fluid. In this way the bubbles need not be treated separately and calculation is made easier.

Another criterion is the temperature of the fluid because air release and vapour pressures are unique for any given temperature. The degree of agitation must also be considered as it can be seen with any carbonated drink that as it is shaken the dissolved CO_2 is released more quickly.

At some point in the system, the oil may become under-saturated as the local pressure increases and the bubbles will dissolve into the oil. Predicting the stability of these bubbles as they increase and decrease in size relies on knowledge of the surface tension and the initial size of the individual bubbles **(17, 21, 22)**. In a pump there are many small bubbles of different sizes and tracking the change in size of each bubble would not be possible and hence, in calculations the individual bubbles are replaced by the void fraction.

2.1.3 METHODS OF PREDICTING AIR RELEASE

Many methods of predicting air release are based on empirical equations, some of which are described in this section. Schweitzer *et al* **(14)** based his equations on the rate of evolution and solution of air from oil in a reservoir. The reservoir was agitated to expel the entrained air at which point the oil was assumed saturated. The pressure in the tank was then suddenly

lowered and the air released from the super-saturated solution was measured. The experiments showed a marked difference between the rate of evolution and solution, which sometimes took over twice as long. This is probably because before being dissolved, the air bubbles are compressed so that the available surface area for diffusion is reduced, which implies that the rate of evolution and solution relies on the existing void fraction. Another experiment used a pressure wave travelling along a pipe in order to measure gas release from water **(19)**. Both experiments showed that the oil reached its new saturation point not instantaneously but it increased exponentially of the form:

$$V_t = \left(V_2 - V_2^*\right)e^{-kt} + V_2^* \qquad 2.1.3.1$$

Where the total volume of air, V_t is a function of the original air volume, V_2 and the air volume at the new pressure, V_2^*. Air release can occur in the suction ports of pumps if the pressure loss is sufficient. Hibi *et al* **(1, 2)** identified four main sources of pressure loss in the suction port of a piston pump. These losses were due to:

i. axial flow velocity;
ii. tangential velocity;
iii. centrifugal force and
iv. oil inertia.

The air that is released in the suction port gradually dissolves into the oil as the pressure rises. It is possible however that air bubbles could be transferred through the pump into the delivery line, which could affect system performance. This method does not predict the rate of air release, just whether it will be released or not. In a pump the air would be released consistently and an equilibrium state would be reached. This steady-state value is of more interest when attempting to model suction port characteristics.

Only the occurrence of air release has been discussed here. Cavitation, which occurs at a far lower pressure (the vapour pressure for oil is usually between 1 and 2mbar), is less likely to be seen in a well designed pump. Theoretical models for predicting cavitation are not good and the understanding of the subject is still shallow **(23)**. Most work that attempts to predict cavitation defines a lower limit to system pressure. When this pressure is reached, continuity is satisfied by a cavity growth term **(24)**. In the case of a vane pump, where the flows are small, the pressure is unlikely to drop below the vapour pressure. Therefore, air evolution is more of a problem than cavitation. The only place where cavitation occurs is at the discharge of the supercharge valve and because the bubbles collapse instantaneously, the dynamics at the rotating group are unaffected. Reference **(2)** states that prototype pumps which have been disassembled after initial tests show evidence of cavitation in the region of the supercharge. The evidence, which is seen in such cases, is in the form of a pitted surface on the inside of the pump in the region where cavitation takes place. This pitting is caused as the vapour bubbles move to an area of higher pressure and collapse. The high pressures caused by the collapsing bubble

creates a miniature explosion which, if in close proximity to a surface can cause wear which over a long period causes a degradation in the surface smoothness. Reference **(2)** goes on to state that durability problems caused through excessive pitting must be avoided and it goes on to give a solution to the problem. This is a method of altering the discharge coefficient of the supercharge by adding chamfers to the edges and therefore reducing the amount of flow separation from the surface.

2.2 FLOW VISUALISATION OF AIR IN SUCTION PORT PASSAGES

The amount of air present in a hydraulic system is difficult to calculate because the rate of evolution and solution of gas bubbles depends upon too many parameters for it to be easy to model. Flow visualisation is therefore a good method of assessing air content under certain operating conditions. Flow visualisation is most easily achieved by placing a Perspex window in the pump housing such as in Figure 2–1. The window displays a section of annulus adjacent to two suction ports. The presence of air and the effect of pump speed and reservoir pressure can be analysed by photographing the window over a range of conditions.

2.2.1 TEST 1: PUMP WITHOUT SUPERCHARGE VALVE

It is known that air comes out of solution in the jet caused by the supercharge valve **(2)** but this test shows that there are other sources of aeration inside the pump. Reference **(2)**, as well as using CFD, uses photography to investigate the flow in the supercharge outlet. The photographs were taken through a window, which was fitted to the pump housing in the region of the supercharge outlet. The photographs clearly show that there is a region where flow separates from the surfaces of the pump and cavities are formed. Further downstream of the outlet, it can be seen that a lot of the bubbles have collapsed. It is in this transitional region where the bubbles collapse that pitting forms on the surface of the pump. In all the tests carried out in Reference **(2)**, the valve is open which does not give the opportunity for examining other potential sources of aeration within the pump. For this reason a window was placed into a pump in the housing surrounding the annulus which feeds oil to the suction ports. It is shown in Figure 2–1 that this window cannot be extended to show the ports, which are located beyond the left and right-hand edges of the window, because of the location of the seals. This pump was then used, with the supercharge sealed closed, in order to highlight that there are other sources of air bubble creation within the suction side of the pump.

The pump was run with reservoir pressures of 1bar and 3bar, a delivery pressure of 20bar and speeds of 1400, 900 and 400rev/min. The oil in the pump was photographed after 10mins to monitor bubble content. Figure 2–2 shows that at 1400rev/min, bubbles came out of solution at 1bar but at 3bar there were no bubbles. The bubbles, which were photographed, collected on the edges of the Perspex plate, which was sealed so that no air could be entrained from the atmosphere. The effect of boosting the pressure was to eliminate the aeration. At lower pump

speeds there were no observable air bubbles at 1bar, which can be seen in Figure 2–3. This test shows that, in an empirical function for air release, both pressure and speed must be taken into account.

2.2.2 TEST 2: PUMP WITH SUPERCHARGE VALVE

The test in §2.2.1 was repeated but with the supercharge valve operating. The valve returns flow from delivery to suction thus giving a uniform delivery flow over a range of speeds. This means that the higher the pump speed, the greater the flow through the valve. The bubbles created in the jet at the valve discharge can be seen. In Figure 2–4, the test at 400rev/min shows that at low speed when the valve is closed there are still no bubbles present. In Figure 2–5, the pump is at 900rev/min and there are some bubbles present but by boosting the reservoir pressure the bubbles remain dissolved in the oil. The same is seen at 1400rev/min, which is shown in Figure 2–6.

2.2.3 DISCUSSION OF FLOW VISUALISATION RESULTS

It can be seen that without the supercharge valve installed in the pump there is a definite correlation between pump speed, pressure and bubble content. With the reservoir at atmospheric pressure the bubble content increases with pump speed. Far fewer bubbles are visible if the reservoir pressure is boosted.

It has been previously demonstrated that bubbles are created in the jet of the supercharge **(2)**. The test in §2.2.2 shows evidence that some of these bubbles are carried into the pump thus decreasing the bulk modulus of the mixture in the annulus around the rotating group. This is best demonstrated in the tests at 900rev/min: in Figure 2–3 there are no bubbles with the supercharge closed but with the valve operating (Figure 2–5), there are bubbles present in the window.

These results will be used later in this thesis as a guide to derive an empirical function to describe bubble content as a function of pump speed and reservoir pressure. No quantitative results can be gained from this study, however trends can clearly be seen which will be useful in defining the bulk modulus, viscosity and density of the oil.

2.3 EQUATIONS FOR FLOW IN BUBBLY MIXTURES

Several algebraic techniques exist to solve two-phase flow problems. For example, there is the Homogeneous Model **(25)** that treats the two phases as one with their properties averaged and does not take the flow pattern into account. In the Drift-Flux Model **(25)**, attention is focused on the relative motions of the two phases. A more general model is the Separated Flow Model **(25)** where the phases are considered to flow side by side and equations of phase interaction are employed to maintain continuity.

The Separated Flow Model has been successfully used to calculate wave propagation in long pipes **(19, 26)** using numerical techniques to solve the resultant simultaneous partial differential equations. In the case of shorter tubes, these equations can be simplified to give results in the form of the wave propagation coefficient. This enables the speed of sound in the mixture to be found and hence the bulk modulus.

Another technique, which has been used to predict wave propagation, is to consider how sonic velocity is influenced by the elasticity of the confining wall between the phases **(27)**. The method has been applied to an oil-column with a homogeneously distributed amount of air-bubbles. The model compares well with experimental data and has been adapted to describe many different types of flow pattern.

2.3.1 THE SEPARATED FLOW MODEL

Consider the control volume containing a two-phase flow, which in the Separated Flow Model are treated separately (Figure 2–7). Two continuity equations can be applied, one for the liquid phase and one for the gas phase:

$$\frac{\partial}{\partial t}(1-\alpha)\rho_1 + \nabla(1-\alpha)\rho_1 w_1 = S_{12} \qquad 2.3.1.1$$

$$\frac{\partial}{\partial t}\alpha\rho_2 + \nabla\alpha\rho_2 w_2 = S_{21} \qquad 2.3.1.2$$

If one dimensional flow and a no slip condition (w_1=w_2) are considered, the equations can be integrated across the cross-section to give:

$$\frac{\partial}{\partial t}(1-\alpha)\rho_1 A + \frac{\partial}{\partial z}(1-\alpha)\rho_1 wA = \int S_{12}dA \qquad 2.3.1.3$$

$$\frac{\partial}{\partial t}\frac{\partial}{\partial t}\alpha\rho_2 A + \frac{\partial}{\partial z}\alpha\rho_2 wA = \int S_{21}dA \qquad 2.3.1.4$$

One more equation of continuity can be added to give the relationship between the two phases. In a pump, the void fraction can be assumed constant when the pump has been running at a constant speed for a long time. If this is the case, the rate of change of phase with respect to time can be considered to be zero, thus:

$$S_{12} = S_{21} = 0 \qquad 2.3.1.5$$

Substituting Equations 2.3.1.3 and 2.3.1.4 into 2.3.1.5 and also assuming the control volume has a constant cross-section, the following relationship is found:

$$-\frac{\partial q}{\partial z}=\frac{A}{B_e}\frac{\partial p}{\partial t} \qquad 2.3.1.6$$

B_e is the effective bulk modulus, which depends on void fraction and is defined in Equation 2.1.1.1.

The other equation which is needed to describe the system is the momentum equation. Again, the two phases are treated separately but the velocity of each phase is once again assumed equal.

$$\rho_1\left(\frac{\partial w}{\partial t}+w\nabla w\right)=f_1-\nabla p \qquad 2.3.1.7$$

$$\rho_2\left(\frac{\partial w}{\partial t}+w\nabla w\right)=f_2-\nabla p \qquad 2.3.1.8$$

The equations are now put into one-dimensional form and combined, assuming that the axial velocity is constant across the control volume, to give:

$$-\frac{\partial p}{\partial z}=\frac{(1-\alpha)\rho_1+\alpha\rho_2}{A}\frac{\partial q}{\partial t}+\frac{f_t}{A} \qquad 2.3.1.9$$

Where, $f_t=f_1+f_2$ which is the combined friction force for the two phases. By taking Fourier transforms of Equations 2.3.1.6 and 2.3.1.9, the two following relationships can be found:

$$\frac{d^2P}{dz^2}=\gamma^2P \qquad 2.3.1.10$$

$$\frac{d^2Q}{dz^2}=\gamma^2Q \qquad 2.3.1.11$$

Where γ is the wave propagation coefficient, which is a frequency dependent term defined as:

$$\gamma=\sqrt{-\frac{\omega^2}{B_e}[(1-\alpha)\rho_1+\alpha\rho_2]+j\frac{f_tA\omega}{B_e}} \qquad 2.3.1.12$$

Hence, the wave propagation coefficient depends on both the void fraction and the friction in the two phases of the flow. If the friction term is neglected, by considering it to be negligible for a short pipe, the term becomes:

$$\gamma=\frac{j\omega}{\sqrt{\frac{B_e}{(1-\alpha)\rho_1+\alpha\rho_2}}}=\frac{j\omega}{c} \qquad 2.3.1.13$$

Hence, if the sonic velocity of the air-oil mixture is known or can be predicted, the motion of the waves in a uniform section can be modelled.

2.3.2 SONIC VELOCITY AS A FUNCTION OF WALL ELASTICITY

Nguyen *et al* **(27)** derived an equation for the sonic velocity in a two-phase mixture by considering the elasticity of the boundaries between the phases. It is an adaptation of the theory that states that sonic velocity of a fluid depends on the elasticity of the walls in which it is contained. In this case, the elastic walls are considered to be equivalent to boundaries between phases. The relationship depends upon the density of each phase, the speed of sound in each phase and the void fraction. The relationship is:

$$c = \frac{1}{(1-\alpha)\sqrt{\frac{1-\alpha}{c_1^2} + \frac{\alpha\rho_1}{\rho_2 c_2^2}} + \alpha\sqrt{\frac{\alpha}{c_2^2} + \frac{(1-\alpha)\rho_2}{\rho_1 c_1^2}}} \qquad 2.3.2.1$$

Equation 2.3.2.1 can be used to define the speed of sound in the mixture, which is required for calculating the wave propagation coefficient in the system.

2.3.3 COMPARISON OF EXPRESSIONS FOR SONIC SPEED

Reference **(27)** details why a different method of computing the speed of sound has been used. Equation 2.3.1.13 uses a method derived from a standard calculation used for determining sonic velocity in single-phase systems. There are no assumptions made as to the form of the bubbles in the fluid, which leads to the use of modified density and bulk modulus terms to take void fraction into account. On the other hand, Reference **(27)** considers the form in which the aeration is found and Equation 2.3.2.1 specifically describes the flow in a homogeneous two-phase flow. That is to say, a flow where there is a uniform distribution of gas bubbles across the entire control volume as opposed to a slug flow or stratified flow, which are also represented in Reference **(27)**. Hence, these different assumptions give rise to two independent approximations to a complicated mechanism in which the speed of sound is not constant but varies according to which medium the wave is travelling through at any given point in time.

In hydraulic systems the percentage of air present as bubbles is usually small. Figure 2–8 shows a comparison for Equations 2.3.1.13 and 2.3.2.1 in the range $0 \leq \alpha \leq 0.05$. The two Equations only show a minute divergence as the void fraction increases. This indicates that either equation (2.3.1.13 or 2.3.2.1) could be used to predict the speed of sound and hence the wave propagation coefficient. Whichever equation is used depends on the parameters that are known.

2.4 EXPRESSIONS FOR THE OIL PROPERTIES

So far in this chapter, aeration has been discussed together with some methods of evaluating the amount of air in the oil and hence the effect on oil properties. There are three properties that must be considered that are necessary for inclusion into a mathematical pump simulation. The properties are the viscosity, the density and the bulk modulus and expressions for each of these are discussed in this section.

2.4.1 VISCOSITY

Viscosity is an important term, which must be known in order to evaluate the viscous damping in a system. As discussed in §2.1.1, Hayward (10) derived the empirical equation (2.1.1.3) for viscosity:

$$\frac{\mu_e}{\mu_0} = 1 + 1.5\alpha \qquad 2.4.1.1$$

The viscosity of the oil can be found from data supplied by the fluid manufacturers and is usually a function of temperature.

2.4.2 DENSITY

Density is the sum of the density of each phase in a mixture multiplied by its proportion:

$$\rho = (1-\alpha)\rho_1 + \alpha\rho_2 \qquad 2.4.2.1$$

The proportion of air (the void fraction) depends on the pressure of the system, as does the density of air. If air is considered to be a perfect gas, the expression becomes:

$$\rho = \left(1 - \frac{p_0\alpha_0}{p}\right)\rho_1 + \frac{p_0\alpha_0}{RT} \qquad 2.4.2.2$$

Figure 2–9 shows the density function at two pressures: atmospheric pressure and at a boosted pressure of 3bar. Both curves show the obvious result that the density of the mixture reduces as the amount of air in the system increases. It can be seen that with boosted pressure, aeration has a lesser effect on the density of the oil because the bubbles take up a smaller proportion of the overall volume.

2.4.3 BULK MODULUS

The bulk modulus of oil depends on the amount of air present and the pressure of the mixture. The bulk modulus of the system can be derived from Equation 2.1.1.1. For a two-phase mixture, Equation 2.1.1.1 can be rewritten, thus:

$$B_e = \frac{B_1 p^2}{p^2 + B_1 \alpha p_0} \qquad 2.4.3.1$$

Figure 2–10 shows that the function has a large effect on the stiffness of the system at atmospheric pressure. For just 1% of air in the oil in the suction line of a pump, the bulk modulus could be reduced by a factor of over 100.

2.5 CONCLUSIONS

Dissolved air coming out of solution may be a major factor affecting the noise characteristics of suction ports. It has been seen that air bubbles alter the bulk modulus, density and viscosity of the fluid. Air is not released instantaneously but gradually and the time constant of evolution is usually considered to be less than that of solution. Inside the pump there is assumed to be a constant amount of air shortly after start-up when the void fraction has increased to a steady state value. It has been seen, though, that there are areas inside the pump where the amount of bubbles may be greater: for instance, the supercharge valve outlet. In this area, there is a low-pressure fluid jet which causes cavitation and air release. This means that whenever the valve is opened, the bulk modulus of the oil is reduced because of the pocket of bubbly oil in the outlet. The bulk modulus will be greater downstream of the supercharge outlet where the pressure is greater and the bubbles reduce in volume until they are eventually absorbed.

Flow visualisation techniques were used to investigate whether air was present in the pump housing. The presence of bubbles in the pump was found to be dependent on three factors:

- pump speed;
- reservoir pressure,
- the supercharge valve.

The speed of the pump controls the speed at which fluid flows from the reservoir. Hence, if the speed of the liquid travelling through orifices inside the pump were increased by running the pump at a higher rate, the pressure at the discharges would reduce allowing more air to come out of solution and be entrained as bubbles. The reservoir pressure represents the starting point from which the pressure drops are subtracted. This means that, the higher the initial pressure, the more losses are allowable before problems with very low pressures begin. The reasons why the supercharge creates bubbles are a function of the two previous examples. For instance, if the pump runs at a low speed, there is no problem of air being introduced into the system by the supercharge valve because it is closed. Also, the reservoir governs the pressure in the supercharge outlet, hence reducing the pressure difference across the valve and lowering the flow rate, which means a reduction in the amount of air coming out of solution.

Two methods of predicting the speed of sound were investigated and elements of these were used to develop functions for the oil properties. The functions for bulk modulus, density and viscosity were developed, which describe the properties of the two-phase mixture. They use the assumption that the control volume, which they describe, has a uniform distribution of bubbles. There is no assumption regarding the shape of the bubbles. This does however still allow for the variation in oil properties in different parts of the pump housing where the void fraction may be different.

FIGURES FOR CHAPTER 2

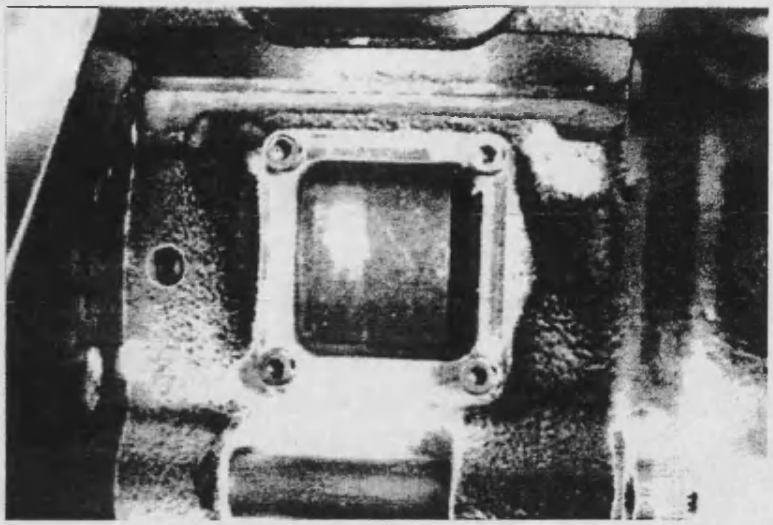

Figure 2–1: Position of Window in Pump Housing

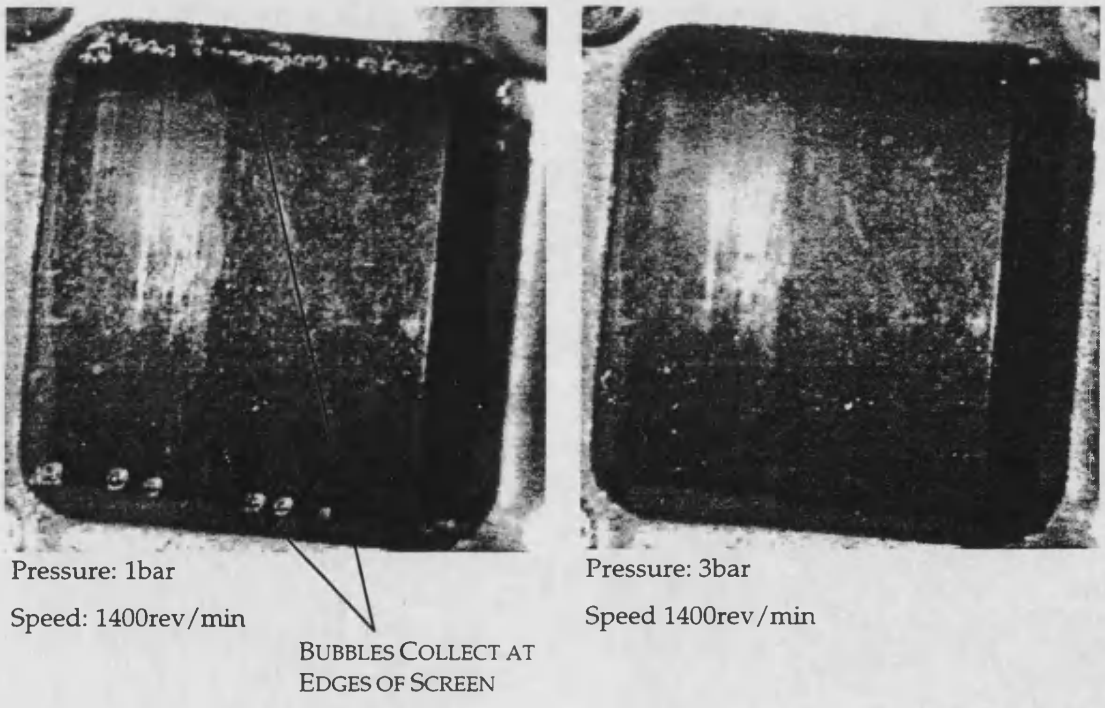

Figure 2–2: Bubble Content in the Pump Housing at 1400rev/min (without Supercharge)

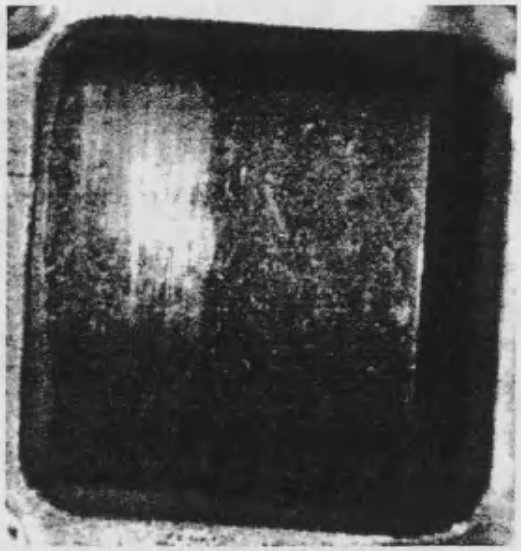

Pressure: 1bar

Speed: 900rev/min

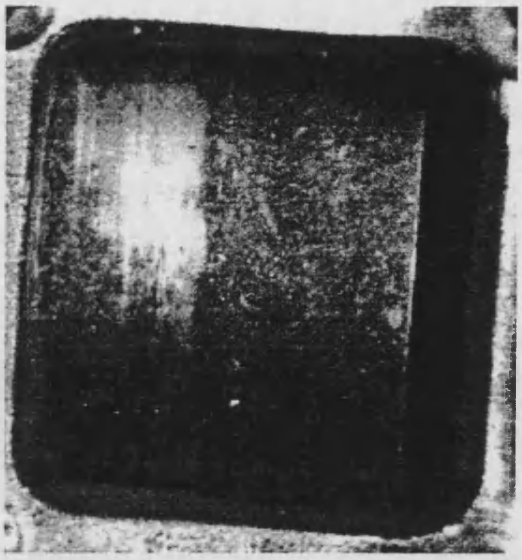

Pressure: 1bar

Speed: 400rev/min

Figure 2–3: Flow Visualisation on Pumps without Supercharge at Low Speed

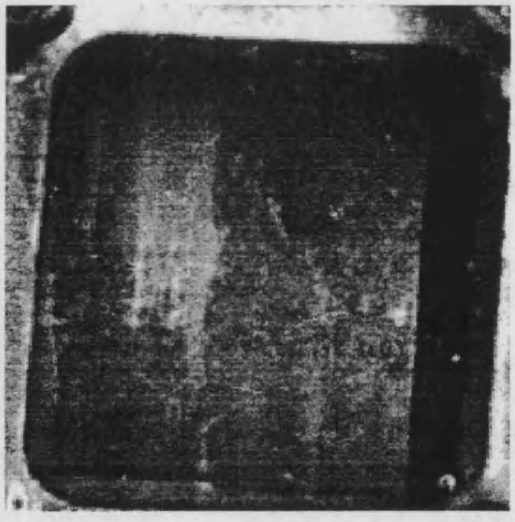

Figure 2–4: Pump with Supercharge at 400rev/min and at Atmospheric Pressure

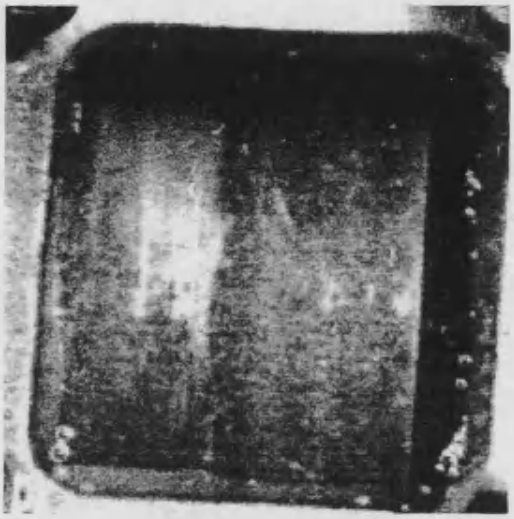

Pressure: 1bar

Speed 900rev/min

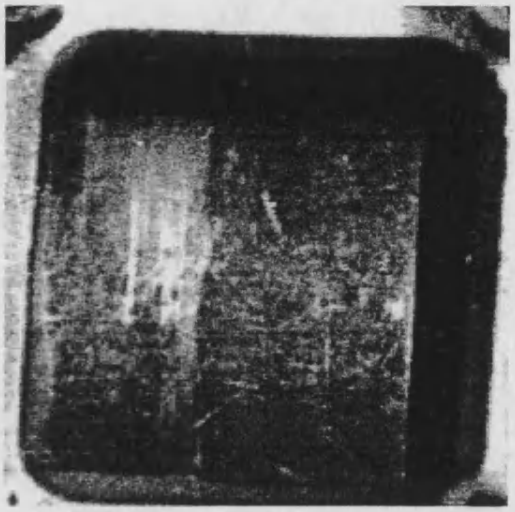

Pressure: 3bar

Speed: 900rev/min

Figure 2–5: Pump with Supercharge at 900rev/min

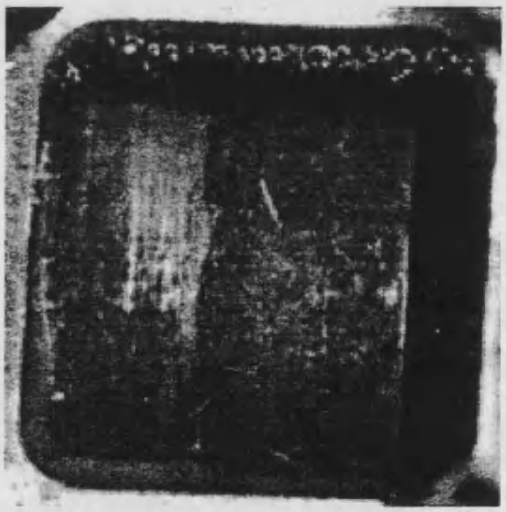

Pressure: 1bar

Speed 1400rev/min

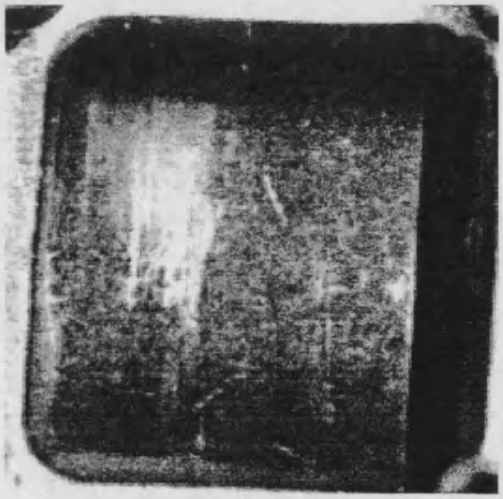

Pressure: 3bar

Speed 1400rev/min

Figure 2–6: Pump with Supercharge at 1400rev/min

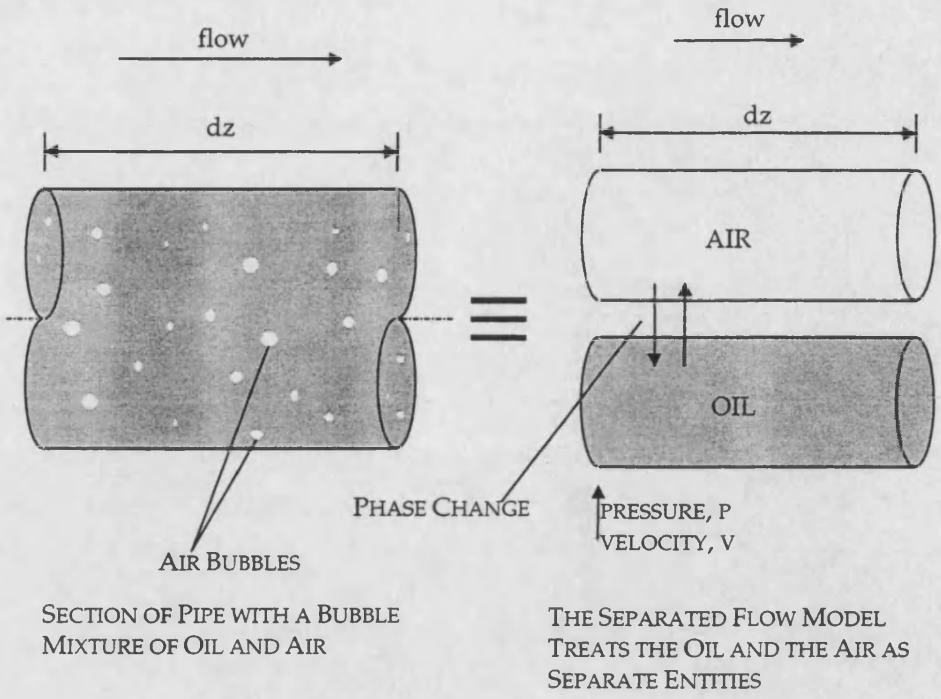

Figure 2–7: Control Volume for the Separated Flow Model

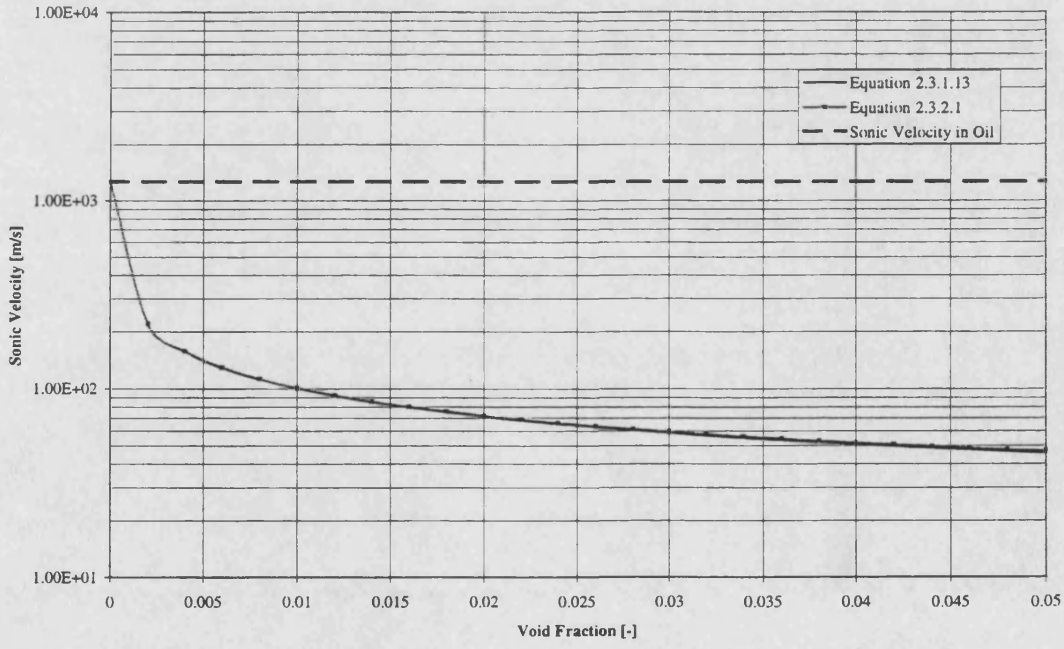

Figure 2–8: Comparison of Equations 2.3.1.13 and 2.3.2.1

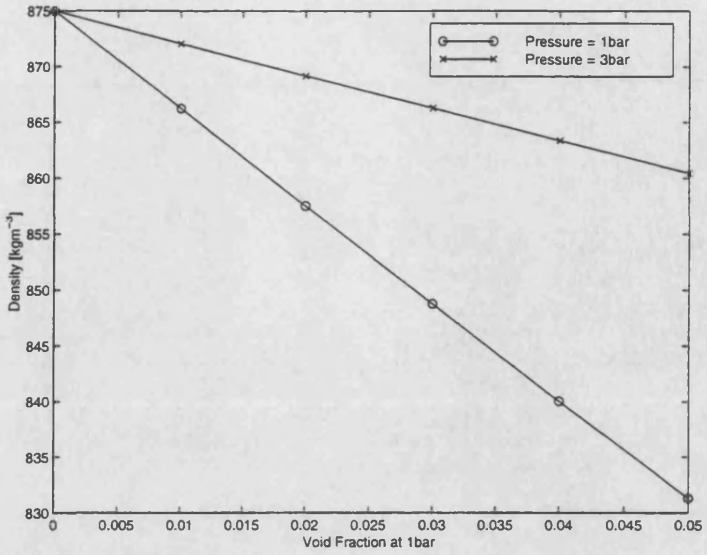

Figure 2–9: Density Function at Two Pressures

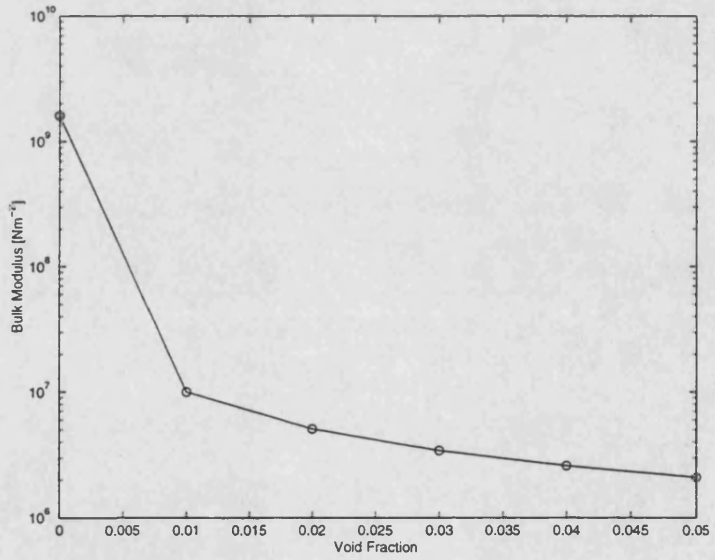

Figure 2–10: Bulk Modulus Function at Atmospheric Pressure

3 SUCTION PORT IMPEDANCE MODEL

3.1 INTRODUCTION

Flow ripple, which is created at the rotating group of a positive displacement pump, interacts with the impedance of the circuit to produce pressure ripple. The impedance of the piping and other uniform-sectioned components can be found by application of the wave equation. However, the geometry of the flow passages inside a pump is not uniform and requires more complicated modelling techniques to predict their impedance. The impedance of components with complicated geometry can be measured but for simulation purposes, a validated mathematical model must be used.

The secondary source method is a good technique for measuring the impedance of hydraulic components **(3, 28, 29, 30)**. Published results show the versatility of the method: the impedance of orifices **(31)**, restrictors and flow control valves **(32)** and relief valves and accumulators **(33)** can all be measured. The method is also suitable for measuring the impedance of the ports on pumps, and, it will be seen from Chapter 5 onwards, it is used to validate the model discussed in this chapter.

Transmission line modelling to solve non-linear lumped networks, which is used in electrical engineering, can be adapted for hydraulic lines **(34, 35, 36)**. This is a matrix based method in which the impedance of each branch of a network is considered as a time-discrete component. It has the advantage that there is a set of rules defined which allow very complicated circuits to be broken down and analysed with ease. The disadvantage is that the matrices have a tendency to become sparse when large, complicated circuits are being modelled. A simpler electrical analogy is the lumped two-port network model **(5)**, which assigns an equivalent resistance, inductance and capacitance to each fluid volume. The lumps are joined together in either series or parallel to give an approximate model of a hydraulic circuit. The method does not, however, take into account wave propagation effects or reflections at line intersections. The model is therefore considered to be too basic for a model where the frequency of interest is comparable to the natural frequency of the lines. This is almost always the case in impedance modelling where, unlike fluid hammer studies which concentrate only on the single frequency of the pressure pulse, a wide range of frequencies is modelled.

The transmission line modelling referred to above **(34, 35, 36)** treats the circuit as a network of lumped branches, whose conditions can only be calculated at the nodes. A true transmission line model uses the solution of the wave equations in order to give a distributed parameter model **(37, 38, 39)**. One such model of the impedance of a pump delivery port has already been published **(40)**. Distributed parameter models use solutions of the wave equations and include terms for wave propagation effects. This technique has been used to examine complicated

circuits, in which dissimilar lines are linked, by calculating reflection coefficients at the joins. One adaptation of this technique is the use of scattering matrices at the links, which is part of the de-coupled waves technique **(41, 42)**. This method is used in modelling transmission lines in the time domain and is efficient because, instead of calculating pressure and flow at discrete intervals along the length of the line, it calculates line effects at the end of the line. This cuts down on the amount of calculation time involved, thus streamlining the simulation.

Distributed parameter models break down the circuit sections into a characteristic impedance and a wave propagation coefficient. These two terms are calculated with the electrical equivalent series impedance and shunt admittance. The series impedance term can be modified to include frequency dependent damping **(43, 44, 45, 46)**, which is derived from the Navier-Stokes equation and represents the effect of viscosity.

The de-coupled waves technique was chosen as the method to calculate the pump's port impedance in this thesis because of its flexibility. The impedance model calculated here is a frequency dependent function but it could however be calculated equally well in the time domain. The initial rationale for choosing a time domain method was superseded because of the requirement to validate the model against test results. It will be seen in Chapter 6 that the test method gives impedance results as a function of frequency and it was therefore decided at an early stage of this study to alter the technique from a time domain to a frequency dependent calculation. However, the method was kept because the initial research suggested its adaptability from time domain to frequency domain and its suitability for the task.

3.2 THEORY

The characteristic impedance and the wave propagation coefficient are necessary whichever of the above modelling techniques is used. Derivations of these properties are found in numerous publications, one example can be found in Reference **(43)**. In hydraulics, they are defined by geometry and oil properties and can be derived from the wave equation, as follows (assuming no damping):

$$\frac{\partial p}{\partial z} = -\frac{\rho}{A}\frac{\partial q}{\partial t} \qquad 3.2.1$$

$$\frac{\partial q}{\partial z} = -\frac{A}{B_e}\frac{\partial p}{\partial t} \qquad 3.2.2$$

The Laplace transform of these equations gives the following:

$$\frac{\partial P}{\partial z} = -Z(s)Q \qquad 3.2.3$$

$$\frac{\partial Q}{\partial z} = -Y(s)P \qquad 3.2.4$$

$Z(s)$ is the series impedance per unit length and $Y(s)$ is the shunt admittance per unit length. The product of impedance and admittance gives the wave propagation coefficient, γ, where:

$$\gamma^2 = Z(s)Y(s) = s^2\frac{\rho}{B_e} \qquad 3.2.5$$

Characteristic impedance, Z_0, which is equivalent to the impedance of an infinitely long, reflectionless line, is defined as:

$$Z_0 = \sqrt{\frac{Z(s)}{Y(s)}} = \frac{\sqrt{\rho B_e}}{A} \qquad 3.2.6$$

These equations apply to uniform transmission lines but they can be used to approximate the characteristics of tapering lines. This obviously introduces errors into the expression for characteristic impedance, which is a function of cross-sectional area. Consider a 12.5mm long line whose area tapers outwards in the form:

$$A(z) = A_0 e^z \qquad 0 \le z \le 1.25\times10^{-2}\,\text{m} \qquad 3.2.7$$

This line has similar dimensions to a section of passageway that might be found inside the suction port of a power steering vane pump. The inductance and capacitance of this line can be calculated exactly as follows:

$$L = \frac{\rho}{A_0}\int_0^{0.0125} e^{-z}dz = -\frac{4.0\times1.0\times10^3}{\pi\left(1.0\times10^{-2}\right)^2}\left(e^{-0.0125}-1.0\right) = 1.5816436\times10^5\ \text{kg/m}^4 \qquad 3.2.8$$

$$C = \frac{A_0}{B_e}\int_0^{0.0125} e^{z}dz = \frac{\pi\left(1.0\times10^{-2}\right)^2}{4.0\times1.6\times10^9}\left(e^{0.0125}-1.0\right) = 6.174433\times10^{-16}\ \text{m}^5/\text{N} \qquad 3.2.9$$

This line has been chosen because there is an exact analytical solution. Most of the time this is not the case and the mean value of this line can be used as an estimation to approximate the tapered line as a uniform one. The average area of this line is as follows:

$$\overline{A} = \frac{1}{\ell}\int_0^{\ell} A(z)dz = \frac{\pi\left(1.0\times10^{-2}\right)^2}{4.0\times1.25\times10^{-2}}\left(e^{0.0125}-1.0\right) = 7.9032742\times10^{-5}\,\text{m}^2 \qquad 3.2.10$$

This mean cross-sectional area term can now be used in the expressions for inductance and capacitance of a uniform line, thus:

$$L = \frac{\rho \ell}{\overline{A}} = \frac{1.0\times10^{3}\times1.25\times10^{-2}}{7.9032742\times10^{-5}} = 1.581623\times10^{5}\ \mathrm{kg/m^4} \qquad 3.2.11$$

$$C = \frac{\overline{A}\ell}{B_e} = \frac{7.9032742\times10^{-5}\times1.25\times10^{-2}}{1.6\times10^{9}} = 6.174433\times10^{-16}\ \mathrm{m^5/N} \qquad 3.2.12$$

It can be seen that this type of approximation gives an exact value for the capacitance but as the line length increases, the approximation of the line inductance becomes more inaccurate. This is not a problem in the case of most of the pump's passageways where the flow paths are short. Later in this chapter, the consequences of using such approximations will be demonstrated in terms of the calculated impedance, especially in the case of longer sections.

3.2.1 AN EXPRESSION FOR DAMPING

Damping due to viscous effects, which is defined by the Navier Stokes equation, plays an important role in the definition of pump source impedance. Figure 3–1 shows fluid travelling along a pipe with a parabolic flow profile, which for one-dimensional flow is defined by the following relationship:

$$\frac{\partial^2 w}{\partial r^2} + \frac{1}{r}\frac{\partial w}{\partial r} - \frac{1}{\nu}\frac{\partial w}{\partial t} = \frac{1}{\nu\rho}\frac{\partial p}{\partial z} \qquad 3.2.1.1$$

Taking Laplace transforms of Equation 3.2.1.1 gives:

$$\left[\frac{\partial^2}{\partial r^2} + \frac{1}{r}\frac{\partial}{\partial r} + K^2\right]W = \frac{1}{\mu}\frac{\partial P}{\partial z} \qquad \text{where } K^2 = -\frac{s}{\nu} \qquad 3.2.1.2$$

If the pressure gradient is assumed to be constant, Equation 3.2.1.2 has the standard solution of the form:

$$W_r = \frac{dP}{dz}\frac{1}{\mu K^2}\left[1 - \frac{J_0(Kr)}{J_1(Kr)}\right] \qquad 3.2.1.3$$

To find the total flow, Q, the flow at a radius, r, and the fluid velocity term, W_r, must be integrated over a surface, i.e.

$$Q = \int_0^R W_r 2\pi r dr = \frac{dP}{dz}\frac{1}{\mu K^2}\left[\pi R^2 + \frac{2\pi R J_0'(KR)}{K J_0(KR)}\right] \qquad 3.2.1.4$$

Using the relationship $J_0'(z) = -J_1(z)$, Equation 3.2.1.4 can be written in terms of the pressure gradient:

$$\frac{dP}{dz}=\frac{\mu K^2 Q}{\pi R^2\left[1-\frac{2J_1(KR)}{KRJ_0(KR)}\right]} \qquad 3.2.1.5$$

It therefore follows that the series impedance is a modified term with a frequency dependent factor describing viscous damping:

$$Z=\frac{\frac{\rho\ell}{\pi R^2}s}{\left[1-\frac{2J_1(KR)}{KRJ_0(KR)}\right]} \qquad 3.2.1.6$$

This modified series impedance term is used to calculate characteristic impedance and the wave propagation coefficient.

3.2.2 Development of the De-Coupled Waves Method

As mentioned in the introduction to this chapter, the de-coupled waves technique was initially chosen for the possibility of modelling impedance in the time domain as well as the frequency domain. This section, however, shows how the equations are applied to the frequency domain, which means that they can be validated using the test method described in Chapter 5. The de-coupled waves method is a 2x2 matrix that links the forward and backward travelling waves at the extremities of a fluid line, which is derived from the following transmission matrix:

$$\begin{bmatrix}P_u\\Q_u\end{bmatrix}=\begin{bmatrix}\cosh\gamma z & Z_0\sinh\gamma z\\ \frac{1}{Z_0}\sinh\gamma z & \cosh\gamma z\end{bmatrix}\begin{bmatrix}P_d\\Q_d\end{bmatrix} \qquad 3.2.2.1$$

The subscript, *u*, refers to the upstream end of the pipe and *d* refers to the downstream end. Flow is considered to be positive if it is flowing into the control volume. If the upstream conditions are known, the inverse transmission matrix is used:

$$\begin{bmatrix}P_d\\Q_d\end{bmatrix}=\begin{bmatrix}\cosh\gamma z & -Z_0\sinh\gamma z\\ -\frac{1}{Z_0}\sinh\gamma z & \cosh\gamma z\end{bmatrix}\begin{bmatrix}P_u\\Q_u\end{bmatrix} \qquad 3.2.2.2$$

Equation 3.2.2.2 can be written as simultaneous equations whose right-hand sides have identical coefficients:

$$P_d\sqrt{\frac{2}{Z_0}}=\frac{1}{\sqrt{2}}\left(\frac{P_u}{\sqrt{Z_0}}+\sqrt{Z_0}Q_u\right)e^{-\gamma z}+\frac{1}{\sqrt{2}}\left(\frac{P_u}{\sqrt{Z_0}}-\sqrt{Z_0}Q_u\right)e^{\gamma z} \qquad 3.2.2.3$$

$$Q_d\sqrt{2Z_0}=\frac{1}{\sqrt{2}}\left(\frac{P_u}{\sqrt{Z_0}}+\sqrt{Z_0}Q_u\right)e^{-\gamma z}-\frac{1}{\sqrt{2}}\left(\frac{P_u}{\sqrt{Z_0}}-\sqrt{Z_0}Q_d\right)e^{\gamma z} \qquad 3.2.2.4$$

If Equations 3.2.2.3 and 3.2.2.4 are written in terms of the two wave components, the expressions for pressure and flow become:

$$P = \sqrt{\frac{Z_0}{2}}(u+v) \qquad 3.2.2.5$$

$$Q = \frac{1}{\sqrt{2Z_0}}(u-v) \qquad 3.2.2.6$$

Where u and v describe the forward and backward travelling waves, which from Equations 3.2.2.3 and 3.2.2.4, for z=0, are defined as:

$$u = \frac{1}{\sqrt{2}}\left(\frac{P}{\sqrt{Z_0}} + \sqrt{Z_0}Q\right) \qquad 3.2.2.7$$

$$v = \frac{1}{\sqrt{2}}\left(\frac{P}{\sqrt{Z_0}} - \sqrt{Z_0}Q\right) \qquad 3.2.2.8$$

If Equations 3.2.2.5 and 3.2.2.6 are substituted into Equation 3.2.2.1, the transmission matrix defines forward and backward travelling waves, which are completely de-coupled from one another:

$$\begin{bmatrix} u_d \\ v_d \end{bmatrix} = \begin{bmatrix} e^{-\gamma x} & 0 \\ 0 & e^{\gamma x} \end{bmatrix} \begin{bmatrix} u_u \\ v_u \end{bmatrix} \qquad 3.2.2.9$$

This is the transmission matrix for a single fluid line that has no changes in cross-sectional area or branches, which was discussed by Boucher *et al* (42) and can be adapted as a mathematical model of suction port impedance. If there are changes in the line, waves are partially reflected and scattering matrices are used to link sections together in order to create more complicated geometry.

3.2.3 SCATTERING MATRICES

When a wave reaches a junction or an area change, some of it is reflected and some is transmitted into the new section. The scattering matrix, which describes the phenomenon, is derived from continuity of pressure and flow at the point of the junction. In the suction port of a pump, there are three cases where scattering matrices are required. They are at closed ends, at changes in cross-sectional area and at three-way junctions.

3.2.3.1 SCATTERING MATRIX AT A CLOSED END

At a blocked end, the flow is equal to zero and so the forward travelling wave is equal to the backward travelling wave:

$$u = v \qquad 3.2.3.1.1$$

Figure 3–2 shows a system consisting of a pipe with a closed end. There are four unknowns, which are the waves at either end of the pipe. These are solved with the following equations.

$$\begin{bmatrix} u_2 \\ v_2 \end{bmatrix} = \begin{bmatrix} e^{-\gamma\ell} & 0 \\ 0 & e^{\gamma\ell} \end{bmatrix} \begin{bmatrix} u_1 \\ v_1 \end{bmatrix} \qquad 3.2.3.1.2$$

$$u_2 = v_2 \qquad 3.2.3.1.3$$

$$u_1 = 1 \qquad 3.2.3.1.4$$

Equation 3.2.3.1.4 sets the forward travelling wave at the entrance to the system to an arbitrary value, in this case unity, as the impedance of the system is the same regardless of the pressure and flow conditions. These equations are solved in matrix form:

$$\begin{pmatrix} 1 & 0 & 0 & 0 \\ 0 & 1 & 0 & -1 \\ -e^{\gamma\ell} & 1 & 0 & 0 \\ 0 & 0 & -e^{-\gamma\ell} & 1 \end{pmatrix} \begin{pmatrix} u_1 \\ u_2 \\ v_1 \\ v_2 \end{pmatrix} = \begin{pmatrix} 1 \\ 0 \\ 0 \\ 0 \end{pmatrix} \qquad 3.2.3.1.5$$

The impedance is then calculated using Equations 3.2.2.5 and 3.2.2.6, which define impedance thus:

$$Z = \frac{P}{Q} \qquad 3.2.3.1.6$$

Substituting Equations 3.2.2.5 and 3.2.2.6 into 3.2.3.1.6 therefore gives the impedance at a given point. To find the entry impedance of the system in Figure 3–2, the waves at the entrance are used thus:

$$Z = Z_{01} \frac{(u_1 + v_1)}{(u_1 - v_1)} \qquad 3.2.3.1.7$$

where Z_{01} is the characteristic impedance of the entrance to the system.

3.2.3.2 SCATTERING MATRIX AT AN AREA CHANGE

At an expansion, shown in Figure 3–3, the flow and pressure at the discontinuity is equal for each section. Hence, from Equations 3.2.2.7 and 3.2.2.8:

$$\sqrt{\frac{Z_{02}}{2}}(u_2 + v_2) = \sqrt{\frac{Z_{03}}{2}}(u_3 + v_3) \qquad 3.2.3.2.1$$

$$\frac{1}{\sqrt{2Z_{02}}}(u_2 - v_2) = \frac{1}{\sqrt{2Z_{03}}}(u_3 - v_3) \qquad 3.2.3.2.2$$

These equations can be written in matrix form to give the scattering matrix for any area change:

$$\begin{bmatrix} v_2 \\ u_3 \end{bmatrix} = \frac{1}{Z_{02} + Z_{03}} \begin{bmatrix} Z_{03} - Z_{02} & 2\sqrt{Z_{02}Z_{03}} \\ 2\sqrt{Z_{02}Z_{03}} & Z_{02} - Z_{03} \end{bmatrix} \begin{bmatrix} u_2 \\ v_3 \end{bmatrix} \qquad 3.2.3.2.3$$

If the pipe shown in Figure 3–3 has a closed end at its right-hand side, the matrix required to solve the system is:

$$\begin{pmatrix} 1 & 0 & 0 & 0 & 0 & 0 & 0 & 0 \\ -T_1^{11} & 1 & 0 & 0 & -T_1^{12} & 0 & 0 & 0 \\ -T_1^{21} & 0 & 0 & 0 & -T_1^{22} & 1 & 0 & 0 \\ 0 & 0 & -T_2^{11} & 1 & 0 & 0 & -T_2^{12} & 0 \\ 0 & 0 & -T_2^{21} & 0 & 0 & 0 & -T_2^{22} & 1 \\ 0 & -S_1^{11} & 0 & 0 & 0 & 1 & -S_1^{12} & 0 \\ 0 & -S_1^{21} & 1 & 0 & 0 & 0 & -S_1^{22} & 0 \\ 0 & 0 & 0 & 1 & 0 & 0 & 0 & -1 \end{pmatrix} \begin{pmatrix} u_1 \\ u_2 \\ u_3 \\ u_4 \\ v_1 \\ v_2 \\ v_3 \\ v_4 \end{pmatrix} = \begin{pmatrix} 1 \\ 0 \\ 0 \\ 0 \\ 0 \\ 0 \\ 0 \\ 0 \end{pmatrix} \qquad 3.2.3.2.4$$

Where T_a^{mn} are the coefficients of the transmission matrices for the two lines and S_a^{mn} are the coefficients of the scattering matrix. The entry impedance is found the same way as in §3.2.3.1.

3.2.3.3 SCATTERING MATRIX AT A THREE-WAY JUNCTION

At a three-way junction (Figure 3–4) the pressure is equal for each section and the flow obeys the continuity equation. Boucher *et al* **(42)** shows that scattering matrices for junctions are easier to define as admittance rather than impedance terms and that they all follow the following formulae:

$$S_{nn} = \frac{2Y_n}{\sum K} - 1 \qquad 3.2.3.3.1$$

$$S_{nm} = \frac{2\sqrt{Y_n Y_m}}{\sum K} \qquad 3.2.3.3.2$$

Where ΣK is the sum of all the admittances of the three sections at the junction. The matrix describing the junction shown in figure 3–4, which is a simple circuit, is 12x12. It can be seen that matrices that describe complicated geometry are very large indeed and can only be efficiently solved by computer modelling techniques.

3.3 MODELLING THE SUCTION PORT SECTIONS

Whether using lumped parameter or distributed parameter analysis, the pump must be split into sections that can be approximated as uniform pipes. The suction port is modelled as seven sections, shown in Figure 3–5, each with its own transmission matrix. Each section is described in a separate sub-section, below. Each section needs to be expressed as characteristic impedance, Z_0, and wave propagation coefficient, γ, which are calculated from the series impedance, Z, and shunt admittance, Y. It has been seen in Section 3.2 that the errors are small in calculating the inductance and capacitance of short sections of line. This error is increased as the line length increases and therefore at any point in this section where the line length is thought to be significant, the errors incurred by using an approximation are discussed.

3.3.1 SUCTION PORT ENTRANCE

The suction port entrance is treated as a short uniform pipe with dimensions shown in Figure 3–6. One end of the section is open where the input signal enters the circuit. The other end is connected by means of a three-way scatter matrix to the supercharge inlet and the inlet sections. The series impedance and shunt admittance are:

$$Z_{sp} = \frac{4\rho\ell_{sp}}{\pi d_{sp}^2}\left[1 - \frac{2J_1(Kd_{sp}/2)}{Kd_{sp}/2J_0(Kd_{sp}/2)}\right]^{-1} \qquad 3.3.1.1$$

$$Y_{sp} = \frac{\pi d_{sp}^2 \ell_{sp}}{4B_e} \qquad 3.3.1.2$$

3.3.2 SUPERCHARGE INLET

The supercharge inlet is considered to be a closed ended pipe whose air content increases as the valve opens and a cavitating jet forms. The air content affects the bulk modulus, which is in the admittance term. The series impedance and shunt admittance are:

$$Z_{sc} = \frac{4\rho\ell_{sc}}{\pi d_{sc}^2}\left[1 - \frac{2J_1(Kd_{sc}/2)}{Kd_{sc}/2J_0(Kd_{sc}/2)}\right]^{-1} \qquad 3.3.2.1$$

$$Y_{sc} = \frac{\pi d_{sc}^2 \ell_{sc}}{4B_e} \qquad 3.3.2.2$$

The section is always considered as closed even when the valve is open because the impedance of the small orifice is very large compared to that of the surroundings.

3.3.3 INLET

The inlet is a pipe which links the suction port entrance and the supercharge inlet with the annulus that surrounds the ports. The series impedance and shunt admittance are:

$$Z_{in} = \frac{4\rho\ell_{in}}{\pi d_{in}^2}\left[1 - \frac{2J_1(Kd_{in}/2)}{Kd_{in}/2J_0(Kd_{in}/2)}\right]^{-1} \quad 3.3.3.1$$

$$Y_{in} = \frac{\pi d_{in}^2 \ell_{in}}{4B_e} \quad 3.3.3.2$$

3.3.4 ANNULUS

The annulus is split into three sections: two sections, of length one-quarter the circumference of the annulus, link the inlet and each pair of ports and the other section is half the length of the circumference. The rotating group is mounted eccentrically to the pump housing and therefore the three sections are tapered. These tapered sections are the longest of the sections used in calculating the impedance of the pump's passageways and it is therefore necessary to assess the different techniques and the errors incurred in calculating the impedance of these lines. Knowledge of the impedance of a tapering tube is required as part of the design process of musical instruments such as clarinets and trumpets. In this case the characteristic impedance is no longer constant for a given section of line, it is a function of the axial co-ordinate, z, the wave propagation coefficient is also affected by the taper **(47)**. Expressions for the series impedance and the shunt admittance are thus defined as **(48)**:

$$Z = \frac{j\omega\rho\ell}{A(z)}\left[1 - \frac{2J_1(Kd(z)/2)}{Kd(z)/2J_0(Kd(z)/2)}\right]^{-1} \quad 3.3.4.1$$

$$Y = \frac{A(z)\ell}{B_e} \quad 3.3.4.2$$

Usually these equations cannot be solved analytically like the example given in Section 3.2. Therefore, the solution of these equations involves integration with respect to z, which must be done numerically. Considering the taper as a series of uniform-sectioned pipes each decreasing or increasing in diameter can approximate this. This gives a staircase effect and is satisfactory if the length of the elements is very small. The method is least accurate at high-frequency but its advantage is that it can be used to model non-uniform tapers **(49)**. A simpler method of approximation to a taper is to consider it to be a uniform section. It has been seen that there is a potential inaccuracy in calculating the inductance with such a method. It is therefore necessary to assess whether this simpler approximation can be used. The two approximations are discussed below.

3.3.4.1 APPROXIMATION TO A TAPERED LINE USING THE DE-COUPLED WAVES TECHNIQUE

It has been shown, in §3.2.3.2, that a sudden expansion in a pipe can be modelled as two lines connected by a scattering matrix. A stepped line can therefore be described as a series of sudden expansions, which is shown in Figure 3–7. There are N forward travelling waves, u, and N backward travelling waves, v, and there are n elements where $n=N/2$. The transmission matrix, $\mathbf{T_T}$, is defined as the relationship between u_1 and v_1, and u_N and v_N, where:

$$\begin{pmatrix} u_N \\ v_N \end{pmatrix} = \mathbf{T_T} \begin{pmatrix} u_1 \\ v_1 \end{pmatrix} \qquad 3.3.4.1.1$$

This matrix is calculated by considering each individual element as being in series with the two either side of it, with scattering matrices at each link, i.e.:

$$\begin{pmatrix} v_{2n} \\ u_{2n+1} \end{pmatrix} = \mathbf{S_n} \begin{pmatrix} u_{2n} \\ v_{2n+1} \end{pmatrix} \qquad 3.3.4.1.2$$

This is true for the case $n=1$ to $n=N/2-1$. The open end at the right-hand side of the taper is dealt with by using the relationship from §3.2.3.1:

$$u_N = -v_N \qquad 3.3.4.1.3$$

A unity forward travelling wave is assumed at the inlet:

$$u_1 = 1 \qquad 3.3.4.1.4$$

The transmission matrix for each element is defined as:

$$\begin{pmatrix} u_{2n} \\ v_{2n} \end{pmatrix} = \mathbf{T_n} \begin{pmatrix} u_{2n-1} \\ v_{2n-1} \end{pmatrix} \qquad 3.3.4.1.5$$

This relationship is true for $n=1$ to $n=N/2$. Hence, there are $2N$ equations and $2N$ unknowns that can be solved in matrix form, as in Equation 3.2.3.2.4.

3.3.4.2 APPROXIMATION TO A TAPER USING A UNIFORM LINE

A tapered section, like a uniform section, is described as a series impedance and a shunt admittance. In order to define the taper, it is therefore necessary to calculate its length and average cross-sectional area such that the inductance and capacitance terms are correct. The cross-sectional area of the section is defined as (Figure 3–8):

$$A(\theta) = \ell_{aR} \sqrt{\left(R_2 \cos\theta + R_E \cos\theta_E\right)^2 + \left(R_2 \sin\theta + R_E \sin\theta_E\right)^2} - \sqrt{R_1^2\left(\cos^2\theta + \sin^2\theta\right)} \qquad 3.3.4.2.1$$

where l_{aR} is the axial length of the rotor and θ is the angle between which the area is to be found. The average cross-sectional area is therefore:

$$\bar{A} = \frac{1}{\theta_2 - \theta_1} \int_{\theta_1}^{\theta_2} A(\theta) d\theta \qquad 3.3.4.2.2$$

The length of the section is therefore equal for that of a taper or a uniform section and is given as the following:

$$\ell_t = \frac{V}{\bar{A}} = \theta_2 - \theta_1 \qquad 3.3.4.2.3$$

3.3.4.3 IMPEDANCE AND ADMITTANCE FOR THE THREE ANNULUS SECTIONS

The two methods for approximating the impedance and admittance for the tapering annulus sections were tested with a very simple representation of one of the annulus sections. The section modelled had the following equation describing the cross-sectional area:

$$A = A_0 + \frac{A_1 - A_0}{\ell} z \qquad 0 \le z \le 9 \times 10^{-2} \text{m} \qquad 3.3.4.3.1$$

A_0 and A_1 are the areas at the inlet and the outlet of the section respectively and have values2.5×10^{-5}m and 5.0×10^{-5}m. The convergence of the stepped line method was first of all examined. Figure 3–9 shows that more than ten segments are required for convergence to take place. However, it can be seen that the initial guess, which is the same as the inductance predicted by taking the mean cross-sectional area in the case of a straight line equation, shows a less than 4% error when compared to the converged value of 2.494×10^{6}kg/m^4. In order to assess the effect of this error, the two above methods were applied to Equation 1.3.4.3.1 to find the impedance of the taper. The impedance was found thus:

$$Z = L\omega + \frac{1}{C\omega} \qquad 1 \le \omega \le 6000\text{Hz} \qquad 3.3.4.3.2$$

The impedance of two uniform sections was also found using the largest area, A_1, and the smallest area, A_0, in order to show the outer limits for an approximation to the given section. The mean cross-sectional area method used the same procedure as in Section 3.2, whereas for the stepped line method the area at the x-co-ordinate of the centre of each segment was used.

Figure 3–10 shows the results of this simple test. It shows that the stepped approximation and the mean cross-sectional area estimate give similar results (once again the error is of the order of 4%). There is a small error between them but for the sake of simplicity of the impedance model, this error can be ignored. The other two results in Figure 3–10 show the potential inaccuracy in choosing the cross-sectional area of an extremity for the approximation. Hence, the mean cross-

sectional area method described in Section 3.3.4.2 gives a good compromise between an accurate approximation and a simple method.

The first annulus section is located at $0 \le \theta < \frac{\pi}{2}$; the second annulus section is between $\frac{3\pi}{2} \le \theta < 2\pi$, and the third is at $\frac{\pi}{2} \le \theta < \frac{3\pi}{2}$. These limits are substituted into Equation 3.3.4.2.1 to find the area of each section. The cross-sectional area term and the length are found using Equations 3.3.4.2.2 and 3.3.4.2.3 respectively. The series impedance and shunt admittance are then found by substitution into Equations 3.3.4.1 and 3.3.4.2.

3.3.5 PORT

There are four suction ports in the vane pump, two in parallel 180° apart from the other two. The two ports in parallel are treated as one, hence the area is doubled to compensate. The port (shown in Figure 3–11) is assumed to be a circular transmission line with length, l_p, and hydraulic diameter, d_{hp}, which is defined as:

$$d_{hp} = \sqrt{2}\frac{2r_p h_p}{(r_p + h_p)} \qquad 3.3.5.1$$

The expressions for series impedance and shunt admittance are:

$$Z_p = \frac{4\rho \ell_p}{\pi d_{hp}^2}\left[1 - \frac{2J_1(Kd_{hp}/2)}{Kd_{hp}/2J_0(Kd_{hp}/2)}\right]^{-1} \qquad 3.3.5.2$$

$$Y_p = \frac{\pi d_{hp}^2 \ell_p}{4B_e} \qquad 3.3.5.3$$

3.4 SUCTION PORT MODEL

The suction port passageway is modelled using the de-coupled waves technique. Each of the seven sections, discussed in §3.3, is connected into the network shown in Figure 3–12, which represents the suction port. Each section has its own transfer matrix, **T**, and there are scattering matrices, **S**, linking them together. The system of equations that must be solved is:

$$\begin{pmatrix} u_2 \\ v_2 \end{pmatrix} = \mathbf{T}_1 \begin{pmatrix} u_1 \\ v_1 \end{pmatrix} \quad \begin{pmatrix} u_4 \\ v_4 \end{pmatrix} = \mathbf{T}_2 \begin{pmatrix} u_3 \\ v_3 \end{pmatrix} \quad \begin{pmatrix} u_6 \\ v_6 \end{pmatrix} = \mathbf{T}_3 \begin{pmatrix} u_5 \\ v_5 \end{pmatrix} \quad \begin{pmatrix} u_8 \\ v_8 \end{pmatrix} = \mathbf{T}_4 \begin{pmatrix} u_7 \\ v_7 \end{pmatrix}$$

$$\begin{pmatrix} u_{10} \\ v_{10} \end{pmatrix} = \mathbf{T}_7 \begin{pmatrix} u_9 \\ v_9 \end{pmatrix} \quad \begin{pmatrix} u_{11} \\ v_{11} \end{pmatrix} = \mathbf{T}_6 \begin{pmatrix} u_{12} \\ v_{12} \end{pmatrix} \quad \begin{pmatrix} u_{16} \\ v_{16} \end{pmatrix} = \mathbf{T}_5 \begin{pmatrix} u_{15} \\ v_{15} \end{pmatrix} \quad \begin{pmatrix} u_{13} \\ v_{13} \end{pmatrix} = \mathbf{T}_7 \begin{pmatrix} u_{14} \\ v_{14} \end{pmatrix}$$

$$\begin{pmatrix} v_4 \\ v_2 \\ u_5 \end{pmatrix} = \mathbf{S}_1 \begin{pmatrix} u_4 \\ u_2 \\ v_5 \end{pmatrix} \quad \begin{pmatrix} v_6 \\ v_{16} \\ u_7 \end{pmatrix} = \mathbf{S}_2 \begin{pmatrix} u_6 \\ u_{16} \\ v_7 \end{pmatrix} \quad \begin{pmatrix} v_8 \\ v_{11} \\ u_9 \end{pmatrix} = \mathbf{S}_3 \begin{pmatrix} u_8 \\ u_{11} \\ v_9 \end{pmatrix} \quad \begin{pmatrix} v_{13} \\ u_{15} \\ u_{12} \end{pmatrix} = \mathbf{S}_4 \begin{pmatrix} u_{13} \\ v_{15} \\ v_{12} \end{pmatrix} \qquad 3.4.1$$

$$u_3 = v_3 \qquad u_{14} = v_{14} \qquad u_{10} = v_{10} \qquad u_1 = 1$$

Once again, there is a unity wave at the entrance to the pump ($u_1 = 1$). The solution of this matrix is explained in the following section.

3.4.1 MODEL SOLUTION

Equations 3.4.1 are put into matrix form and are solved using MATLAB (50), which is a matrix-based environment for mathematical function solving. The equation which is solved is of the form:

$$\mathbf{M} \begin{pmatrix} u_1 \\ \vdots \\ u_{16} \\ v_1 \\ \vdots \\ v_{16} \end{pmatrix} = \begin{pmatrix} 1 \\ 0 \\ \vdots \\ \vdots \\ \vdots \\ 0 \end{pmatrix} \qquad 3.4.1.1$$

The solution of this equation gives the amplitude and phase of all the waves. Only the waves at the suction port entrance, u_1 and v_1, are required to find the entry impedance of the pump. First of all, the pressure and flow at the entrance are found using Equations 3.2.2.7 and 3.2.2.8:

$$P_{sp} = \sqrt{\frac{Z_{01}}{2}}(u_1 + v_1) \qquad 3.4.1.2$$

$$Q_{sp} = \frac{1}{\sqrt{2Z_{01}}}(u_1 - v_1) \qquad 3.4.1.3$$

Where Z_{01} is the characteristic impedance term for the suction port entrance section, which is found by substituting Equations 3.3.1.1 and 3.3.1.2 into Equation 3.2.6:

$$Z_{01} = \sqrt{\frac{Z_{sp}(s)}{Y_{sp}(s)}} \qquad 3.4.1.4$$

The pump impedance can be found by using impedance notation, which states that pressure is proportional to flow in the following relationship.

$$P_{sp} = ZQ_{sp} \qquad 3.4.1.5$$

The suction port impedance, *Z*, varies with frequency. It also varies for pumps with different sized housings and with changes in oil properties because the series impedance and shunt admittance terms contain parameters for geometry as well as oil properties. Therefore aeration of the oil when the pump is running at high speed with a low reservoir pressure has an effect on the impedance. The model will be validated against test results and an empirical equation will be derived to predict air content in the oil.

3.5 THE EFFECT OF PARAMETERS ON IMPEDANCE MODEL RESULTS

The impedance of the suction port is complicated, which reflects the complexity of the geometry. Figure 3–13 shows a typical impedance result modelled using the de-coupled waves technique. The impedance is capacitive at low frequency which implies that the system acts as a closed ended pipe. Figure 3–14 shows a comparison between the resonant frequency of a 225mm pipe of 10mm diameter at atmospheric pressure and at 100bar. It can be seen that across a range of void fractions, there is little change in resonant frequency at 100bar but at 1 bar it drops to very low frequencies. This demonstrates that there is likely to be greater variations in impedance characteristics at low pressure than would be seen in a delivery port.

The areas of resonance and anti-resonance do not tend towards infinity and minus infinity respectively because of viscous damping, described in §3.2.1. The position of these points is of interest especially in future validation stages. At this stage, it is sufficient to examine the behaviour of the impedance as different parameters are varied. Two types of parameters can be varied: the oil properties and the passageway geometry.

3.5.1 THE EFFECT OF OIL PARAMETERS ON IMPEDANCE

Three properties of the oil are present in the equations for series impedance and shunt admittance. These are the bulk modulus, which affects the compressibility of the system, the density, which governs system inertia, and the viscosity, which affects the damping.

3.5.1.1 THE EFFECT OF BULK MODULUS ON IMPEDANCE

Figure 3–15 shows the impedance with two bulk modulus terms. The solid line is the true bulk modulus for power steering fluid and the dotted line is for a bulk modulus reduced by a factor of ten, which translates to approximately 0.625% of air at 1bar. The reduction in overall system stiffness translates the resonance and anti-resonance positions to lower frequencies. This effect may be seen in a pump that is producing large amounts of air bubbles. The 10:1 change in bulk

modulus does not however show large changes in impedance. This suggests that the effect of the 1% air content is greater than the bulk modulus of the oil.

Pressure can also affect the compressibility of the system. Increasing the reservoir pressure can raise the bulk modulus; this can compensate for loss of system stiffness from aeration. The effect of raising tank pressure can be seen in Figure 3–16. The resonant and anti-resonant peaks are translated to a higher frequency thus representing an increase in system stiffness.

3.5.1.2 THE EFFECT OF DENSITY ON IMPEDANCE

Density is part of the series impedance term, which is the inertia term for the system. A decrease in density of the oil would therefore indicate an increase in the resonant frequency of a system due to decreased inertia. Figure 3–17 shows a comparison between the impedance with normal fluid density and with half the density and it shows an increase in frequency of the resonant and anti-resonant peaks.

3.5.1.3 THE EFFECT OF VISCOSITY ON IMPEDANCE

The viscosity of the oil affects the damping. At higher temperatures the viscosity reduces, which means that there is less system damping. This is shown in Figure 3–18, where the resonant and anti-resonant peaks are sharper suggesting that at very low viscosity they will tend toward infinity and zero respectively. Figure 3–19 shows the effect of very high viscosity on the impedance, which implies that at very low temperatures all the peaks are damped out.

3.5.2 THE EFFECT OF GEOMETRY ON IMPEDANCE

The geometry of the pump is mainly affected by machining tolerance. However, movement of the housing can be caused by pressure imbalance **(51)** but in this study, this effect is assumed to be negligible. Figure 3–20 shows the effect of calculating the impedance with the annulus terms at maximum and minimum diameter according to tolerance. There is very little difference between the two results, which suggests that the effect of machining tolerance on impedance is negligible compared with oil property effects.

3.6 CONCLUSIONS

A distributed parameter model was chosen to model the impedance of the pump's suction port. The solution of the wave equation was manipulated such that the forward and backward travelling waves in each section were de-coupled. This method was chosen above all because of its flexibility in being adaptable for either frequency or time domain calculations. It was however finally decided that, bearing in mind the test method which was used to validate the model, it would be better to proceed with a frequency domain impedance model.

Several approximations were used in building up a circuit which was representative of the pump's suction port passageways. These approximations were shown to have greater effect on the predicted inductance of the line rather than the capacitance. It was, however, demonstrated that the errors incurred by using the approximations were small if line lengths were small. The error between the impedance of a 9cm tapering section, which represents a section of the annulus, was measured using two approximations. The simple mean cross-sectional area approximation showed a less than 4% error when compared to an approximation using ten segments. It was therefore decided that the simpler approximation could be used when required in the impedance model.

The pump was then broken down into small sections which were linked together using the rules of the de-coupled waves technique. This led to a matrix of equations which was suited to solution in the MATLAB environment. Oil properties had the greatest effect on the results from the simulation, which suggests that air bubble content of the oil may be the most important factor in accurately predicting pump impedance.

FIGURES FOR CHAPTER 3

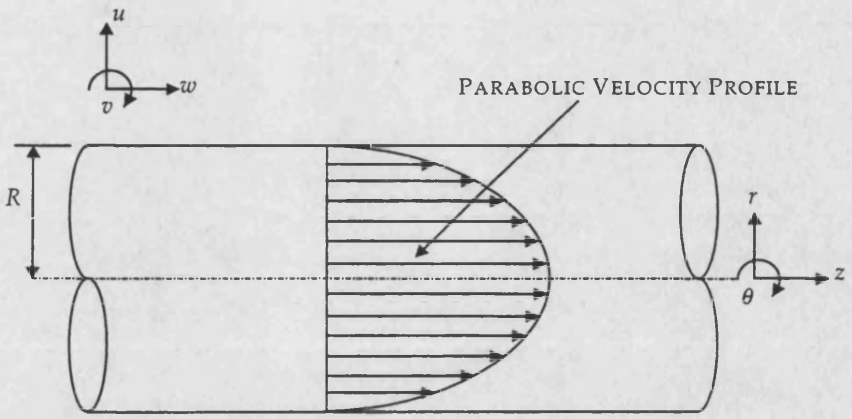

Figure 3–1: Parabolic Flow in a Straight Pipe

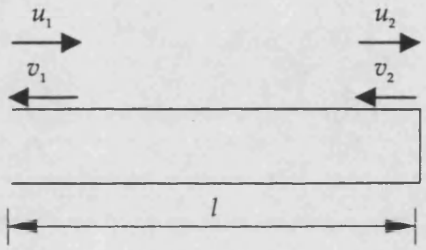

Figure3–2: Schematic for Pipe with Closed End

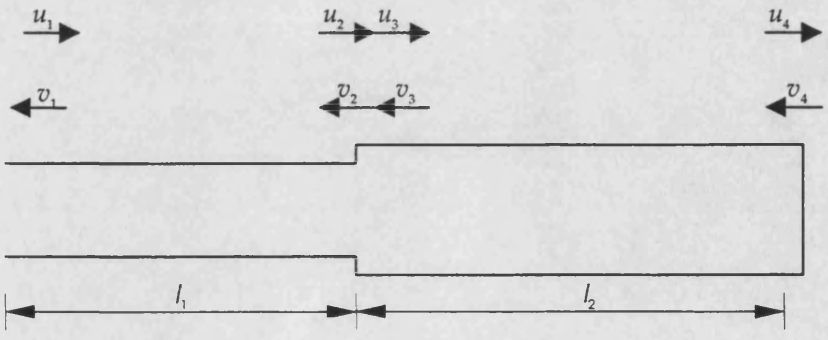

Figure 3–3: Schematic of Closed Ended Pipe with an Expansion

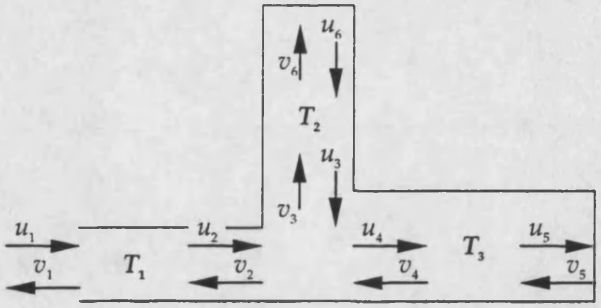

Figure 3–4: Schematic for a Three-way Junction with Two Closed Ends

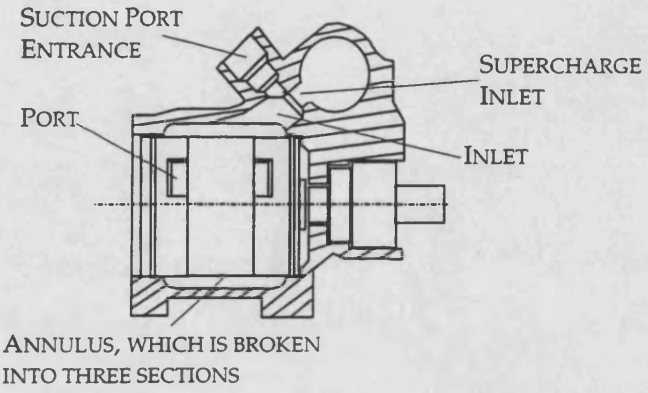

Figure 3–5: Seven Sections of the Suction Port Passageway

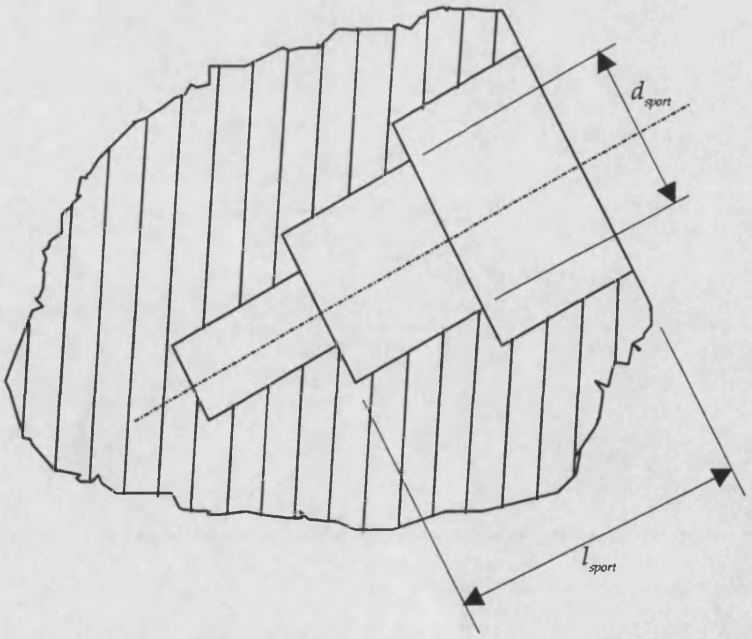

Figure 3–6: Suction Port Entrance Dimensions

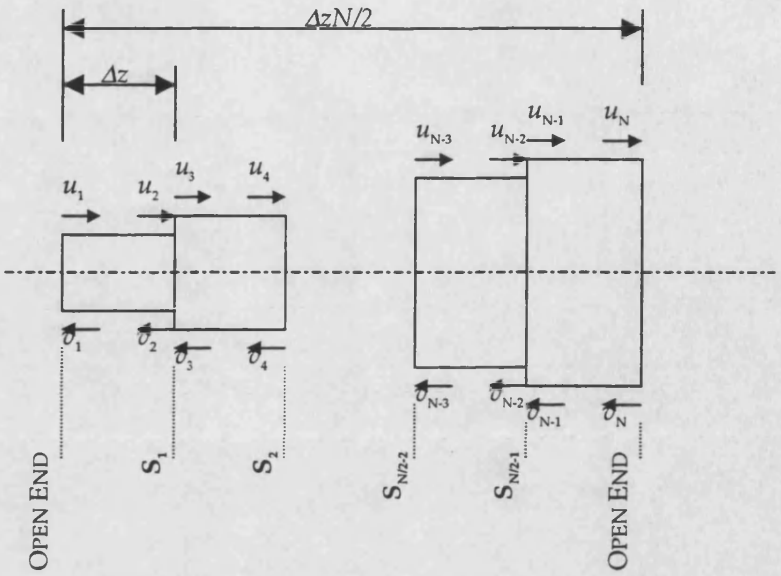

Figure 3–7: Generalised Diagram of Stepped-Tapered Line

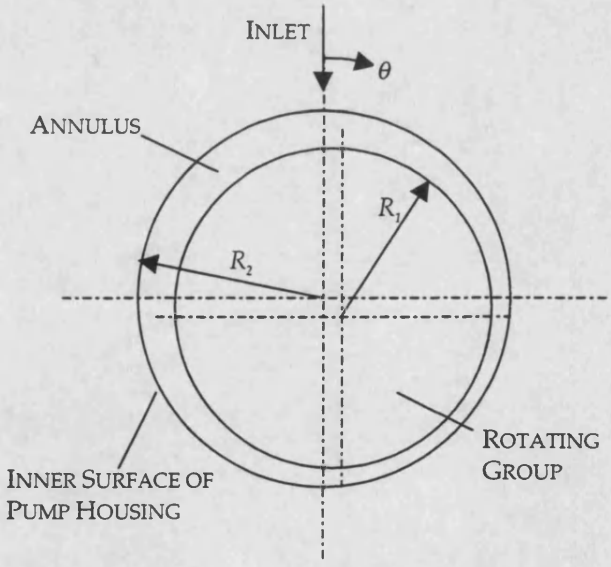

Figure 3–8: Diagram of Annulus Dimensions

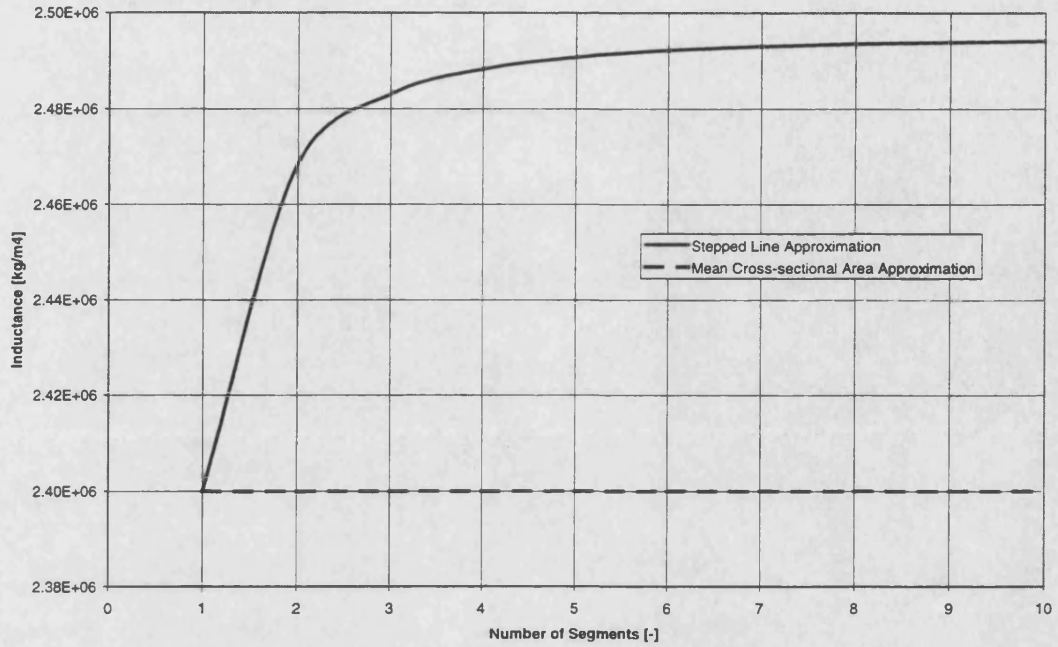

Figure 3–9: Convergence of the Stepped Line Approximation

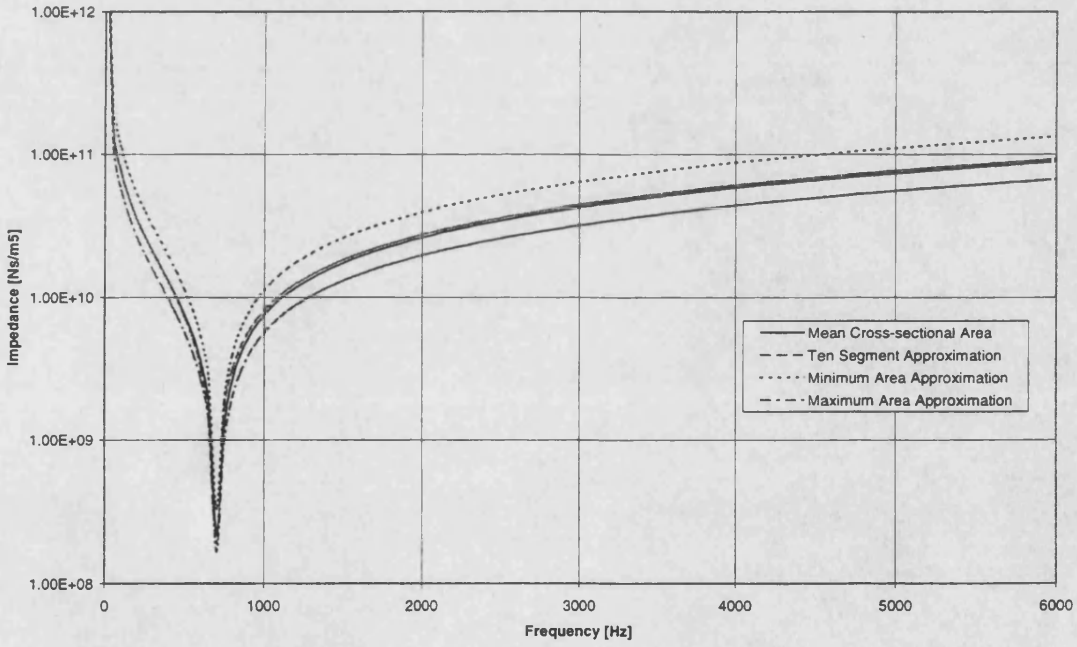

Figure 3–10: Results of Impedance Approximation Test

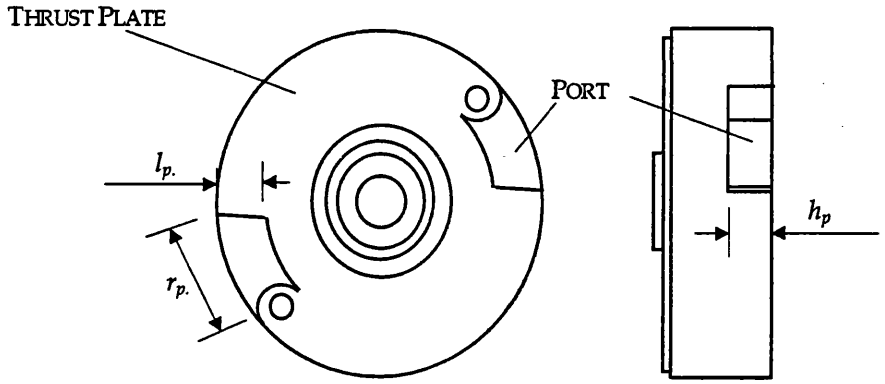

Figure 3–11: Port Dimensions

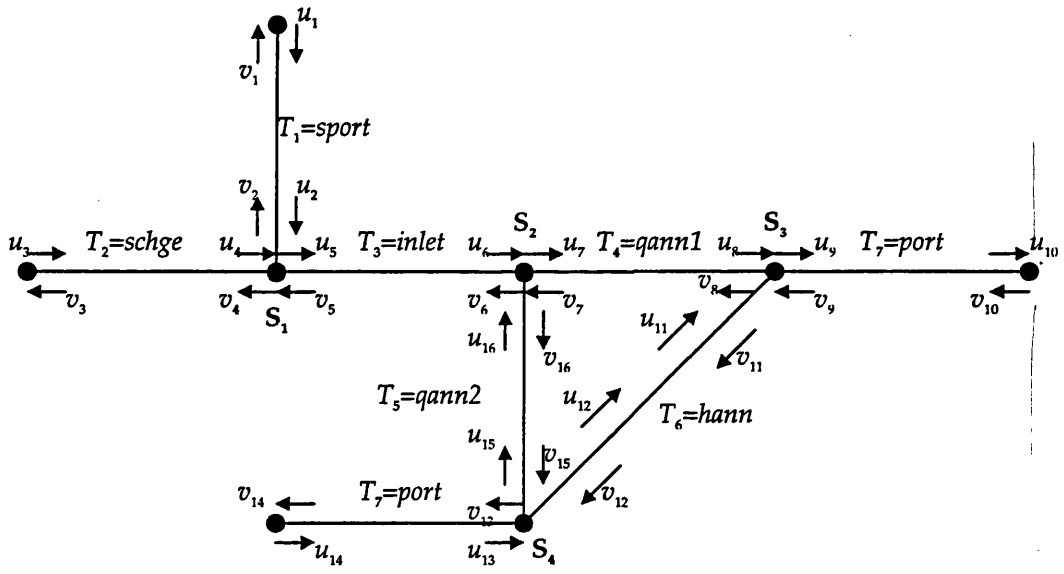

Figure 3–12: Circuit Diagram for Suction Port Impedance Model

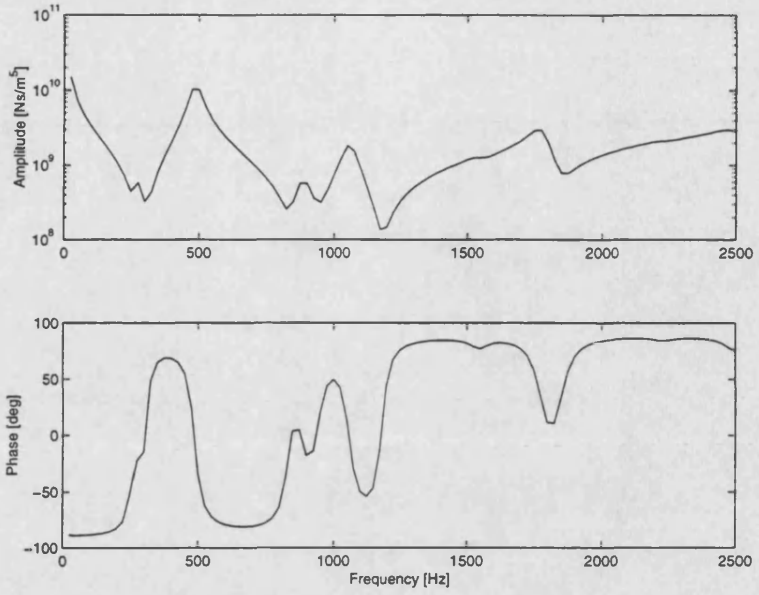

Figure 3–13: Modelled Impedance Result

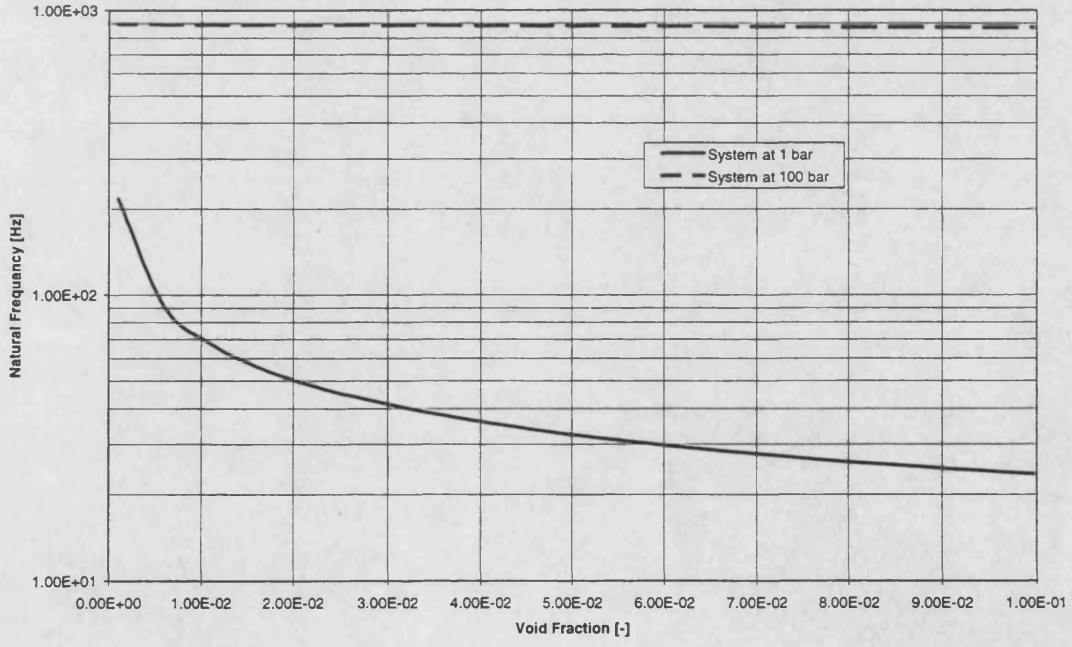

Figure 3–14: Natural Frequency of a 225mm Pipe at 1bar and 100bar

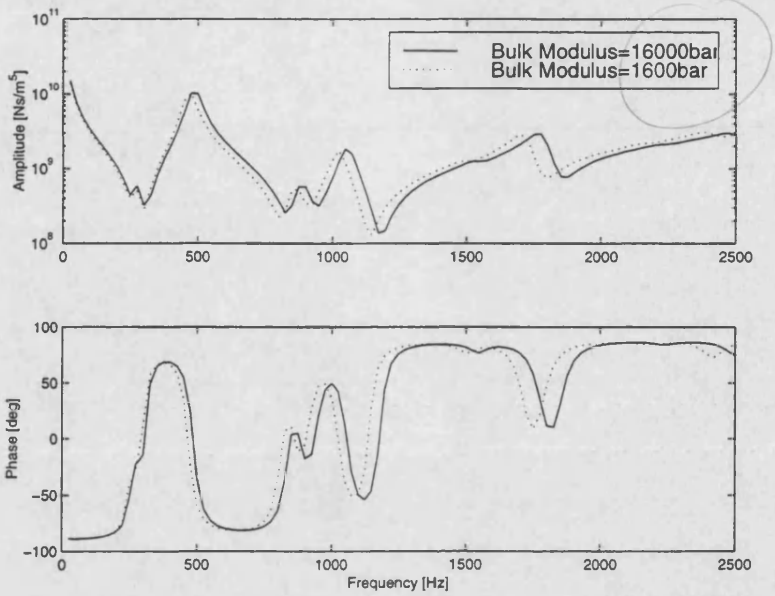

Figure 3–15: The Effect of Bulk Modulus on Impedance

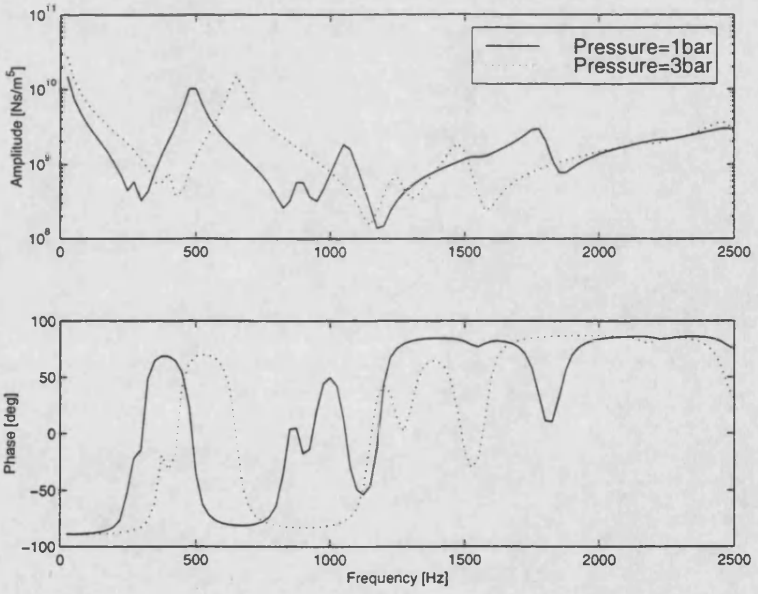

Figure 3–16: The Effect of Pressure on Impedance

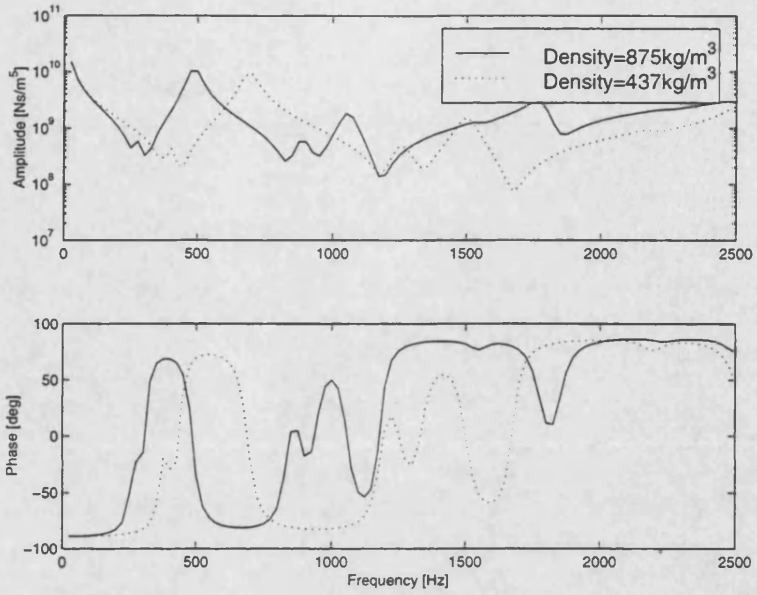

Figure 3–17: The effect of Density on Impedance

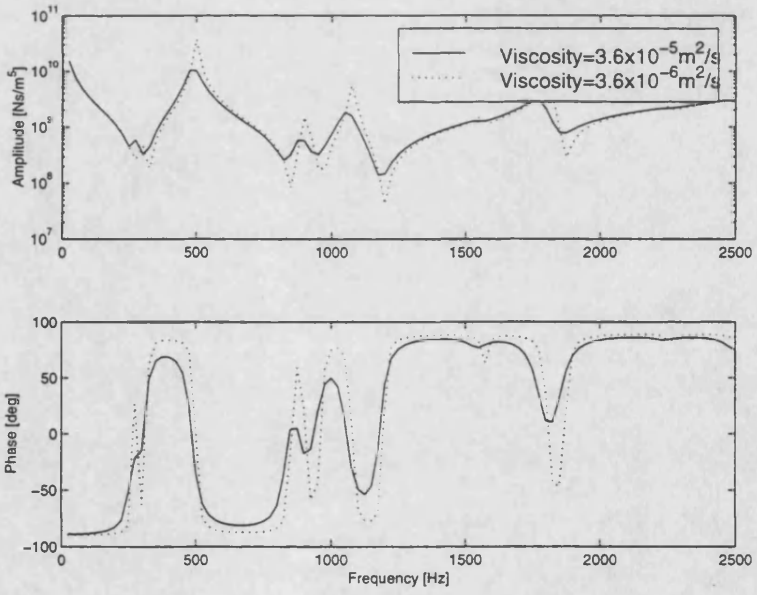

Figure 3–18: The Effect of Lowered Viscosity on Impedance

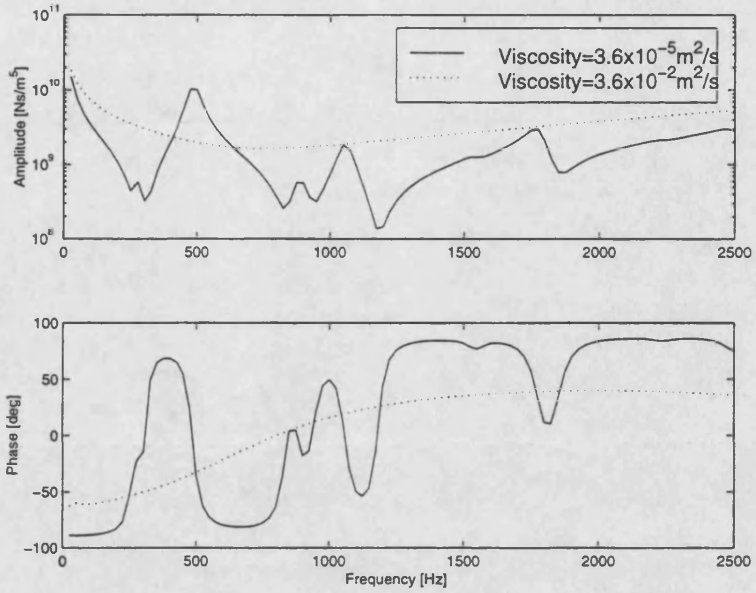

Figure 3–19: The Effect of Raised Viscosity on Impedance

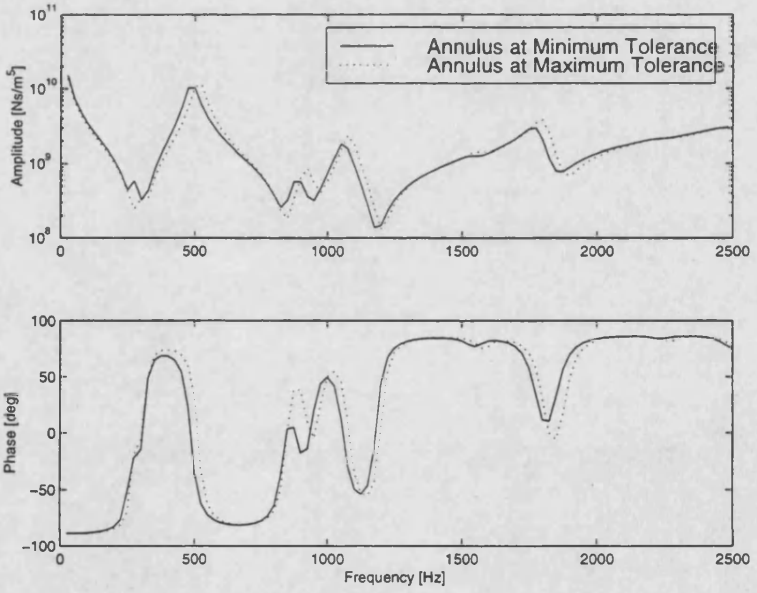

Figure 3–20: The Effect of Annulus Tolerance on Impedance

4 FLOW RIPPLE SIMULATION

4.1 INTRODUCTION

The positive displacement pump is a major source of noise in a power steering system. Unsteady flow is created as each individual pumping element opens and closes to a port. The resultant flow ripple interacts with the circuit impedance to create pressure ripple. Pressure ripple emitted from both the delivery and suction ports produces standing waves in the fluid lines. In certain cases, fluid borne noise can be transmitted through the system structure and cause high levels of audible noise. The audible noise emitted from a power steering system never reaches dangerous levels but it can be a nuisance. Therefore, in order to increase passenger comfort, it is necessary to reduce the levels of fluid borne noise emitted by the pump. High-pressure lines are normally considered to be the most problematic and have been the focal point of most previous investigations.

Measurement of fluid borne noise levels is a good technique for quantifying the noise but a validated simulation is an important design tool. In a dynamic simulation, flow ripple can be derived from predicted pressure in each of the pumping elements. Several simulation models exist which concentrate on delivery flow ripple: one model focuses on vane pump flow ripple at the rotating group discharge **(1)**. The pressure in each chamber is calculated and is used to obtain the net discharge flow ripple. It is a flexible model that allows changes in geometry so that flow ripple can be evaluated for a range of pumps. As well as computing pressure and flow, this model considers the force balance on each vane. If the net force on the vane is inwards in a radial direction, the vane may separate from the cam surface. This can affect the leakage flow between chambers, which can have a major influence on the net delivery flow ripple. Another model takes the deformation of the pump housing into account **(51)**. Deformation of the cam ring can affect the chamber volume, which in turn can change the effective bulk modulus. The predicted flow ripple in both of these models compares well with measurements.

Another simulation is used to predict the transient pressure characteristic of a vane pump **(52)**. Pressure in the pre-compression phase is measured and predicted. Pre-compression occurs before a chamber opens to the delivery port and therefore a pressure transducer was fitted to the port plate in order to make measurements. Measured and predicted results for pre-compression transients and load pressure ripple are compared and good agreement is found.

Simulations of piston pumps are very similar to vane pump models and they are used for the same design purposes. One such simulation uses a modified piston pump model to investigate the effect of delivery port position on flow ripple. The simulated delivery port opening is delayed so that a heavily damped check-valve can be inserted before, which helps to attenuate

the flow ripple **(53)**. Another study involves modification of a piston pump simulation to look at the effects of relief grooves **(54)**.

A dynamic simulation of a positive displacement pump must be designed with ease of modification in mind. A modular program must be created where subroutines can be added to assess phenomena that were not envisaged by the original programmer. This chapter describes such a model, which has been designed specifically to investigate suction port flow ripple. The model differs from Reference **(1)** in several aspects. One is that the amount of leakage flow paths considered here is less than considered in Reference **(1)**. The assumptions behind this statement are expanded on in Section 4.3.7. The simulation described here is capable of giving results in more forms than in Reference **(1)**. The types of flow ripple are described in Section 4.4. The other main difference between this simulation and the previous publications is the calculation of the inertial length. In previous publications, this length is considered to be related to the size of the relief groove. This assumption is not accepted here and a finite element approach, described in Section 4.3.5, has been used to predict this parameter.

4.2 THEORY

The section of the vane pump that is of interest is shown in Figure 4–1. Adjacent vanes on two sides, the thrust plate, pressure plate, cam ring and the rotor border each pumping chamber. The suction ports are located in both the thrust and pressure plates. There are two sets diametrically opposed to each other.

The pressure inside each pumping element must be predicted in order to calculate the flow ripple at the rotating group. Four main flows are considered: the rate of change of chamber volume with time; suction port flow, when the chamber is open to the suction line; delivery flow, when the chamber is open to the delivery line, and the leakage of fluid between adjacent chambers at different pressure. The following continuity equation must therefore be solved:

$$\frac{dp}{dt} = \frac{B_e}{V_C}\left(-\frac{dV_C}{dt} + q_i - q_{del} + q_\ell\right) \qquad 4.2.1$$

Two of the flow terms are described in §4.3, which deals with special functions: the rate of change of volume is defined in §4.3.6 and the leakage flow in §4.3.7. Flow through the delivery and suction ports depends on two main components: the orifice flow characteristic and the fluid inertia term. This gives the two following differential equations:

$$\frac{dq_i}{dt} = \frac{A_{SP}}{\rho \ell_{SP}}\left(p_{RES} - p_C - \frac{\rho}{2}\frac{q_i|q_i|}{(C_d A_{SP})^2}\right) \qquad 4.2.2$$

$$\frac{dq_{del}}{dt} = \frac{A_{del}}{\rho \ell_{del}} \left(p_C - p_{del} - \frac{\rho}{2} \frac{q_{del}|q_{del}|}{(C_d A_{del})^2} \right) \quad 4.2.3$$

The orifice area and length vary with time and are described in §4.2.4 and §4.2.5 respectively. The discharge coefficient, C_d, which is set to a constant value of 0.7, is an asymptotic approximation for spool valves, which is discussed in Reference (55). The reservoir and delivery pressure are approximated as constants, and the assumptions regarding this are presented in §4.3.8

Equations 4.2.2 and 4.2.3 are non-zero only when the orifice area term is greater than zero. The equations are only calculated when the relevant port is open and at other times flow is forced to decay to zero, thus:

$$\frac{dq_i}{dt} = -1.0 \times 10^4 q_i \quad 4.2.4$$

$$\frac{dq_{del}}{dt} = -1.0 \times 10^4 q_{del} \quad 4.2.5$$

Equations 4.2.4 and 4.2.5 have time constants of 0.1ms which means that the flow terms can be considered to be zero 0.4ms after the port closes, which is equal to 3.6° at 1500rev/min. This time constant has been chosen both to ensure that the flow is zero before the port opens again and also so that there are no oscillations caused by choosing too small a time constant. This is discussed in detail in §4.3.9. The five differential equations must be solved simultaneously using a numerical algorithm.

4.2.1 Numerical Solution of Simultaneous ODEs

Equations 4.2.1-4.2.5 are solved using a quasi-constant step size stiff system solver algorithm called *ode15s* (56). A stiff system solver is needed because there are transients of different rates concerning compression and kinematic flow ripple. The kinematic flow ripple is defined by pump geometry and can be considered as slow compared to the compression flow ripple, which is controlled by the port opening suddenly.

Numerical solution of ODEs is a slow process and so simplifications to the model must be found that will speed up the calculation. One such simplification concerns the pump geometry. The power steering vane pump is a balanced vane pump (Figure 4–2), which has two compression phases per revolution. This means that the pressure in a chamber is periodic each half revolution so, for a pump with an even number of equally spaced vanes, only half the number of chambers needs to be solved.

4.2.2 SIMULATION ENVIRONMENT

The simulation is created in the MATLAB environment (57), which runs mathematical script files as non-compiled code. This means that any modifications that need to be made do not have to be compiled and linked with the integrator. The integrator, discussed in §4.2.1, is part of the MATLAB in-built function library. Functions may be added to this library, which perform complicated mathematical functions. The functions, which have been added for this simulation, are described in §4.3.

4.3 SPECIALISED FUNCTIONS USED IN THE SIMULATION

Equations 4.2.1–4.2.3 contain several functions that vary with time or pump rotation. Each one must be recalculated after each integration step. These algorithms are described in this chapter.

4.3.1 CHAMBER POSITION

The position of each chamber is a function of the speed of the pump and time. The three co-ordinates, shown in Figure 4–3, the positions of the leading and trailing edge of the vane, which are required in order to be able to calculate leakage between adjacent vanes, and the centre point of the chamber are required. The co-ordinate at the centre of the chamber is needed as the pressure is assumed to be at this point and all areas and volumes are calculated here.

The position of each chamber must be evaluated at each time step. Hence, each vane position function gives vectors of size n_v. The three expressions are, where n_c is an integer in the range $1 \le n_c \le n_v$:

$$\theta_{CA}^{n_c} = \frac{tN_P\pi}{30} + \frac{t_V}{2r_1} + \frac{2\pi(n_C - 1)}{n_V} \qquad 4.3.1.1$$

$$\theta_{CB}^{n_c} = \frac{tN_P\pi}{30} - \frac{t_V}{2r_1} + \frac{2\pi n_C}{n_V} \qquad 4.3.1.2$$

$$\theta_{CC}^{n_c} = \frac{tN_P\pi}{30} + \frac{\pi(2n_C - 1)}{n_V} \qquad 4.3.1.3$$

Three extra variables are calculated, which show how many full multiples of π are contained in each co-ordinate position. These values are subtracted from Equations 4.3.1.1-4.3.1.3 in order to restrain all calculations to the region $0 \le \theta_c < \pi$. Equations 4.3.1.1-4.3.1.3 therefore become:

$$\theta_{CA}^{n_c*} = \theta_{CA}^{n_c} - int\left(\frac{\theta_{CA}^{n_c}}{\pi}\right)\pi \qquad 4.3.1.4$$

$$\theta_{CB}^{nc*} = \theta_{CB}^{nc} - int\left(\frac{\theta_{CB}^{nc}}{\pi}\right)\pi \qquad 4.3.1.5$$

$$\theta_{CC}^{nc*} = \theta_{CC}^{nc} - int\left(\frac{\theta_{CC}^{nc}}{\pi}\right)\pi \qquad 4.3.1.6$$

These co-ordinates are used as the basis for calculations for the other specialised functions.

4.3.2 CAM PROFILE FUNCTION

The vanes that enclose the chambers follow a cam which alters their volume as they pass from suction to delivery. As a chamber passes from suction to delivery, the chamber is at its maximum volume, which coincides with a dwell in the cam profile. In some pumps this is not a dwell and the cam profile falls slightly, which reduces the volume of the chamber and is known as pre-compression. Pre-compression serves two purposes: Firstly, it insures against decompression, which occurs if machining tolerance of the cam dwell is such that there is a small rise. In this case, the fluid enclosed in the chamber could cavitate causing damage to the pump surfaces and excessive noise. Secondly, pre-compression raises the pressure in the chamber so that when it opens to delivery the difference in pressure across the port orifice is reduced and the flow ripple due to fluid inertia is reduced. Similarly, there is a dwell at minimum volume as the chamber passes from delivery to suction. This can be machined to have a decompression rise to reduce the pressure towards suction pressure. An example of this type of cam profile is shown in Watton *et al.* (52).

In this function, the cam profile has no pre-compression or decompression phase because, as it is shown in §4.3.3, the error in the volume calculations incurred by this simplification is very small. Constant acceleration (parabolic) rises and falls link the two dwells. The chamber increases in volume as it passes the suction port and the cam rises. Similarly, the cam fall coincides with the opening of the delivery port. The cam profile is defined as a piece-wise polynomial shown in Figure 4–4. The break points are at the extremities of the dwells and at the midpoints of the rise and fall where there is a point of inflexion. There are therefore six equations defining the cam profile:

$$y_{cam} = \left(\frac{Y_B - Y_A}{X_B - X_A}\right)^2 x^2 - 2X_A\left(\frac{Y_B - Y_A}{X_B - X_A}\right)^2 x + X_A^2\left(\frac{Y_B - Y_A}{X_B - X_A}\right)^2 + Y_A \qquad X_A \le x < X_B \qquad 4.3.2.1$$

$$y_{cam} = \left(\frac{Y_B - Y_C}{X_B - X_C}\right)^2 x^2 - 2X_C\left(\frac{Y_B - Y_C}{X_B - X_C}\right)^2 x + X_C^2\left(\frac{Y_B - Y_C}{X_B - X_C}\right)^2 + Y_C \qquad X_B \le x < X_C \qquad 4.3.2.2$$

$$y_{cam} = Y_C \qquad X_C \le x < X_D \qquad 4.3.2.3$$

$$y_{cam}=\left(\frac{Y_B-Y_C}{X_E-X_D}\right)^2 x^2-2X_D\left(\frac{Y_B-Y_C}{X_E-X_D}\right)^2 x+X_D^2\left(\frac{Y_B-Y_C}{X_E-X_D}\right)^2+Y_C \qquad X_D \le x < X_E \qquad 4.3.2.4$$

$$y_{cam}=\left(\frac{Y_B-Y_A}{X_E-X_F}\right)^2 x^2-2X_F\left(\frac{Y_B-Y_A}{X_E-X_F}\right)^2 x+X_F^2\left(\frac{Y_B-Y_A}{X_E-X_F}\right)^2+Y_A \qquad X_E \le x < X_F \qquad 4.3.2.5$$

$$y_{cam}=Y_A \qquad X_F \le x < X_A \qquad 4.3.2.6$$

The cam profile produced by this piece-wise polynomial is shown in Figure 4–5. The volume of each chamber can now be calculated with the chamber position and the cam profile functions.

4.3.3 CHAMBER VOLUME FUNCTION

The chamber volume and its rate of change of volume with respect to time are calculated using separate functions. In this section, a processing-time efficient approximation to the chamber volume is demonstrated, whereas the derivation for the rate of change of volume can be seen in §4.3.6.

The volume of the chamber is required in Equation 4.2.1. As described in §4.3.2, the volume of a chamber varies as two adjacent vanes follow the cam profile. This function gives an approximation to the actual volume in order to keep computations to a minimum. The radius of the cam at the leading vane is usually different to the radius at the trailing edge. Here, the radius of each is considered to be equal to the radius at the midpoint of the chamber. This radius is found by substituting the chamber-centre co-ordinate, θ_{CC}, into the cam profile function (Equations 4.3.2.1-4.3.2.6). The volume of the chamber, shown in Figure 4–5, is therefore defined as:

$$V_C=\frac{\theta \ell_{aR}}{2}\left(r_2^2-r_1^2\right) \qquad 4.3.3.1$$

The outer radius of the chamber, r_2, is a function of the inner radius, r_1, and the cam lift, y_{cam}:

$$r_2=r_1+y_{cam}(\theta_{CC}) \qquad 4.3.3.2$$

Hence, Equations 4.3.3.1 and 4.3.3.2 can then be written as follows:

$$V_C=\frac{\theta \ell_{aR}}{2}\left(\left(y_{cam}(\theta_{CC})\right)^2+2r_1 y_{cam}(\theta_{CC})\right) \qquad 4.3.3.3$$

Where θ is the angle between two consecutive vanes and l_{aR} is the axial length of the rotor. Figure 4–6 shows the function of chamber volume as it varies with chamber position. The errors incurred by using this approximation can be assessed by considering the volume enclosed by equation 4.3.2.1, which can be solved exactly. Considering X_A=0, the actual volume is given by:

$$V_{act} = \ell_{aR}\int_0^{1.25\times10^{-2}}\left(\frac{Y_B - Y_A}{X_B - X_A}\right)^2 x^2 - 2X_A\left(\frac{Y_B - Y_A}{X_B - X_A}\right)^2 x + X_A^2\left(\frac{Y_B - Y_A}{X_B - X_A}\right)^2 + Y_A dx \quad 4.3.3.4$$

Using the values in Appendix 1, this expression equals:

$$V_{act} = 1.78\times10^{-2}\left(\frac{3.55\times10^{-2}\times\left(1.25\times10^{-2}\right)^3}{3} + 2.75\times10^{-3}\times1.25\times10^{-2}\right) \quad 4.3.3.5$$

This gives a volume of $3.0665\times10^{-7}m^3$. The approximation shown in Equation 4.3.3.3 however gives the following expression:

$$V_C = \ell_{aR}x\left[\left(\frac{Y_B - Y_A}{X_B - X_A}\right)^2\left(\frac{x}{2}\right)^2 + Y_A\right] \quad 4.3.3.6$$

Using the values in Appendix 1, this expression gives:

$$V_C = 1.78\times10^{-2}\times1.25\times10^{-2}\times\left(\frac{3.55\times10^{-2}\times\left(1.25\times10^{-2}\right)^2}{4} + 2.75\times10^{-3}\right) \quad 4.3.3.7$$

This gives an approximate chamber volume of $3.0676\times10^{-7}m^3$, which shows that the short distance between two consecutive vanes means that the straight line approximation incurs very small errors. This demonstrates the error incurred when approximating the volume during a cam rise which has a far greater gradient than the pre-compression phase. It can therefore be assumed that the errors involved in ignoring the pre-compression are negligible and can be left out to further simplify the model.

4.3.4 ORIFICE FUNCTIONS

There are two orifice functions: one for the suction port and one for the delivery port. Similar to §4.3.3, an orifice is assumed to have a uniform outer radius based on the cam profile at the orifice centre point. If the chamber is fully open to an orifice, the chamber centre point is used to calculate the outer radius. If the chamber is opening to an orifice the mid-point between the leading vane and the orifice opening co-ordinate is taken and for the chamber closing, the mid-point between the trailing vane and orifice closing co-ordinate is taken. Figure 4–1 shows that a chamber actually opens to two suction (or delivery) ports at once. In order to compensate for this, the algorithm calculates the area of one orifice and doubles it.

Figure 4–7 shows the profile of the suction and delivery ports superimposed on one another. The suction port is situated between 165° and 70°, and the delivery port is between approximately 80° and 165°. The profile of both ports is correct except that there is a break of about 10° between the end of the suction port and the beginning of the delivery port, which is

where the relief groove for the delivery port is situated. Relief grooves reduce the gradient of the opening thus decreasing flow ripple due to inertia. Just as the two orifice functions have been superimposed on one another, it is possible to superimpose another orifice, which represents a relief groove. This is demonstrated in Figure 4–8, which shows the superimposition of the two orifice functions and a relief groove function representing the delivery port opening.

After the simulation is validated, it will be used as a design tool and the facility of adding a relief groove to the model can be utilised. It can be seen on Figure 4–7 that the gradient of the closing of the suction port is also large. One possibility would be to reduce to suction port length by ten degrees and to replace it with a relief groove in order to examine the effect on flow ripple. . This is discussed in Chapter 8, where design suggestions are put forward.

4.3.5 JET LENGTH FUNCTION

The flow ripple simulation treats the flow through an orifice as a series resistance and inertia (Equation 4.2.2 and 4.2.3). The resistance term depends on the orifice equation and the inertia term on the amount of fluid that must be accelerated. The mass of fluid is usually approximated as the amount of fluid in the relief groove of the port **(1)**. In the case of this simulation there is not always a relief groove and so a different approximation is required.

Numerical models have been used to study flow through valves **(58)** and this technique could be adapted to model flow through any orifice. Two-dimensional modelling can be performed without the need for commercial CFD packages and, in this study, a discretised solution of the fluid equations is used. The relationship between theoretical and corrected orifice length can be derived and used to find the accelerated mass for the inertia term.

4.3.5.1 THEORY

The finite volume method requires a grid of spacing Δx by Δy. Each square has a pressure, P_{ij}, and four flows normal to the sides of the squares (Figure 4–9). The continuity equation for one square (assuming a unit thickness and incompressible flow) is therefore:

$$u_{i-1,j}\Delta y - u_{i,j}\Delta y + v_{i,j-1}\Delta x - v_{i,j}\Delta x = 0 \qquad \text{4.3.5.1.1.}$$

The equations of momentum in the x and y direction are:

$$\rho\frac{\partial u}{\partial t} = -\frac{\partial p}{\partial x}$$
$$\rho\frac{\partial v}{\partial t} = -\frac{\partial p}{\partial y} \qquad \text{4.3.5.1.2.}$$

These equations can be applied to the finite volume, with the spatial derivatives replaced with a forward difference approximation and Fourier transforms taken:

$$U_{i,j} = -\frac{1}{j\omega\rho}\frac{P_{i+1,j} - P_{i,j}}{\Delta x}$$
$$V_{i,j} = -\frac{1}{j\omega\rho}\frac{P_{i,j+1} - P_{i,j}}{\Delta y} \qquad 4.3.5.1.3.$$

Substituting equations 4.3.5.1.3 into the continuity equation 4.3.5.1.1 gives an equation in terms of pressure.

$$(P_{i,j} - P_{i-1,j})\frac{\Delta y}{\Delta x} - (P_{i+1,j} - P_{i,j})\frac{\Delta y}{\Delta x} + (P_{i,j} - P_{i,j-1})\frac{\Delta x}{\Delta y} - (P_{i,j+1} - P_{i,j})\frac{\Delta x}{\Delta y} = 0 \qquad 4.3.5.1.4.$$

This equation can be manipulated so that the current value of pressure is in terms of the four adjacent values of pressure, which were solved, in the previous iteration.

$$P_{i,j}^{new}(2\Delta y^2 + 2\Delta x^2) = (P_{i-1,j}^{new} + P_{i+1,j}^{old})\Delta y^2 + (P_{i,j-1}^{new} + P_{i,j+1}^{old})\Delta x^2 \qquad 4.3.5.1.5.$$

Once the new value, $P_{i,j}^{new}$, is found, the value is modified using the Over-Relaxation Factor, w:

$$P_{i,j} = (1-w)P_{i,j}^{old} + wP_{i,j}^{new} \qquad 4.3.5.1.6.$$

The convergence criterion is that continuity of flow is obeyed between the inlet and the outlet. Flow is updated after an iteration of pressure, thus:

$$Q_u = \sum_{j=1}^{nj}\frac{P_{1,j} - P_{2,j}}{\Delta x}$$
$$Q_d = \sum_{j=1}^{nj}\frac{P_{nx-1,j} - P_{nx,j}}{\Delta x} \qquad 4.3.5.1.7.$$

At the first iteration there is only flow at the inlet and no flow at the outlet. The solution is considered to have converged when the ratio of the flows is within a tolerance, ε:

$$\left|\frac{Q_d}{Q_u} - 1\right| < \varepsilon \qquad 4.3.5.1.8.$$

4.3.5.2 APPLICATION TO THE SUCTION PORT

A grid is defined for the suction port assuming two-dimensional flow (Figure 4–10). Pressure is set to one at x=0 and to zero at x=$\Delta x.ni$. This grid is then solved for a range of orifice diameters so that an empirical equation can be formed for inclusion in the flow ripple simulation. The effective orifice length is defined in terms of jet length and diameter (28). All of these terms can be calculated from the grid dimensions and the pressure and flow solved in the iteration. The orifice length is defined using the equation for fluid inertia:

$$\ell_{SP} = \frac{1}{\rho j \omega} \frac{(P_{1,nj-1} - P_{ni,2})(Y_1 - Y_2)}{Q_u} \qquad 4.3.5.2.1.$$

The theoretical inertial length depends on the geometry of the orifice. In this case the sum of the area ratios of the two chambers is required:

$$l_{th} = X_1 \frac{(Y_1 - Y_2)}{(nj\Delta y - Y_2)} + (ni\Delta x - X_1)\frac{(Y_1 - Y_2)}{Y_1} \qquad 4.3.5.2.2.$$

The end correction, ξ, is therefore the difference between the jet length, l_{SP}, and the theoretical length, l_{th}. This is usually expressed as the ratio of length correction to orifice diameter, thus:

$$\xi = \frac{(l_{SP} - l_{th})}{d} \qquad 4.3.5.2.3.$$

This procedure is repeated for a range of values for Y_1. The empirical equation linking length correction, ξ, and orifice size can then be integrated in the pump flow ripple model.

4.3.5.3 RESULTS

The grid was used to compare the theoretical and corrected jet length over a range of values. Figure 4–11 shows this relationship, which can be approximated by the following quadratic equation:

$$\ell_{SP} = r_{SP}\left(0.0445\left(\frac{\ell_{th}}{r_{SP}}\right)^2 + 0.2544\left(\frac{\ell_{th}}{r_{SP}}\right) + 0.082\right) \qquad 4.3.5.3.1$$

This relationship can be substituted into Equation 4.2.2 and 4.2.3 to give the jet length terms shown in Figure 4–12. The orifice length for both the suction and delivery port is shown, the suction port is between 170° and 70° and the delivery port is between approximately 80° and 160°.

4.3.6 RATE OF CHANGE OF CHAMBER VOLUME FUNCTION

The function for the rate of change of volume is part of the compressibility flow term in Equation 4.2.1. It is based on the chamber volume function (Equation 4.3.3.3) and the volume change in a short time, δt.

$$\frac{\delta V_C}{\delta t} = \ell_{aR}\left(\frac{(y_{cam}(\theta_{CA}))^2}{2} - \frac{(y_{cam}(\theta_{CB}))^2}{2}\right)\frac{\delta\theta}{\delta t} \qquad 4.3.6.1$$

In the limit as $\theta \to 0$, Equation 4.3.6.3 becomes:

$$\frac{dV_C}{dt} = \ell_{aR}\left(\frac{(y_{cam}(\theta_{CA}))^2}{2} - \frac{(y_{cam}(\theta_{CB}))^2}{2}\right)\frac{\pi N_P}{30} \qquad 4.3.6.2$$

Where $\frac{d\theta}{dt}$ is the speed of the pump, N_P, in rads^{-1}. The rate of change of volume plotted against chamber position is shown in Figure 4–13.

4.3.7 LEAKAGE FUNCTION

Reference (1) states that there are three main leakage paths into and out of the chamber which must be considered. These are the leakage either side of the vane from one chamber to another, the leakage over the vane and leakage under the vane. It can be assumed that each leakage gap is small and that flow is laminar hence Poiseuille's equation can be used:

$$Q_\ell = \frac{h^3}{12\mu}\frac{dP}{dx} + U\frac{h}{2} \qquad 4.3.7.1$$

If the pressure in the chamber is P_i, and the pressure in the two adjacent ones is P_{i-1} and P_{i+1}, then the sign conventions, shown in Figure 4–14, must be kept. The magnitude of the flow in the three cases depends most importantly upon the height and length of each leakage path. The assumed values in each case are summarised in the following table:

		Under Vane	Over Vane	Beside Vane
Height, h	[m]	2.5×10^{-5}	1.0×10^{-5}	5.0×10^{-5}
Viscosity, μ	[kg/m/s]	3.6×10^{-2}	3.6×10^{-2}	3.6×10^{-2}
Length, dx	[m]	1.0×10^{-2}	1.3×10^{-3}	1.3×10^{-3}
Speed, U	[m/s]	0.0	2.8	2.8

Table 4-1: Leakage Path Dimensions

These three cases were applied to Equation 4.3.7.1 for a range of pressure drops between one and seventy bar. It can be seen, in Figure 4–15, that the larger gap found beside the vanes creates the largest flow and that the other two cases have only a small influence on the total leakage flow. Hence, for the sake of simplicity, the under vane and over vane flow can be neglected.

4.3.8 ASSUMPTION FOR ORIFICE PRESSURE DROP

In Equations 4.2.2 and 4.2.3, the pressure downstream of the orifice is assumed to be constant. This can only be assumed true if the impedance directly downstream of the orifice is small compared to that of the orifice. Figure 4–16 shows the impedance of the orifice and the port into which the fluid enters up to a frequency of 3kHz. It can be seen that this simple model, which considers each element to be a series resistance and inductance with a capacitance in parallel, that the impedance of the port is considerably smaller than that of the orifice. Hence, it is a valid

assumption that small variations of pressure downstream of the orifice have little effect on the overall result of Equations 4.2.2 and 4.2.3.

4.3.9 FLOW AT SMALL ORIFICE AREAS

The simulation uses a limit of $7.0\times10^{-7}m^2$ as the minimum orifice size, which Figure 4–17 shows gives a resistance to flow of 10^3 times that of the fully open orifice at approximately $2.75\times10^{-5}m^2$. This indicates that the mean flow rate through the orifice is reduced by a similar factor, although the pressure drop across the orifice will inevitably vary between these two cases. This flow rate is considered to be zero and the exponential decay is then used only to ensure that the flow is indeed zero, in order to avoid cumulative errors occurring in the integrator due to successive openings of the port at non-zero flow rates.

The consequences of this are that the oscillations at the immediate opening and closing of the port may not be accurately predicted. This may affect some of the higher frequency harmonics of the flow ripple. It does however avoid unnecessary stiffness in the differential equations, which would greatly increase run times.

4.4 INTERPRETATION OF SIMULATION RESULTS

The raw data from the flow ripple simulation must be converted into a form where it can be validated and then used as a design tool. Each chamber has three sets of results relating to its pressure its suction-port flow and its delivery-port flow. The time domain data for the suction-port flow in each chamber, which is of interest here, is shown in figure 4–18. The simulation is run for 1¼ revolutions and the first quarter revolution is discarded because the transient, seen in the upper graph of Figure 4–18, is an inherent problem occurring when using numerical integration from initial conditions that do not correspond with steady running conditions. The rest of the trace is used to give the internal flow ripple by summing the flow in all the chambers.

Before the suction port opens, the pressure in the pumping chamber is usually higher than that in the suction port so that when the port opens the fluid is exposed to the low pressure in the suction port. This results in a sharp outflow of fluid as the fluid in the chamber decompresses, causing the large negative flow spikes that can be seen in figure 4–18. The rate of decompression and the magnitude of the spikes depend on the rate at which the orifice area A_{sp} increases and on the theoretical length l_{the}.

It is also useful to look at the flow ripple as a harmonic spectrum, which is found by performing a fast Fourier transform on the internal flow ripple waveform. The top graph of Figure 4–19 shows the flow ripple spectrum up to 10kHz. In reality, the first ten harmonics at the pumping frequency are adequate to describe the flow ripple and so these are extracted (bottom graph of Figure 4–19). The flow ripple harmonics can be manipulated to give flow ripple at the pump

exit rather than at the rotating group, which can be used to validate the model against measurements. As well as internal flow ripple, the simulation outputs two other types. These three types of flow ripple are described in §4.4.1 - §4.4.3.

4.4.1 INTERNAL FLOW RIPPLE

Internal flow ripple is the waveform that would be observed emitting from the rotating group if it were discharging into a system with zero entry impedance. It is useful for studying the compression spike caused by fluid inertia as chambers open or close to a port. Internal flow ripple is therefore a good tool for assessing relief groove performance.

4.4.2 OPEN CIRCUIT FLOW RIPPLE

Open circuit flow ripple assumes that the source of ripples is at the opening to the pump housing and that it discharges into a circuit of zero entry impedance. This can be found by manipulating the impedance model, discussed in §3.4. Equations 3.4.1 are modified so that there is a flow input at the rotating group, which is the internal flow ripple, and the inlet acts as an open end. Hence, to find the open circuit flow ripple, the following set of equations is used:

$$\begin{pmatrix} u_2 \\ v_2 \end{pmatrix} = \mathbf{T}_1 \begin{pmatrix} u_1 \\ v_1 \end{pmatrix} \quad \begin{pmatrix} u_4 \\ v_4 \end{pmatrix} = \mathbf{T}_2 \begin{pmatrix} u_3 \\ v_3 \end{pmatrix} \quad \begin{pmatrix} u_6 \\ v_6 \end{pmatrix} = \mathbf{T}_3 \begin{pmatrix} u_5 \\ v_5 \end{pmatrix} \quad \begin{pmatrix} u_8 \\ v_8 \end{pmatrix} = \mathbf{T}_4 \begin{pmatrix} u_7 \\ v_7 \end{pmatrix}$$

$$\begin{pmatrix} u_{10} \\ v_{10} \end{pmatrix} = \mathbf{T}_7 \begin{pmatrix} u_9 \\ v_9 \end{pmatrix} \quad \begin{pmatrix} u_{11} \\ v_{11} \end{pmatrix} = \mathbf{T}_6 \begin{pmatrix} u_{12} \\ v_{12} \end{pmatrix} \quad \begin{pmatrix} u_{16} \\ v_{16} \end{pmatrix} = \mathbf{T}_5 \begin{pmatrix} u_{15} \\ v_{15} \end{pmatrix} \quad \begin{pmatrix} u_{13} \\ v_{13} \end{pmatrix} = \mathbf{T}_7 \begin{pmatrix} u_{14} \\ v_{14} \end{pmatrix}$$

$$\begin{pmatrix} v_4 \\ v_2 \\ u_5 \end{pmatrix} = \mathbf{S}_1 \begin{pmatrix} u_4 \\ u_2 \\ v_5 \end{pmatrix} \quad \begin{pmatrix} v_6 \\ v_{16} \\ u_7 \end{pmatrix} = \mathbf{S}_2 \begin{pmatrix} u_6 \\ u_{16} \\ v_7 \end{pmatrix} \quad \begin{pmatrix} v_8 \\ v_{11} \\ u_9 \end{pmatrix} = \mathbf{S}_3 \begin{pmatrix} u_8 \\ u_{11} \\ v_9 \end{pmatrix} \quad \begin{pmatrix} v_{13} \\ u_{15} \\ u_{12} \end{pmatrix} = \mathbf{S}_4 \begin{pmatrix} u_{13} \\ v_{15} \\ v_{12} \end{pmatrix} \qquad 4.4.2.1$$

$$u_3 = v_3 \qquad u_{14} - v_{14} = Q_i \sqrt{2Z_{0port}} \qquad u_{10} - v_{10} = Q_i \sqrt{2Z_{0port}} \qquad u_1 = -v_1$$

Hence the open circuit flow ripple is found by solving the above equations in the method described in §3.4.1. The expression is:

$$Q_E = \frac{1}{\sqrt{2Z_{0sport}}}(u_1 - v_1) \qquad 4.4.2.2$$

Figure 4–20 shows a graphical representation of the calculation of open circuit flow ripple, where the pressure and flow at the pump exit are, P_0 and Q_0. Equation 4.4.2.1 forces the waves at the suction port opening, u_1 and v_1, to be equal at all frequencies, hence P_0 is zero (see Equation 3.4.1.2). As this is the case the source flow, Q_S, which is modified by the impedance, Z_S, to give the open circuit flow ripple, Q_E, is equal to the flow at the pump exit, Q_0.

4.4.3 ANECHOIC FLOW RIPPLE

Although this has no real meaning, this is a good comparative rating of flow ripple and is used for comparison with test results. It is like the open circuit flow ripple except that this is assumed to discharge into a reflectionless or infinitely long line of characteristic impedance, Z_0. Anechoic flow ripple is related to open circuit flow ripple by the following relationship:

$$Q_A = \frac{Q_E Z_S}{Z_S + Z_0} \qquad 4.4.3.1$$

4.5 EFFECT OF PARAMETERS ON SIMULATION RESULTS

In order to understand the simulation better, it was run several times with different parameters and the results were observed. This showed that the program could be simplified by neglecting certain effects. It is desirable to simplify the program as much as possible in order to limit run times.

4.5.1 THE EFFECT OF DELIVERY PRESSURE

To see if the delivery pressure has any effect on the suction flow ripple, the simulation was run with delivery pressures of 20 and 50 bar. Low delivery pressure should give a lower level of flow ripple because the pressure change in the chamber as it passes between delivery and suction is lower. Figure 4–21 shows the suction flow ripple at the two pressures. There is an increase in the amplitude of the flow ripple with increasing delivery pressure. However, the pattern of the harmonics remains similar. This shows that delivery pressure cannot be neglected from the simulation even if it is only suction pressure that is being examined.

4.5.2 THE EFFECT OF LEAKAGE ON SUCTION FLOW RIPPLE

It has been shown that there is a definite delivery flow ripple characteristic associated with leakage between adjacent chambers (1). The simulation was run twice to observe the effect of leakage on suction flow ripple. It was run once with the leakage equations (Equation 4.3.7.1) included and a second time without the leakage function. Figure 4–22 shows that in this case there is no effect from the leakage equations. For investigating suction flow ripple, the simulation therefore can be streamlined by omitting leakage.

4.5.3 THE EFFECT OF CHAMBER VOLUME ON FLOW RIPPLE

The minimum chamber volume is governed by the difference between the rotor diameter and the minimum diameter of the cam ring. Two rotor diameters were used in consecutive simulations in order to investigate the influence of chamber volume on flow ripple (shown in Figure 4–23). In this case, the smaller rotor diameter gave a minimum dead volume of $8.7431 \times 10^{-8} m^3$, and the larger rotor diameter gave a dead volume of $7.6817 \times 10^{-8} m^3$.

4.6 CONCLUSIONS

A dynamic pump simulation was written in order to understand flow ripple phenomena. The simulation, once validated, can be used as a design tool. In order to use the simulation for design, it was decided that it should be a modular program, which was easy to modify and add to. For this purpose MATLAB was used for the simulation environment and the in-built ODE solvers were used. In order to shorten the run time of the simulation as much as possible, several simplifications were made to the model. In all cases, these were shown to have a small effect on the outcome of the simulation but considerably simplified the model. For example, the amount of leakage paths was initially reduced to one because the flow either side of the vane was found to be by far the greatest contributor to the total leakage flow. It was subsequently found that this leakage path had no effect on suction flow ripple and leakage was therefore totally eliminated from the simulation.

The output from the simulation was manipulated to give internal, open circuit and anechoic flow ripple, which meant that, in combination with the impedance model discussed in Chapter 3, a wide range of cases could be validated against the test rig.

FIGURES FOR CHAPTER 4

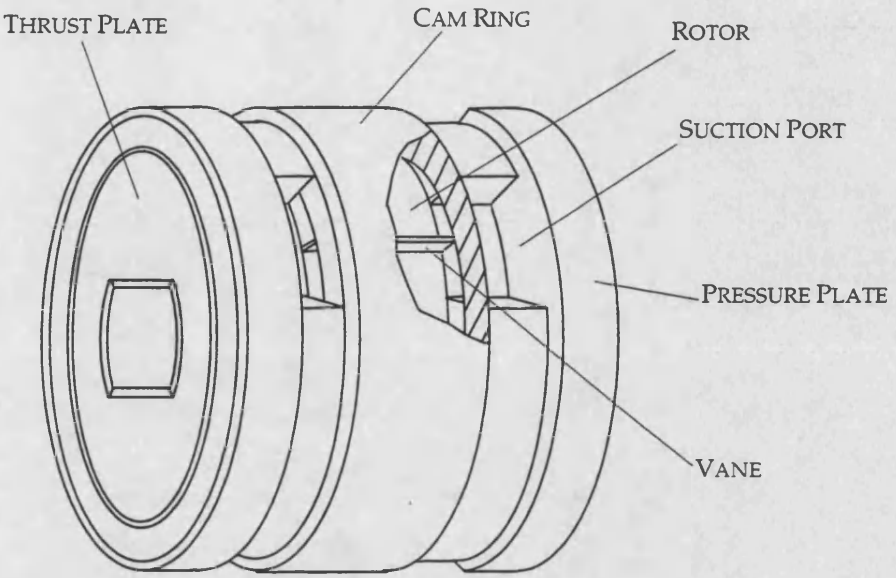

Figure 4–1: Vane Pump Rotating Group Construction

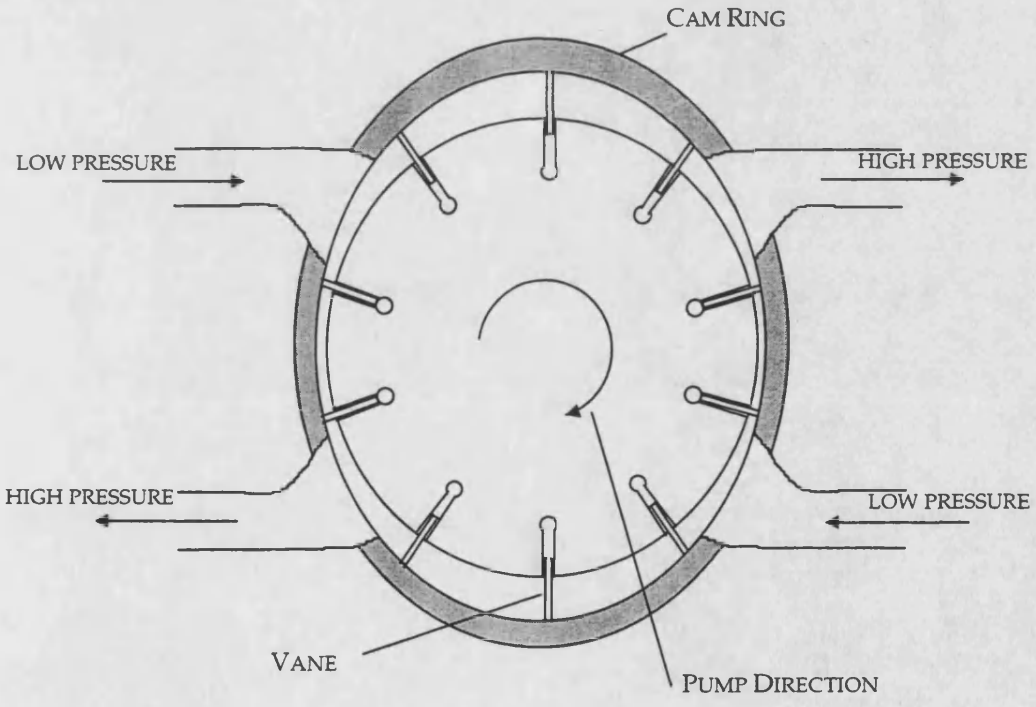

Figure 4–2: Balanced Vane Pump Schematic

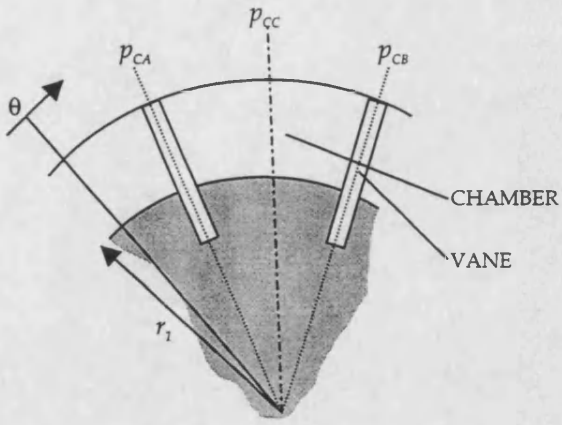

Figure 4–3: Position of Vane and Chamber Co-ordinates

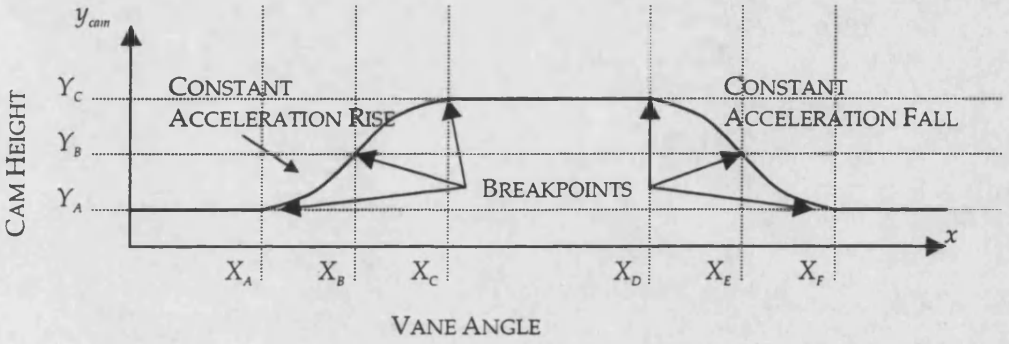

Figure 4–4: Position of Breakpoints and Polynomial Coefficients on Cam Profile

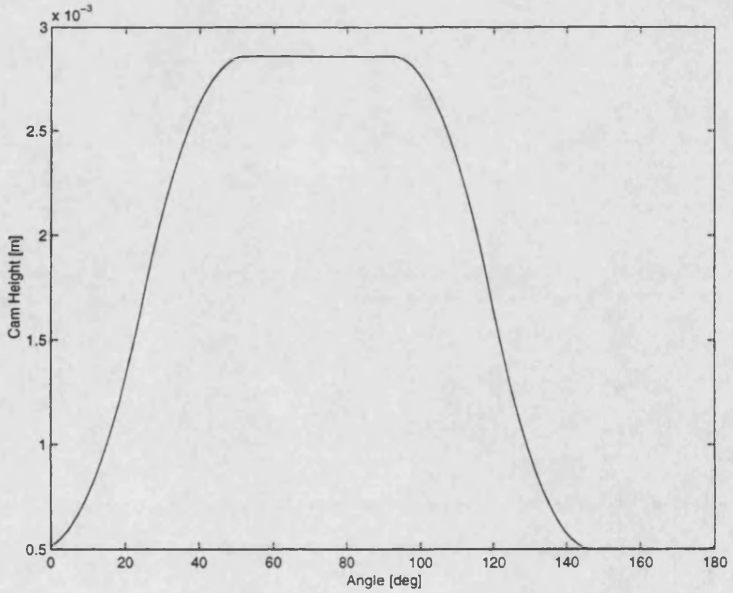

Figure 4–5: Cam Profile Function

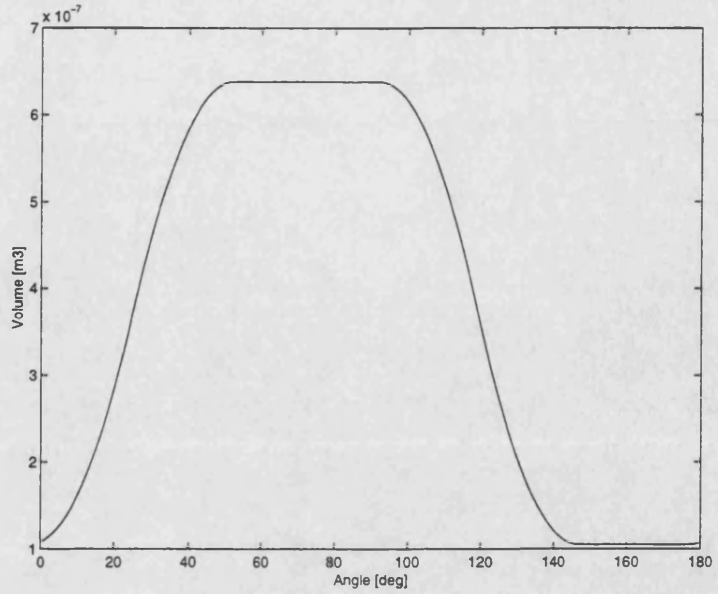

Figure 4–6: Chamber Volume Function

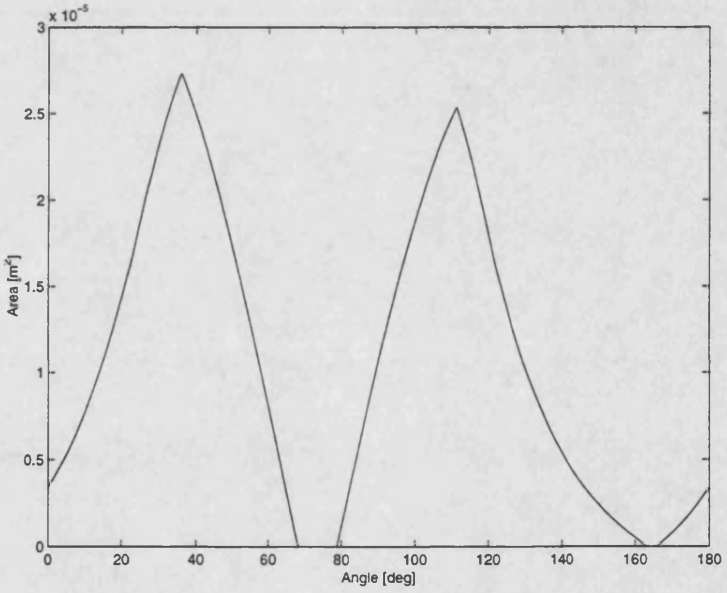

Figure 4–7: Suction and Delivery Orifice Functions

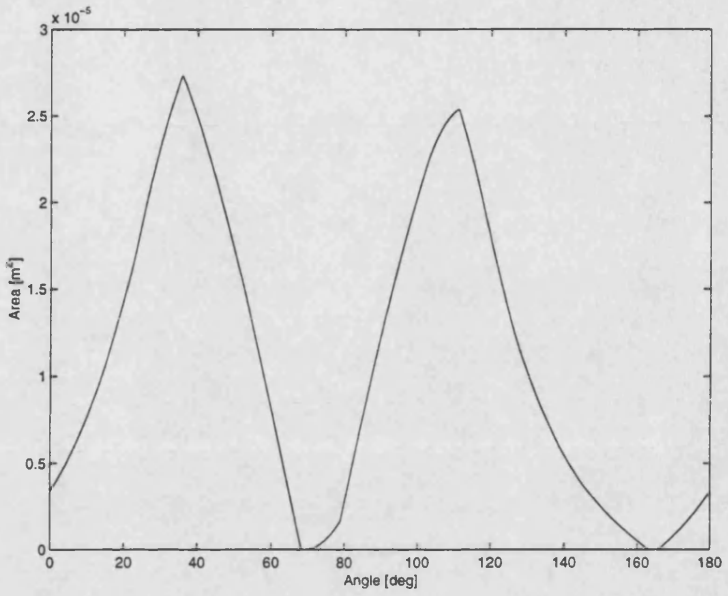

Figure 4–8: Suction and Delivery Orifice Functions with Relief Groove Function

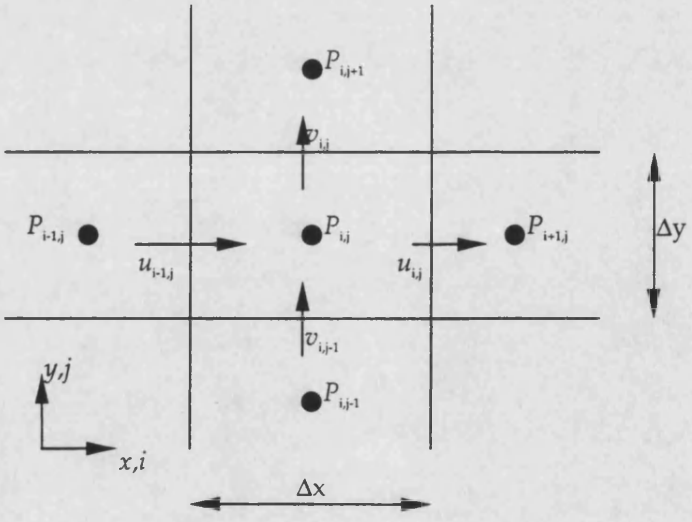

Figure 4–9: Finite Volume Grid

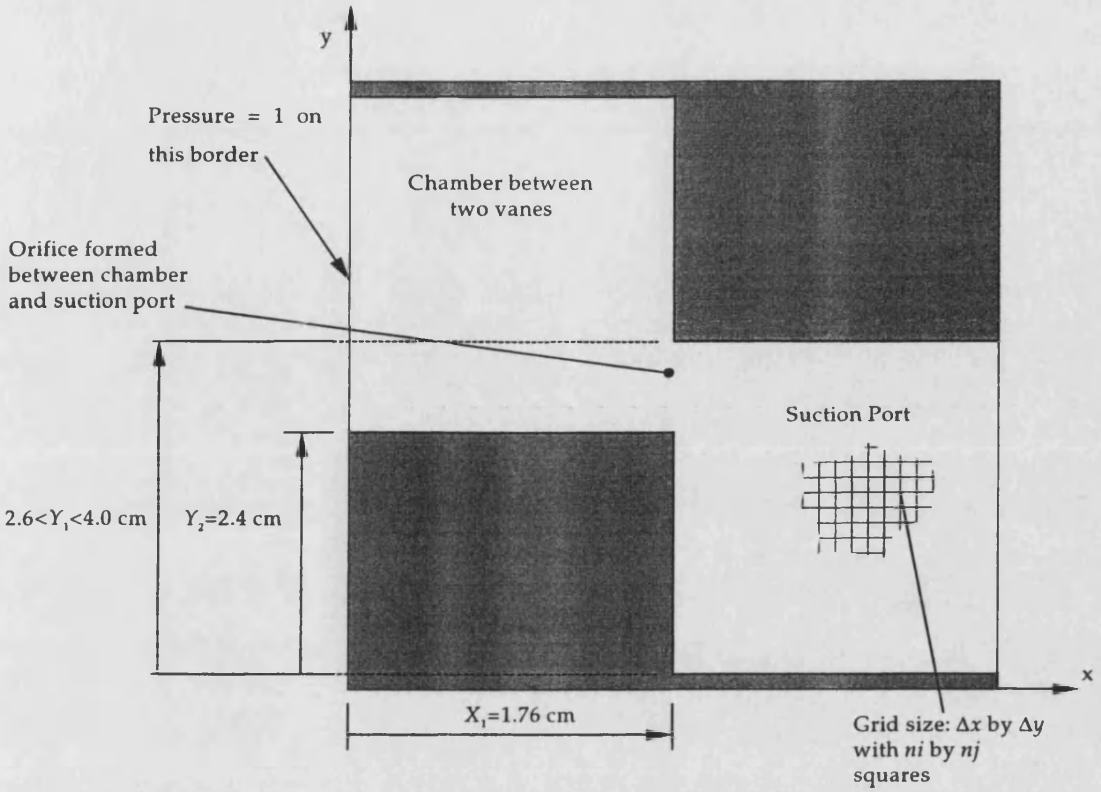

Figure 4–10: Grid Size and Dimensions

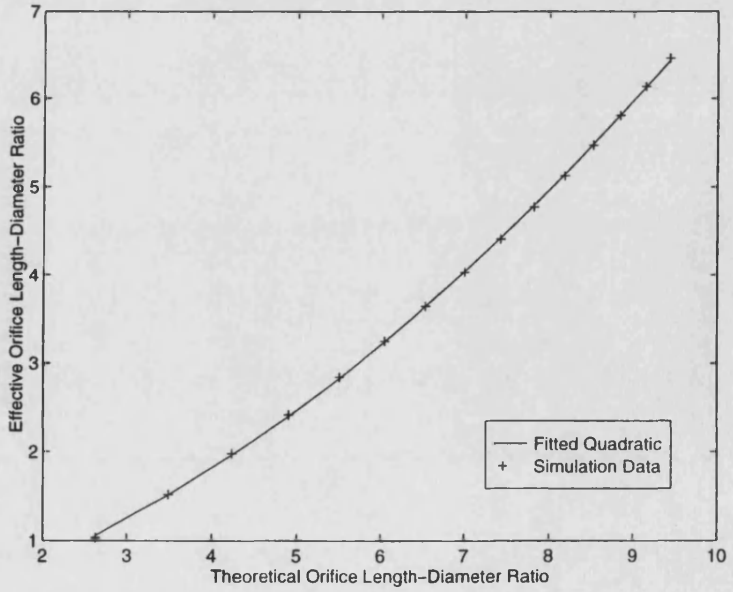

Figure 4–11: Graph of Effective Vs Theoretical Jet Length

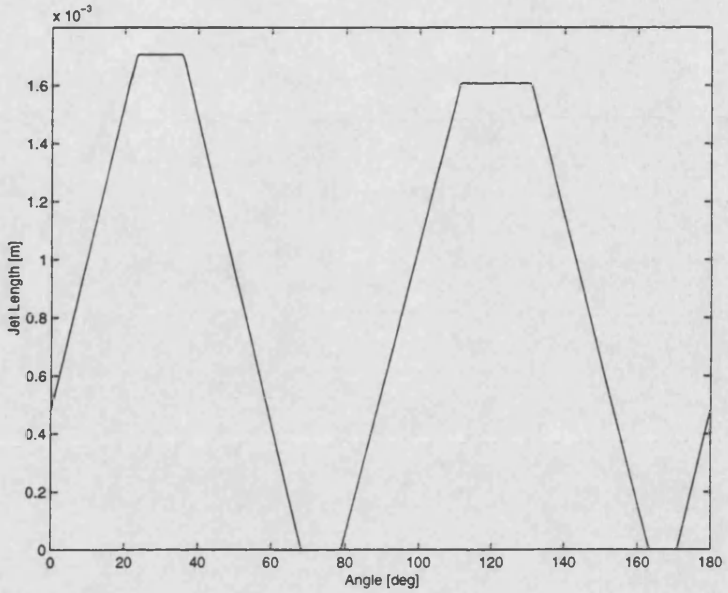

Figure 4–12: Jet Length Function

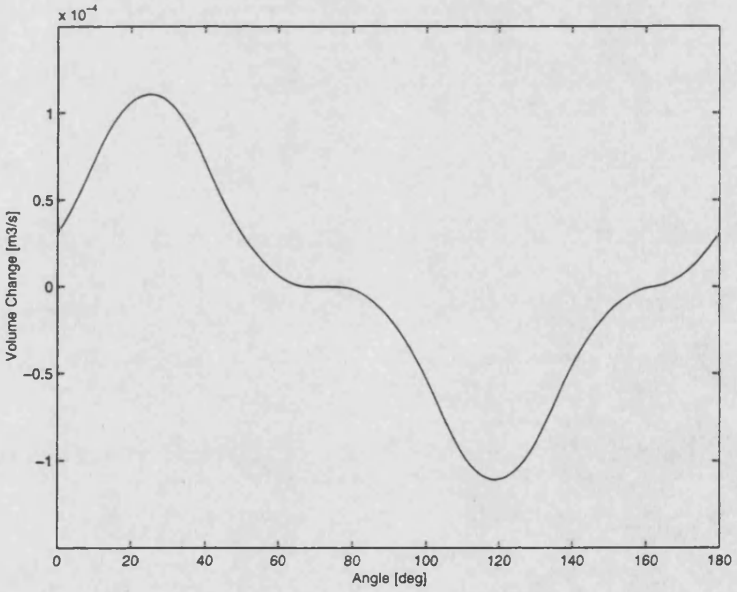

Figure 4–13: Rate of Change of Chamber Volume Function

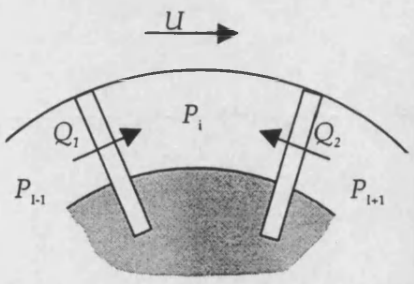

if $P_{i-1} > P_i$ Q_1 = +ve (flow in) U = +ve	if $P_{i+1} > P_i$ Q_2 = +ve (flow in) U = -ve
if $P_i > P_{i-1}$ Q_1 = -ve (flow out) U = -ve	if $P_i > P_{i+1}$ Q_2 = -ve (flow out) U = +ve

Figure 4–14: Sign Convention for Leakage Flow

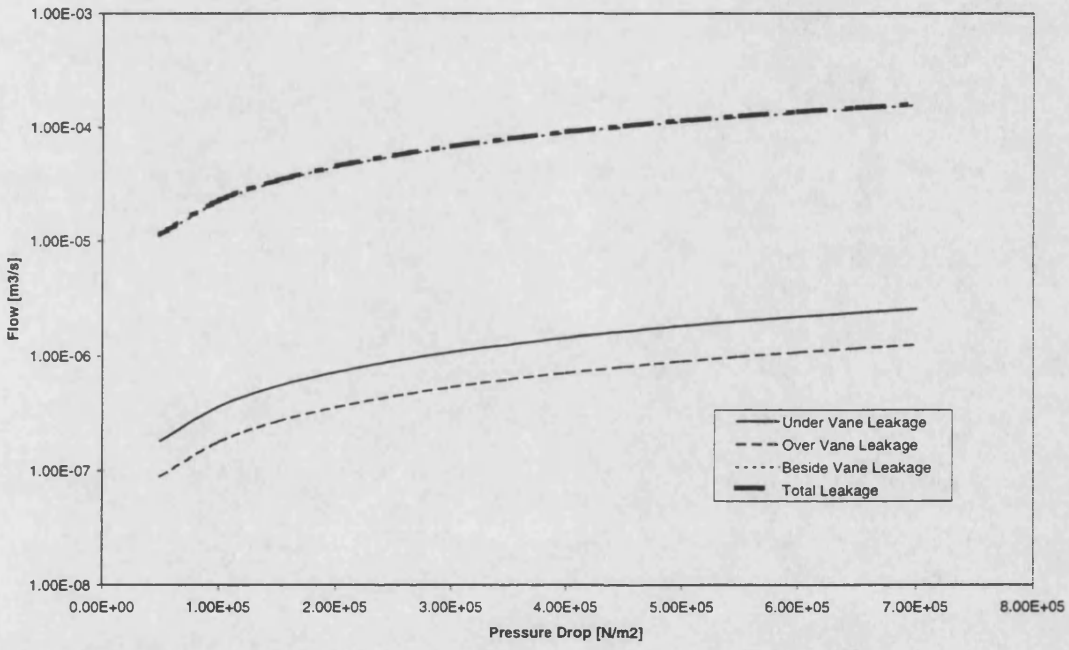

Figure 4–15: Flow Vs Pressure Drop for the Main Leakage Paths

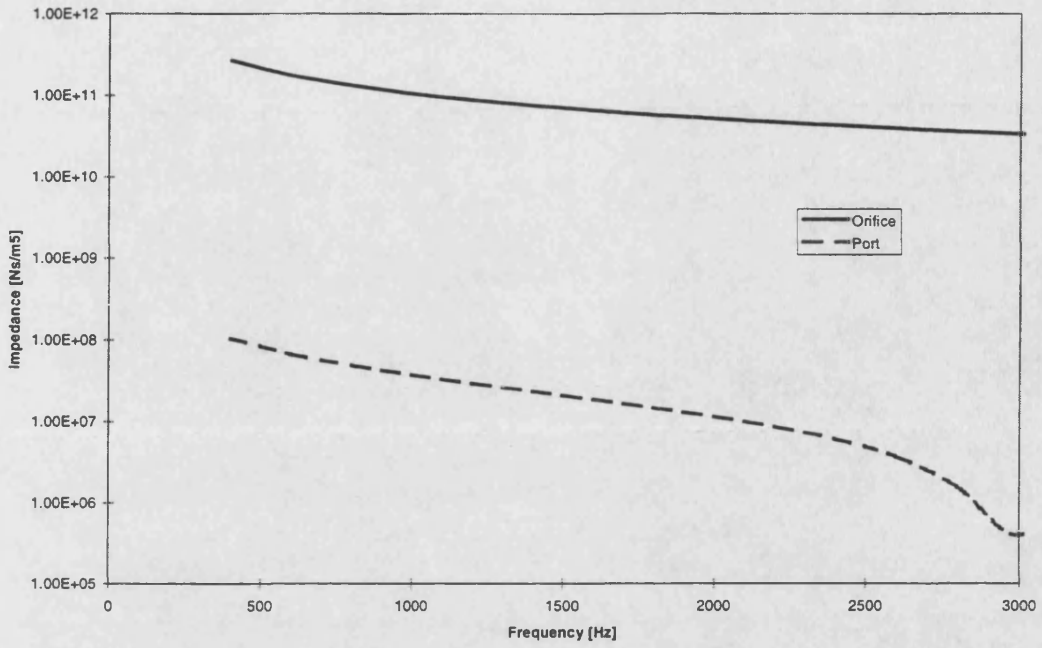

Figure 4–16: Comparison of Orifice and Port Impedance

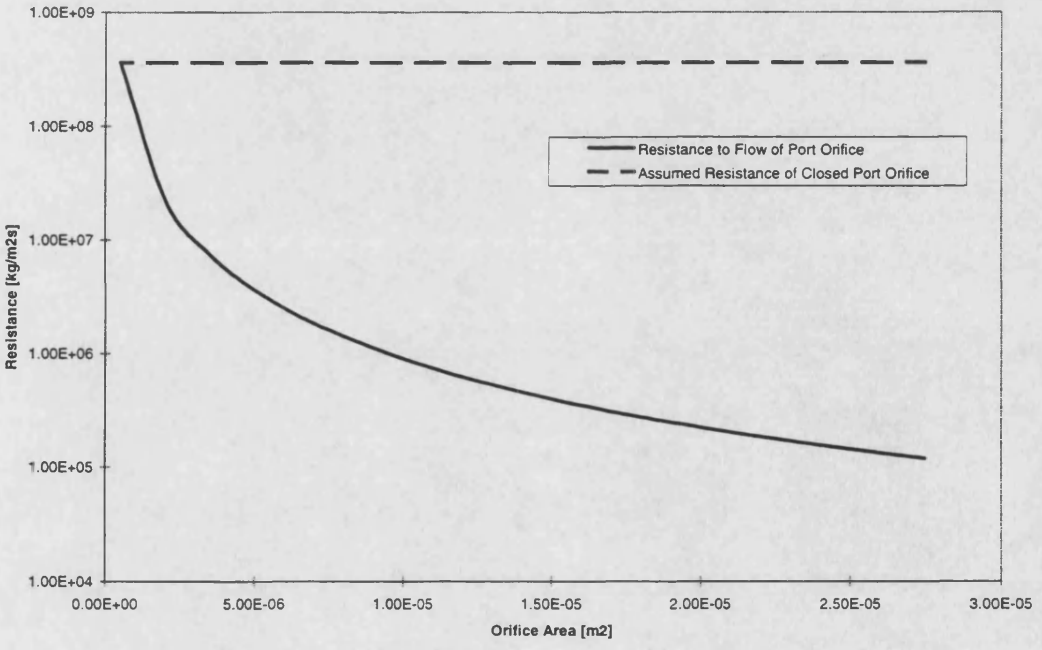

Figure 4–17: Resistance to Flow of a Closing Port Orifice

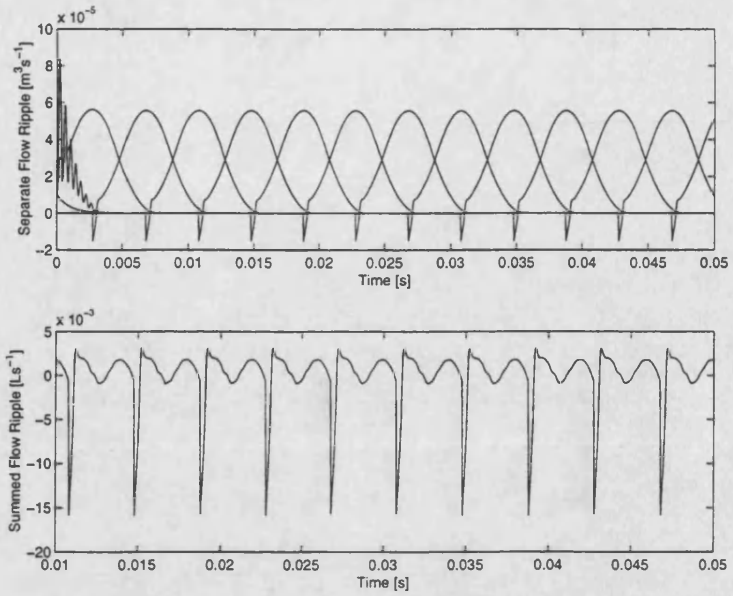

Figure 4–18: Flow in Separate Chambers and Summed Flow

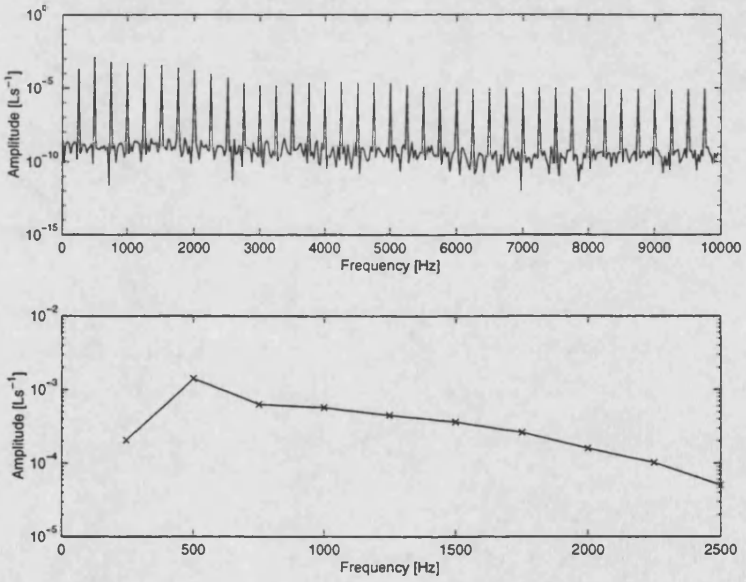

Figure 4–19: Flow Ripple Spectra

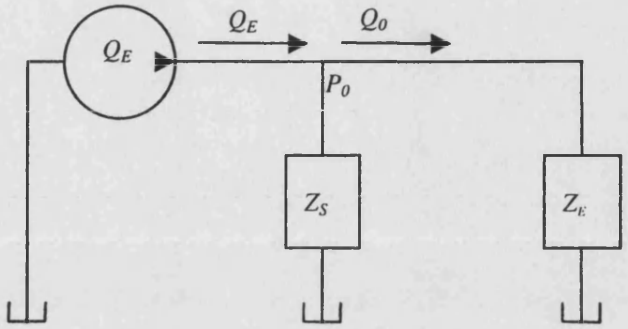

Figure 4–20: The Pump Passageway as a Norton Equivalent Model

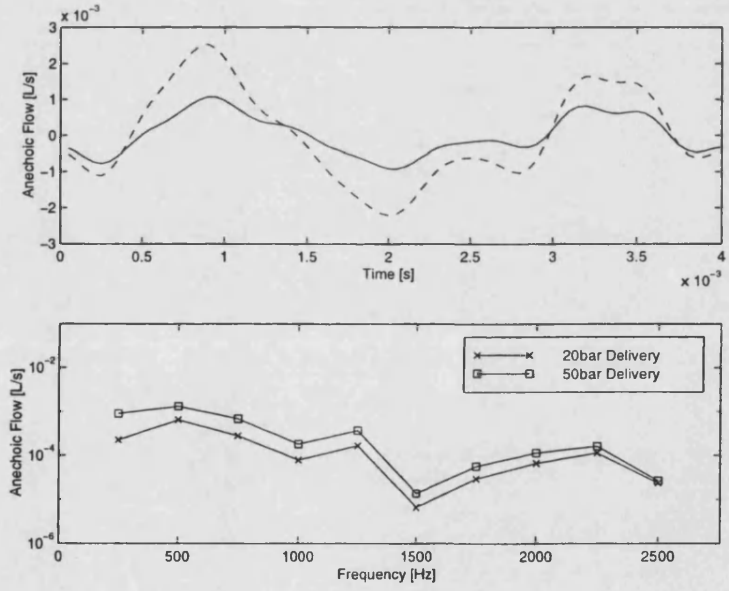

Figure 4–21: Effect of Delivery Pressure on Suction Flow Ripple

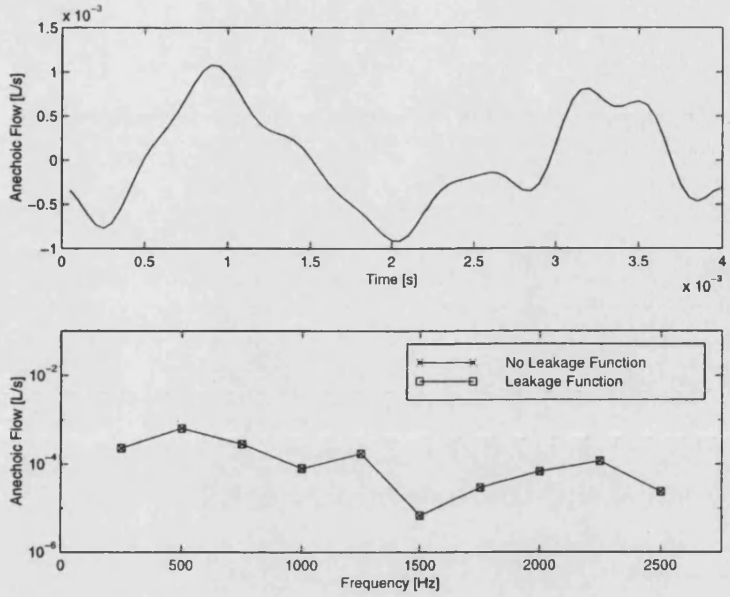

Figure 4–22: Effect of Leakage on Suction Flow Ripple

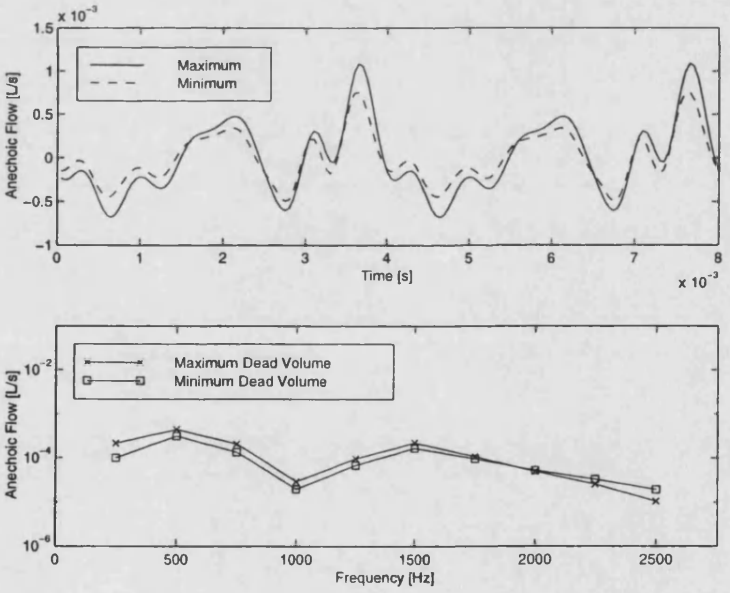

Figure 4–23: Effect of Chamber Volume on Suction Flow Ripple

5 TEST STAND DEVELOPMENT

5.1 INTRODUCTION

A successful test method is one that provides a standard measure of fluid borne noise emitted by a pump regardless of the circuit in which it is installed. This means that non-similar pumps can be compared easily under laboratory conditions thus cutting down on installation and commissioning time. Results from such a test method can also be used as validation data for simulations. Simulations usually concentrate on individual components and therefore the effect of circuit resonance is not calculated. Over the last few decades there have been many proposals for measurement techniques to quantify the flow ripple at the outlet of positive displacement pumps by isolating circuit resonance effects.

Flow ripple is created by all positive displacement pumps and is due to inherent construction characteristics. Pressure ripple, which is observed in a hydraulic system, is a result of the interaction between the flow ripple and the circuit impedance. Flow ripple cannot be directly measured whereas pressure ripple can. It is therefore necessary to know the circuit impedance in order to calculate the flow ripple from the measured pressure ripple data. The earliest techniques involve measuring the pressure ripple at the end of a very short discharge line that is terminated by a needle valve **(59, 60)**. Wave propagation effects can therefore be neglected and a simple lumped parameter impedance model can be used. Unfortunately, the assumption that a restrictor valve acts as a simple orifice leads to inaccuracies in the solution.

In a later method **(61)**, the impedance of circuit components is measured using a number of pressure transducers distributed along a pipe. Theoretically, it should be possible to find the source impedance and flow from just two transducers and two different lengths by using this method. However, it is susceptible to small errors in pressure measurement and multiple measurements must be taken with different transducer positions with the mean values being used to derive the results. This is known as the *Extending Pipe* method and is very time consuming and has been superseded by simpler methods. One such method is the *Hydraulic Trombone* **(62)** where the pipe can be extended by the addition of a sliding section in the circuit piping. In these test methods, the length of the measurement pipe means that wave propagation effects have to be considered. The characteristic impedance of the measurement section and the derivation of the reflection coefficients come from the solutions of the wave equation and are described in Johnston **(28)**. Detailed summaries of the above measurement techniques are summarised in Bowns *et al* **(63)** and Johnston **(64)**.

There have been fewer attempts at measuring fluid borne noise in the suction lines of positive displacement pumps. De Freitas *et al* **(65, 66)** carried out one such study in which the *extending pipe* method was used in a modified form termed the *tuned length* method. This modification

means that fewer pipe lengths are required to give an accurate result. This study concentrates on axial piston pumps and external gear pumps.

5.2 THE SECONDARY SOURCE TEST METHOD

The *Secondary Source Test Method* **(28)** is a more accurate method of measuring source impedance and flow ripple, which has been developed at the University of Bath. The test circuit (Figure 5–1) contains three major elements: The test pump, pressure transducers and a secondary source of pressure pulsation, which is required in order to measure the impedance of the pump's port. The three transducers measure the standing wave produced by the secondary source and the pump impedance is found by a manipulation of the wave equation **(28)**. Usually, the secondary source is a rotary valve but any source of pressure fluctuations will suffice. For example, an electromagnetic vibrator and piston or a 'noisy' positive displacement pump or motor have been suggested **(64)**.

The rotary valve creates a pressure pulse by periodically opening the high-pressure discharge line to the low-pressure return line. If the pressure difference between the delivery and return line is small (or the suction line is being tested) then the pulse emitted from the secondary source is weak. In order to test at low pressure, an additional pump (Figure 5–1) is required to produce the pressure difference across the valve. The main disadvantage to using a rotary valve in suction port measurements is that cavitation can occur in the jet from the rotary valve thus increasing the amount of air released from solution into the pipe containing the pressure transducers and reducing the frequency content of the pressure pulse. The presence of air bubbles in this part of the circuit makes the standing waves unsteady and hence gives inaccurate results. A suitable alternative to the rotary valve is needed that is equally effective as a secondary source at low and high pressure.

5.3 MODIFIED TEST STAND

Although hoses tend to attenuate pressure ripple passing through them **(67)**, by axially vibrating the closed end of a hose, pressure ripple can be generated **(68)**. The efficiency of this generation process depends on the type and length of hose. Measurements of hose impedance matrices including axial force and velocity **(4)** provide information on this. This was the method chosen to provide a secondary source in the suction line. Resonance causes the ripple generation to vary with frequency but in a circuit with significant line lengths this is inevitable with any type of source.

Figure 5–2 shows the modified Secondary Source Test Stand incorporating a flexible hose as pulse generator: an electro-dynamic vibrator drives the hose and the pulsation is transferred into fluid-borne noise. A signal generator drives the vibrator through a user-defined frequency range. The frequency-step is variable so that higher definition can be used at places of interest.

The hose produces vibrations without creating cavitation and therefore is more suitable for suction port measurements.

5.3.1 TEST STAND EQUIPMENT

Three pressure transducers are unequally spaced in a straight, rigid suction line. The transducers are flush-mounted so that the inner diameter of the line is uniform so that the only reflected waves come from the suction port. If there are reflections from sharp edges inside the measurement pipe, the impedance data for the suction port will be inaccurate. Pipe A must have a higher impedance than the transducer line so that it does not absorb the pressure fluctuation from the hose. Pipe A therefore has a smaller diameter and a greater length than the measurement pipe. The pressure drop between the reservoir and the pump must however be monitored to make sure that cavitation does not occur.

The reservoir is pressurised by means of a piston that can be loaded with weights (Figure 5–3). The piston can move freely up and down to compensate for changes in oil volume due to temperature variation. There are two reasons for using a pressurised reservoir: to compensate for the static pressure loss in the long suction line, and to observe the effect of a boosted suction pressure on flow ripple and impedance. The inlet pressure affects fluid bulk modulus, and hence flow ripple and impedance **(65)**. The decrease of bulk modulus with the loss of static pressure can be described by Henry's Law, which states that the amount of air dissolved in oil is directly proportional to the static pressure. Hence, if the pressure drops the over-saturated oil releases air in the form of bubbles.

The temperature of the oil in the test circuit is regulated by a heat exchanger. A 30L tank of hot water is kept at a constant temperature throughout the tests. The oil temperature varies depending on loading conditions and mean flow-rate but the much larger volume of constant temperature water damps this variation out.

5.3.2 DATA ACQUISITION

A PC fitted with a high-speed data acquisition card and a signal generator card controls the test stand. The user interface is a frequency-response-analyser/signal-generator package, which outputs a sine wave to the vibrator and measures the pressure readings from the three pressure transducers. The program can be used to measure the suction port impedance and the flow ripple.

To measure the port impedance the pump and the secondary source must be running. Readings from the pressure transducers are triggered by the signal from the pulse generator. From the pressure readings the amplitude of the forward and backward travelling wave are calculated **(28)**, and the impedance is derived.

The flow ripple is calculated by moving the trigger to the pump and switching the secondary source off. Pressure measurements can either be made at harmonics of the shaft frequency or the pumping frequency. The resulting flow ripple can be calculated using impedance notation as described by Edge *et al* (28).

5.3.3 TEST STAND VALIDATION

Three hoses, shown in Table 5–1, were tested to assess their suitability as vibration transmitters. Each hose was placed in the test stand, described in §5.3, and the pressure amplitude at the suction port was measured in a frequency range of 200-1000Hz. The interaction of the circuit impedance characteristic and the pressure wave from the secondary source means that the pressure amplitude is not constant across the whole frequency band.

	TYPE	DIAMETER [mm]	LENGTH [mm]
HOSE 1	SPIRAL	10	400
HOSE 2	HIGH-EXPANSION	10	500
HOSE 3	HIGH EXPANSION	10	280

Table 5–1: Hose types Tested for Suitability as Secondary Sources

There is no standard minimum value for pressure amplitude emitted by a secondary source, so it can be assumed that the magnitude of the pressure must be greater than the general level of circuit noise. One such method of defining the minimum amplitude is to compare the secondary source amplitude with the amount of scatter produced on an impedance result. Figure 5–4 shows the comparison between the pressure amplitude and the impedance result for hose 1. There are two areas of scatter on the impedance data that occur when the amplitude of the pressure pulsation is below approximately 10mbar. This indicates that a good rule of thumb is that the minimum amplitude emitted by the secondary source must be greater than 10mbar.

The pressure amplitudes emitted by the three hoses are shown in Figure 5–5. Hose 3 does not satisfy the 10mbar minimum amplitude above 250Hz. It is therefore not suitable as a secondary source. Hoses 1 and 2 have large bandwidths where the amplitude is above the 10mbar limit. Hose 1, however, only satisfies the criterion below 700Hz, whereas Hose 2 may show some scattered results in a small bandwidth located around 500Hz but is above 10mbar for all other frequencies tested.

Figure 5–6 shows a comparison of pressure amplitude and impedance data for Hose 2 between 200 and 2500Hz. There is a small amount of scatter at 500Hz; however, there is little scatter above 1900Hz where the pressure amplitude drops below the 10mbar minimum. This is because the background noise at high frequency is not as great as at low frequency, hence the secondary source signal does not need to be as strong. Hose 2 was therefore chosen as the secondary source for the test stand.

Considering the small amount of hoses used for this study, it would not be prudent to recommend that any type of hose is best for incorporating into a test stand. However, a general

rule of thumb, which would need to be verified by an extensive test program, can tentatively be put forward. From the study it has been seen that a high expansion hose produced the best signal over a large frequency range. During the testing of these hoses, the length and shape of the test stand's piping was changed several times in order to compensate for a lack of space in the laboratory and, although the hoses performed slightly differently in each configuration, the high expansion hose was always the best. One other generalisation can be made from these three tests, which is that a shorter high expansion hose may be used for carrying out measurements at a lower frequency than a longer hose may.

5.4 SUITABILITY OF THE VIBRATING-HOSE FOR DELIVERY LINE TESTS.

In §5.3 a vibrating hose was found to be a good secondary source of vibrations for measuring impedance at low pressure. There was no available published data for suction port impedance and so an indirect method was used to validate the test method. However, in the case of delivery port impedance, a direct comparison of secondary sources can be made. Pumps were tested using, firstly, a rotary valve and, secondly, a vibrating hose as secondary source. The pump speed and the mean pressure were varied to assess the range of use of each secondary source.

The secondary source test method is used as the British Standard **(69)**, and has been proposed as an ISO standard **(70)**, of measurement of delivery pressure ripple, and the rotary valve is accepted as the standard secondary source. Impedance results gained from using the rotary valve as secondary source will therefore be used as a benchmark. The vibrating hose will be compared to this benchmark and will add support to the validation of the method described in §5.3.

5.4.1 IMPEDANCE MEASUREMENTS USING A ROTARY VALVE

The secondary source test stand, shown in Figure 5–1, was set up and two pumps were tested. Two pumps were used whose discharge volumes were different in order to show the effect of volume on the results. Pump 1 had a smaller volume than Pump 2.

Figure 5–7 shows the impedance for pump 1 running at 1500 rev/min and 40bar. There is some scatter above 2kHz but it is possible to locate the position of the anti-resonance. Figure 5–8 shows the impedance data for the same pump but with the delivery pressure reduced to 20bar. Here the scatter above 2kHz increases but the impedance trace is still legible. This scatter does not become a problem unless it occurs at a point of interest.

Figure 5–9 shows the impedance of Pump 2. The impedance is calculated at the frequencies coinciding with the harmonics of the rotary valve. Here, the harmonics are widely spaced giving low definition and the positions of the anti-resonance at 400Hz and the effect at 2kHz are ill defined. This problem can be overcome by carrying out the tests with five or six different

rotary valve speeds whose harmonics coincide with these points of interest. Therefore it is advisable to do two tests for a pump: the first to find possible places of interest, the second to refine the definition at these points by choosing rotary valve speeds that have harmonics at the place of interest.

5.4.2 Impedance Measurements using a Vibrating Hose

The test stand shown in figure 5–10 was used to measure the impedance of the two pumps described in §5.4.1. Figure 5–11 shows the impedance of Pump 1. Below 800Hz, there is some scatter in the data but at high frequency, the results are smooth. The function generator sets the frequency step and therefore even in the area of scatter there is enough definition to accurately measure the position of the anti-resonance. The scatter is due to a low signal being produced by the secondary source at low frequency and could be remedied by replacing the hose with one that produces a higher pressure amplitude at low frequency. Figure 5–5 shows that this may be achieved by using Hose 3 for tests for frequencies up to 200 Hz.

5.4.3 Comparison of the Two Secondary Sources

Figure 5–12 shows the impedance of pump 2 measured with: a) rotary valve and, b) vibrating hose. Below 1.7kHz, the curves are similar but above this value there is some divergence. Results using the rotary valve have been seen to show scatter above 2kHz and it is therefore the vibrating hose result that is probably most accurate. The definition around the anti-resonance at 400Hz is better with the vibrating hose due to the control of frequency step in the function generator. Figure 5–13 (the impedance of Pump 1) shows that the definition gained from the rotary valve can be much higher if care is taken with the rotary valve speeds. It also shows that the divergence of the curves in Figure 5–12 is not a characteristic of the test method, but it is due to the scatter of data points.

5.5 Conclusions

A flexible hose attached to an electro-magnetic vibrator was chosen as a secondary source of pressure ripple for measuring the impedance of low-pressure circuits. It was found that the hose was required to produce pressure ripple above 10mbar amplitude in order to give good results. The suitability of the method was examined by monitoring the amount of scatter on test results. A high-expansion hose, 500mm long with a diameter of 10mm, was chosen as the secondary source.

The versatility of the vibrating hose secondary source was also examined by testing delivery port impedance. These results were compared against data obtained using a rotary valve as secondary source. The two methods showed generally good agreement, with the rotary valve technique giving better results at low frequency and the vibrating hose being better at high frequency.

FIGURES FOR CHAPTER 5

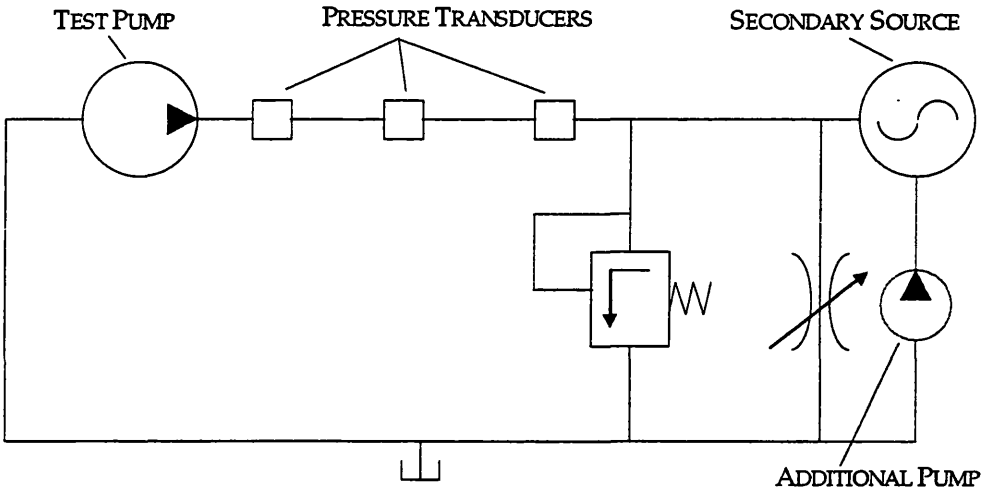

Figure 5–1: The Secondary Source Test Circuit

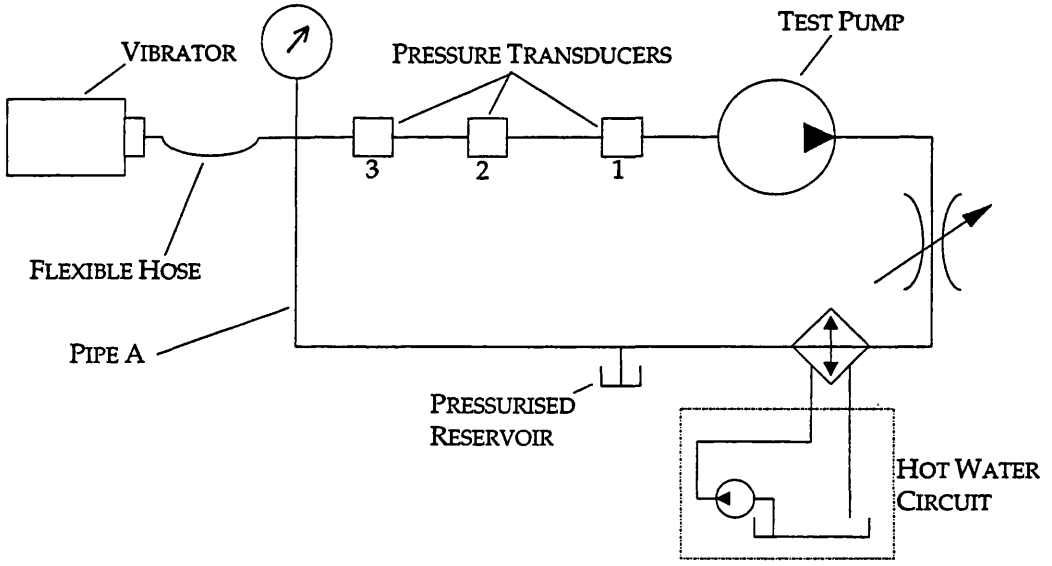

Figure 5–2: The Modified Secondary Source Test Circuit

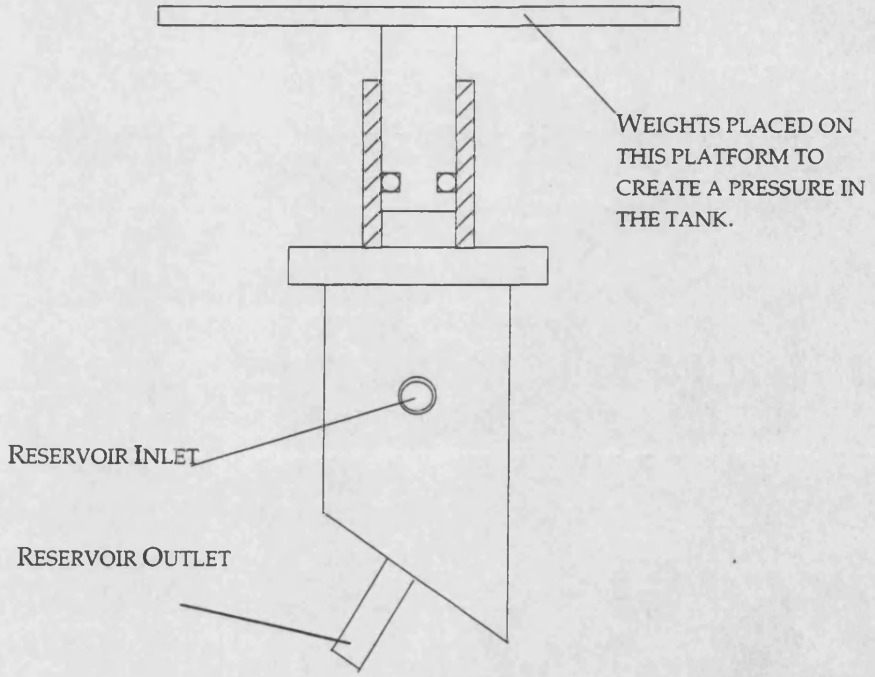

Figure 5–3: Reservoir Construction

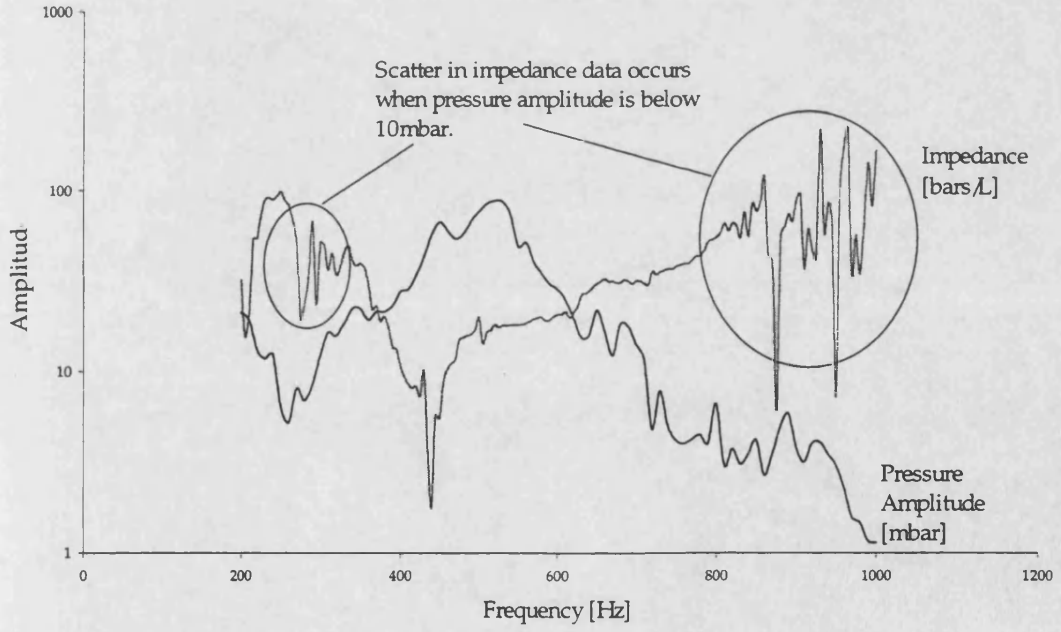

Figure 5–4: Comparison of Pressure Amplitude and Impedance Result Scatter for Hose 1

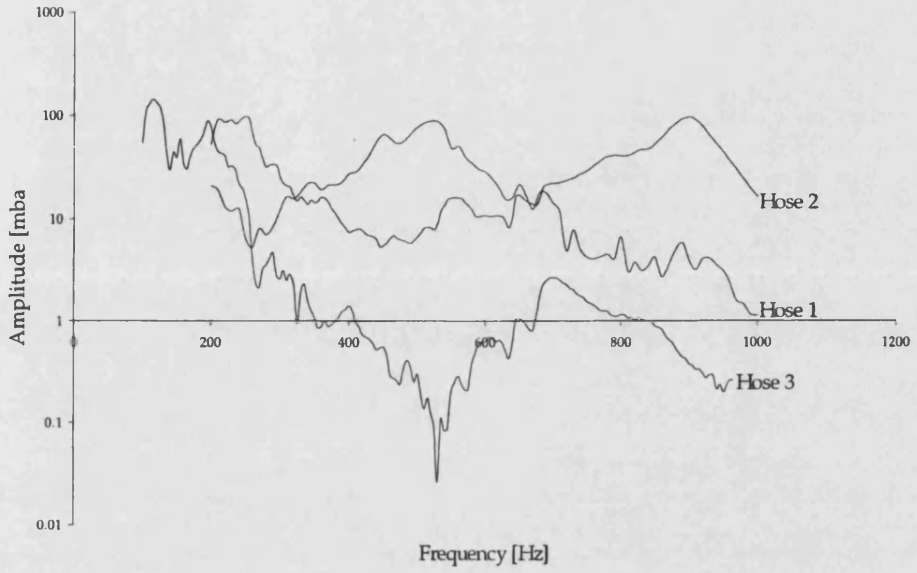

Figure 5–5: Pressure Amplitude of the Three Secondary Source Hoses

Figure 5–6: Comparison of Pressure Amplitude and Impedance Result for Hose 2

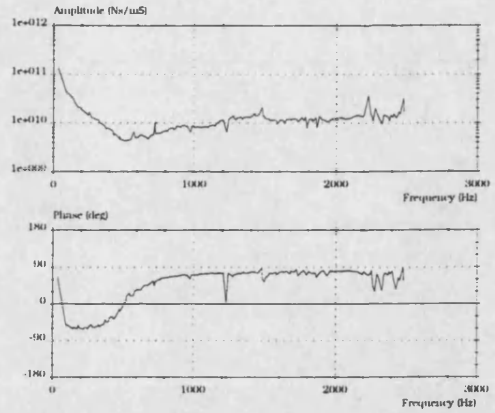

Figure 5–7: Delivery Port Impedance of Pump 1 (1500 rev/min, 40bar, Rotary Valve)

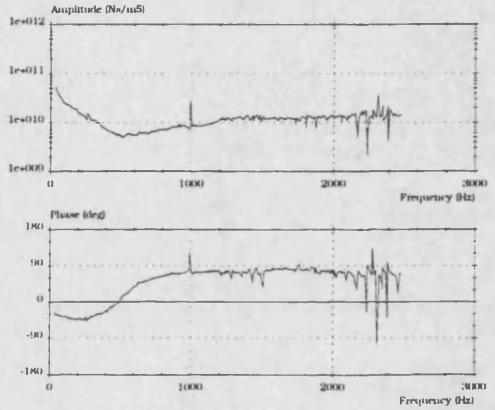

Figure 5–8: Delivery Port Impedance of Pump 1 (1500 rev/min, 20bar, Rotary Valve)

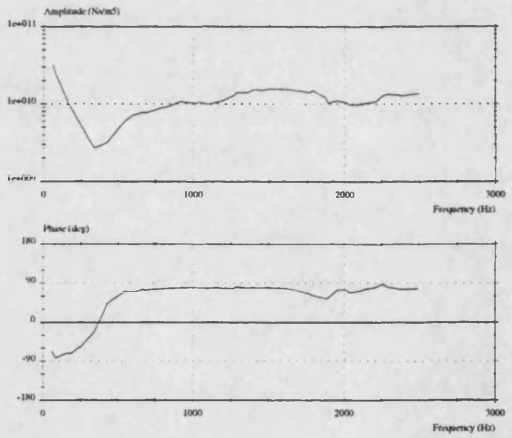

Figure 5–9: Delivery Impedance of Pump 2 (1500 rev/min, 40bar, Rotary Valve)

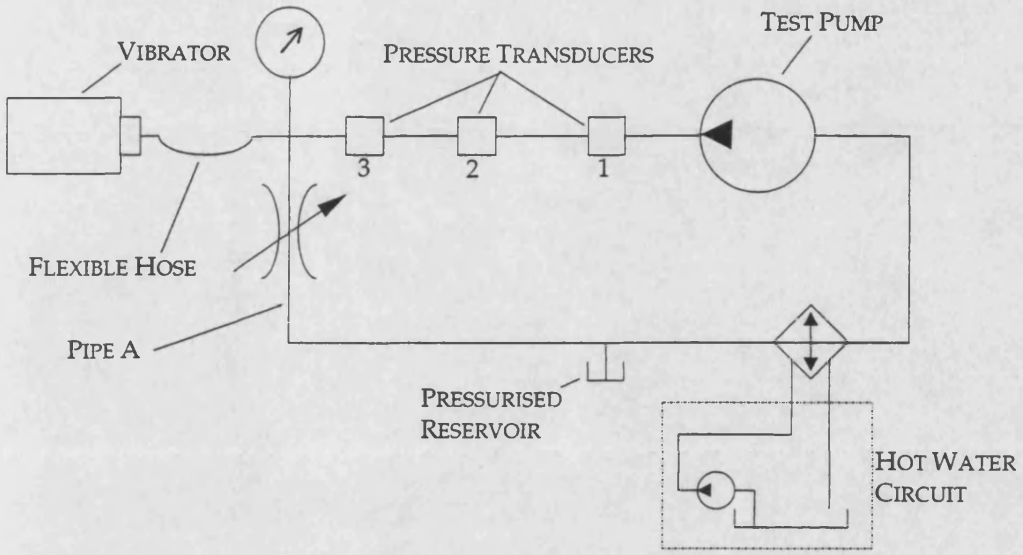

Figure 5–10: Test Stand for Measuring Delivery Impedance with Vibrating Hose

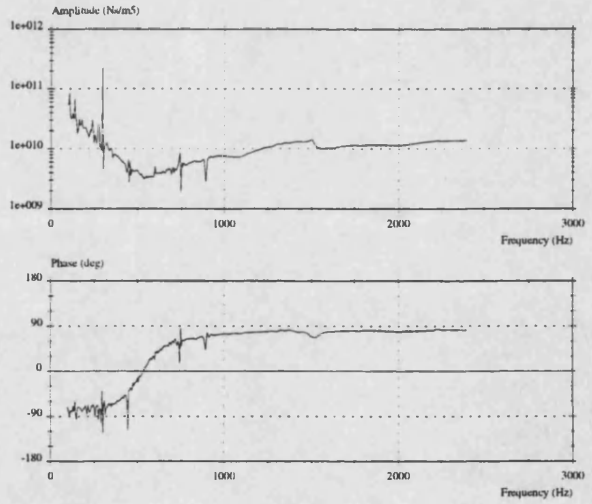

Figure 5–11: Delivery Impedance of Pump 1 (1500 rev/ min, 40bar, Vibrating Hose)

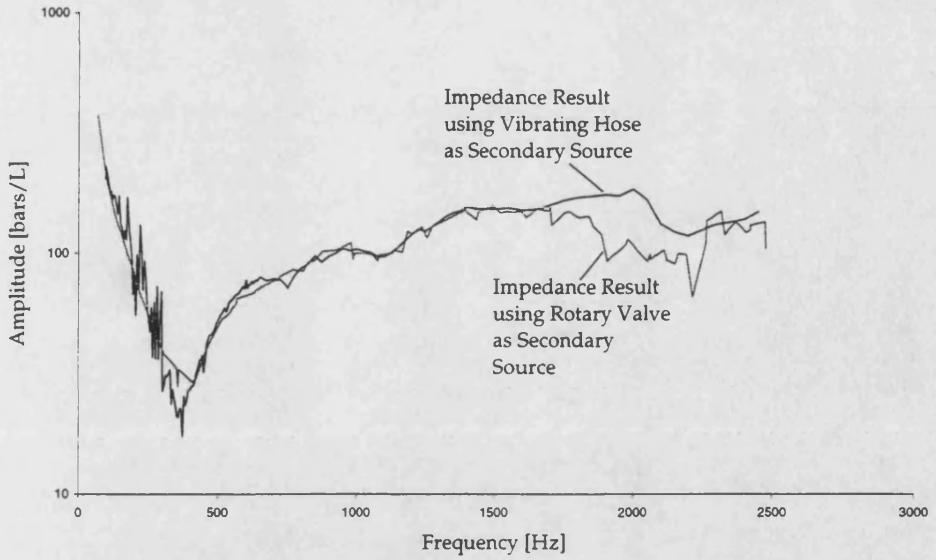

Figure 5–12: Impedance Results using Both Secondary Sources (Pump 2)

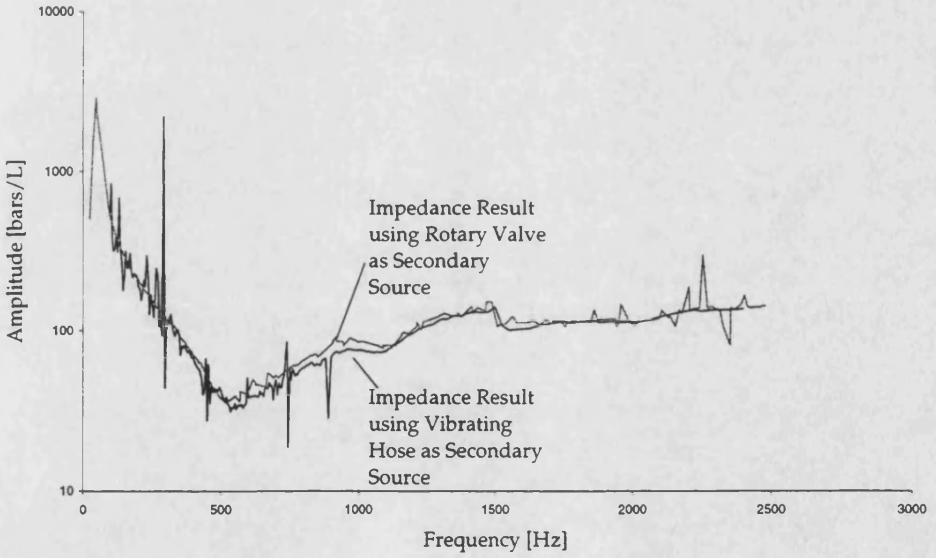

Figure 5–13: Impedance Result using Both Secondary Sources (Pump 1)

6 TEST RESULTS

6.1 INTRODUCTION

The secondary source method (28) was used to test a variety of pumps for their impedance and flow ripple characteristics. A vibrating hose was used as secondary source to find the impedance, which enabled the flow ripple to be calculated from pressure ripple measurements. The variation in impedance and flow ripple was analysed as a function of both pressure and pump speed. The results can be used to increase understanding of the pump dynamics and for validation of the simulation. Once the pump dynamics are understood, the simulation can then be used as a design tool to reduce flow ripple emitted from the pump.

6.2 TEST PROCEDURE

Data from the test stand was processed using the *FBN2* software (71), which uses the following procedure:

- Start pump and secondary source
- Measure pressure signal from secondary source
- Process secondary source signal to find port impedance
- Fit mathematical impedance model to impedance results
- Switch off secondary source
- Measure pressure signal from pump
- Process pressure signal from pump using impedance model to find flow ripple

Impedance and flow ripple tests at various conditions were carried out on six pumps, which are shown in Table 6–1. Duplicate pumps were tested to show repeatability of experiments and to observe the effect of machine tolerance on the results.

PUMP NAME	PUMP TYPE
Pump 1	Saginaw TC60
Pump 2	Saginaw TC60
Pump 3	Saginaw TC88
Pump 4	Saginaw TC88
Pump 5	Saginaw CB60
Pump 6	Saginaw CB60

Table 6–1: Test Pump Identity

6.3 SUCTION PORT IMPEDANCE RESULTS

The impedance of the six pumps was measured at three speeds: 450, 900 and 1500 rev/min, at several delivery pressures and at two suction pressures: atmospheric pressure and 3bar. The repeatability, the effect of delivery pressure, suction pressure and pump speed were observed.

6.3.1 REPEATABILITY OF IMPEDANCE TESTS

To test the repeatability of the test method, Pump 1 was tested on consecutive days and the results were compared in Figure 6–1. Apart from a discrepancy in amplitude above 1500Hz, the test on Pump 1 showed good repeatability. The difference is most likely due to small variations in oil properties across the two days.

The repeatability of results from different pumps with the same specification was also analysed. Figure 6–2 shows a comparison between the measured impedance of Pump 1 and Pump 2. There is a small difference in the position of the phase changes, which implies that Pump 2, shown in a dotted line, is a stiffer system than Pump 1. This is probably due to the air content in the oil, which affects bulk modulus. By ignoring these small variations, results can be assumed to be identical for different pumps with the same specification. Figure 6–3 shows a comparison between Pump 5 and Pump 6, which also shows good correlation.

6.3.2 THE EFFECT OF DELIVERY PRESSURE ON IMPEDANCE

Figure 6–4 shows the suction impedance characteristic for Pump 1 at three different delivery pressures: 20, 35 and 50bar. Differences in the impedance may be expected because the delivery pressure affects the pressure in the pumping chambers as they open to suction, i.e. the pressure at which a chamber opens is higher if the delivery pressure is higher. The effect of this would be to change the air bubble content that may collect next to the rotating group, which would alter the bulk modulus of the system. This is not observed in figure 6–4, which shows that the delivery pressure has negligible effect on the suction impedance.

6.3.3 THE EFFECT OF RESERVOIR PRESSURE ON IMPEDANCE

Figure 6–5 shows the effect of suction port pressure at 450rev/min when the supercharge valve is closed and is not introducing air into the system. There is a difference between the measured impedance at atmospheric pressure, shown as a solid line, and at 3bar, shown in dotted. In the 3bar condition, the first resonant and anti-resonant peaks are increased by about 100Hz, which suggests that reservoir pressure affects system stiffness. The increase in stiffness is partly due to the reduced size of the air bubbles under pressure, which increases both the density and bulk modulus of the system. This phenomenon is demonstrated in Figure 3–16, which shows that the predicted impedance due to an increased pressure behaves in the same manner.

Figure 6–6 shows the effect of reservoir pressure on impedance at 1500rev/min when the supercharge valve is open. Immediately, a difference can be seen between Figure 6–5 and Figure 6–6: The results of the 3bar tests, in dotted on both figures, are identical. However, there is a decrease in frequency in all of the resonant and anti-resonant peaks in the high-speed case and there is also a lot of scatter on the results. Air entrained into the pump housing from the supercharge valve could be a possible cause of this large increase in system compressibility. Another reason why there would be more aeration could be that the lowered pressure from an increased flow has caused air to evolve from solution. The standing waves, which are measured to find the impedance, may become unsteady if there were a high air content, which would account for the scattered results.

6.3.4 THE EFFECT OF PUMP SPEED ON IMPEDANCE

Pump speed tests are shown in Figures 6–7, 6–8, 6–9 and 6–10 for Pumps 1 and 5. Speed has a much greater effect on the impedance at atmospheric pressure. The results for the 3bar tests (Figure 6–7 and Figure 6–9) show only very slight changes when the pump speed is increased (The tests shown are at 450, 900 and 1500rev/min). On the other hand, at atmospheric pressure (Figure 6–8 and Figure 6–10), there is a much more marked change in the impedance characteristic. At 450rev/min (shown as a solid line) and 900rev/min (dotted line), there is little change in the impedance. However, at 1500rev/min (dash-dot-dot line) when the supercharge valve is open, aeration causes the system stiffness to be reduced thus altering the impedance characteristic.

6.4 SUCTION PORT FLOW RIPPLE

Pressure ripple emitted by the pump was measured and using impedance models, based on the results in Section 6.3, the flow ripple was calculated. Anechoic flow ripple was used to compare the results, as it is a good comparative rating which is not affected by circuit resonance.

In Chapter 1, the mechanisms involved in converting flow ripple to pressure ripple and finally to airborne noise were described. However, the potential for fluid borne noise on the suction side to create as great a nuisance as that which is found on the delivery side is much lower due to the construction of the power steering system. According to Reference (2), the main transmission path from fluid borne to airborne noise is via the steering column and into the passenger compartment. The suction port of the pump is not directly linked to the valve, and hence the steering column, and so this means of transmission must be assumed to be much smaller than is the case for delivery. The comparison of delivery and suction fluid borne noise cannot therefore be equated on equal terms when considering their potential to cause airborne noise. Only on insertion into a simulation of an entire power steering system could the true impact of suction port flow ripple be assessed.

6.4.1 REPEATABILITY OF FLOW RIPPLE TESTS

Flow ripple from the test pumps was not as repeatable as the impedance results. Pump 1 and Pump 2, shown in Figure 6–11, show discrepancies at all harmonics. The comparison between Pump 3 and Pump 4, in Figure 6–12, is much better, with the flow ripple spectra showing the same shape and only small errors between the amplitude of each harmonic. Pump 5 and Pump 6, Figure 6–13, show good agreement between the 1st, 3rd and 4th harmonic, but the 2nd harmonic shows a large difference.

The reasons that flow ripple results are not as repeatable as impedance results are probably due to machining tolerances and random effects created by localised air bubbles and cavitation. In the case of machine tolerances it was shown in Chapter 3 that, while there was little effect on impedance due to tolerances, no evidence was found to support this argument with a view to flow ripple. In other words, small variations in the opening of a chamber between different pumps may alter the flow ripple waveform significantly, whereas no noticeable difference in impedance may be detected. This may also be the case regarding gas pockets, which may only exist for short periods of time, thus affecting the short-duration flow ripple tests and not the longer duration impedance tests.

6.4.2 THE EFFECT OF PUMP SPEED ON FLOW RIPPLE TESTS

Figure 6–14 shows flow ripple from the three types of pumps, Pump 1, Pump 3 and Pump 5, at 450rev/min. The peak to peak value for all pumps is within $\pm 0.001 Ls^{-1}$ with no pump having a noticeably greater or smaller flow ripple. The flow ripple at 900rev/min and 1500rev/min are shown in Figure 6–15 and Figure 6–16, respectively. At 900rev/min, the peak to peak flow ripple values are about $0.0024 Ls^{-1}$ for Pump 3, decreasing to $0.001 Ls^{-1}$ for Pump 1. So, in the case of Pump 3, there is an increase in flow ripple with speed but for Pump 1, even though there is an increase in the 1st harmonic amplitude, the higher harmonics have helped to reduce the peak to peak level of the waveform. At 1500rev/min, the 1st harmonic of flow ripple for each pump has reduced, which could be due to lower impedance reducing the anechoic flow ripple in relation to the internal flow ripple. The higher harmonics are very dominant, which implies that the flow ripple at high-speed is due more to compression and fluid inertia.

6.4.3 THE EFFECT OF RESERVOIR PRESSURE ON FLOW RIPPLE

Figure 6–17 shows the flow ripple waveform for Pump 1 at 1500rev/min. At 1 bar the flow ripple magnitude is seen to be lower than at the boosted pressure of 3 bar. Figure 6–18 shows Pump 5 at 450rev/min where there is less air present than in Figure 6–17. Here, the flow ripple at 1bar and 3bar have similar spectra for two tests where the amount of air in the pump would be expected to be similar. The general rule of thumb therefore is that the lower the flow ripple level is, the greater the amount of air that is present. This is a situation which is governed by the

supercharge valve more than the reservoir pressure because the effects are more noticeable at high speed when the valve is open.

6.5 COMPARISON OF SUCTION AND DELIVERY FLOW RIPPLE

In order to assess the overall contribution of suction port noise to the entire noise emitted by the pump, it is necessary to compare it to the delivery flow ripple. The delivery flow ripple was measured in the same way as the suction flow ripple, with three pressure transducers. The signals emitted from each port were measured simultaneously to ensure uniformity of conditions and an accurate relationship between the phase of the two signals. The effect of delivery pressure on suction flow ripple and vice versa was analysed.

6.5.1 DELIVERY FLOW RIPPLE AS A FUNCTION OF RESERVOIR PRESSURE

Figure 6–19 shows the delivery anechoic flow ripple from Pump 1 at 450rev/min and two reservoir pressures. There is little detectable difference between the two results apart from some small experimental errors. In Figure 6–20, the delivery pressure of Pump 3 is set to 10bar and apart from a small difference in the 2nd harmonic, there is still no great effect from varying the suction pressure. Figure 6–21 shows that similar results were obtained for Pump 5.

These results highlight three points:

- The pressure drop across the pump, between delivery and suction, is more important than the reservoir pressure in affecting delivery flow ripple.
- As long as there is no cavitation, and in this case the reservoir pressures are high enough to avoid this, the performance of the pump is not going to be greatly affected by suction pressure.
- The amount of air entrained into the pumping chambers is similar for each of the tests carried out in this section. If this were not the case, the evidence of varying air content would be detectable in the delivery flow ripple. In the following chapter, Figures 7–26 and 7–27 demonstrate the effect that the chambers' air content has on flow ripple but this is not seen in these tests.

6.5.2 SUCTION FLOW RIPPLE AS A FUNCTION OF DELIVERY PRESSURE

Figure 6–22 shows Pump 3 at 450rev/min with the suction line pressure set to atmospheric and the delivery line pressure at 10bar and 50bar. The flow ripple in the suction line can be seen to increase as the delivery line pressure increases. This is due to the mean pressure in the pumping chambers being greater as they open to the suction port. This is also shown in Figure 6–23, where five delivery pressures (10, 20, 30, 40 and 50bar) are superimposed upon one another. The amplitude can be seen to increase as the delivery pressure does. The exception to this rule is seen at 1500rev/min when the supercharge valve is open. Figure 6–24 shows the flow ripple in

the suction line at 10bar and 50bar at 1500rev/min, which represents straight-ahead driving and a parking manoeuvre, respectively. This clearly shows a greater flow ripple at the lower delivery pressure and can be explained by the impedance characteristic for this condition, which is shown on Figure 6–6. The impedance below 1 kHz is much lower than usual and it is the interaction of this with the lower harmonics of the source flow ripple which produces the higher amplitude waveform.

6.5.3 COMPARISON OF SUCTION AND DELIVERY FLOW RIPPLE

Figure 6–25 shows the suction and delivery flow ripple for Pump 3 at 900rev/min, the reservoir is at atmospheric pressure and the delivery pressure is at 50bar. It can be seen that the first three harmonics of delivery flow ripple are the greater, but the higher harmonics in each set of results are about the same value. In Figure 6–26, which shows Pump 5 at 1500rev/min, 1bar suction and 10bar delivery, the first seven harmonics of suction flow ripple are greater than the delivery flow ripple. This indicates that suction flow ripple could cause significant pressure ripple and possibly vibration. It can be seen, in Figure 6–27, that if the reservoir pressure is boosted to 3bar, the first and third harmonic of the suction flow ripple are reduced below the level of the delivery flow ripple, but the rest are still at a higher level.

There is usually an order of magnitude drop in the amplitude of delivery flow ripple between the first and fourth harmonic. For the pumps tested, this drop in magnitude with harmonic number is less marked for the suction flow ripple. The reason is that the delivery ports have relief grooves whereas the suction ports do not. The relief grooves slow down the rate of change of pressure in the pumping chamber as the port opens, and hence reduce the amplitude of the higher frequency harmonics. At lower pressure there is less of a pressure change as the suction port opens so the higher harmonics of the suction flow ripple are reduced. A validated flow ripple simulation could be used as a design tool to analyse the effect of adding relief grooves to the suction port. If this reduces the higher harmonics in the case of Figure 6–25, the suction flow ripple would become negligible compared with delivery flow ripple. The addition of relief grooves to the suction ports is discussed in Chapter 8.

The case shown in Figure 6–26 requires additional problems to be addressed in order to reduce the suction flow ripple to a level below delivery. Relief grooves may reduce the higher harmonics' amplitude but the level of aeration needs to be addressed in order to reduce the level of the lower harmonics. This could be done by modifying the supercharge valve **(2)**, to reduce the amount of bubbles entrained into the housing, or by boosting the reservoir pressure. In a real situation the latter is an impractical solution and so redesign of the supercharge outlet would be more effective. The methods employed in modifying the valve are discussed in Section 2.1.3.

6.6 CONCLUSIONS

The impedance of the suction port was found to vary with pump speed and reservoir pressure. As the pump speed increases, the air content rises thus changing the oil properties, which affects the impedance. The impedance results reflect the reduction in bulk modulus due to aeration, which is seen as a reduction in frequency of the resonant and anti-resonant peaks as the speed increases. Air evolves from the fluid as pressure decreases due to increased flow rate and it is also entrained from the supercharge valve. Boosting the reservoir pressure can reduce the effects of air.

Flow ripple was greatly affected by the mean pressure in the delivery line with the highest level corresponding to the highest delivery pressure. The level of the first three harmonics of flow ripple was found to be generally lower for suction than delivery. However, the higher harmonics were sometimes dominant in the suction line, which is possibly due to the lack of relief grooving on the suction ports.

The main findings from this series of experiments were that aeration should be reduced at high pump speed and that the higher harmonics of suction flow ripple should be reduced. If this were the case suction noise levels could be reduced to negligible levels in comparison with the delivery line. The aeration could be reduced by modifying the discharge of the supercharge valve so that the jet did not cavitate, and the higher harmonics could be reduced by adding relief grooves to the suction ports.

FIGURES FOR CHAPTER 6

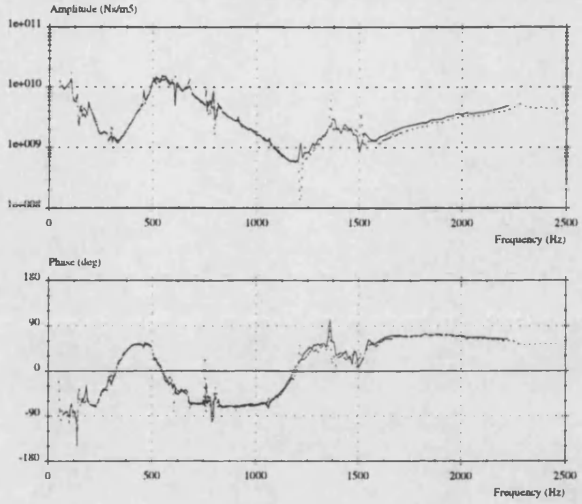

———	PUMP 1	REPEATABILITY TEST1	DATE:	21 JAN, 1997
.....	PUMP 1	REPEATABILITY TEST2	DATE:	22 JAN, 1997

Figure 6–1: Repeatability of Test Method

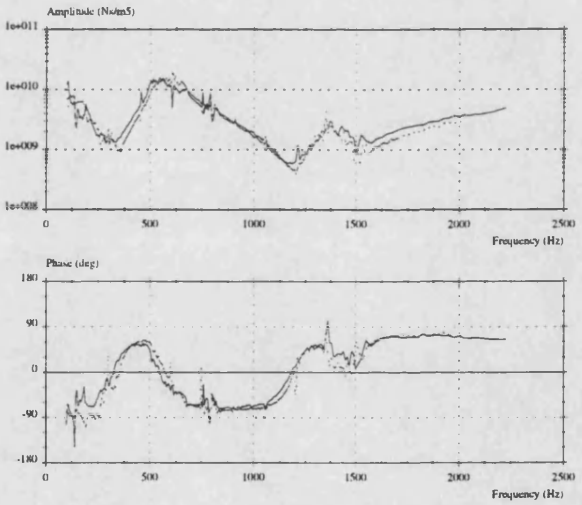

———	PUMP 1	900REV/MIN	3BAR RESERVOIR	20BAR DELIVERY
.....	PUMP 2	900REV/MIN	3BAR RESERVOIR	20BAR DELIVERY

Figure 6–2: Comparison of Pump 1 and Pump 2

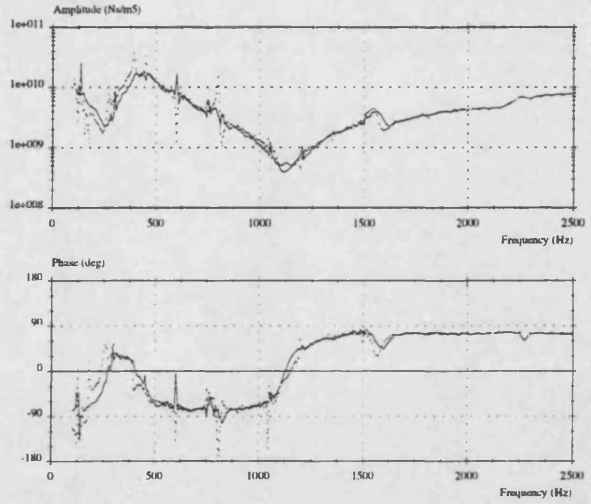

———	PUMP 5	900REV/MIN	3BAR RESERVOIR	20BAR DELIVERY
.....	PUMP 6	900REV/MIN	3BAR RESERVOIR	20BAR DELIVERY

Figure 6–3: Comparison of Pump 5 and Pump 6

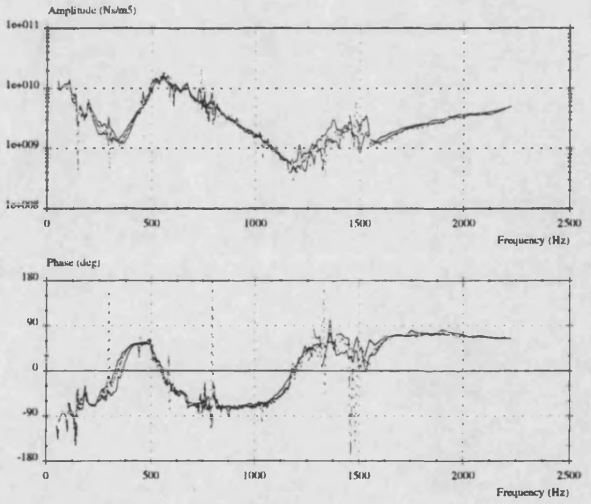

———	PUMP 1	900REV/MIN	3BAR RESERVOIR	20BAR DELIVERY
.....	PUMP 1	900REV/MIN	3BAR RESERVOIR	35BAR DELIVERY
—·—·—	PUMP 1	900REV/MIN	3BAR RESERVOIR	50BAR DELIVERY

Figure 6–4: Effect of Delivery Pressure on Suction Port Impedance

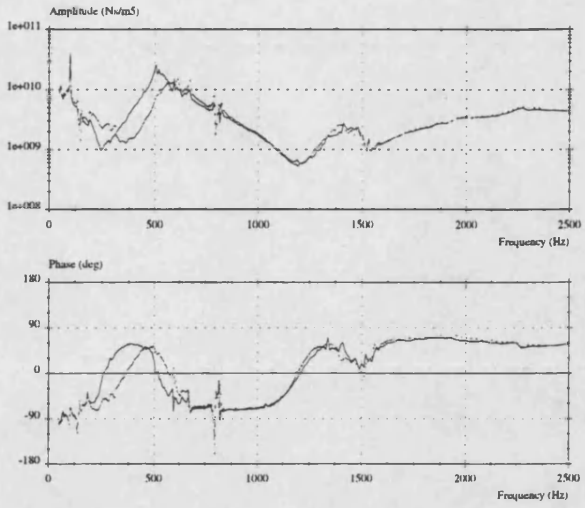

PUMP 1 450REV/MIN 1BAR RESERVOIR 20BAR DELIVERY
PUMP 1 450REV/MIN 3BAR RESERVOIR 20BAR DELIVERY

Figure 6–5: Effect of Reservoir Pressure on Suction Port Impedance at 450rev/min

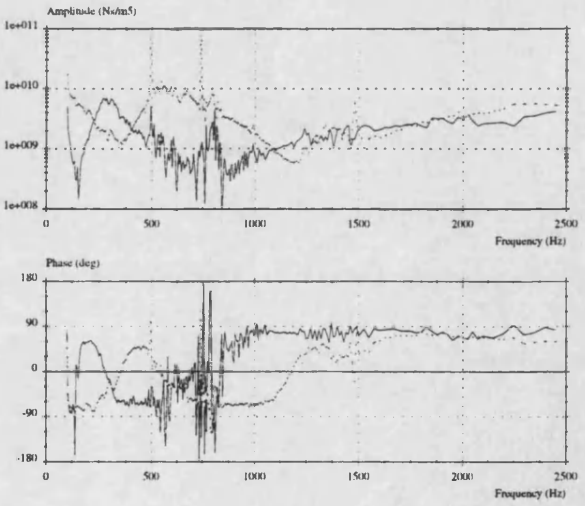

PUMP 1 1500REV/MIN 1BAR RESERVOIR 20BAR DELIVERY
PUMP 1 1500REV/MIN 3BAR RESERVOIR 20BAR DELIVERY

Figure 6–6: Effect of Reservoir Pressure on Suction Port Impedance at 1500rev/min

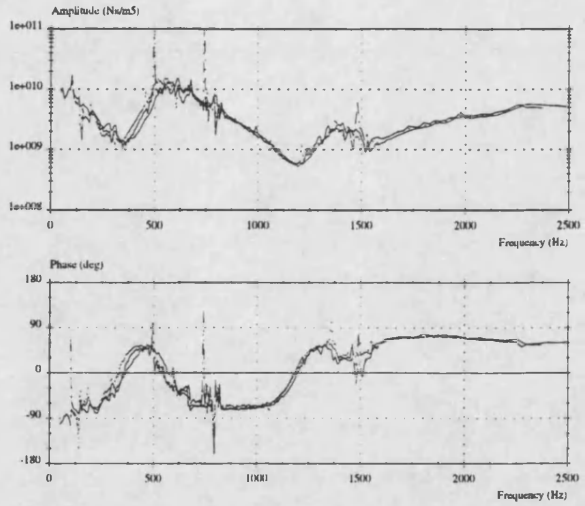

———	PUMP 1	450REV/MIN	3BAR RESERVOIR	20BAR DELIVERY
.....	PUMP 1	900REV/MIN	3BAR RESERVOIR	20BAR DELIVERY
—·—·—·—	PUMP 1	1500REV/MIN	3BAR RESERVOIR	20BAR DELIVERY

Figure 6–7: Effect of Speed on Pump 1 with 3bar Inlet Pressure

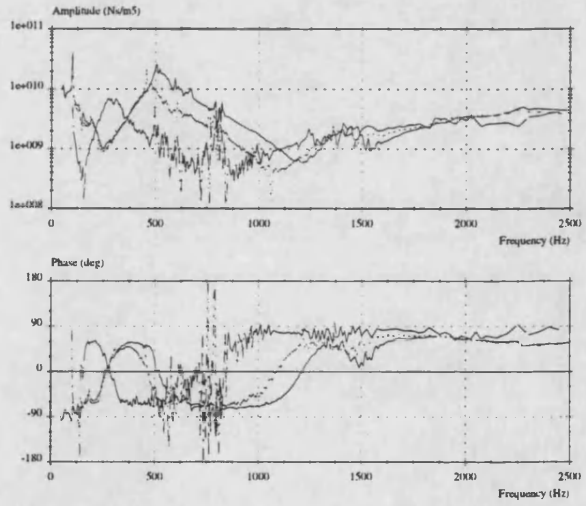

———	PUMP 1	450REV/MIN	1BAR RESERVOIR	20BAR DELIVERY
.....	PUMP 1	900REV/MIN	1BAR RESERVOIR	20BAR DELIVERY
—·—·—·—	PUMP 1	1500REV/MIN	1BAR RESERVOIR	20BAR DELIVERY

Figure 6–8: Effect of Speed on Pump 1 with 1bar Inlet Pressure

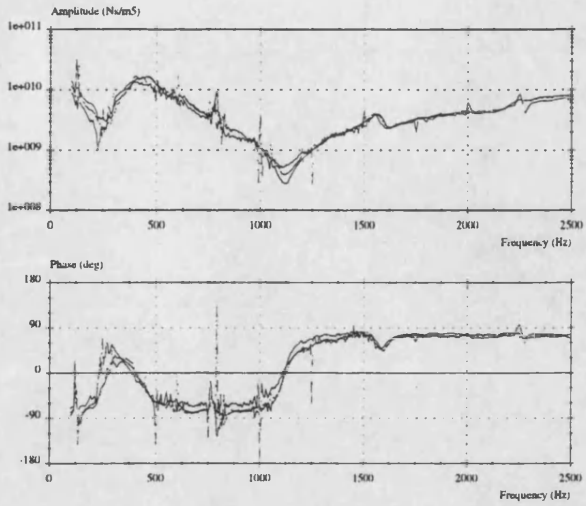

———	PUMP 5	450REV/MIN	3BAR RESERVOIR	20BAR DELIVERY
·····	PUMP 5	900REV/MIN	3BAR RESERVOIR	20BAR DELIVERY
—·—·—·—	PUMP 5	1500REV/MIN	3BAR RESERVOIR	20BAR DELIVERY

Figure 6–9: Effect of Speed on Pump 5 with 3bar Inlet Pressure

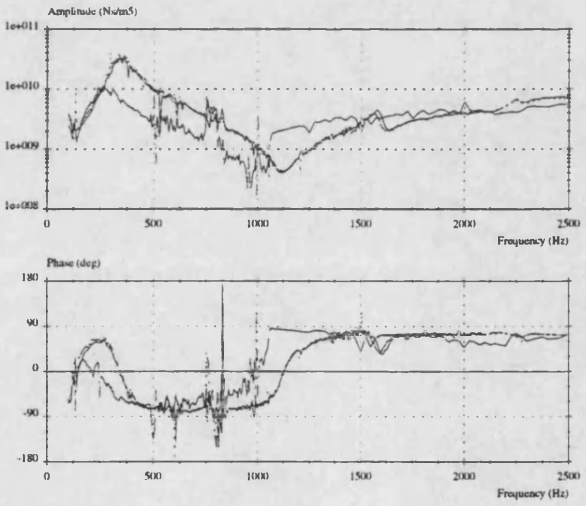

———	PUMP 5	450REV/MIN	1BAR RESERVOIR	20BAR DELIVERY
·····	PUMP 5	900REV/MIN	1BAR RESERVOIR	20BAR DELIVERY
—·—·—·—	PUMP 5	1500REV/MIN	1BAR RESERVOIR	20BAR DELIVERY

Figure 6–10: Effect of Speed on Pump 5 at 1bar Inlet Pressure

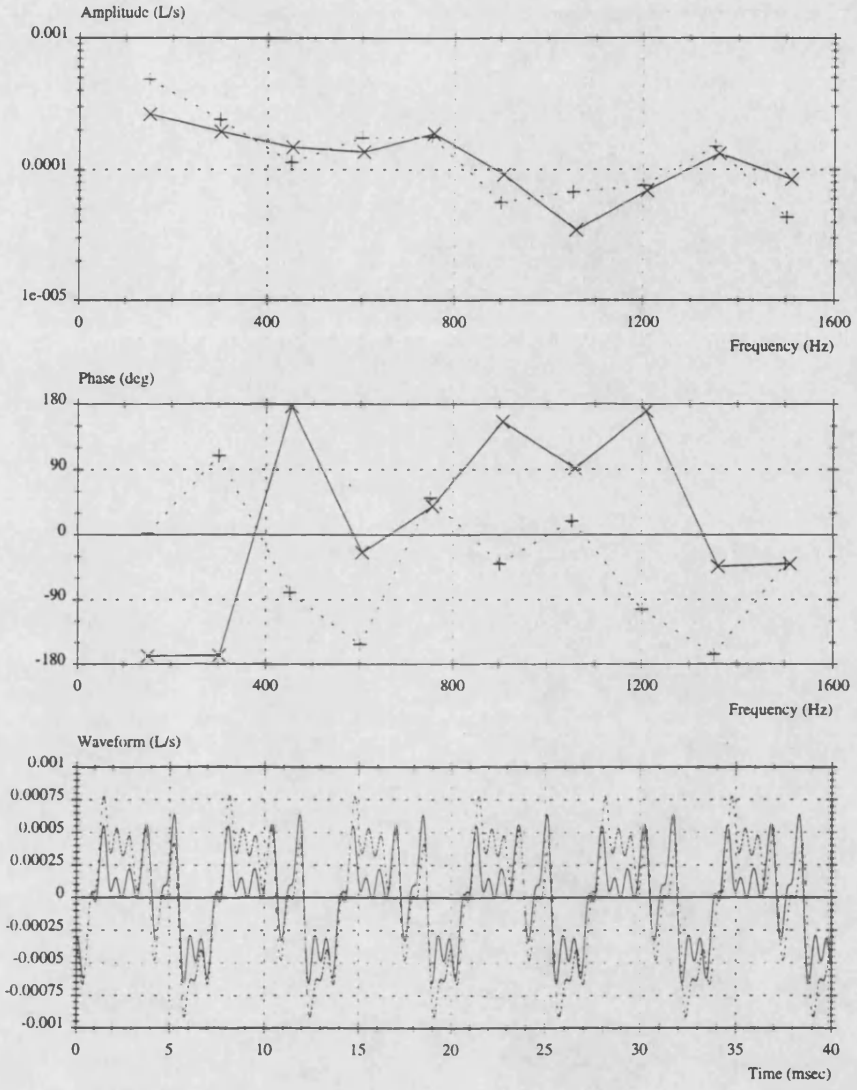

×——×	PUMP 1	900REV/MIN	3BAR RESERVOIR	20BAR DELIVERY
+·····+	PUMP 2	900REV/MIN	3BAR RESERVOIR	20BAR DELIVERY

Figure 6–11: Anechoic Flow Ripple for Pump 1 and Pump 2 at 900rev/min

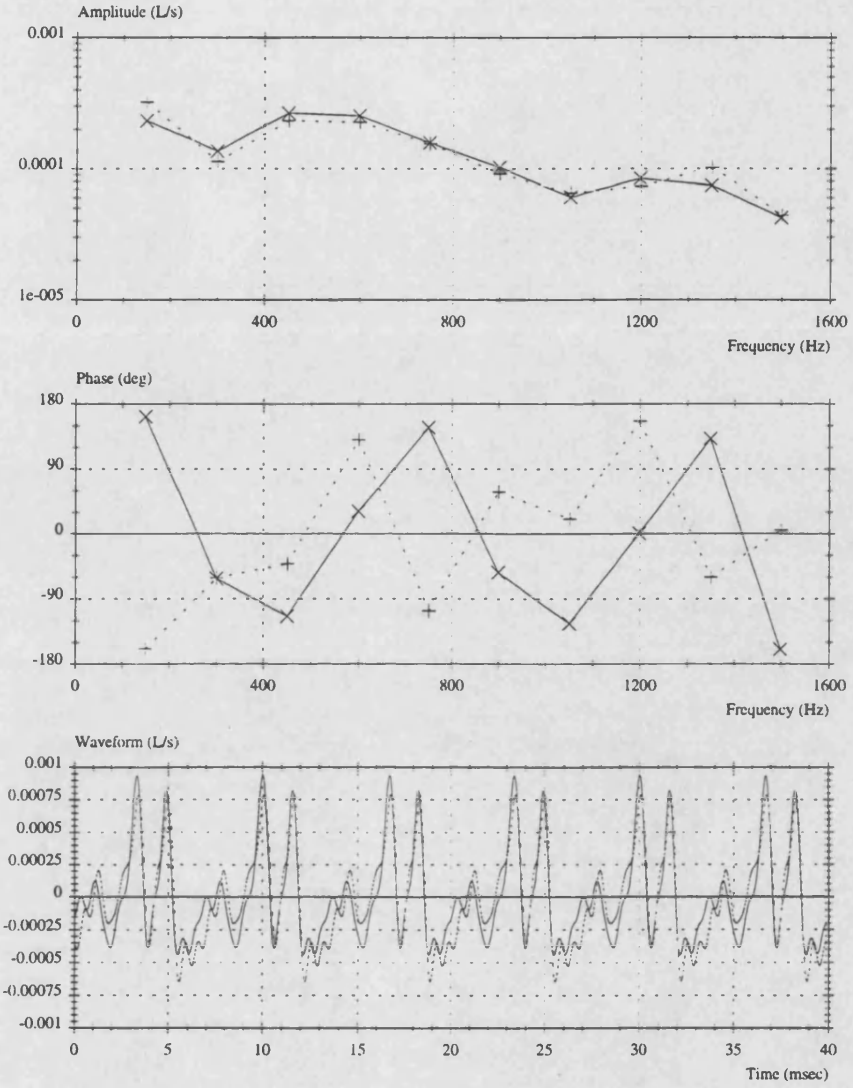

×——×	PUMP 3	900REV/MIN	3BAR RESERVOIR	20BAR DELIVERY
+·····+	PUMP 4	900REV/MIN	3BAR RESERVOIR	20BAR DELIVERY

Figure 6–12: Anechoic Flow Ripple for Pump 3 and Pump 4 at 900rev/min

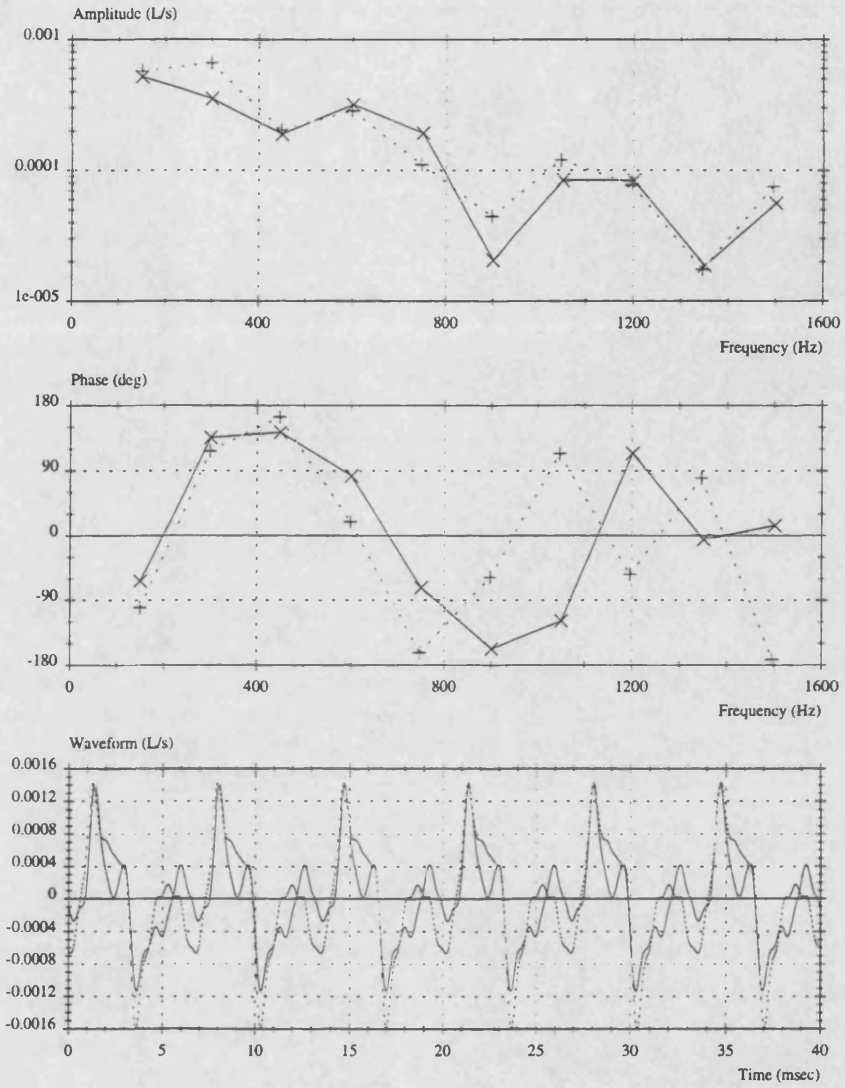

×——×	PUMP 5	900REV/MIN	3BAR RESERVOIR	20BAR DELIVERY
+····+	PUMP 6	900REV/MIN	3BAR RESERVOIR	20BAR DELIVERY

Figure 6–13: Anechoic Flow Ripple for Pump 5 and Pump 6 at 900rev/min

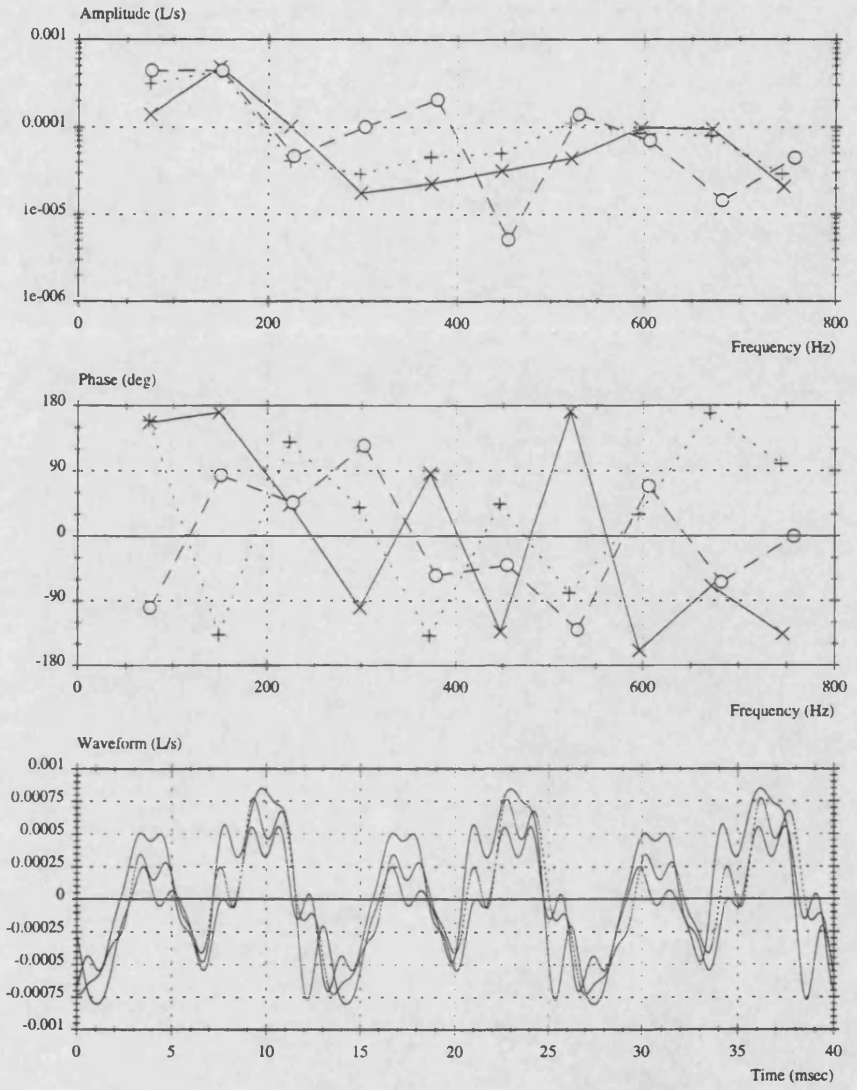

×——×	PUMP 1	450REV/MIN	3BAR RESERVOIR	20BAR DELIVERY
+·····+	PUMP 3	450REV/MIN	3BAR RESERVOIR	20BAR DELIVERY
○-------○	PUMP 5	450REV/MIN	3BAR RESERVOIR	20BAR DELIVERY

Figure 6–14: Anechoic Flow Ripple in Pump 1, Pump3 and Pump 5 at 450rev/min

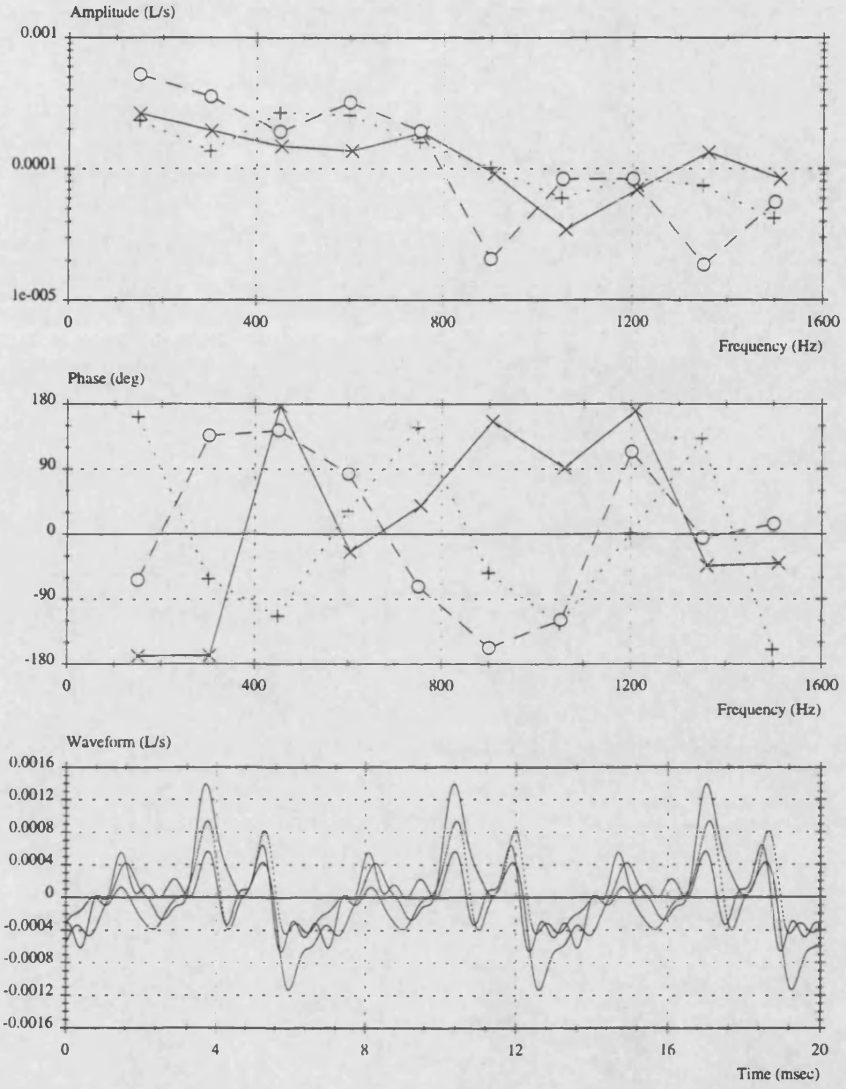

×——×	PUMP 1	900REV/MIN	3BAR RESERVOIR	20BAR DELIVERY
+·····+	PUMP 3	900REV/MIN	3BAR RESERVOIR	20BAR DELIVERY
○-------○	PUMP 5	900REV/MIN	3BAR RESERVOIR	20BAR DELIVERY

Figure 6–15: Anechoic Flow Ripple in Pump 1, Pump3 and Pump 6 at 900rev/min

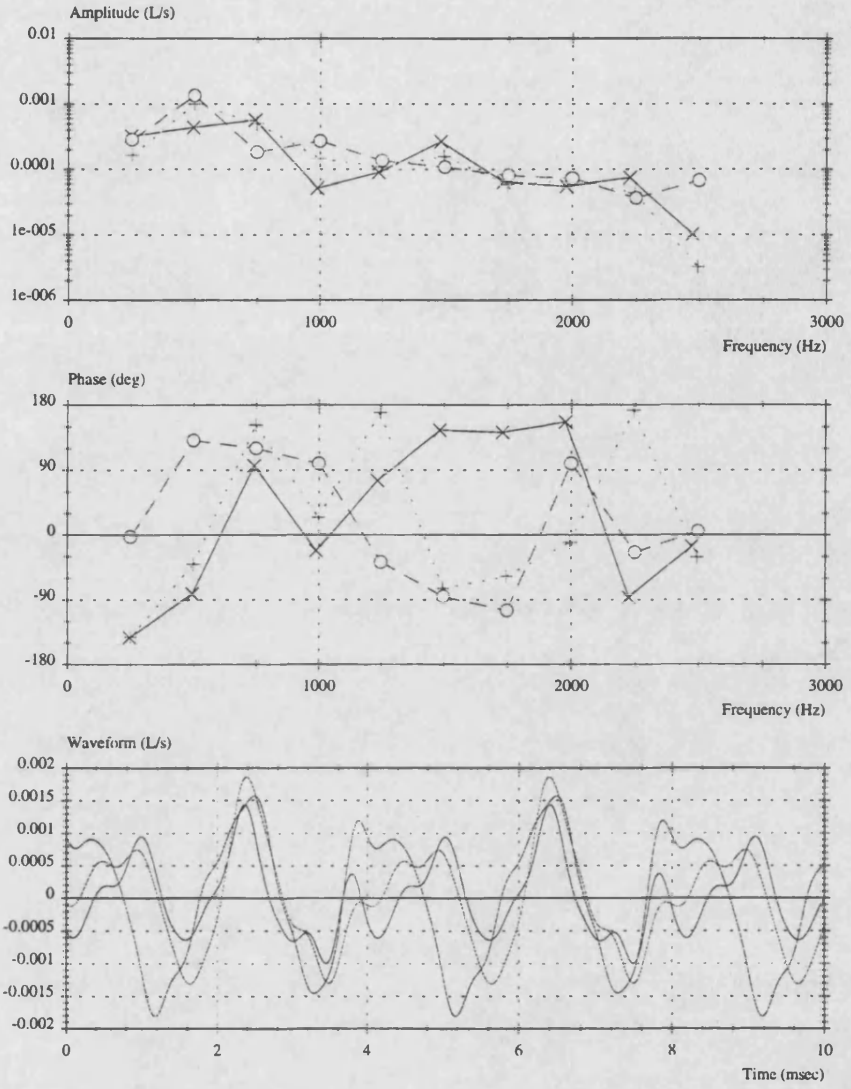

×——×	PUMP 1	1500REV/MIN	3BAR RESERVOIR	20BAR DELIVERY
+····+	PUMP 3	1500REV/MIN	3BAR RESERVOIR	20BAR DELIVERY
○-------○	PUMP 5	1500REV/MIN	3BAR RESERVOIR	20BAR DELIVERY

Figure 6–16: Anechoic Flow Ripple in Pump 1, Pump3 and Pump 6 at 1500rev/min

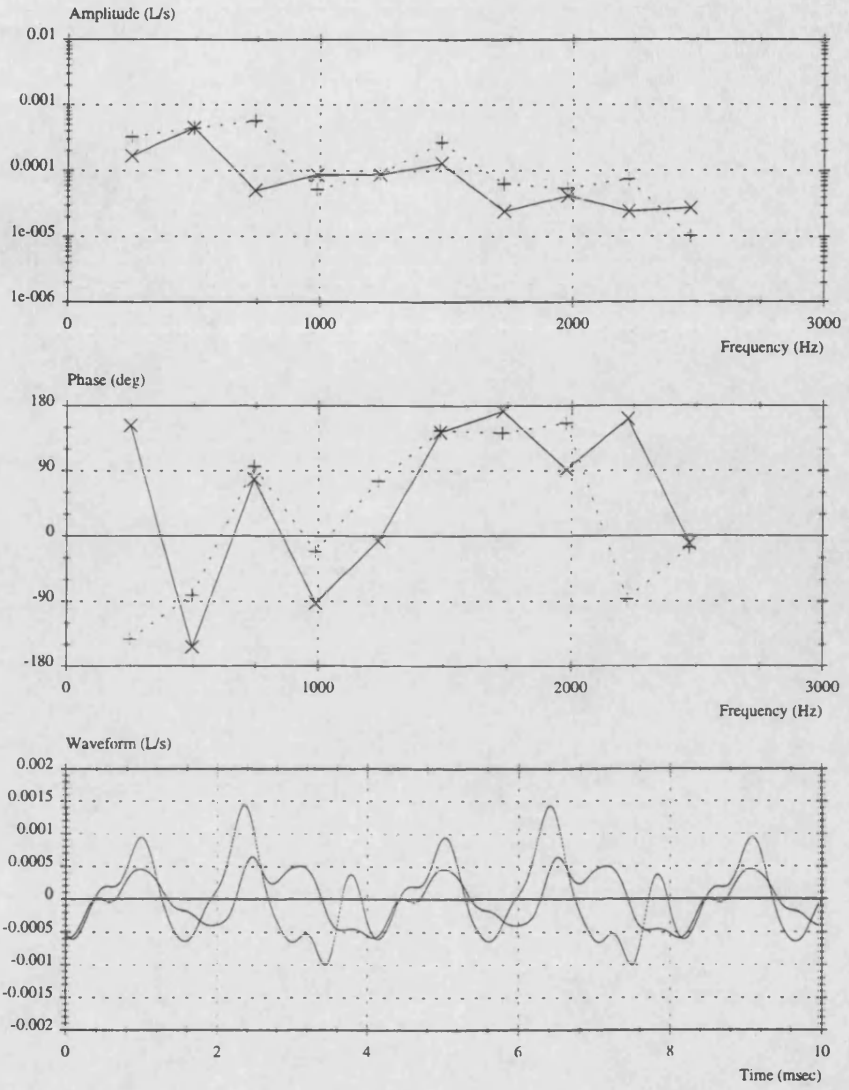

×——×	PUMP 1	1500REV/MIN	1BAR RESERVOIR	20BAR DELIVERY
+·····+	PUMP 1	1500REV/MIN	3BAR RESERVOIR	20BAR DELIVERY

Figure 6–17: Effect of Reservoir Pressure on Pump 1 at 1500rev/min

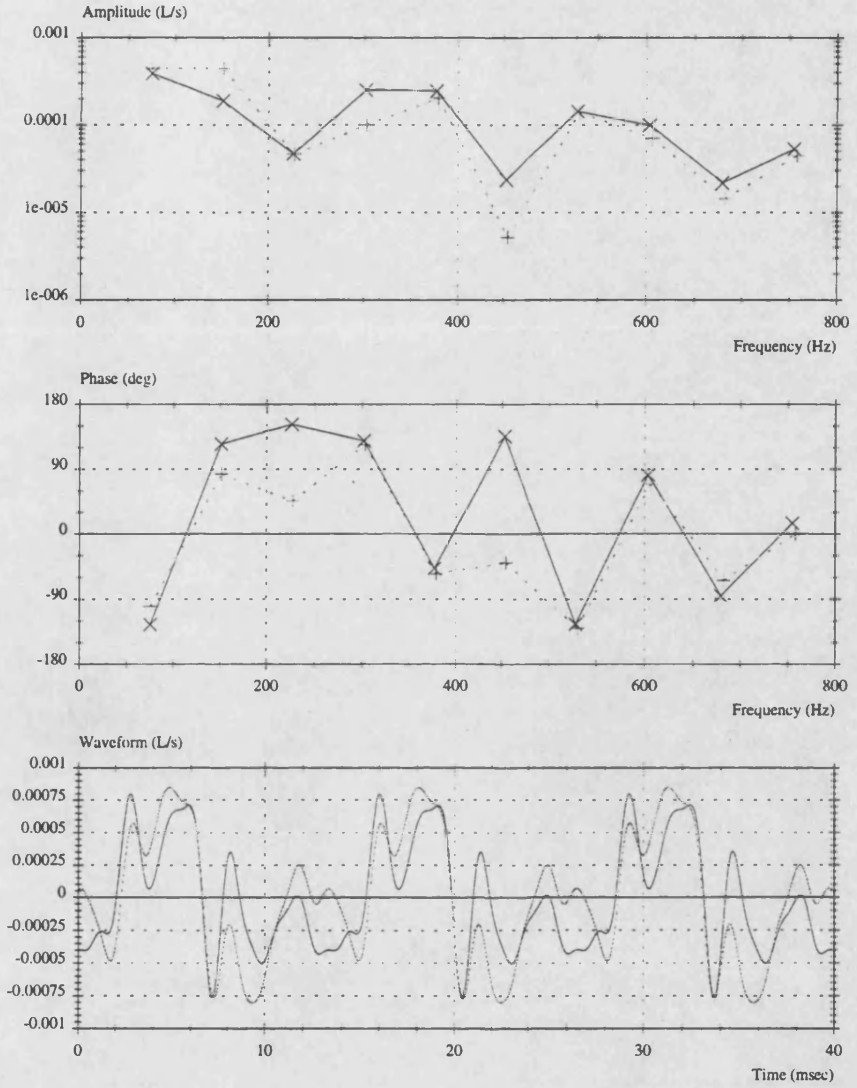

× ——— ×	PUMP 5	450REV/MIN	1BAR RESERVOIR	20BAR DELIVERY
+ ····· +	PUMP 5	450REV/MIN	3BAR RESERVOIR	20BAR DELIVERY

Figure 6–18: Effect of Reservoir Pressure on Pump 5 at 450rev/min

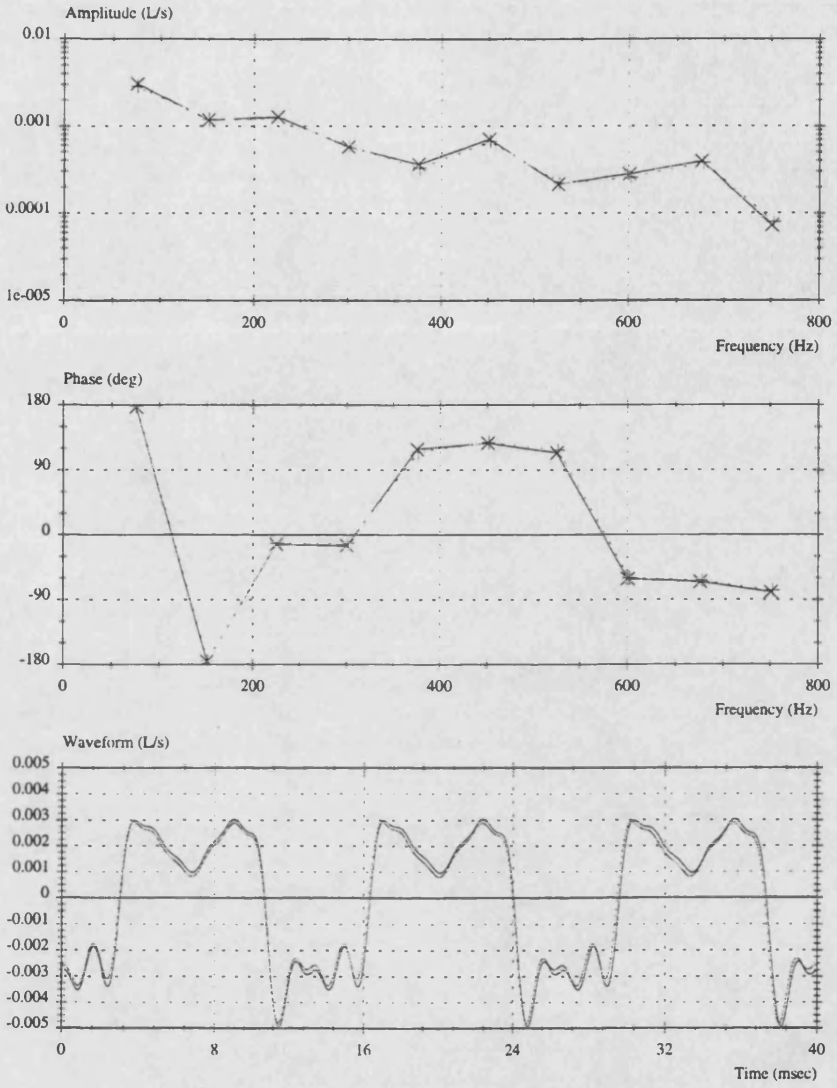

×——×	PUMP 1	450REV/MIN	1BAR RESERVOIR	50BAR DELIVERY
+·····+	PUMP 1	450REV/MIN	3BAR RESERVOIR	50BAR DELIVERY

Figure 6–19: Effect of Reservoir Pressure on Delivery Flow Ripple in Pump 1

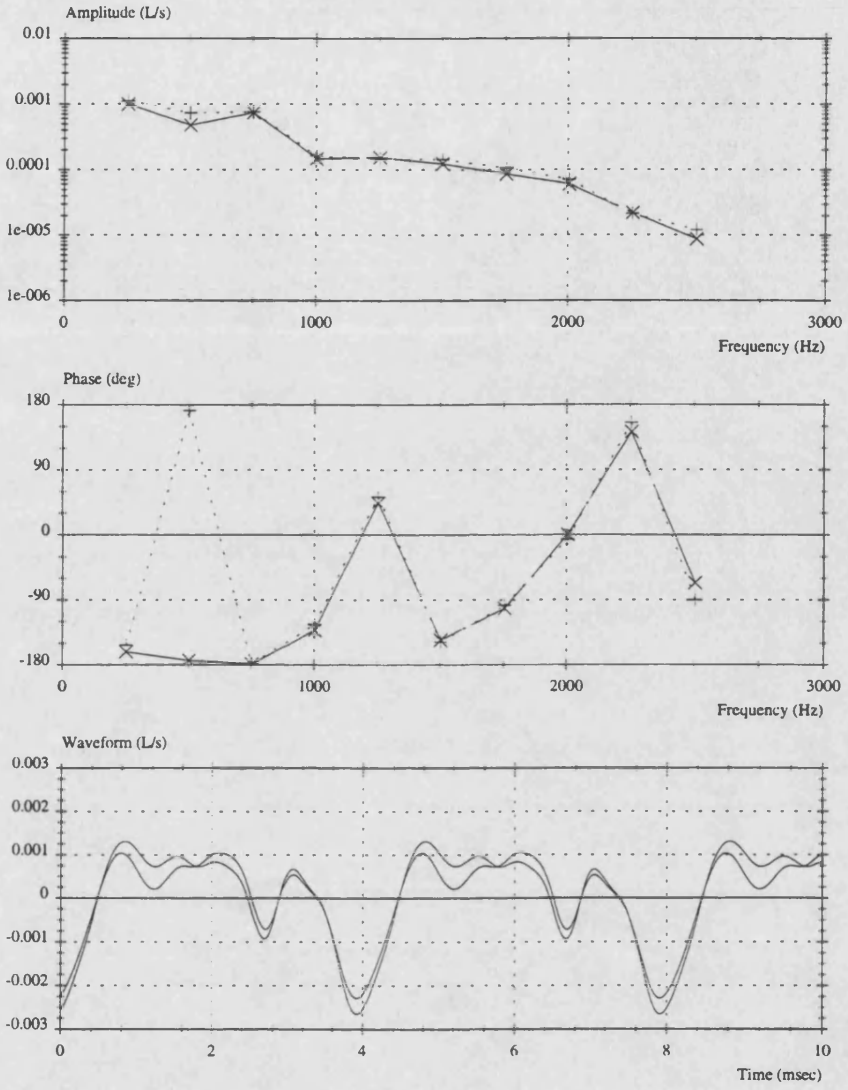

×——×	PUMP 3	1500REV/MIN	1BAR RESERVOIR	10BAR DELIVERY
+····+	PUMP 3	1500REV/MIN	3BAR RESERVOIR	10BAR DELIVERY

Figure 6–20: Effect of Reservoir Pressure on Delivery Flow Ripple in Pump 3

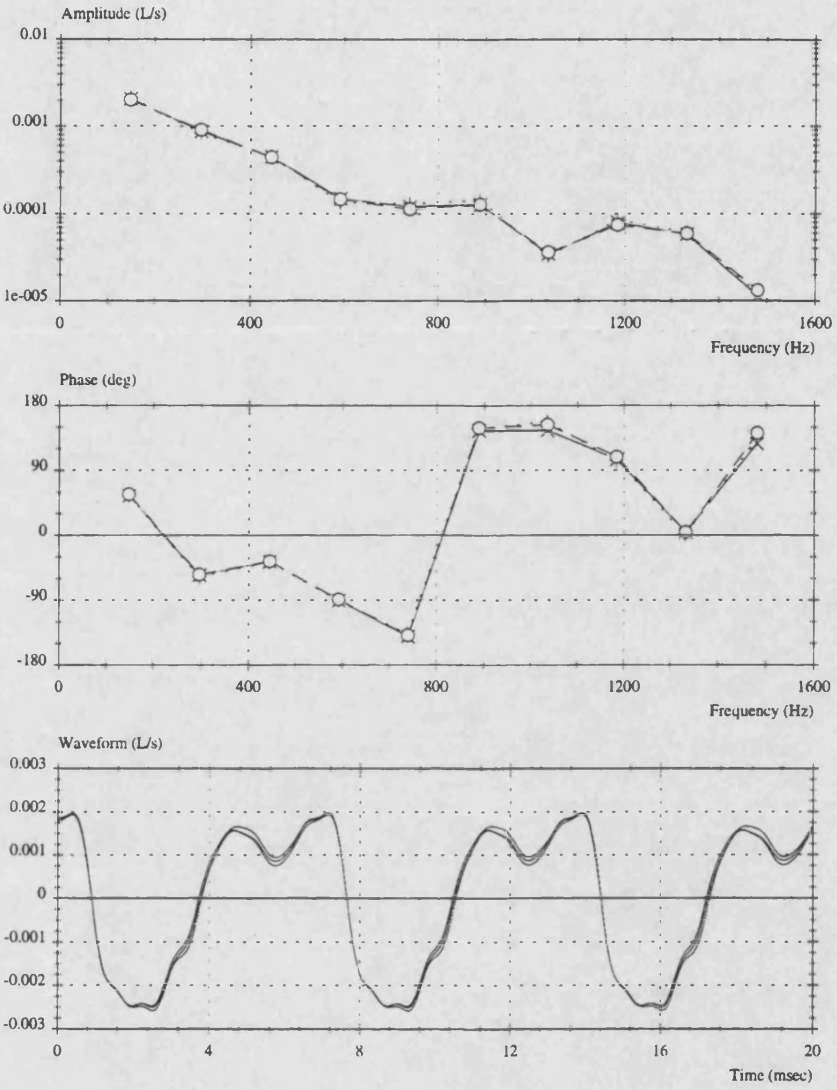

×——×	PUMP 5	900REV/MIN	1BAR RESERVOIR	40BAR DELIVERY
+····+	PUMP 5	900REV/MIN	2BAR RESERVOIR	40BAR DELIVERY
○-------○	PUMP 5	900REV/MIN	3BAR RESERVOIR	40BAR DELIVERY

Figure 6–21: Effect of Reservoir Pressure on Delivery Flow Ripple in Pump 5

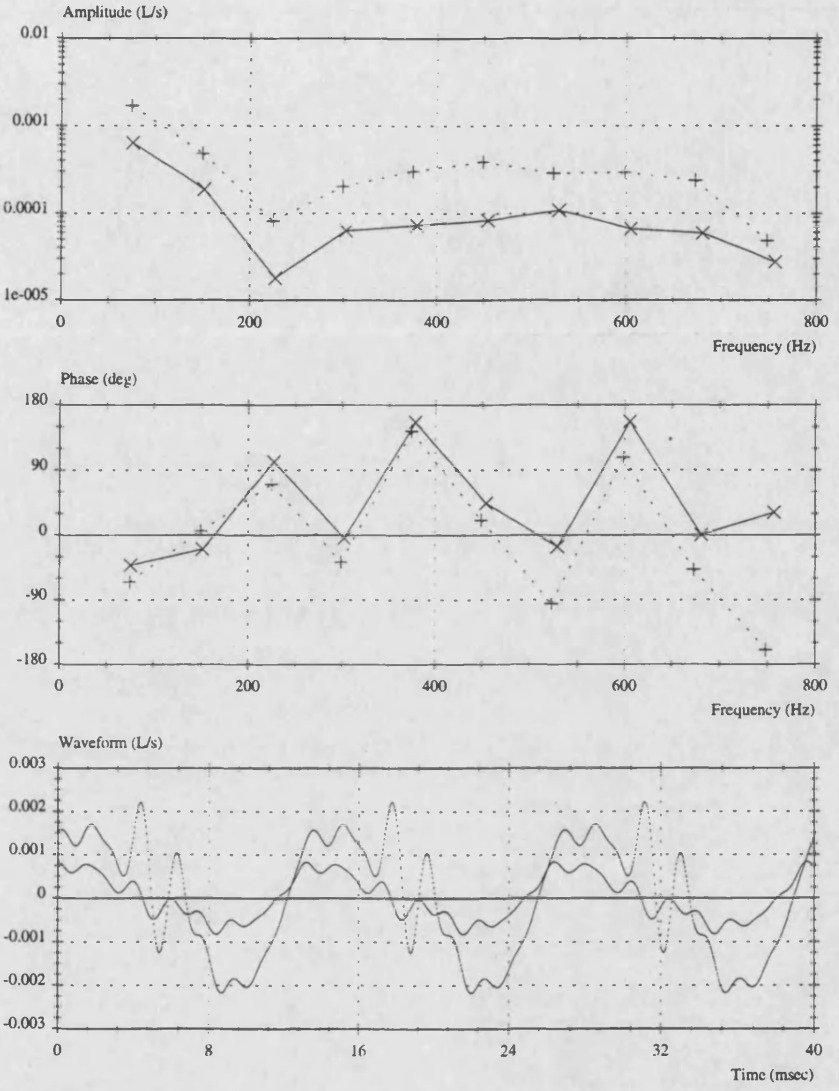

×——×	PUMP 3	450REV/MIN	1BAR RESERVOIR	10BAR DELIVERY
+····+	PUMP 3	450REV/MIN	1BAR RESERVOIR	50BAR DELIVERY

Figure 6–22: The Effect of Delivery Pressure on Suction Flow Ripple in Pump 3

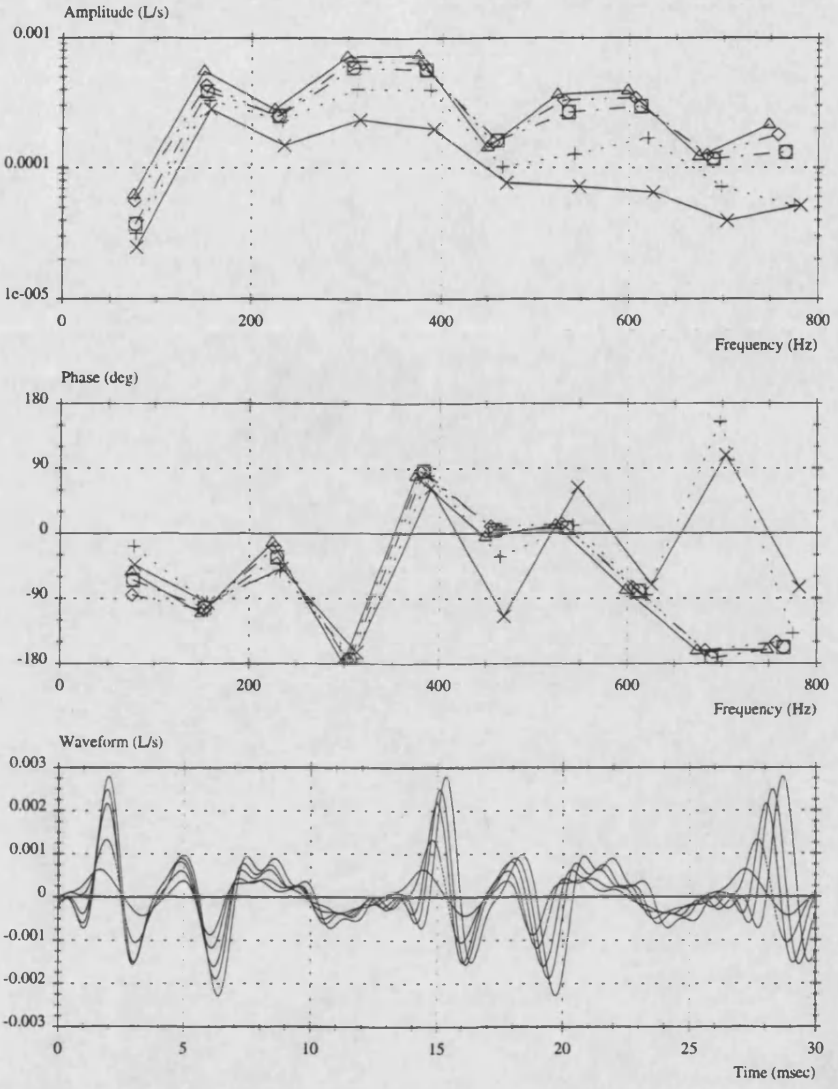

PUMP 5	450REV/MIN	1BAR RESERVOIR	10BAR DELIVERY
PUMP 5	450REV/MIN	1BAR RESERVOIR	20BAR DELIVERY
PUMP 5	450REV/MIN	1BAR RESERVOIR	30BAR DELIVERY
PUMP 5	450REV/MIN	1BAR RESERVOIR	40BAR DELIVERY
PUMP 5	450REV/MIN	1BAR RESERVOIR	50BAR DELIVERY

Figure 6–23: The Effect of Delivery Pressure on Suction Flow Ripple in Pump 5

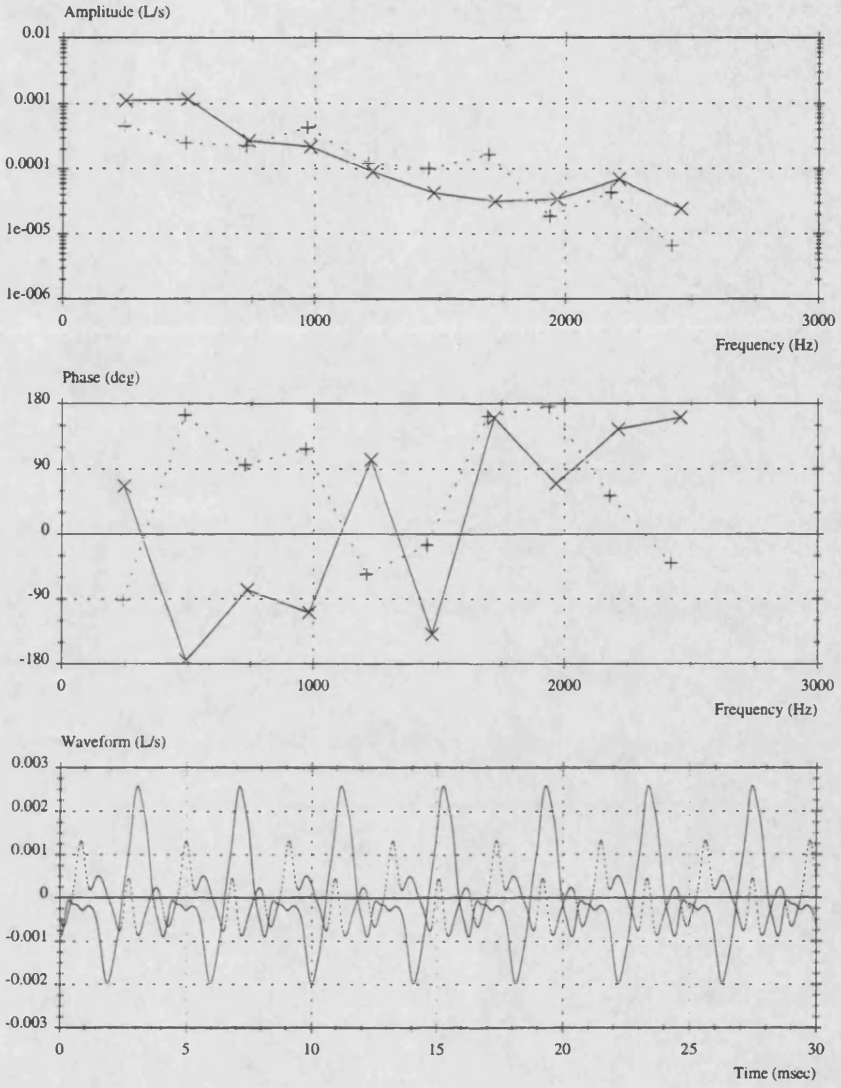

PUMP 5 1500REV/MIN 1BAR RESERVOIR 10BAR DELIVERY

PUMP 5 1500REV/MIN 1BAR RESERVOIR 50BAR DELIVERY

Figure 6–24: The Effect of Delivery Pressure on Suction Flow Ripple in Pump 5 at 1500rev/min

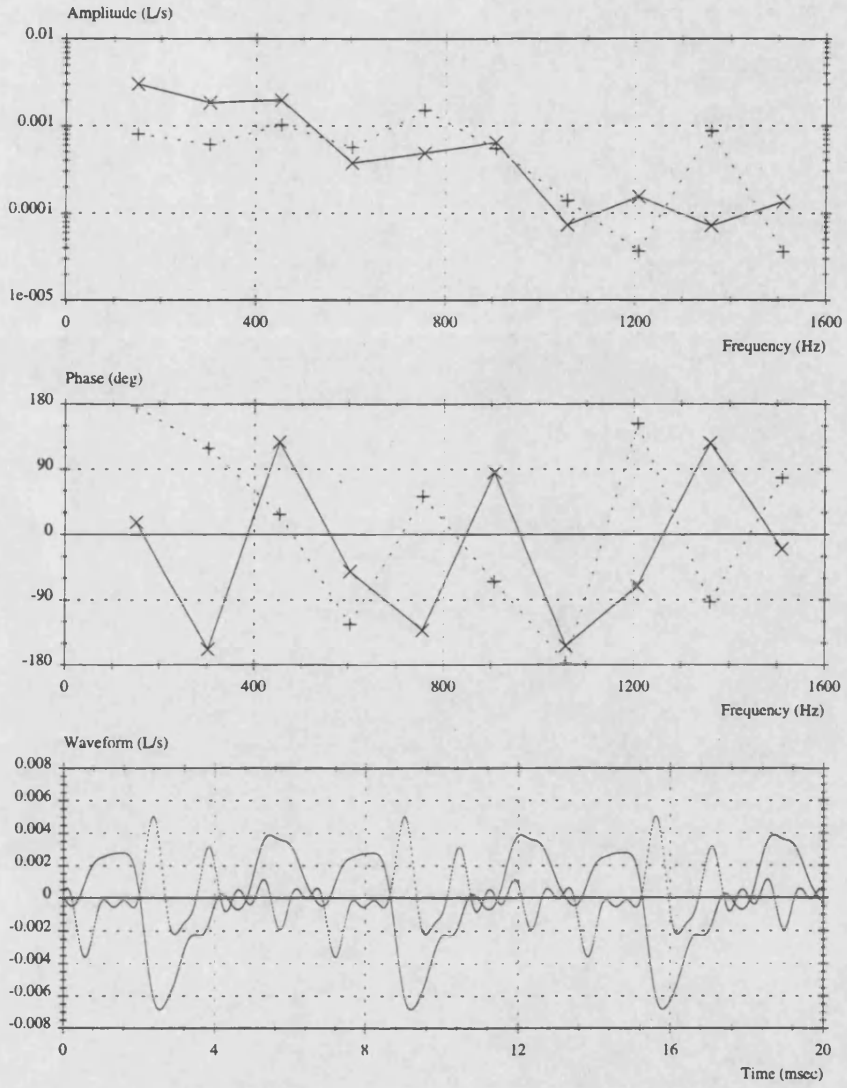

×——×	PUMP 3 DELIVERY	900REV/MIN	1BAR RES.	50BAR DEL.
+····+	PUMP 3 SUCTION	900REV/MIN	1BAR RES.	50BAR DEL.

Figure 6–25: Delivery and Suction Flow Ripple in Pump 3 at 900rev/min

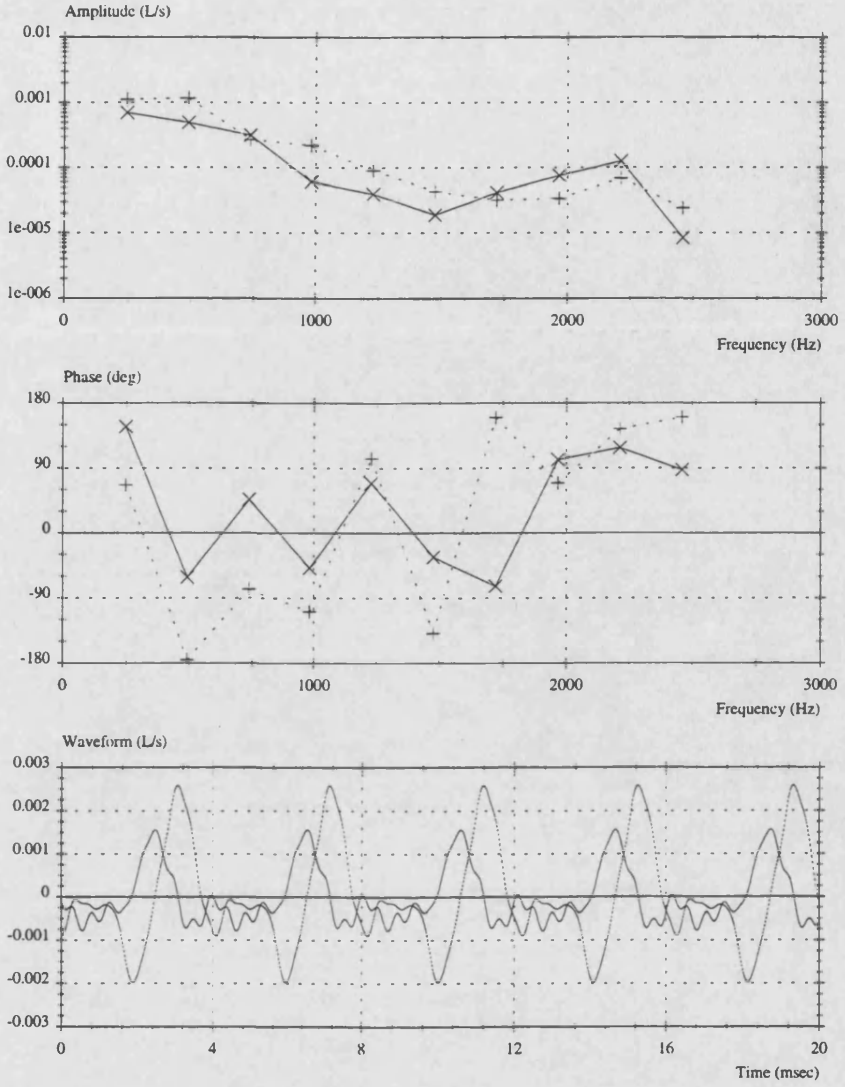

PUMP 5 DELIVERY 1500REV/MIN 1BAR RES. 10BAR DEL.
PUMP 5 SUCTION 1500REV/MIN 1BAR RES. 10BAR DEL.

Figure 6–26: Delivery and Suction Flow Ripple in Pump 5 at 1500rev/min, 1bar Suction

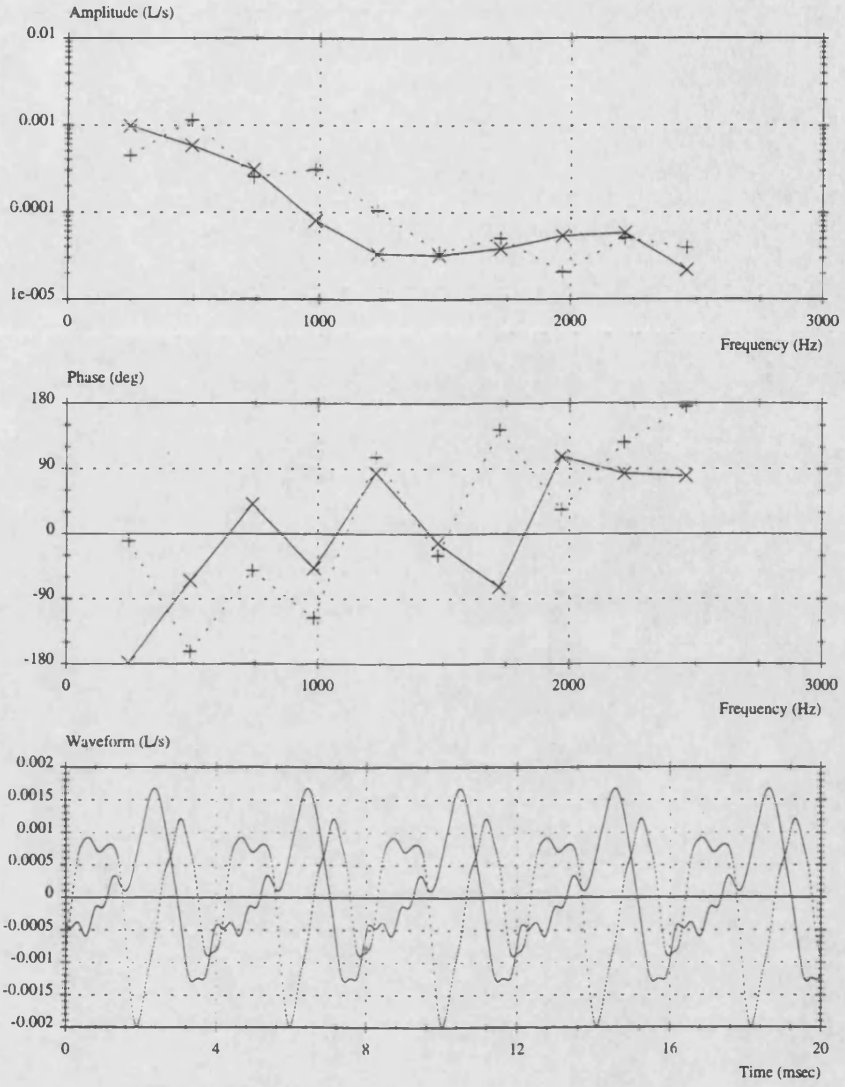

×——×	PUMP 5 DELIVERY	1500REV/MIN	3BAR RES.	10BAR DEL.
+····+	PUMP 5 SUCTION	1500REV/MIN	3BAR RES.	10BAR DEL.

Figure 6–27: Delivery and Suction Flow Ripple in Pump 5 at 1500rev/min, 3bar Suction

7 VALIDATION OF SIMULATION

7.1 INTRODUCTION

The impedance model and flow ripple simulation must be validated against experimental results in order that they can be used as part of the design process. The amount of air in the pump is not known and therefore must be derived indirectly from flow visualisation (discussed in Chapter 2) data and from impedance results (Chapter 6). Hence, before validating the model, an empirical function to predict air content must be derived and added to the impedance model and flow ripple simulation.

The simulation can be validated separately from the impedance model by comparing measured and predicted source flow ripple. However, the drawback with this is that the test method **(71)** uses an impedance model which is much less complex than the one developed here in Chapter 3. It is therefore better to validate the impedance model and the flow ripple simulation together. In this way, the simplified impedance model used in FBN2 **(71)** is not used to interpret the experimental data. The two simulations can therefore be validated together by comparing anechoic flow ripple results to experimental data. The impedance model can be compared directly to measurements. If there is good agreement between measured and predicted results, the simulations can be assumed adequate as design tools.

7.2 AN EMPIRICAL FUNCTION FOR AERATION

The impedance of the suction port varies with reservoir pressure and speed, both of which affect the amount of entrained air. It has however been seen in Chapter 6, that the impedance of the pump remains virtually constant over a wide range of speeds if the supercharge valve remains closed. This is therefore a good starting place for deriving the aeration function, which can later be later be expanded to incorporate the effect of speed.

As stated in Chapter 5, the secondary source test method can be used to measure the bulk modulus of a fluid in a hydraulic line. Reference **(33)** describes this method as closely predicting the manufacturer's data for isentropic tangent bulk modulus in high-pressure pipes. However, very few tests were done at low pressure and the method appears to ignore the lowered density found in bubbly oil at low pressure, which is demonstrated in Chapter 2 of this thesis. For this reason, the bulk modulus has been derived from observations made during the course of this project. However, if this test method were proved to be accurate at low pressure it would still not be prudent to use the value of bulk modulus measured outside of the pump to describe the stiffness of the oil in each section of the pump. This would assume that air does not collect in pockets inside the pump, for example at sharp edges such as where the port plates meet the cam ring or in the outlet of the closed supercharge valve.

The basic form of the impedance, which is shown in Figure 7–1, describes the suction port impedance for all cases where there is little aeration (For example, at speeds below 900rev/min or when the reservoir pressure is boosted to 3bar). The impedance model compares quite well with this case except for slight discrepancies between the model and experimental results concerning the peak at 1450Hz, which is situated at 900Hz in the predicted impedance. This indicates that there is a problem regarding the sizing of the impedance model described in Chapter 3. Many simplifications were involved in the definition of this model and the cumulative effect of these may be to produce this discrepancy. This is not however a practical problem because it only affects the higher harmonics of flow ripple, which are usually weak and difficult to measure accurately.

At high speed (Figure 7–2), the impedance is altered in that all the resonant and anti-resonant peaks are shifted to lower frequency, which suggests a more compliant system. The impedance shows a less compliant characteristic if the reservoir pressure is increased, which suggests that the bubbles are compressed or dissolved. An empirical function was developed to compensate for the increased compressibility. The air content in each section of the pump was varied and the best fit to the experimental data was found as a function of reservoir pressure and pump speed. It was assumed that the air was not uniformly distributed about the pump. The explanation of this assumption is contained in the following sub-sections.

7.2.1 Possible Explanations for the Occurrence of Air Pockets

In §2.1, two types of aeration were discussed; they were entrained air and dissolved air. Both types of air could affect different sections of the pump passageways in different ways.

7.2.1.1 Aeration in the Supercharge Inlet

In the jet from the supercharge valve, there is a large decrease in pressure over a short distance. This would cause the oil to become over-saturated and air would be released. Although some of this air would be entrained in the oil as bubbles, the effect of the constant jet would be to create an air pocket in the outflow of the supercharge valve. The amount of air in this pocket would depend on the flow rate through the valve. Hence, the empirical air function for the supercharge inlet is a function of pump speed, which dictates whether the supercharge valve is open or not, and pressure, which controls the amount of air that collects in the pocket. This effect would also be witnessed in the adjacent section of the passageway, which is the inlet to the annulus. Figure 7–3 shows that increasing the air content in this section reduces the frequency of the resonant and anti-resonant peaks located around 1kHz.

7.2.1.2 Aeration in the Annulus Sections

Air which comes out of solution in the supercharge inlet would first of all be entrained into the two quarter-annulus sections of the pump. This would be added to the entrained air which is

also present in the annulus. In §2.1.3, Hibi *et al.* **(6, 7)** showed that oil-speed was a major cause of pressure-loss inside the pump and hence air release. At low speeds (below ~900rev/min) oil from the reservoir is unlikely to become over-saturated and release air, but at higher speeds more air is released due to the drop in pressure. This is shown in the flow visualisation, discussed in §2.2. Air that does not enter the rotating group from the annulus may collect in the half-annulus section between the ports where the under-saturated fluid would dissolve some of the entrained air depending on the pressure. The lower frequency features are affected by the bubble content in the half-annulus, which links the ports together (Figure 7–4). The shorter amount of time that entrained air is in the two quarter-annulus sections suggests that pressure has a smaller effect on air content than speed does in these sections.

7.2.1.3 AERATION IN THE PORTS

Aeration in the ports would occur from both entrained air from the annulus sections and from the sudden opening of the chambers, which agitates the oil and causes air to be released (discussed in §2.1.2). The amount of air that is released from this process cannot be predicted and the behaviour of the air in the chambers has not been studied in the scope of this thesis. However, it was found that the port air content did not have a great effect on the modelled impedance but has more effect on the flow ripple. Figures 7–26 and 7–27 show that a value of 1.5% for the amount of air in the chambers is a good approximation. In Section 6.5.1 evidence is given to support the assumption that this figure should remain constant.

7.2.2 PROCEDURE FOR DERIVING THE AERATION FUNCTION

The procedure of varying the air content in each section (as in Figures 7–3 and 7–4) and in combinations of sections was continued until there was a good understanding of the system. The impedance model was then fitted to impedance results at six different running conditions: 450, 900 and 1500rev/min all at 1 and 3bar. When a good fit was found for a certain condition, the void fraction in each pump section was recorded. When all six conditions were satisfied, curves were fitted to the data and the empirical functions shown in Figure 7–5, were inserted into the impedance model. This curve fitting does however mean that in some cases the air-content function does not correspond exactly to the best result and so some discrepancies in the impedance model are seen.

This manual procedure was preferred to using a genetic algorithm so that the explanation in §7.2.1 could be closely followed. This ensured that there were no anomalous results that would allow the curves to fit the experimental results but gave unrealistic values for air content.

The function for air content completes the flow ripple simulation and impedance model, which now must be validated against experimental data. The air content function, which is also used

in the flow ripple simulation, must be verified. The three types of flow ripple and the impedance must then be checked over a wide range of operating conditions.

7.3 RESULTS OF VALIDATION EXERCISE

The simulation predicts four results: the impedance of the suction port, the source flow ripple, the open-circuit flow ripple and the anechoic flow ripple. Each result is checked against experimental results at three speeds, 450, 900 and 1500rev/min, and two reservoir pressures, atmospheric and 3bar. The same procedure is repeated for each of the three types of test pump shown below.

PUMP NAME	PUMP TYPE
Pump 1	Saginaw TC60
Pump 2	Saginaw TC88
Pump 3	Saginaw CB60

Table 7-1: Pumps used in Validation

The simulation was developed using a parameter file based on the dimensions of Pump 1. Pumps 2 and 3 have different parameter files, which run with the same simulation. Part of the validation procedure will therefore be to see whether a generalised simulation of this type is satisfactory. It is also necessary to ascertain whether the air release function developed for Pump 1 is valid for the other pumps.

7.3.1 VALIDATION OF SIMULATION OF PUMP1

The parameter file for Pump 1, which is shown in Appendix 1, is the model on which the simulations for the other two pumps are based.

7.3.1.1 IMPEDANCE MODEL VALIDATION

The impedance model gives a similar result for all speeds at the 3bar reservoir pressure, which are shown in Figures 7–7, 7–9 and 7–11. The position of the second resonance is approximately 100Hz too high in all cases. There are also errors in the amplitude above 600Hz, which in the 450rev/min case affects only the higher harmonics of flow ripple. The effect on the flow ripple at higher speeds may be greater because of the discrepancies.

At atmospheric pressure the agreement between predicted and measured results is better. At 450rev/min, Figure 7–6, the tenth harmonic of flow ripple is at 750 Hz. Up to this point there is good agreement except that the first anti-resonance has more damping in reality, which means that there is some discrepancy between 250 and 500Hz. At 900rev/min, Figure 7–8, the fifth and sixth harmonics lie at a point where there is a large error between measured and predicted

results. It is more difficult to compare the results at 1500rev/min because of the experimental scatter (Figure 7–10) but the agreement is good up to the tenth harmonic at 2500Hz.

The results show that the impedance model with the empirical air content function shows good agreement for most of the first ten harmonics at a range of speeds. The positions where there is not so good agreement between predicted and measured results may show up as errors in the open-circuit and anechoic flow ripple.

7.3.1.2 INTERNAL FLOW RIPPLE VALIDATION

Figure 7–12 shows a comparison of the waveforms for a pump running at 1500rev/min with a 1bar reservoir. It can be seen that the negative spike due to fluid compressibility is much greater on the simulation results than in the tests. This may be due to discrepancies in the impedance model used for calculating the internal flow ripple from measured results. It is not however due to the exponential decays described in Equations 4.2.4 and 4.2.5, which would tend to reduce the amplitude of these spikes. The kinematic flow shows the same form for both, although the amplitude is slightly greater in reality than in simulation. This is due to the compressibility of the oil in the chamber not being accurately predicted. The effect of chamber void fraction is discussed later, in §7.3.2.1.

The simulated internal flow ripple at 450rev/min and 900rev/min are shown in Figure 7–13 and Figure 7–14. The amplitudes of the first ten harmonics are compared with three experimental results. The waveforms show the same slender compression spike as in Figure 7–12. The predicted amplitude of the first three harmonics become less accurate as the speed reduces, which suggests a problem with the kinematic flow ripple term, which could be due to the constant amount of air assumed to be in the chambers regardless of conditions.

Internal flow ripple cannot be measured directly using the secondary source test method. An impedance model is used in the data processing software, which is an approximation to the measured impedance. The impedance models available in the FBN2 package **(71)** for calculating internal flow ripple are not adequate for describing the complicated impedance of the suction port. For this reason a comparison of the predicted and measured internal flow ripple is not satisfactory.

7.3.1.3 OPEN-CIRCUIT FLOW RIPPLE VALIDATION

Figure 7–15 shows a comparison of the waveforms for the pump running at 1500rev/min and the reservoir set to 1bar. There are small discrepancies between some of the harmonics but there is generally good agreement. At 900rev/min (Figure 7–16), the predicted higher harmonics diverge from the experimental results but the dominant first five harmonics show good agreement. Only the simulated waveform is shown in order to improve the clarity of the results. Figure 7–15 shows that even with only two super-imposed waveforms, the graphs become

difficult to interpret, therefore for this stage of validation, only the harmonic spectra are compared and the simulated waveform is displayed as a guide. Figure 7–17 shows the open circuit flow ripple at 450 rev/min with the reservoir set to 1bar. There are discrepancies between the first three harmonics between measured and predicted results, which indicates that there is an error in the impedance model at 450rev/min. The first three harmonics are at 75, 150 and 225 Hz, the impedance model (Figure 7–6) does not show good agreement with tests at these frequencies. Therefore the air content function may be at fault at this particular running condition.

7.3.1.4 ANECHOIC FLOW RIPPLE VALIDATION

An alternative method of comparing theory with experiment is to calculate the anechoic flow ripple at the pump inlet from the theoretical internal flow ripple. Anechoic flow ripple is defined as the flow ripple into an infinitely long or reflectionless pipe of a particular diameter. Of the various measures of ripple that can be defined at the pump inlet or outlet, anechoic flow ripple has the advantage of not being affected by resonances in the external circuit. Again, knowledge of the impedance characteristics of the intervening passageways is necessary but in this case use has been made of the impedance model developed in Chapter 3.

At 450rev/min (Figures 7–18, 7–19), the simulation compares well with test results, however there is a large difference between the predicted and measured first harmonic. In Figures 7–20 and 7–21, the lower harmonics at each pressure (up to the fifth) show good agreement. The best comparison between simulation and experiment is shown at 1500rev/min (Figures 7–22 and 7–23) where most of the simulated harmonics are within the experimental error between the three sets of test results. The waveform associated with the pump, which is running at 1500rev/min with a 3bar reservoir (Figure 7–23), shows slight discrepancies between measured and predicted.

7.3.2 VALIDATION OF SIMULATION OF PUMP 2

The housing of Pump 2 has the same dimensions as Pump 1, which means that both the measured and the predicted impedance for the two pumps are identical. The difference between the pumps is in their capacity; the difference between the major and the minor radius of the cam is larger on Pump 2, which is shown in Appendix 2. This therefore affects the flow ripple characteristic. Comparing the measured and predicted anechoic flow ripple at atmospheric pressure can demonstrate the validity of the model for simulating Pump 2.

Figure 7–24 shows the anechoic flow ripple of the pump at 1500rev/min. There is generally good agreement between measured and predicted results. At 450rev/min, shown in Figure 7–25, there is also good agreement in all harmonics.

7.3.2.1 EFFECT OF CHAMBER VOID FRACTION ON SIMULATION RESULTS

Figure 7–26 shows measured and predicted results for Pump 2 at 900rev/min, which shows minor differences in the first six harmonics and then a divergence of results at higher frequency. The simulation was run with a chamber air content of 1.5%. Figure 7–27 shows the effect of reducing the air content of the chamber, in this case to 1%. The peak to peak value of flow ripple has halved to approximately 0.75mL/s. This demonstrates that the inaccuracy in some of the simulated first harmonics are due to bad definition of the void fraction in the chambers.

An empirical function could be developed by fitting simulated flow ripple to experimental results and recording the air content as a function of speed and pressure, as with the impedance model. This has not been done because there is no photographic evidence to support the theory that it is air in the chambers which is affecting the flow ripple results.

7.3.3 VALIDATION OF SIMULATION OF PUMP 3

Pump 3 has different housing and cam ring dimensions to the other two pumps (shown in Appendix 3), which means that both impedance and flow ripple are different to Pump 1 and must be examined.

7.3.3.1 IMPEDANCE OF PUMP 3 VALIDATION

The impedance model uses the aeration function that was developed for Pump 1 and the disadvantages of this can be seen in the predicted impedance results shown in Figures 7–28, 7–29 and 7–30. The position of the first anti-resonance is predicted quite accurately but the predicted position of the second anti-resonance in all three cases is too low. This suggests that the amount of air produced in the outlet from the supercharge valve is lower in Pump3 than in the other two pumps.

7.3.3.2 ANECHOIC FLOW RIPPLE

Despite the inaccuracy of the predicted impedance, the anechoic flow ripple compares well with experiments. The error due to the incorrect air-content function only ever affects the higher harmonics. A customised air-content function must be derived for Pump 3 before it can be used as a design tool.

7.4 CONCLUSIONS

An empirical aeration function was derived from impedance results for one of the pumps but it was used in the simulations for all three pumps. There were some discrepancies in the results due to this simplification and a separate function for each model of pump would be ideal.

The impedance model generally compares well with experimental results. The parts with the largest divergence between measured and predicted results were found to have only a minor

effect on flow ripple prediction because the errors usually affected the high frequency, low-amplitude harmonics.

The component of internal flow ripple due to compressibility shows up as a spike, which in the simulation was found to be narrower than in experiment. The dynamic component of flow ripple was generally good except at low pump speed, where the amplitude was too low. This would suggest that air content inside the chambers should not be assumed to be constant but should be a function of pressure and speed. Anechoic flow ripple was mainly used for the validation. All pumps showed good correlation between measured and predicted results, which suggests that the method of using a modular program with different parameter files for each pump is sound and predicted results can be relied upon as recommendations for design.

FIGURES FOR CHAPTER 7

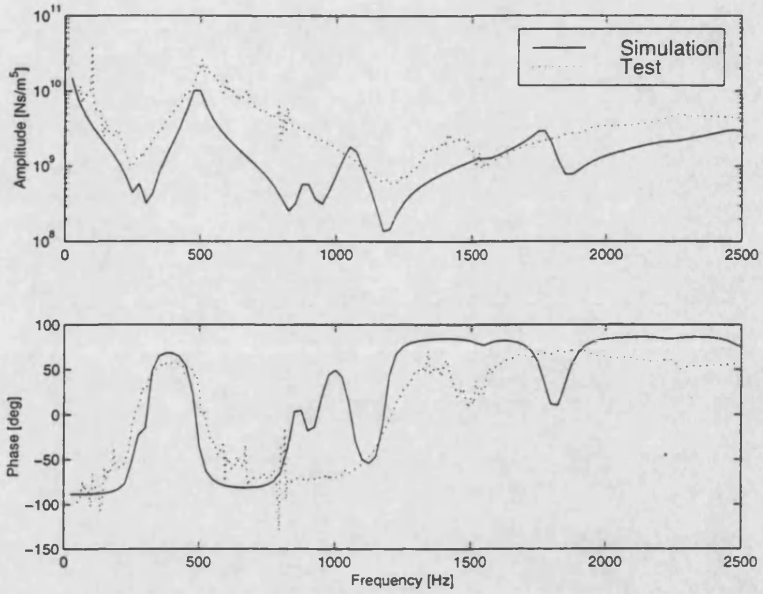

Figure 7–1: Impedance Characteristic with Little Aeration (450rev/min, 1bar reservoir)

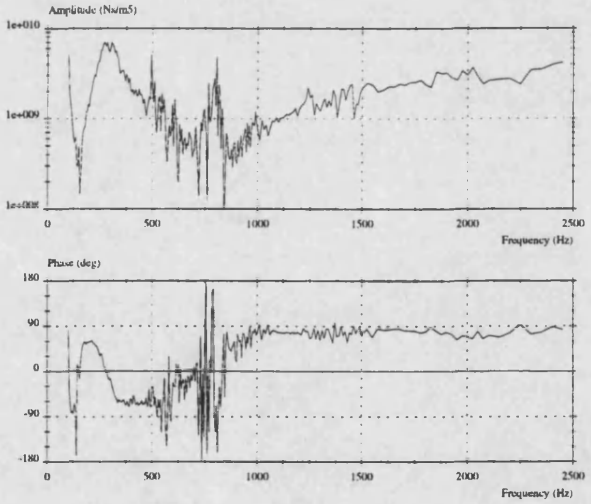

Figure 7–2: Impedance Characteristic with Aeration (1500rev/min, 1bar reservoir)

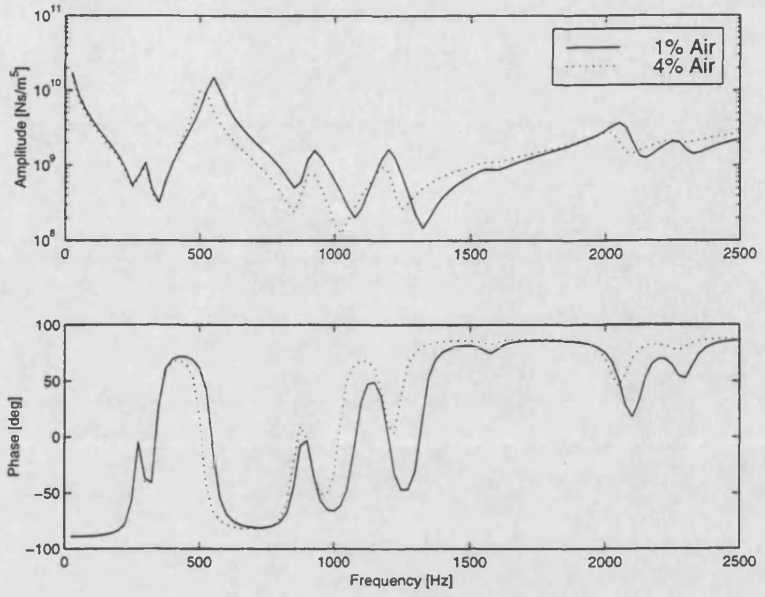

Figure 7–3: Effect of Air Content in Supercharge Passageway on Impedance Characteristic

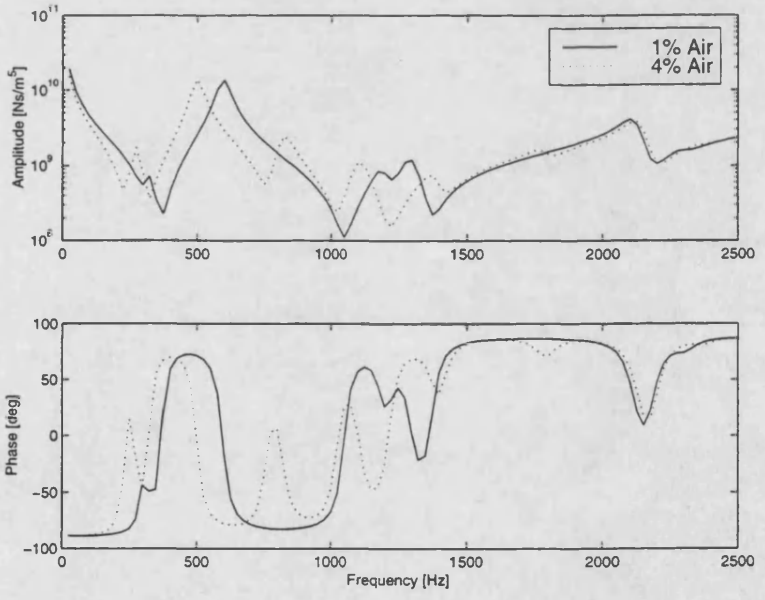

Figure 7–4: Effect of Air Content in the Half-Annulus Section on Impedance Characteristic

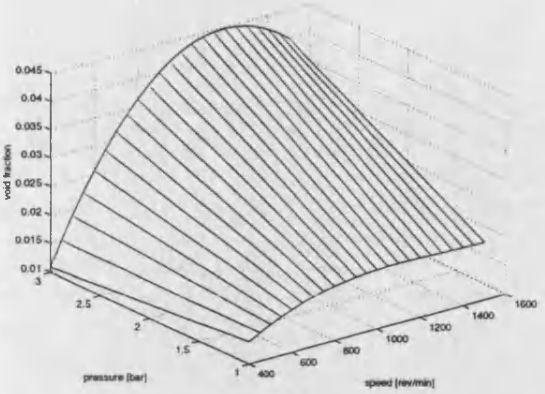

Supercharge Discharge

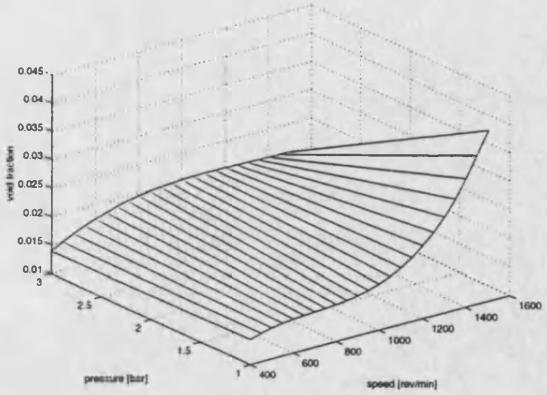

Inlet to Annulus

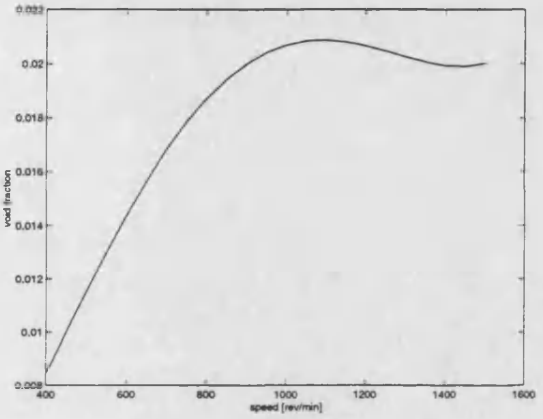

First Quarter Annulus Section

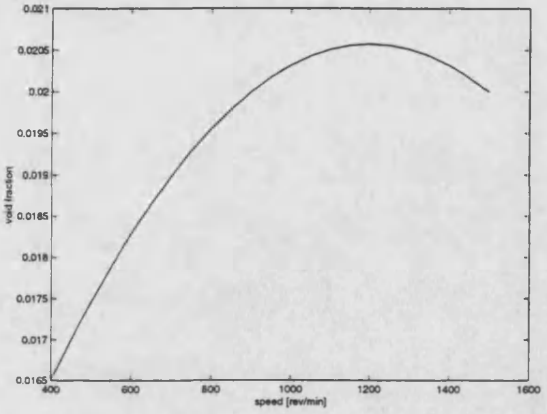

Second Quarter Annulus Section

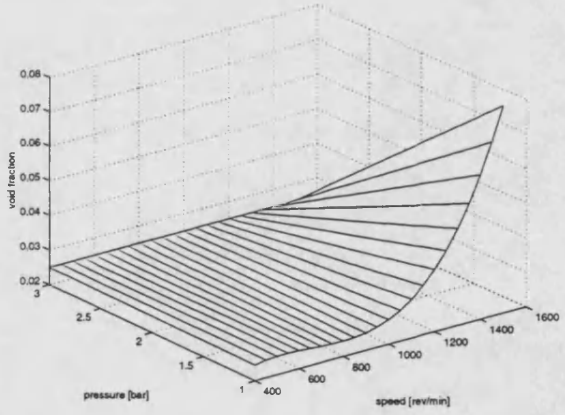

Half Annulus Section

Figure 7–5: Empirical Air Content Function

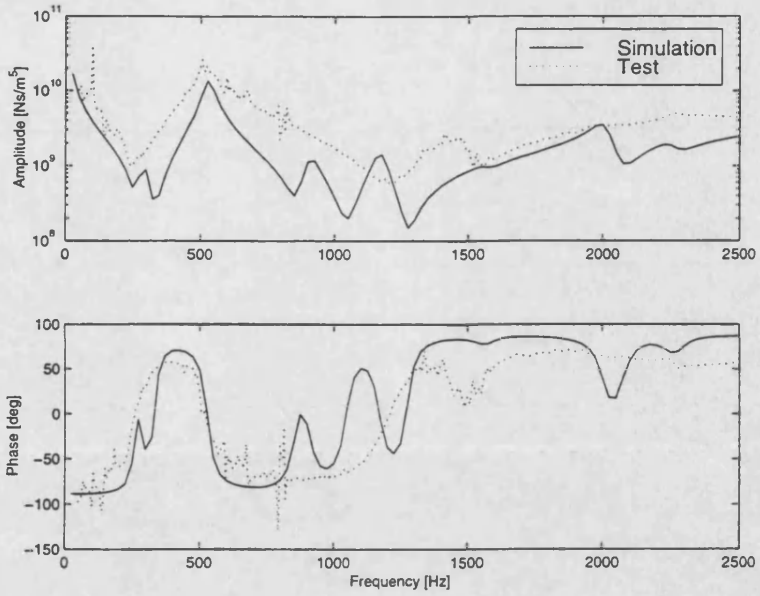

Figure 7–6: Impedance: 450rev/min. 1bar

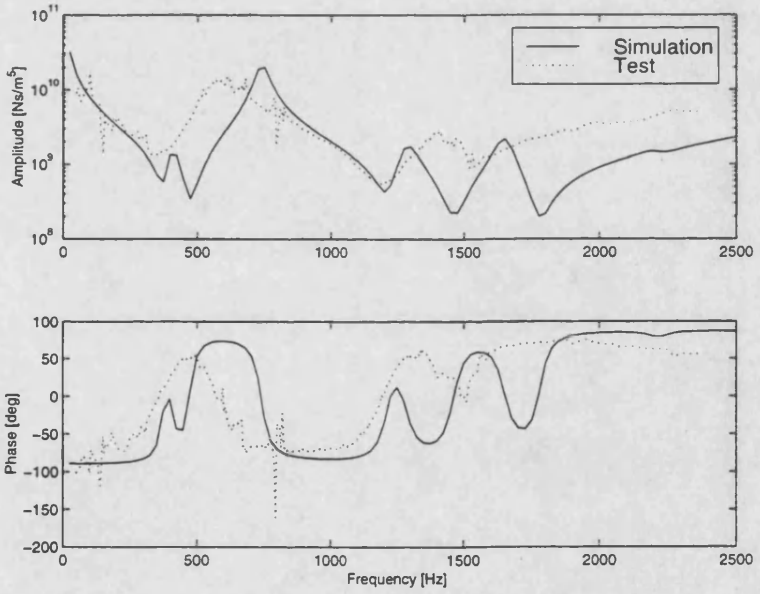

Figure 7–7: Impedance: 450rev/min. 3bar

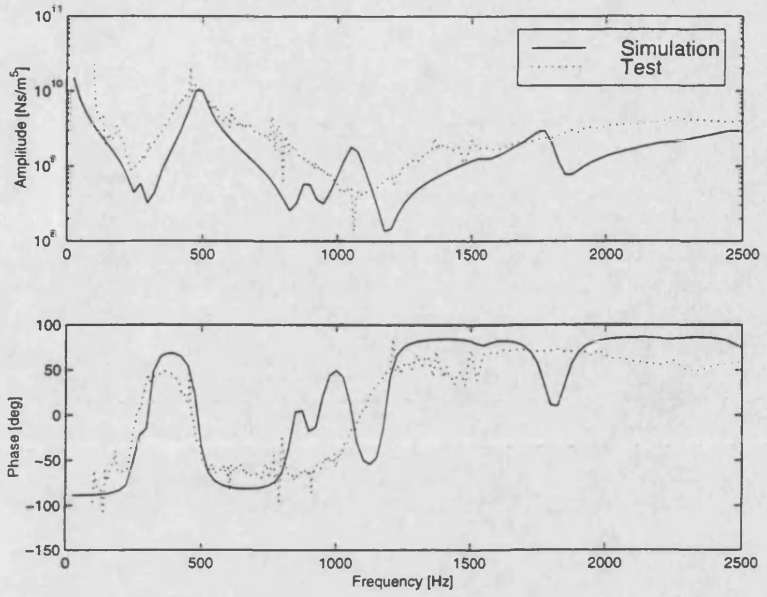

Figure 7–8: Impedance: 900rev/min. 1bar

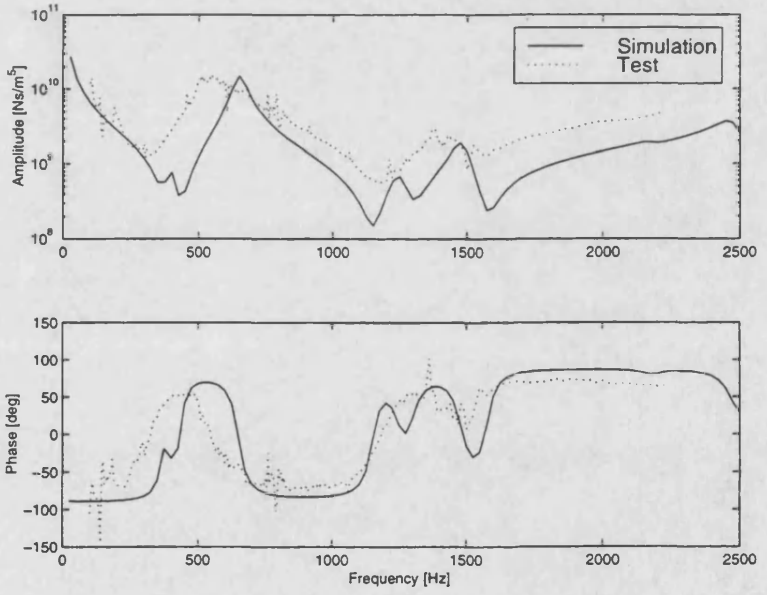

Figure 7–9: Impedance: 900rev/min. 3bar

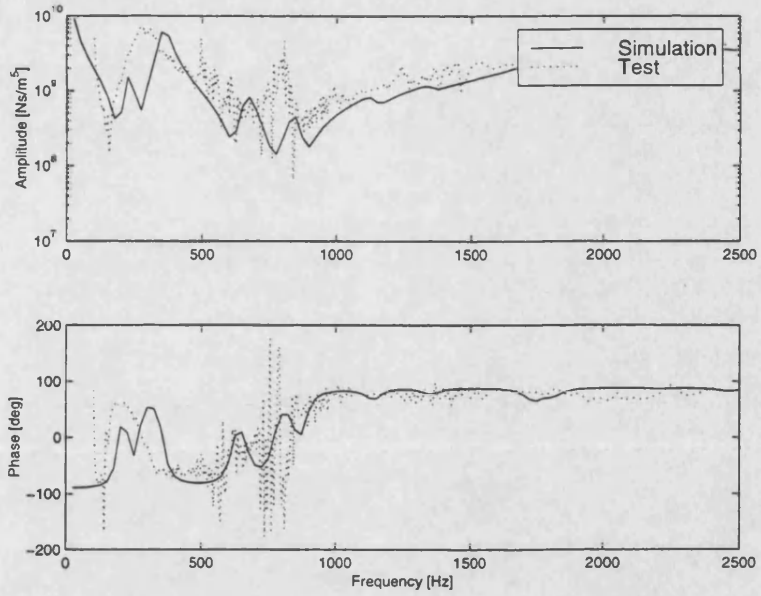

Figure 7–10: Impedance: 1500rev/min. 1bar

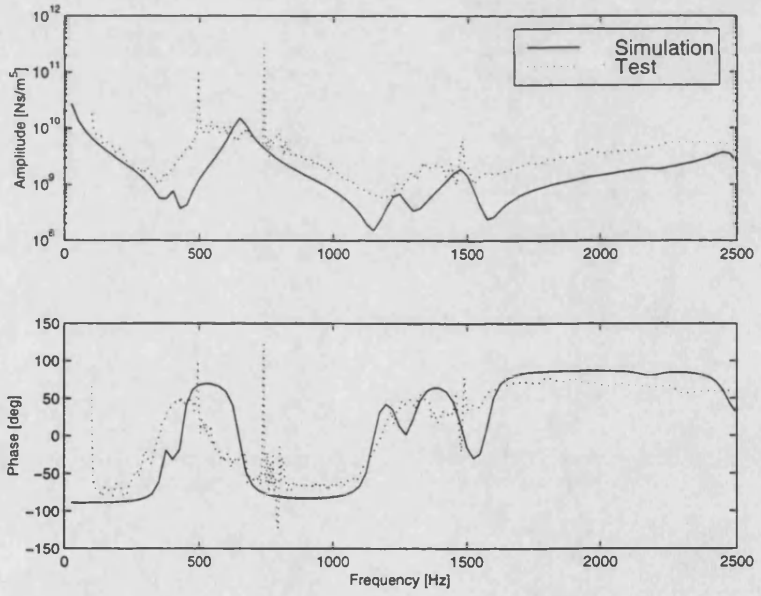

Figure 7–11: Impedance: 1500rev/min. 3bar

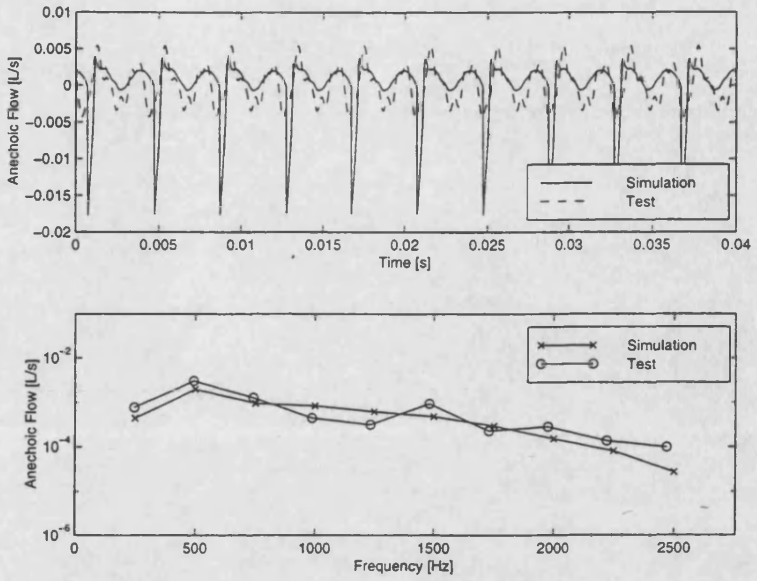

Figure 7–12: Comparison of Measured and Predicted Waveforms for Internal Flow Ripple

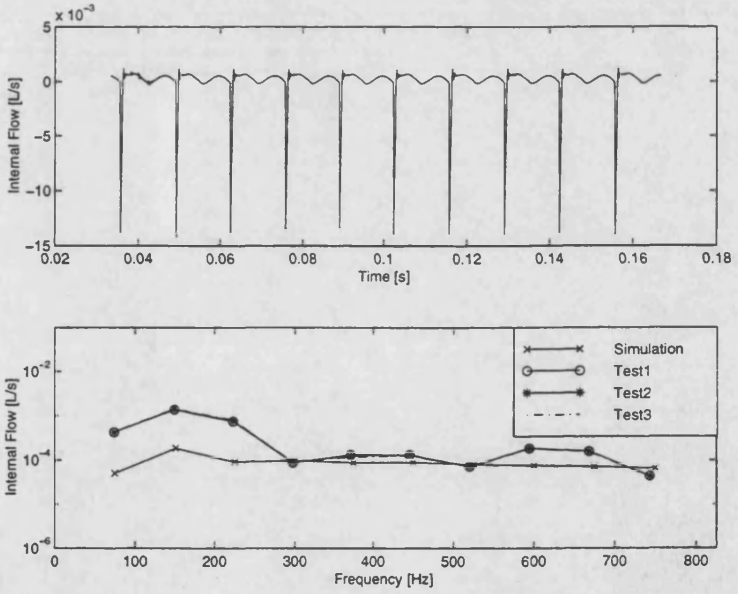

Figure 7–13: Internal Flow Ripple at 450rev/min and 1bar

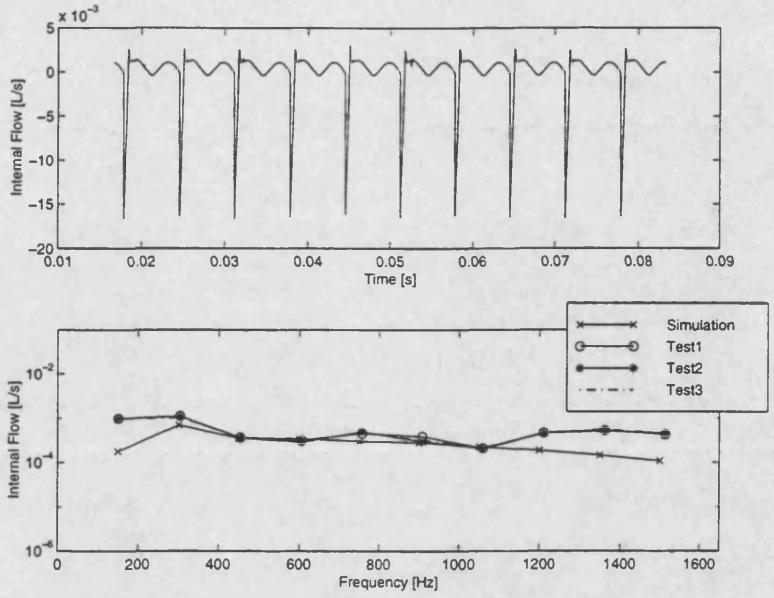

Figure 7–14: Internal Flow Ripple at 900rev/min and 1bar

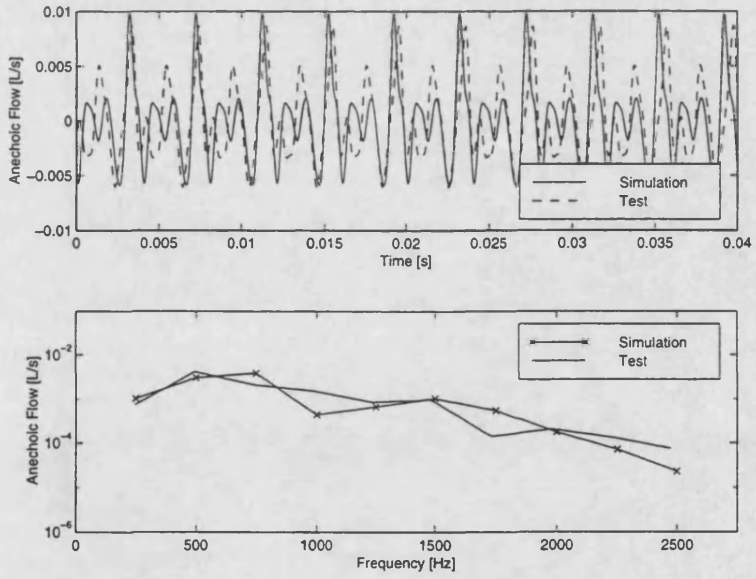

Figure 7–15: Open Circuit Flow Ripple at 1500rev/min and 1bar

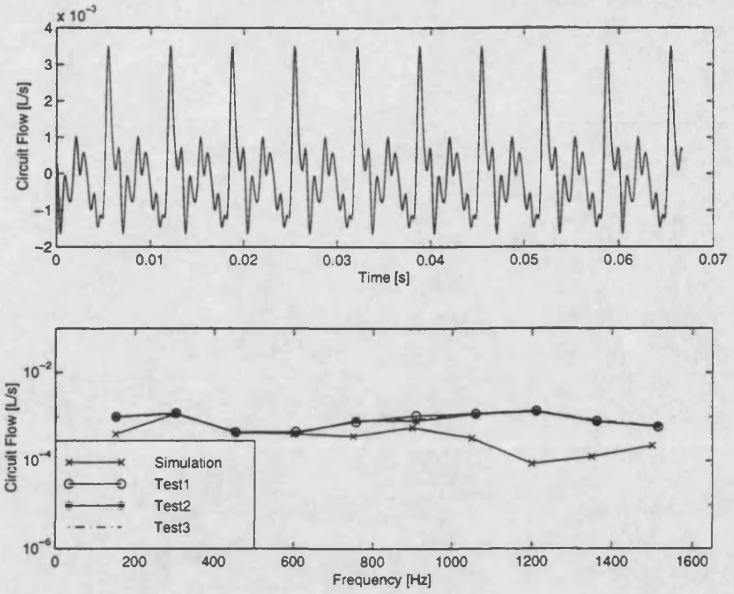

Figure 7–16: Open Circuit Flow Ripple at 900rev/min and 1bar

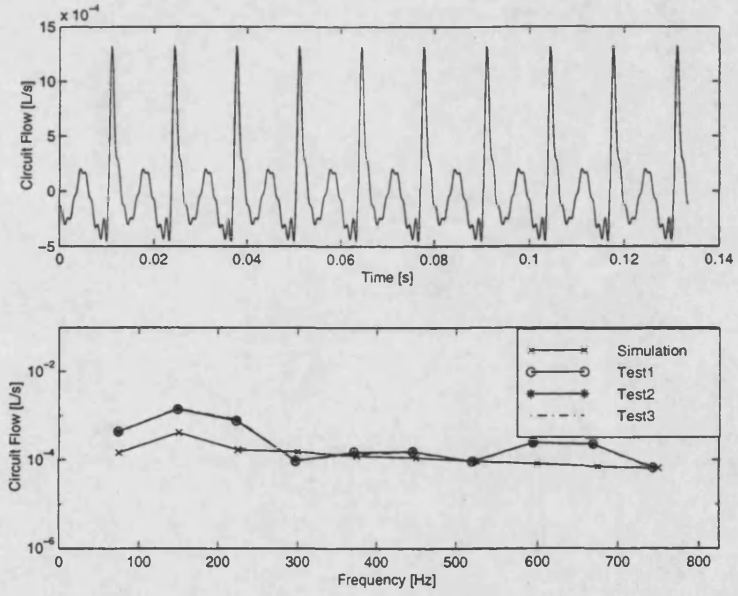

Figure 7–17: Open Circuit Flow Ripple at 450rev/min and 1bar

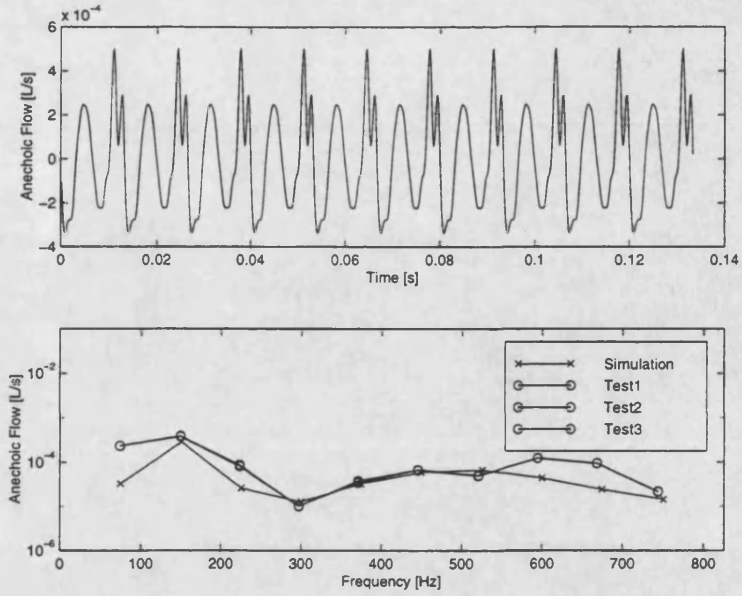

Figure 7–18: Anechoic Flow Ripple: 450rev/min, 1bar

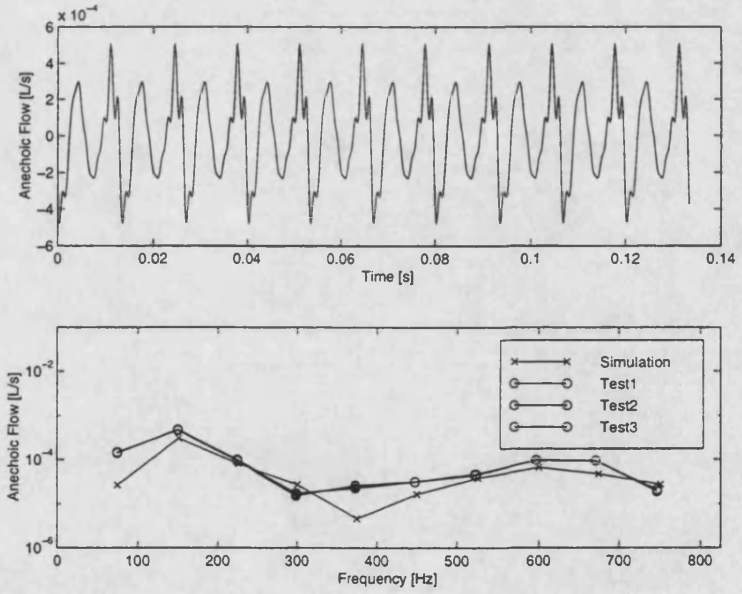

Figure 7–19: Anechoic Flow Ripple: 450rev/min, 3bar

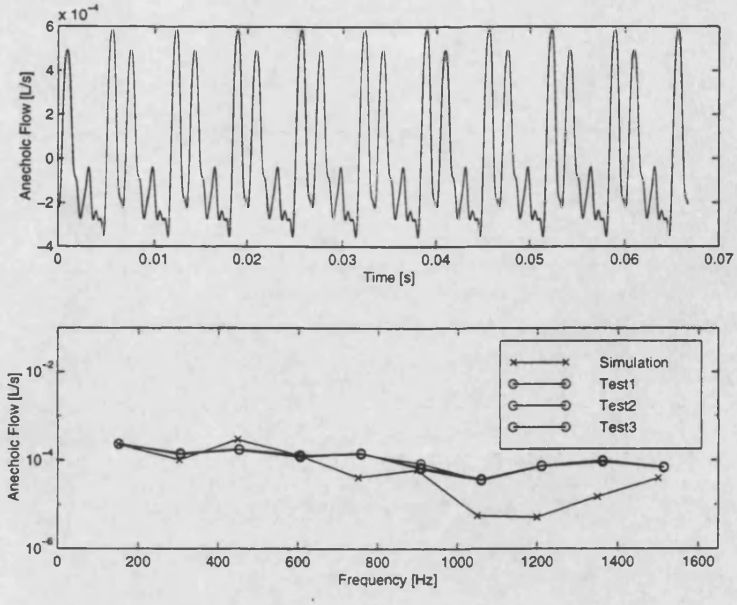

Figure 7–20: Anechoic Flow Ripple: 900rev/min, 1bar

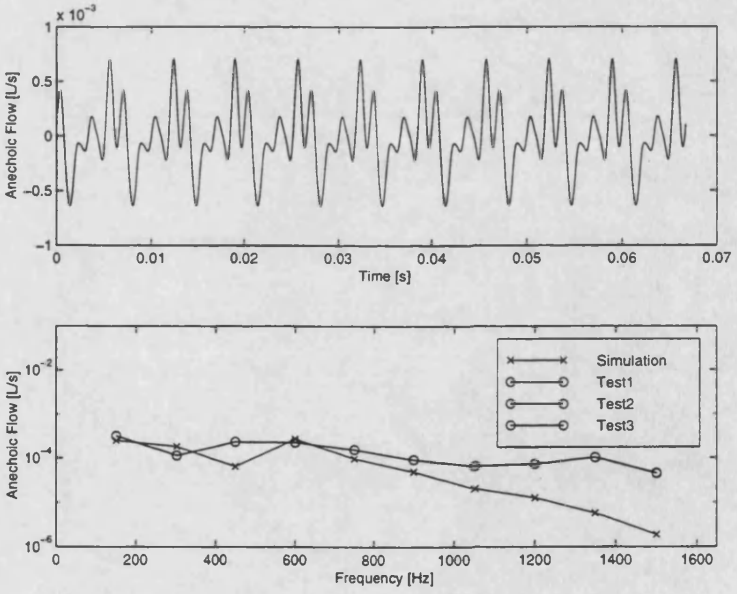

Figure 7–21: Anechoic Flow Ripple: 900rev/min, 3bar

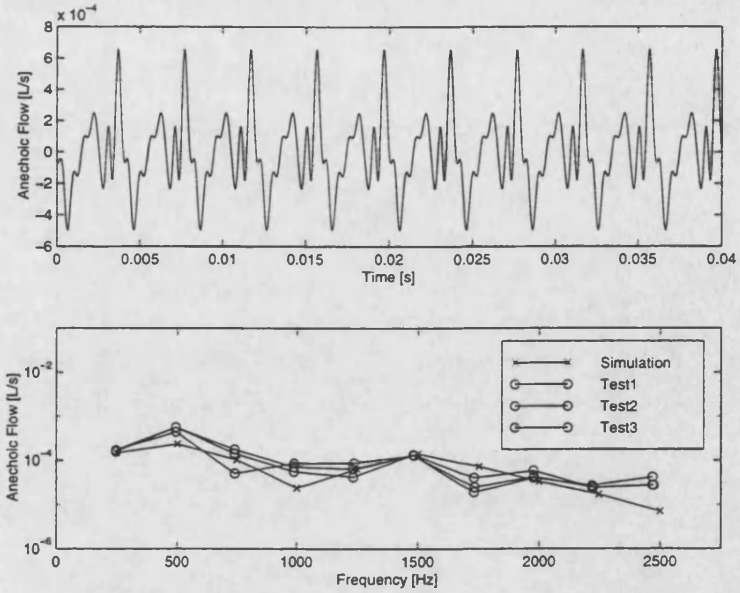

Figure 7–22: Anechoic Flow Ripple: 1500rev/min, 1bar

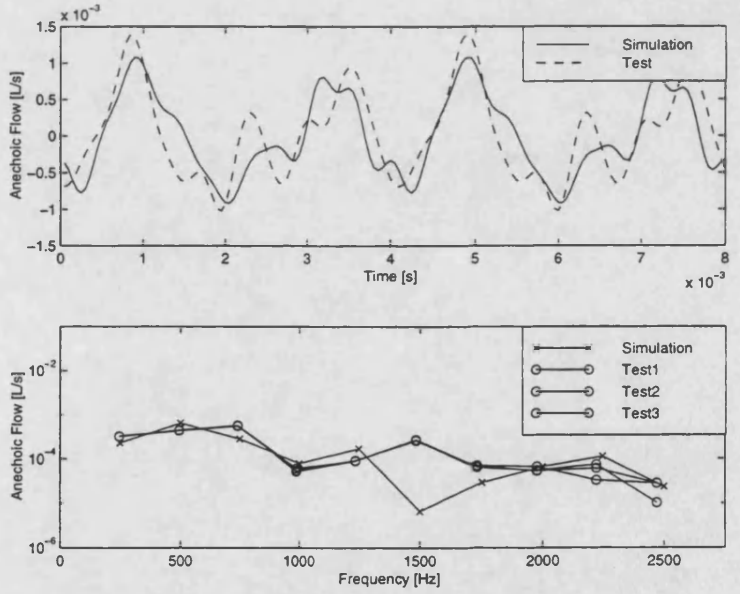

Figure 7–23: Anechoic Flow Ripple: 1500rev/min, 3bar

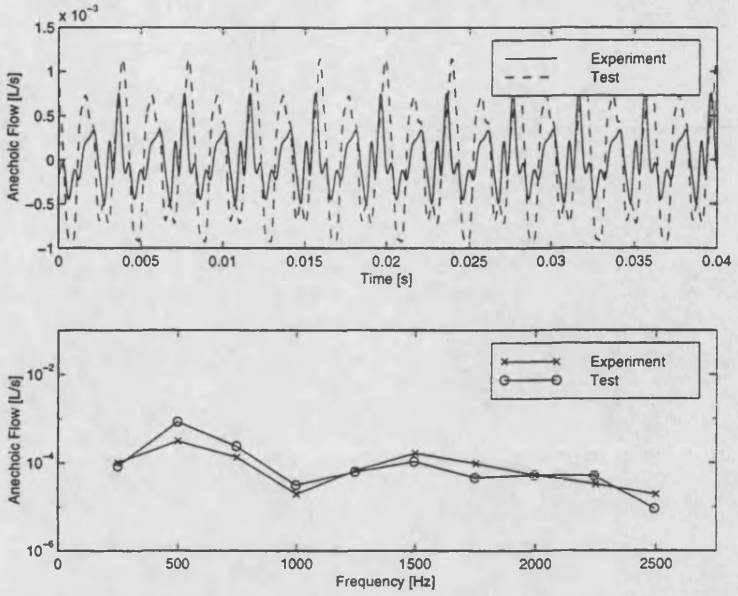

Figure 7–24: Anechoic Flow Ripple of Pump2 at 1500rev/min

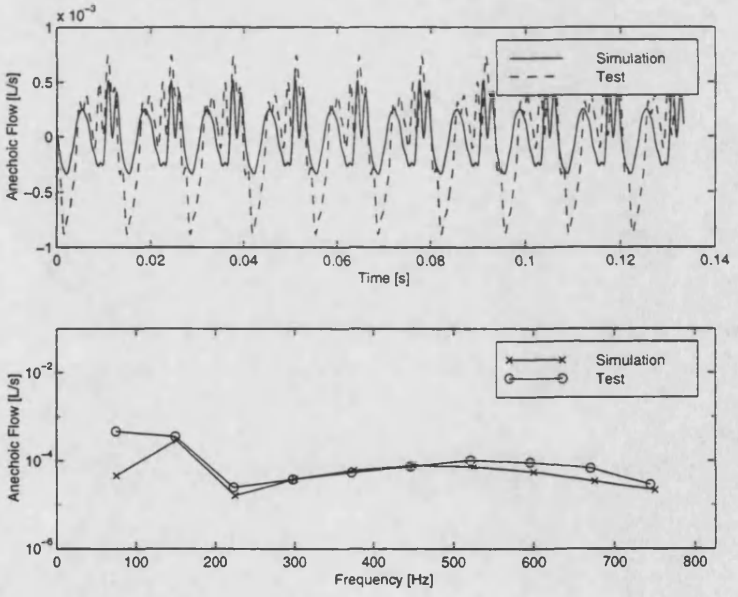

Figure 7–25: Anechoic Flow Ripple of Pump2 at 450rev/min

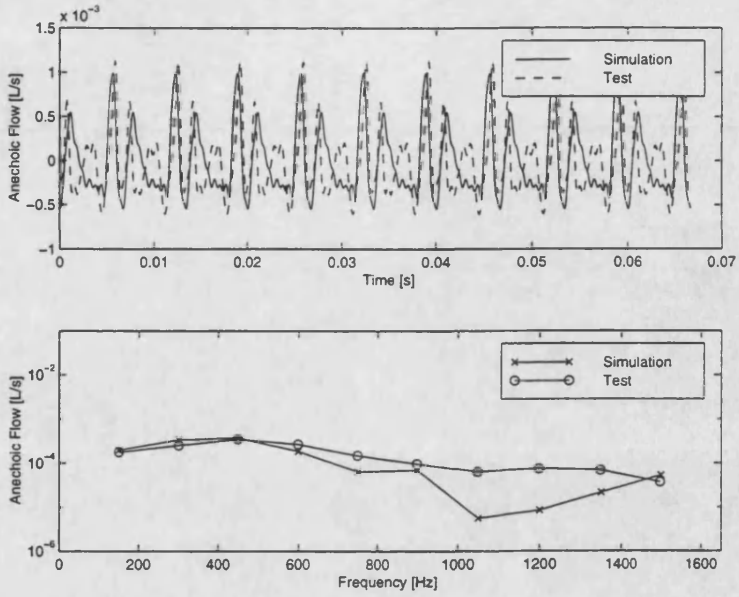

Figure 7–26: Simulated Flow Ripple at 1.5% Chamber Air Vs Test Results

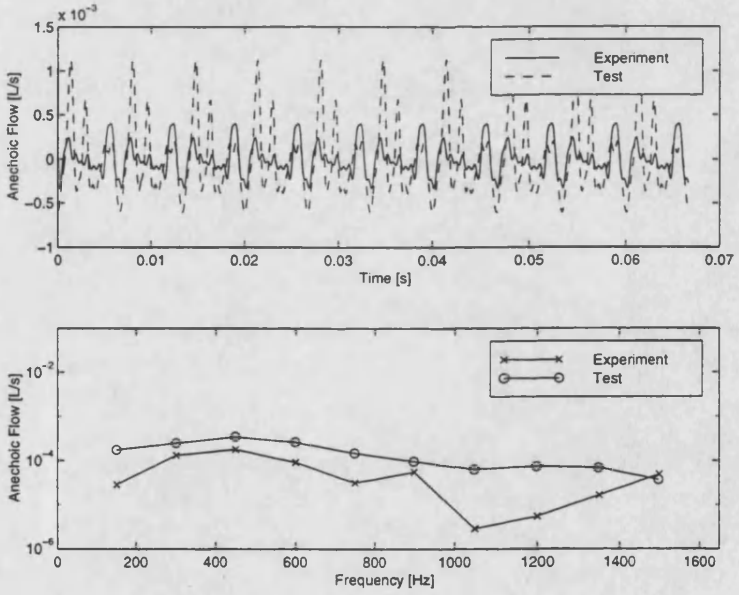

Figure 7–27: Simulated Flow Ripple at 1% Chamber Air Vs Test Results

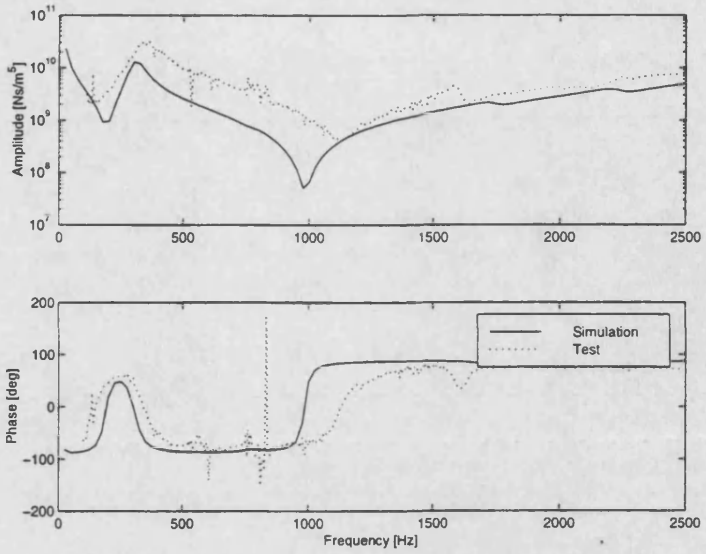

Figure 7–28: Impedance of Pump3 at 450rev/min

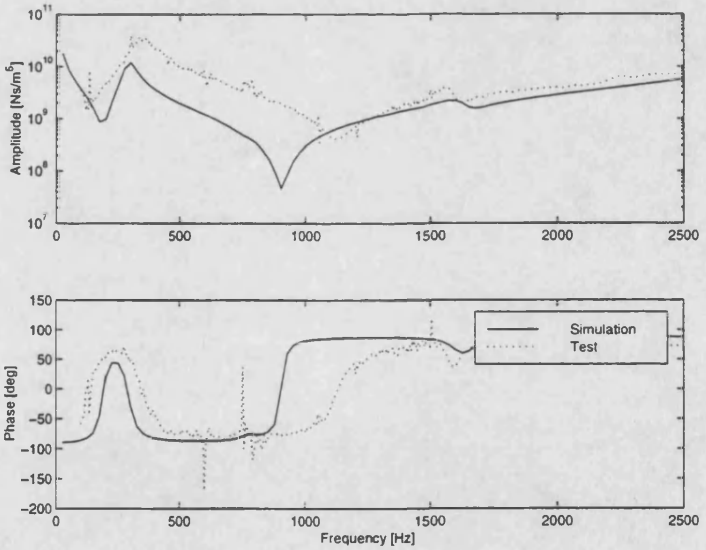

Figure 7–29: Impedance of Pump3 at 900rev/min

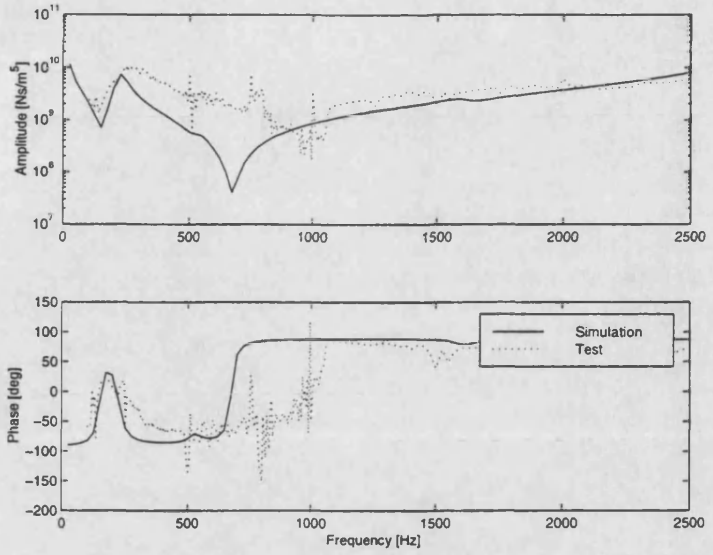

Figure 7–30: Impedance of Pump3 at 1500rev/min

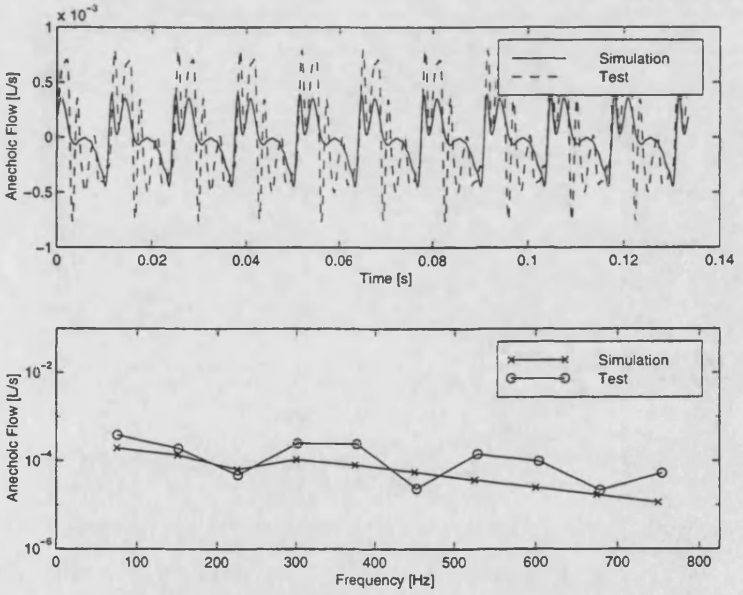

Figure 7–31: Anechoic Flow Ripple of Pump3 at 450rev/min

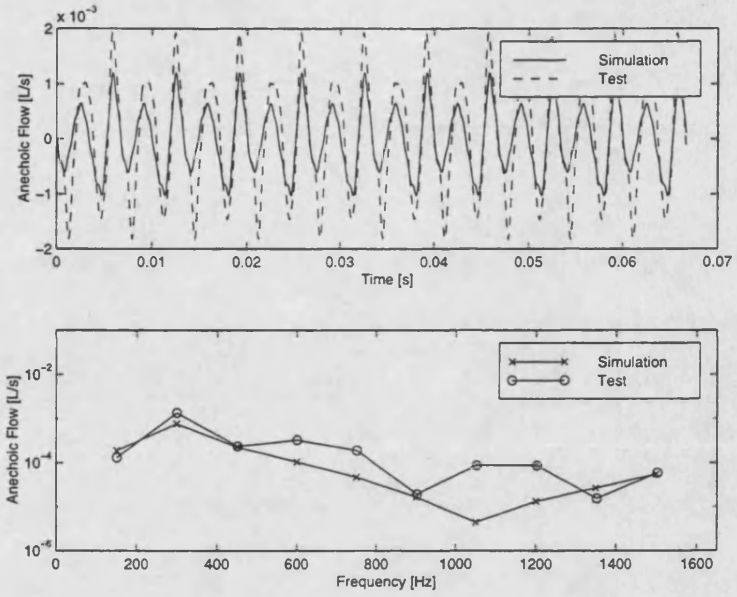

Figure 7–32: Anechoic Flow Ripple of Pump3 at 900rev/min

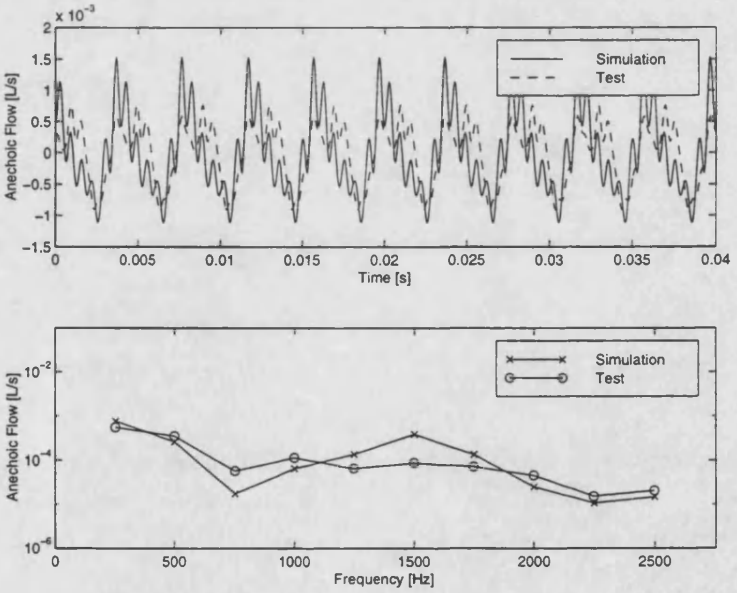

Figure 7–33: Anechoic Flow Ripple of Pump3 at 1500rev/min

8 DESIGN RECOMMENDATIONS FROM SIMULATION RESULTS

8.1 INTRODUCTION

In Chapter 7, it has been shown that the simulation and impedance models give a good guide to suction port flow ripple. It is therefore possible to use the models as design tools with some degree of confidence, however there are some limitations of the model that should be noted. The simulation cannot predict any pump-casing modifications that affect aeration because the empirical air content function is unique for each design of pump. Therefore, the exact effect of changes to the supercharge valve geometry on air content cannot be predicted. Other modifications, which do not directly affect the air content, are discussed in this chapter.

8.2 USING RELIEF GROOVES TO REDUCE SUCTION FLOW RIPPLE

The transition from a closed pumping chamber to an open one can sometimes be very sudden and, if the pressure in the chamber and the port is not equal, large gradients occur. The effect of large pressure gradients is to create oscillations of pressure due to fluid inertia. One method of gradually reducing the pressure difference is the insertion of a relief groove to the opening of the port. Figure 8–1 shows the pressure plate of a typical vane pump, there is a triangular relief groove at the opening of the delivery port but none on the suction port. The observed effect of a relief groove is to reduce the higher harmonics of flow ripple. In other words, the high frequency oscillations caused by fluid inertia.

In §6.5.3, the higher harmonics of suction flow ripple were sometimes found to be dominant when compared with delivery flow ripple. One reason for this could be due to the absence of relief grooving on the suction port. The simulation can be used to look at the effect of relief grooves on the flow ripple. Figure 8–2 shows the simulated flow ripple of a pump running at 1500rev/min with 1bar reservoir and 10bar delivery pressure, which is used as the baseline model for this study. Four different port configurations are assessed for their relative performance against the baseline.

8.2.1 CONFIGURATION 1

The first configuration considers the addition of a relief groove to the opening of the port, similar to the case of the delivery port. The port opening is delayed by 5° and a 5° triangular relief groove is inserted, the modified orifice profile is shown in Figure 8–3.

This configuration shows a very small change in flow ripple (Figure 8–4), which is negligible when measurement error is taken into account. This relief groove is unacceptable because the modified area profile is greater than the original, which is defined by the area between the rotor and the cam ring and is therefore at the maximum allowable.

8.2.2 CONFIGURATION 2

A 5° relief groove is added to the opening of the port as in §8.2.1, but the port opening is delayed by 10°. The overall area of the port, shown in Figure 8–5, is not greatly affected by the delayed port opening. Figure 8–6, which shows the flow ripple, shows that all harmonics above the third are reduced by up to an order of magnitude. The first harmonic, however, is increased by about the same amount, which is possibly caused by the decompression in the chamber due to the delay in its opening. The waveform shows that the overall effect of this configuration is to reduce the peak to peak value of flow ripple from $0.8mLs^{-1}$ to $0.5mLs^{-1}$.

Figure 8–7 shows the predicted chamber pressure for this configuration. There is more decompression prior to the opening of the suction port due to the 5° delay. In this case, the pressure is reduced to 0.3bar, which could cause air release and in extreme cases cavitation. The amount of de-compression that would be seen in tests may be less than in the simulation but this must be verified on the prototype.

8.2.3 CONFIGURATION 3

In configuration 3, the port opening is delayed by 10°, as in Configuration 2, but a 10° relief groove is inserted. This is to reduce the amount of de-compression, which is seen in Configuration 2. The modified orifice profile (Figure 8–8) is very similar to the original but it exceeds the constraints of the cam profile, as in Configuration 1. The anechoic flow ripple produced by this configuration (Figure 8–9) is greater than that of the benchmark pump and therefore the design must be rejected.

8.2.4 CONFIGURATION 4

The area profile of the benchmark pump, shown in Figure 8–8, shows a very steep gradient at the closing of the port. In configuration 4, a 5° relief groove is placed at the port closing to give the profile shown in Figure 8–10. There is a similar reduction in flow ripple as seen for Configuration 2 (Figure 8–11), which when compared with Configuration 2 (Figure 8–12) suggests that the closing of the port has little effect on the flow ripple.

8.2.5 DISCUSSION OF PORT CONFIGURATIONS

Configurations 1 and 4 show only small changes in flow ripple characteristics. In both configurations, the relief groove opens to the port at the same position as the port opens in the benchmark pump, which means there is only a very small difference between the geometry of the orifices. In both these cases, the area profile of the relief groove exceeds the limit set by pump geometry, i.e. the area between the rotor and the cam ring. These modifications must therefore be rejected.

Configurations 2 and 4 show large reductions of an order of magnitude in the harmonics above the fourth. In each case the opening of the port has been delayed by 10° and a 5° relief groove has been inserted at the opening of the port. In Configuration 4, there is a relief groove at the opposite end of the port, which in comparison with Configuration 2 shows little added benefit.

The ideal port design is therefore Configuration 2, which has a 10° delay of opening and a 5° relief groove whose maximum height is 1mm, at the base of the triangular section where it meets the port. This design will have to be tested, which includes manufacturing the modified port plates and comparing the results to a benchmark pump, as in the simulation. The size of the port has been reduced, which may affect other aspects of performance outside the scope of the simulation, which can only be observed in the tests.

8.2.6 Relief Groove Performance Under Different Operating Conditions

The relief groove and delayed port opening was optimised at only one speed and pressure. In this section the performance of the relief groove over a range of pressure (delivery and suction), and speed is analysed.

Figure 8–13 shows the anechoic flow ripple for the modified pump at high speed with a high delivery pressure: At 1500rev/min and a delivery pressure of 50bar, the modified pump compares well with the simulated benchmark. There is a reduction in flow ripple of an order of magnitude in all but the first harmonic, which is the same size as the benchmark value. The peak to peak value of the waveform has also been reduced from $1.3mLs^{-1}$ to $0.5mLs^{-1}$. Figure 8–14 shows that there is some de-pressurisation due to the delayed port opening but in this case, the minimum pressure of 0.5bar is unlikely to cause cavitation.

Figure 8–15 shows the anechoic flow ripple of the modified pump at low speed: 450rev/min at 10bar delivery. This also shows a considerable reduction in the magnitude of the higher harmonics of flow ripple and the peak to peak value of the waveform is reduced from $0.25mLs^{-1}$ to $0.1mLs^{-1}$. In this case, there is only a small amount of de-pressurisation due to the delayed opening, which would not cause cavitation problems (Figure 8–16).

Figure 8–17 shows that the modification is also effective with a boosted reservoir pressure of 3bar. The modified pump, running at 900rev/min and 50bar delivery, also shows a decrease in amplitude of flow ripple of about an order of magnitude in all but the first harmonic.

These results suggest that delaying the opening of the port can reduce the flow ripple by equalising the pressure of the port and chamber. Pressure equalisation can also be achieved by replacing the minor dwell of the cam with a decompression zone. In other words, instead of an area of constant chamber volume, the chamber increases linearly in volume until it opens to the

port and the parabolic rise begins. This was discussed in Section 4.2, where the possibility of cavitation was mentioned especially if the pressure at the beginning of decompression is low.

8.3 INCREASING THE NUMBER OF VANES TO REDUCE FLOW RIPPLE

The benchmark pump has 10 vanes that are equally spaced around the rotor thus creating ten pumping chambers. If the amount of vanes were increased the volume of each chamber would be decreased and the flow ripple would therefore be altered. A smaller chamber has a smaller mass of fluid within so the inertia would be less than in the benchmark pump. Also there is less fluid pumped per chamber, which may lead to an overall decrease in flow ripple. The simulation was used to look at the possible effects of increasing the number of vanes.

Figure 8–18 shows the comparison between the benchmark and a modified pump with 14 vanes. There is no real pattern to the comparison of harmonic amplitude but it must be noted that there are of different frequency to one another: the benchmark pump harmonics are at multiples of 250Hz and the modified pump is at multiples of 350Hz. These are the pumping harmonics whose fundamental frequency is given by the shaft speed multiplied by the number of vanes. The peak to peak value of the waveform, however, does show a reduction from $0.8mLs^{-1}$ to $0.6mLs^{-1}$. Figure 8–19 shows that further increasing the number of vanes reduces the peak to peak value of flow ripple even more.

Increasing the number of vanes does decrease the level of flow ripple and would be more effective if the cam and port position were optimised for the new configuration. The disadvantage is that the modified pump has more parts and more machining is required and so the cost of the pump would be increased.

Using an odd number of vanes has not been discussed in this section because of the balancing problems associated with such a design. In an even-numbered vane pump, the flow ripple emerging from each port is in phase whereas in a pump with an odd number of vanes, there is a phase difference between the two signals. This could reduce the flow ripple due to cancellation of the out of phase components. Unfortunately, the unequal forces caused by the unsymmetrical design of the pump means that there would be increased wear on the bearings. Therefore, structural vibration from the imbalance of pressure and a shortened life from bearing wear offset any potential noise reduction.

8.4 THE EFFECT OF UNEVEN VANE SPACING ON FLOW RIPPLE

It is possible to adapt the simulation to predict the performance of a vane pump whose chambers are of unequal size. Figure 8–20 shows the vane spacing for an unevenly spaced ten-vane pump, which is periodic every 180° in order to ensure a force balance between opposite chambers. In order to compare the results of such a simulation with the baseline pump, there

must be some modification to the results processing. It is sufficient to measure the pumping harmonics of an equally spaced vane pump in order to ascertain the flow ripple because the intermediate harmonics have negligible energy in comparison. This is because the signal is periodic at the pumping frequency. In an unequally spaced pump, more harmonics must be measured. In the case of the design in Figure 8–20, the flow ripple waveform is periodic every half a pump revolution, which suggests that flow ripple harmonics at the shaft frequency need to be measured in order to fully describe the wave form. Taking the harmonics at the shaft frequency means that every second harmonic is negligible and the Fourier transform of the waveform is a series of peaks.

The effect of using uneven spacing is to produce fluid borne noise which is richer in harmonics than for an evenly spaced rotating group. This may not decrease the amplitude of the waveform but it does have the effect of spreading the energy over a much wider frequency band, which may reduce the amplitude of resonances. The audible tone of the modified flow ripple must also be assessed in order to judge whether the sound emitted by an evenly spaced pump is more or less pleasant to the ear than an unevenly spaced pump. Although such tests are purely subjective, it may be possible to isolate certain components of noise that, to the majority of people, are more pleasant to listen to than others. This method of noise analysis is however out of the scope of this thesis and for the sake of this study three examples of unevenly spaced pumps are compared to benchmark simulations at 1500rev/min, 1bar reservoir and 10bar delivery and the simulated flow ripple spectra and waveforms are examined. If a pump shows good reduction, a prototype can be built and the aesthetic quality of the noise can be assessed.

8.4.1 AN UNEVENLY SPACED 10 VANE PUMP

This pump, whose rotating group spacing is shown in Figure 8–20, is not a practicable design because some of the more widely spaced vanes allow a chamber to be open to both suction and delivery at the same time. This decreased the volumetric efficiency of the pump because in this position there is a large back-flow from delivery to suction because of the pressure difference. This can be seen in the simulated internal flow ripple (Figure 8–21), which shows four large negative spikes per revolution. The other spikes, which are due to compression flow ripple, are about the same magnitude as the benchmark figure. The effect of the four large back-flow spikes is to increase the magnitude of the sub-pumping-frequency harmonics such that they become dominant.

The anechoic flow ripple, which is shown in Figure 8–22, is particularly dominated by the low harmonics. The spikes seen on the internal flow ripple at four times the pump frequency become the dominant harmonic of the anechoic flow ripple (The peak at 100Hz is almost one order of magnitude greater than the next highest at 300Hz). This is seen on the waveform as a very large amplitude flow ripple, which makes the benchmark results look negligible. 100Hz is

however at the lower end of human hearing and, from an aesthetic point of view, may be less of a nuisance than harmonics between 500Hz and 800Hz, say, which are high-pitched and rather unpleasant to be subjected to.

8.4.2 AN UNEVENLY SPACED 12 VANE PUMP

A pump with twelve vanes was simulated to ensure that none of the chambers was so large as to be open to suction and delivery at the same time. This has not been compared to the benchmark but to a simulated evenly spaced twelve-vane pump, which as demonstrated in §8.3 would have a smaller amplitude flow ripple than the benchmark. The vane spacing, which is periodic every 180° to give balance of forces in opposite chambers, is shown in Figure 8–23.

At a glance, it can be seen that there is very little difference between the amplitude of the internal flow ripple of the two waveforms (Figure 8–24). The difference between the two sets of results is that the compression spike on the modified pump is not as regularly spaced as on the evenly spaced pump. The anechoic flow ripple for the two simulations is also similar (Figure 8–25), which may not be the same for all unequally spaced twelve-vane pumps. Figure 8–26 shows another twelve-vane configuration, which contains one chamber that is considerably smaller than the other five in the period. The effect of this is to reduce the magnitude of the internal flow ripple harmonic at 600Hz (Figure 8–27), the first pumping harmonic for the evenly spaced pump, because of the offset of two of every twelve compression spikes due to the small chamber. This has the effect of reducing the peak to peak value of anechoic flow ripple, which is shown in Figure 8–28, from $0.5mLs^{-1}$ to $0.4mLs^{-1}$. Once again, the aesthetic appeal of this more irregular waveform cannot be assessed from the simulation. Therefore prototype pumps must be manufactured to be sure that an unevenly spaced vane pump will reduce unpleasant noise.

8.5 CONCLUSIONS

This chapter contains only simulation, so no results can be relied upon until prototypes have been manufactured and tested. The trends that are shown by the simulation can however be relied upon, so there is some evidence that these prototypes should behave as predicted.

The first modification that was discussed was the reduction of flow ripple by changing the port geometry. It was found that delaying the port opening and adding a relief groove reduced the flow ripple due to fluid inertia, which is indicated by the high frequency harmonics. The solution was tested over a wide range of operating conditions and was found in most cases to reduce harmonics above the 3rd by approximately an order of magnitude.

Increasing the number of vanes in the pump was also found to reduce the flow ripple. There were no trends visible in the spectra of pumps with different numbers of vanes but the peak to

peak values of the flow ripple waveforms gave a good indication of the amount of noise reduction that was possible.

Unevenly spaced vanes were also considered. Ten vane pumps with uneven spacing were found to be unsuitable because in all cases at least two chambers had to be so large that they would open to both suction and delivery at the same time. This made the volumetric efficiency very low and introduced very large low-frequency harmonics. Twelve vane pumps were found to be better and one design with two very small chambers was found to be very effective at reducing flow ripple.

FIGURES FOR CHAPTER 8

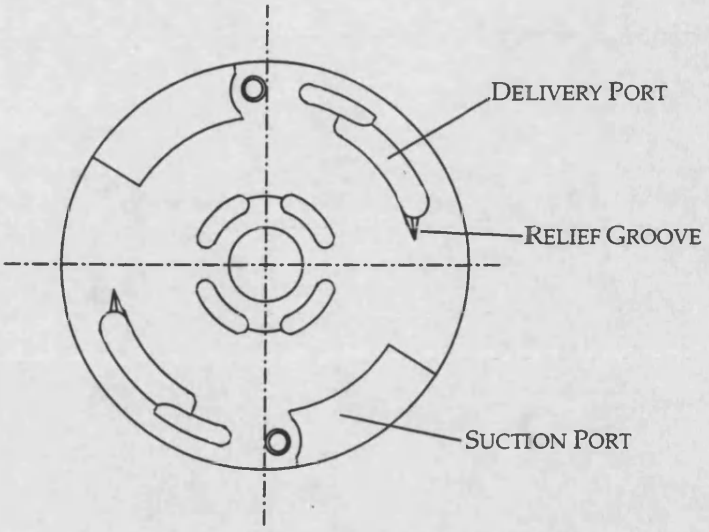

Figure 8–1: Pressure Plate showing Ports and Relief Grooves

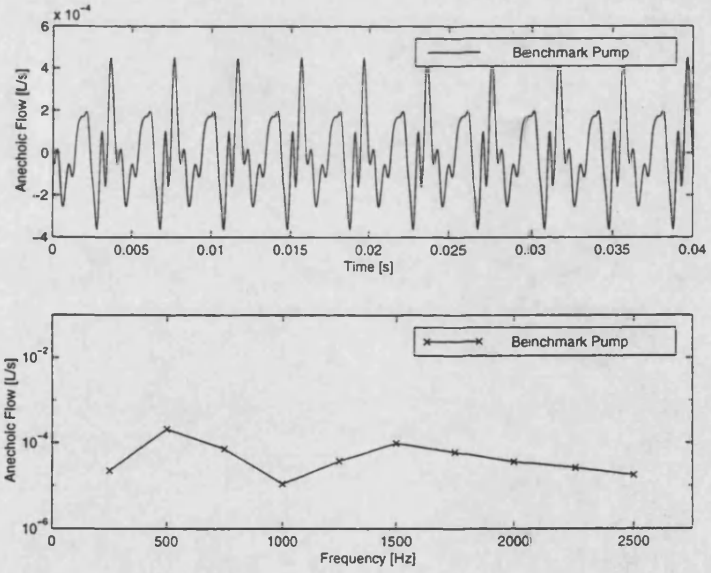

Figure 8–2: Baseline Pump (1500rev/min, 1bar reservoir, 10bar delivery)

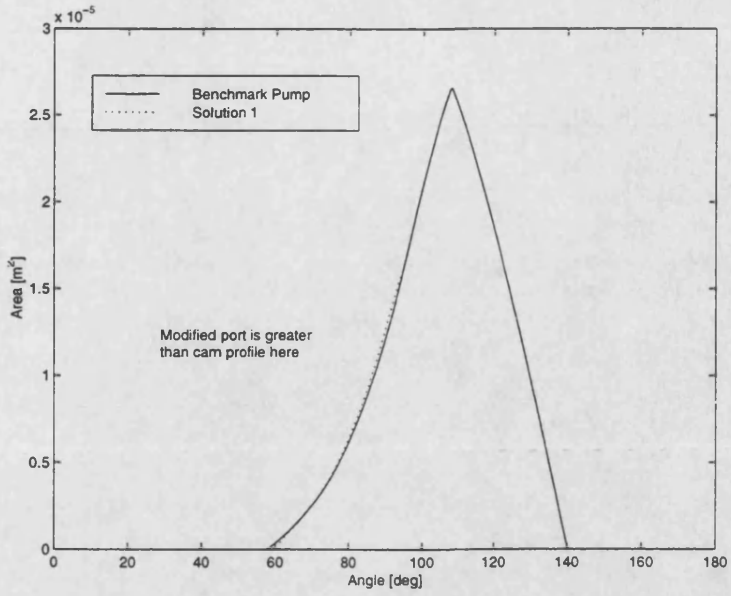

Figure 8–3: Port Orifice Area for Configuration 1

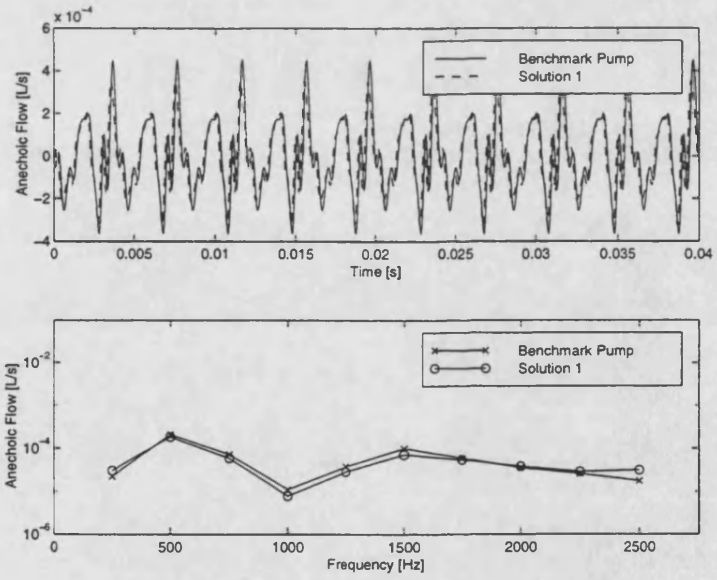

Figure 8–4: Modified Flow Ripple for Configuration 1

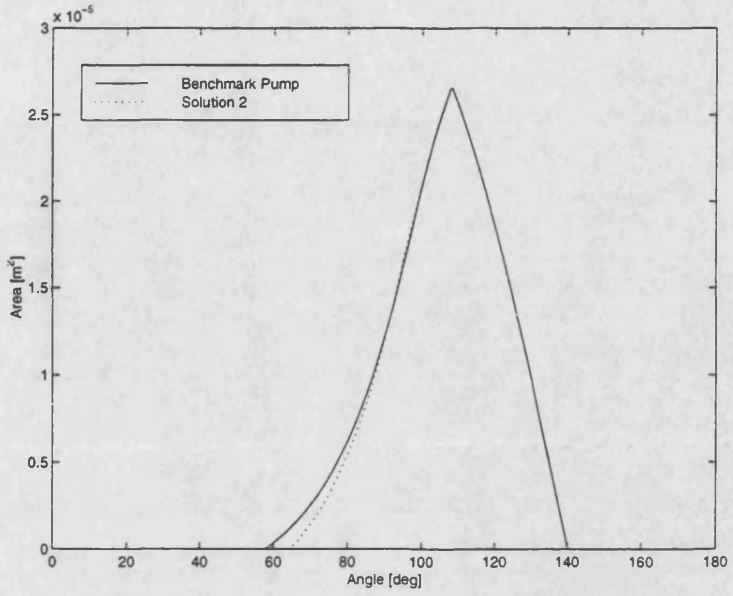

Figure 8–5: Port Orifice Area for Configuration 2

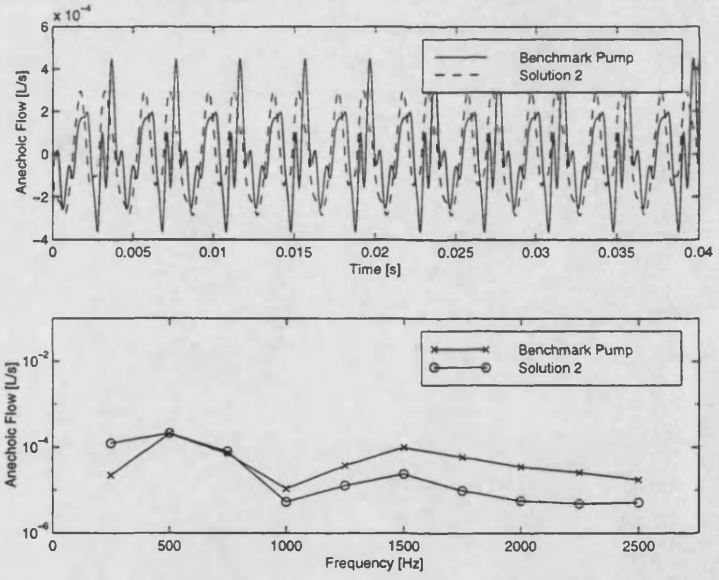

Figure 8–6: Modified Flow Ripple for Configuration 2

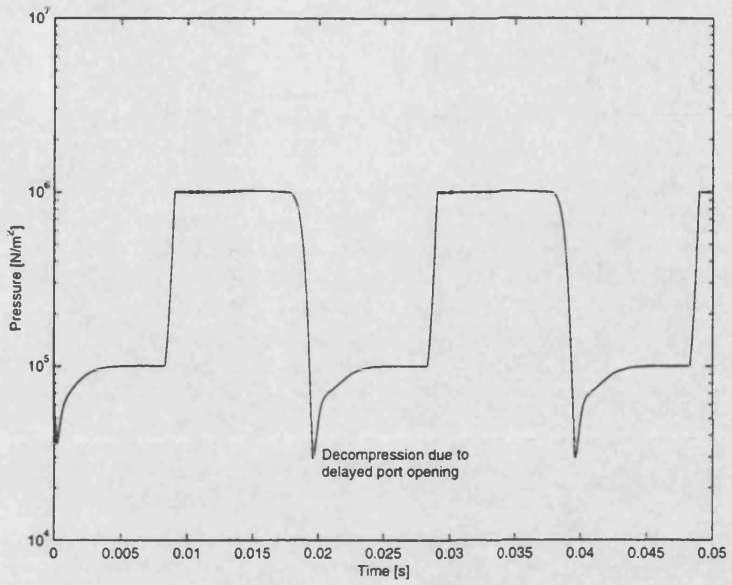

Figure 8–7: Pressure Plot for Configuration 2

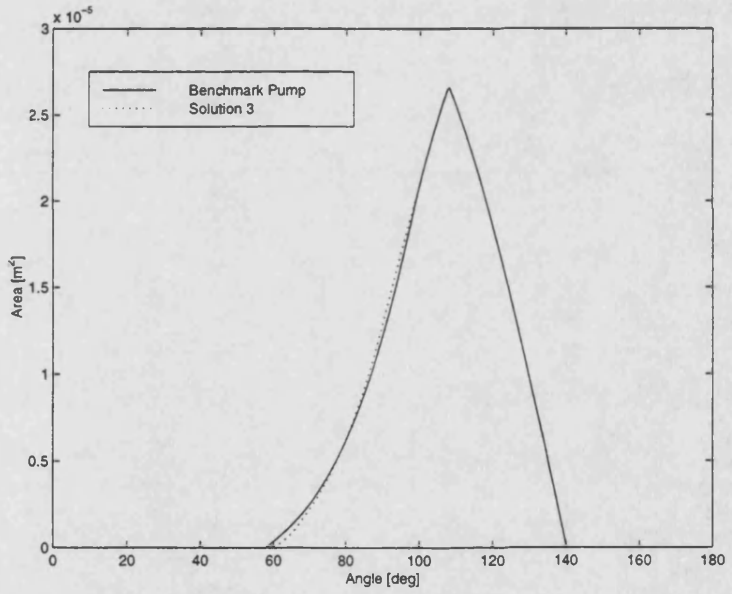

Figure 8–8: Port Orifice Area for Configuration 3

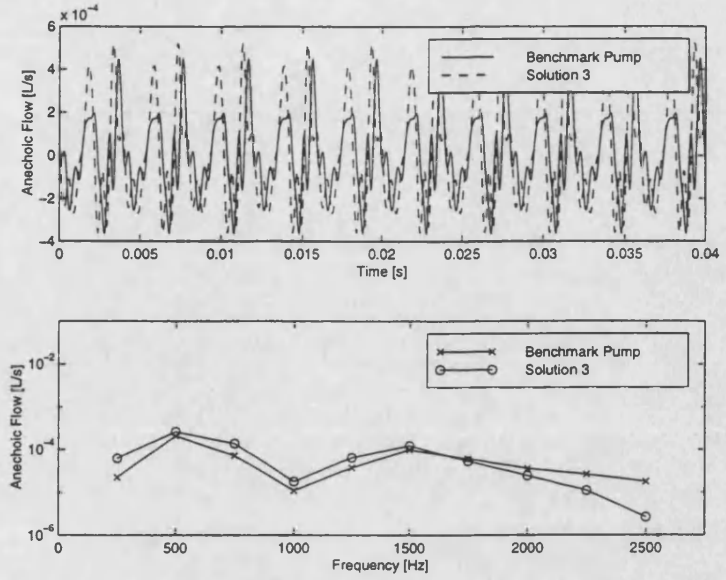

Figure 8–9: Modified Flow Ripple for Configuration 3

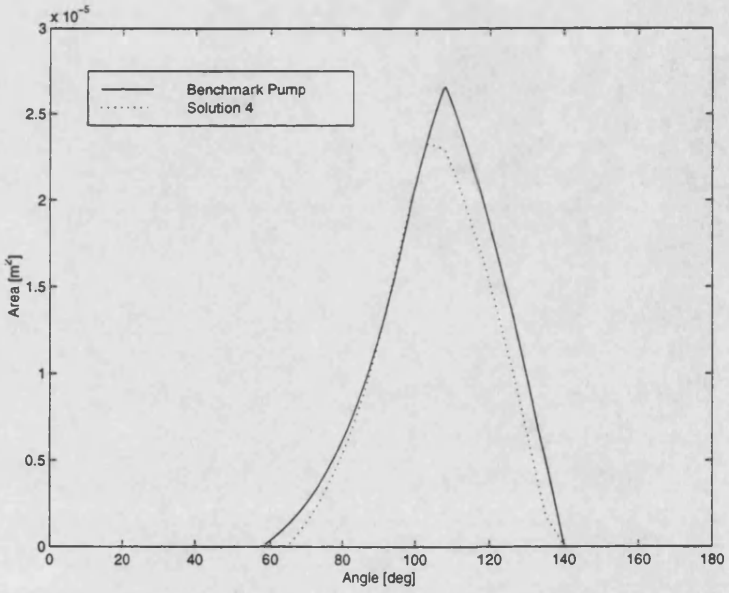

Figure 8–10: Port Orifice Area for Configuration 4

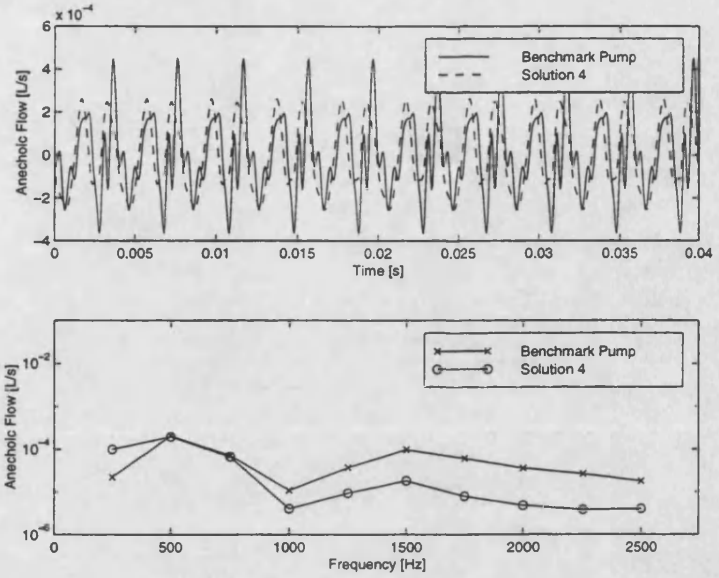

Figure 8–11: Modified Flow Ripple for Configuration 4

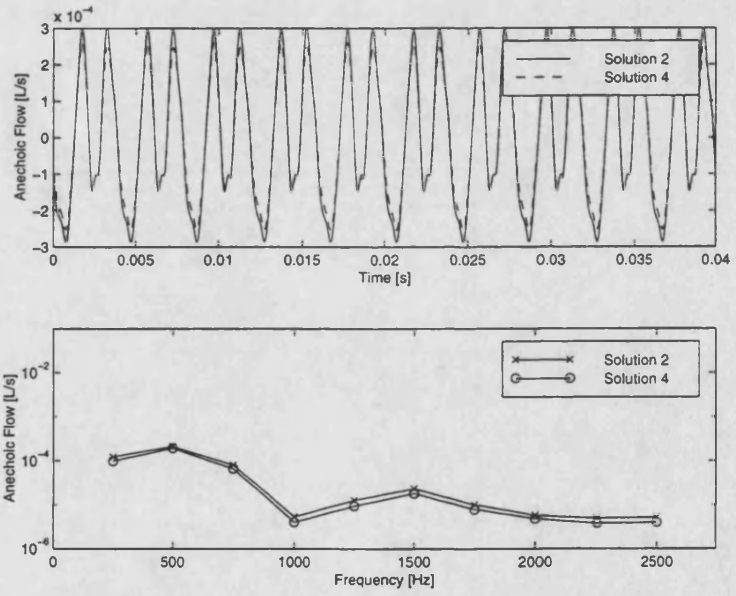

Figure 8–12: Comparison of Configuration 2 and Configuration 4.

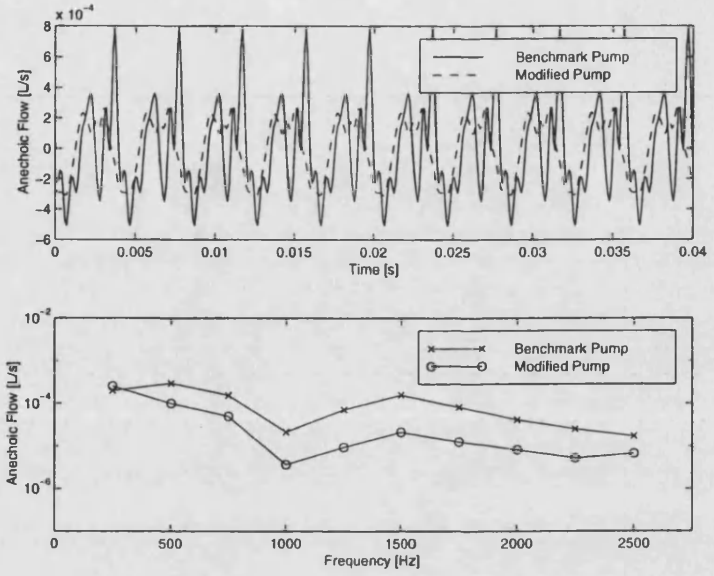

Figure 8–13: Anechoic Flow Ripple of Modified Pump at 1500rev/min, 50bar Delivery

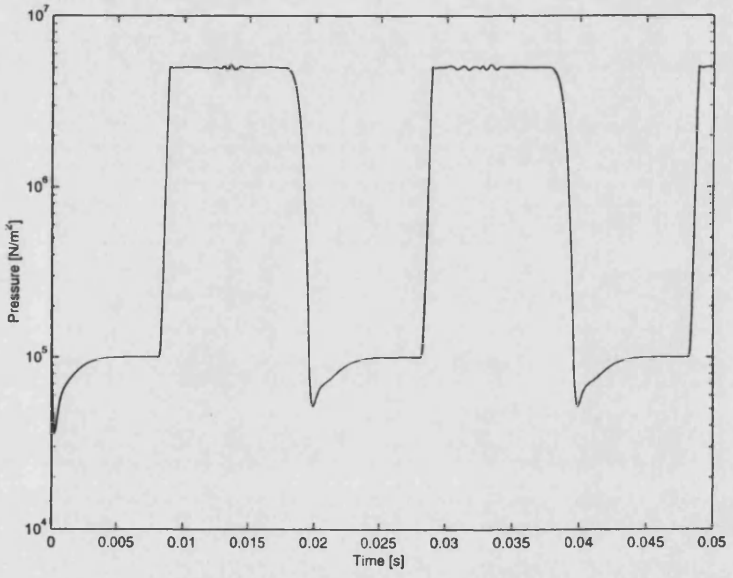

Figure 8–14: Chamber Pressure of Modified Pump at 1500rev/min, 50bar Delivery

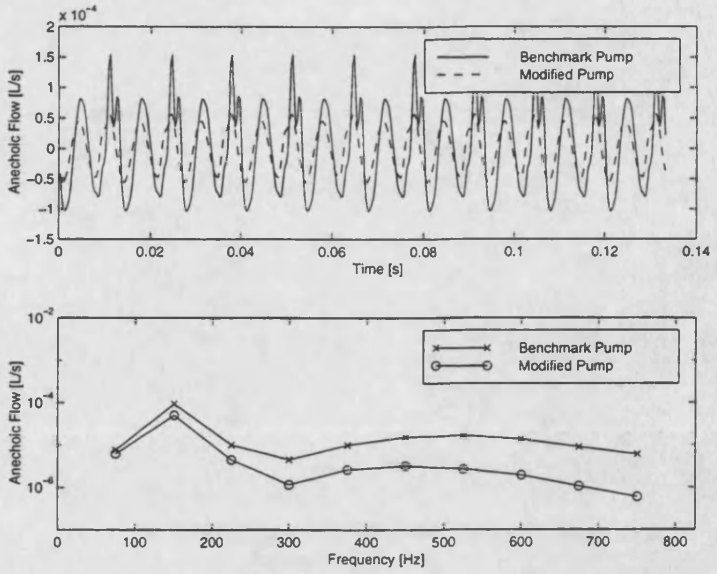

Figure 8–15: Anechoic Flow Ripple of Modified Pump at 450rev/min, 10bar Delivery

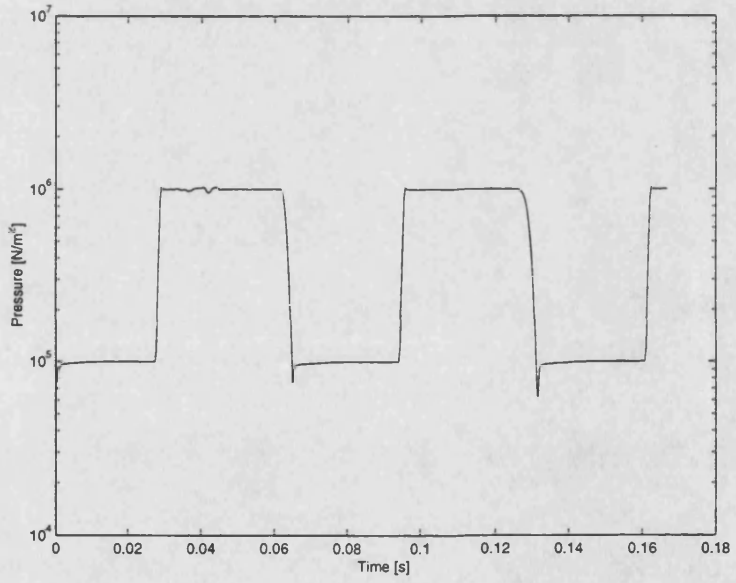

Figure 8–16: Chamber Pressure of Modified Pump at 450rev/min, 10bar Delivery

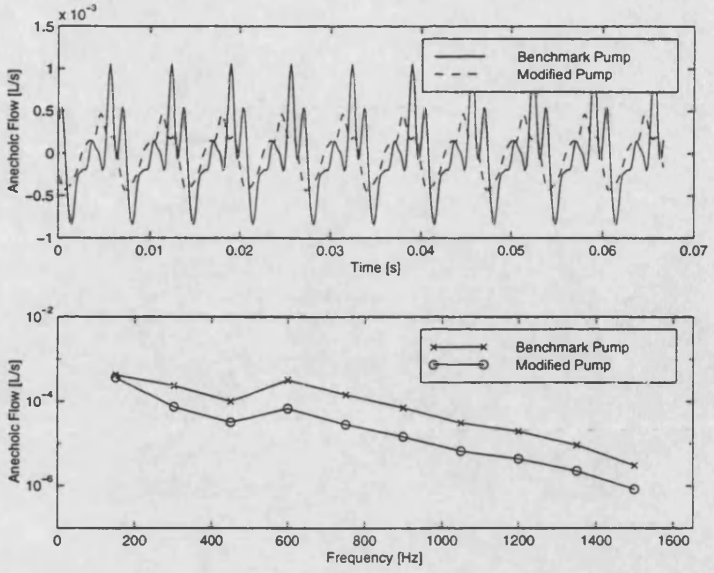

Figure 8–17: Flow Ripple of Modified Pump at 900rev/min, 1bar Reservoir 50bar Delivery

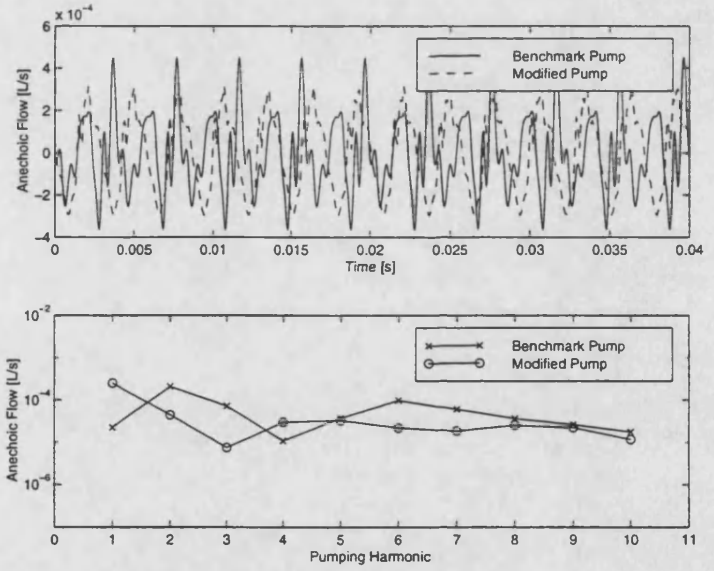

Figure 8–18: Anechoic Flow Ripple from Pump with 14 Vanes

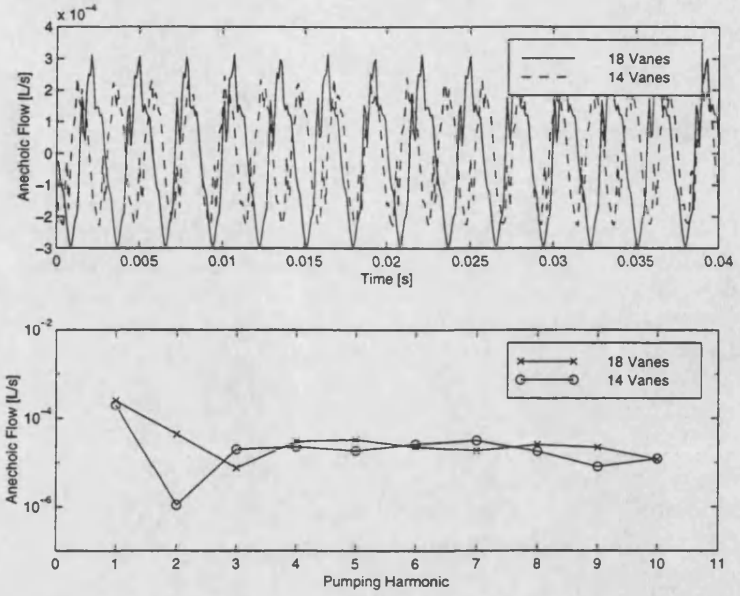

Figure 8–19: Comparison of Pumps with 14 and 18 Vanes

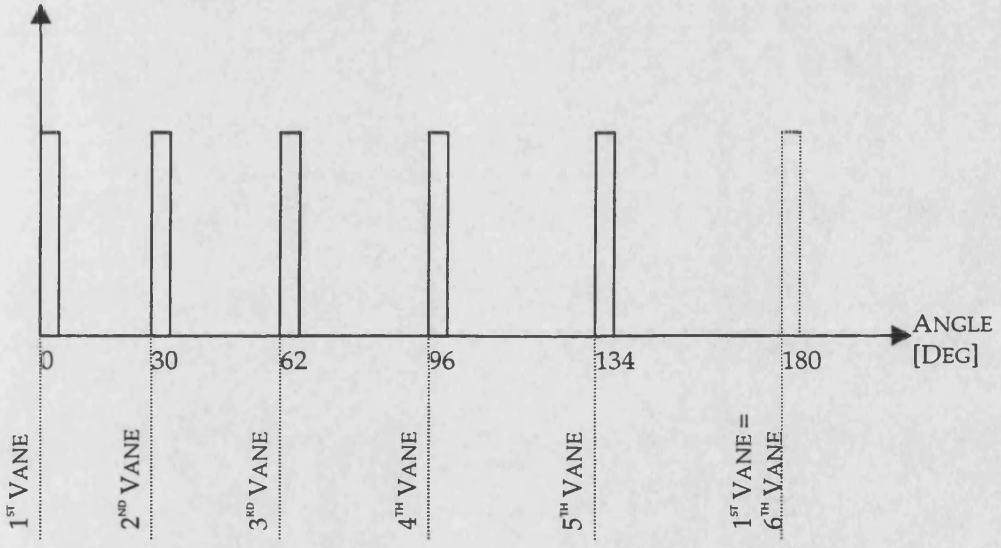

Figure 8–20: Spacing for Unevenly Spaced 10 Vane Pump

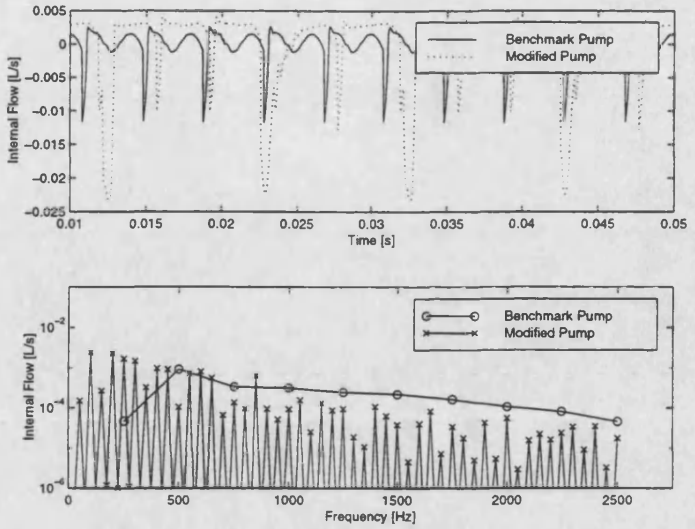

Figure 8–21: Internal Flow Ripple of an Unequally Spaced 10 Vane Pump

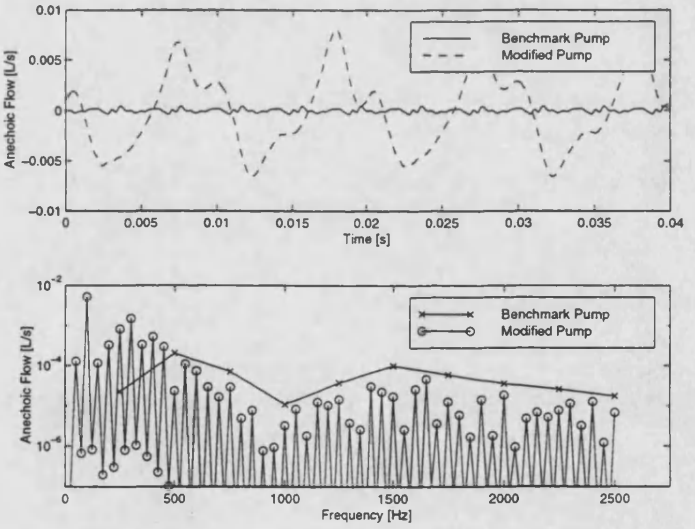

Figure 8–22: Anechoic Flow Ripple of an Unequally Spaced 10 Vane Pump

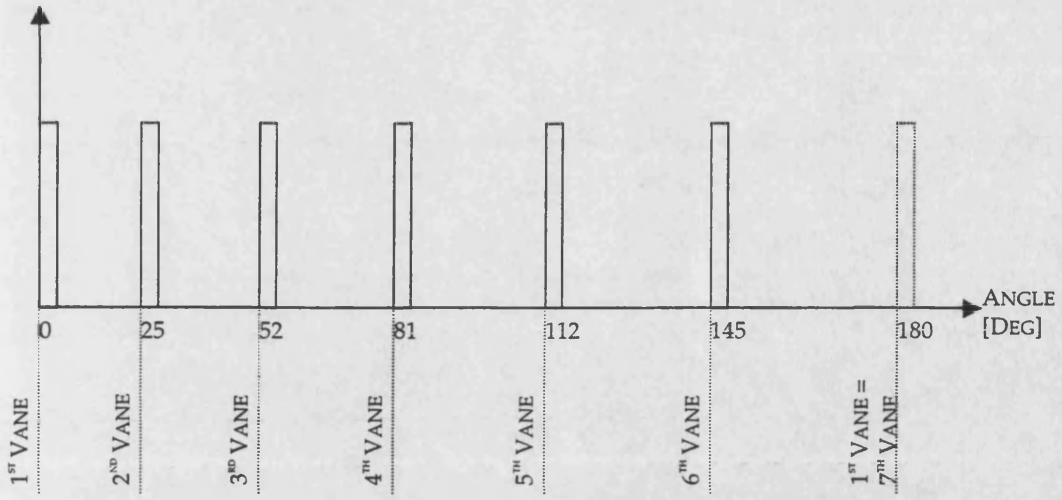

Figure 8–23: Spacing for Unevenly Spaced 12 Vane Pump

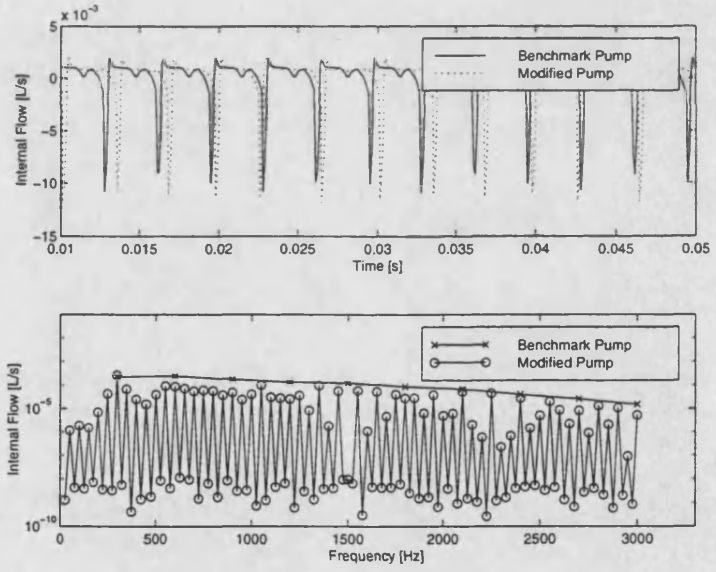

Figure 8–24: Internal Flow Ripple of an Unequally Spaced 12 Vane Pump

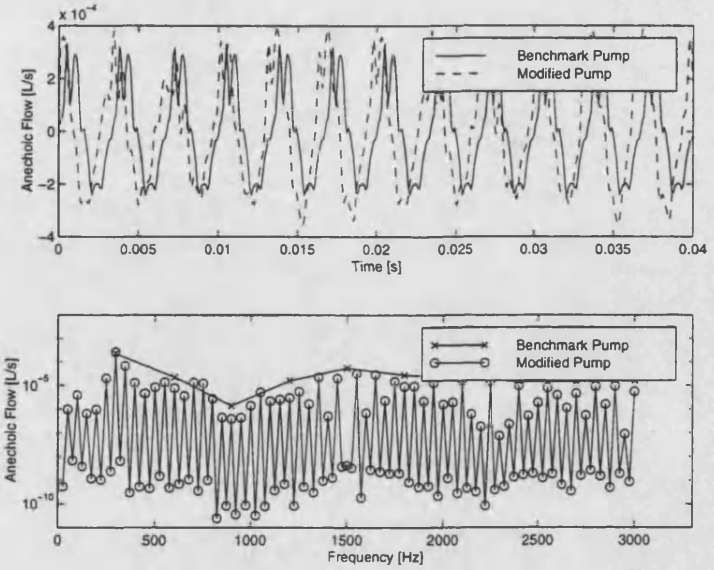

Figure 8–25: Anechoic Flow Ripple of an Unequally Spaced 12 Vane Pump

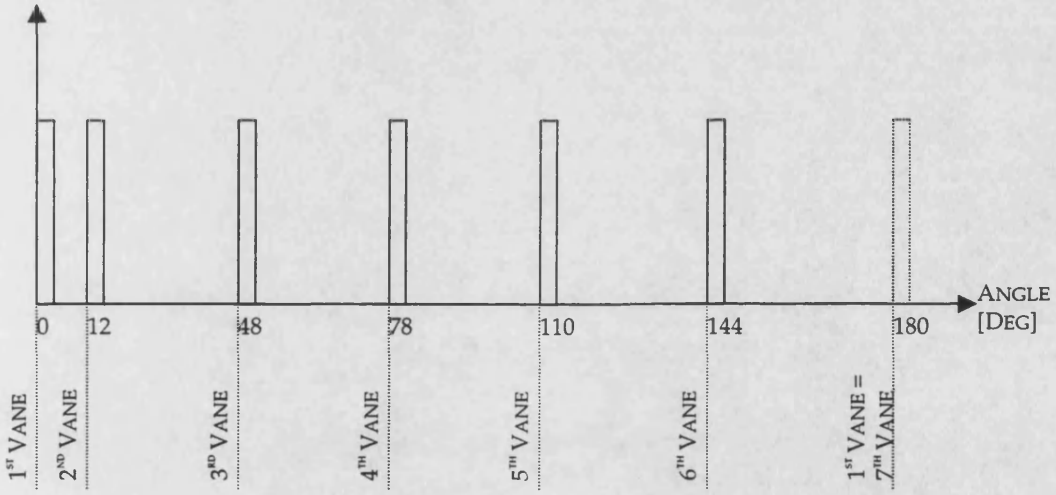

Figure 8–26: Alternative Configuration for an Unevenly Spaced 12 Vane Pump

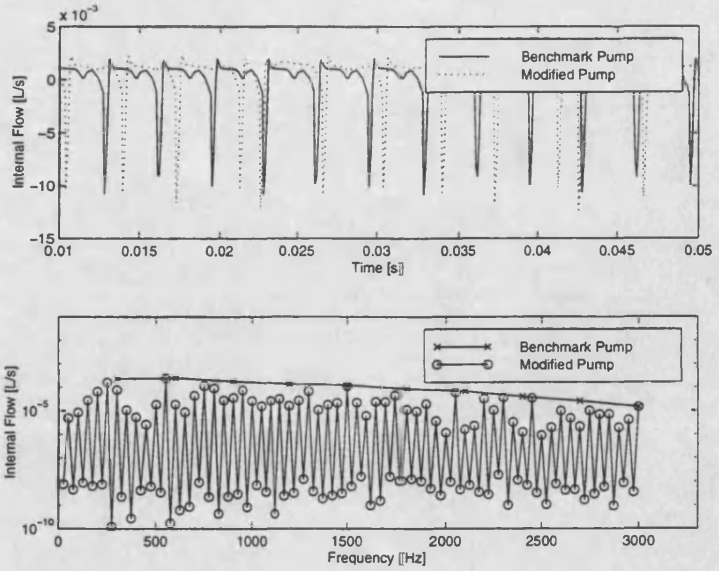

Figure 8–27: Internal Flow Ripple of an Alternative Unequally Spaced 12 Vane Pump

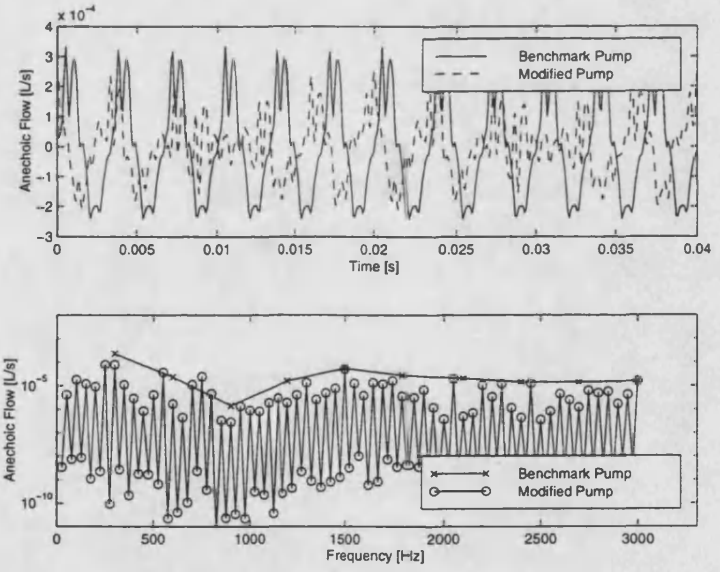

Figure 8–28: Anechoic Flow Ripple of an Alternative Unequally Spaced 12 Vane Pump

9 CONCLUSIONS

In this thesis, the noise characteristics of suction ports of positive displacement pumps have been investigated. Measured and predicted results were required to fully explain some of the phenomena involved. Simulation has allowed insight into the role that separate components play in the overall results. It has enabled small locations inside the housing to be isolated and focused upon, which in real life are inaccessible. The measured results have helped to validate the simulation and have provided empirical data for air content that was required to complete the modelling. It was then possible to use the validated model as a design tool in order to give recommendations for future work.

Overall, the influence of suction port noise on the total fluid borne noise emissions was considered to be great enough to warrant further investigation. Future work on modified port plates may show the advantages of this thesis in a considerable reduction in the noise emitted from power steering systems.

9.1 SIMULATION AND MODELLING

First of all methods of predicting the speed of sound in bubbly mixtures of air and oil were investigated. This led to functions describing oil properties. From this, the series impedance and shunt admittance for each section of the complicated suction port passageway was derived. Using these values, a distributed parameter model of the passageway was developed using a theory of separated waves. The impedance of the suction port was found using this model and its variation over a range of oil properties was observed.

Secondly, a simulation of the flow ripple emitted by the rotating group was written. The model also contained the above derivations for oil properties. The time domain results from this program were transformed into the frequency domain in order to observe the effect of the port impedance on the flow ripple spectrum. Three types of flow ripple were measured: internal, open-circuit and anechoic flow ripple. The simulation was modular so that modifications to the pump geometry were easy to add. Parameter files defined the geometry of different capacity pumps and the vane co-ordinate file could be adapted to describe alternative vane spacing.

The simulation was validated against test results and was shown to give good correlation over a range of pressure and speed. An aeration function was derived from impedance measurements, which allowed the characteristics of a range of pumps to be assessed. It is recommended though that if a pump which differs greatly from the baseline pump used here were to be analysed that a set of experiments would need to be done in order to redefine the aeration function.

9.2 TEST RESULTS

A flexible hose attached by one end to a vibrator and the other to the test circuit was used as a secondary source of pressure ripple to measure the source impedance of the suction port. This versatile method was used to measure suction and delivery impedance. Comparing the delivery impedance to conventionally measured results showed the validity of the test method.

Impedance was found to be constant except when the supercharge valve was open. The increase in air, which was concentrated near to the entrance of the pump, severely reduced the stiffness of the system and hence altered the impedance characteristic.

The delivery pressure affected suction flow ripple such that its amplitude increased as delivery pressure increased. The higher harmonics of flow ripple were quite large in relation to the fundamental, which suggested that relief grooves would reduce high frequency flow ripple by decreasing acceleration of the fluid as chambers opened to the port.

Suction flow ripple was most severe at high speed when there was a lot of air in the system. A reduction in air should reduce the flow ripple level. This was indicated by comparing a pump at atmospheric pressure to one with a boosted reservoir.

9.3 RECOMMENDATIONS FOR FURTHER WORK

The aeration equations were derived from experimental data but have not as such been validated. Research into quantifying the concentration of air and the locations where it could collect would add extra support to the simulation. Particularly difficult would be the study of air inside a pumping chamber as it moves through its cycle. This would require knowledge of evolution and solution time constants as a function of pressure and the amount of agitation there is in the chamber. Computational fluid dynamics could be used if moving 3-dimensional nets were constructed and two-phase flow could be modelled to include evolution and solution. Flow visualisation using high-speed video and photography would need to be used in order to validate the modelling, which adds the extra problem of having a transparent pump that could run at a realistic pressure. This subject is possibly complicated enough to form the core of a separate PhD project but the results would be very useful for the purpose of validating the impedance model and flow ripple simulation.

The impedance model has already been integrated into the flow ripple simulation. There is a possibility that the whole power steering circuit could be simulated and run with an input to the steering wheel and an output at the front wheels. The transfer function of the whole system in different operating conditions could be monitored and data at the inlet and outlet of each component could be recorded and displayed as required. This would have to be a compiled code as the current simulation with fifteen states already runs quite slowly. There are C++

compilers that can translate MATLAB M-Files into compiled code, which considerably increases the speed of simulation.

The test stand can be adapted for measurement of other low-pressure components. Single port devices that could be measured include suction ports and reservoirs. A test stand could also be developed to measure the transfer matrices of two-port devices such as return lines, coolers/heat exchangers and strainers. For the latter, three pressure transducers at either end of the port are used and measurements are taken at two operating conditions to find all the coefficients of the matrix.

The design recommendations in Chapter 8 could be manufactured and tested. These designs, if they should indeed do what the simulations say, would further enforce the validity of the simulation.

Gear pumps are becoming increasingly more talked about as the next generation of power steering pump. The impedance and air theory contained in this thesis is very similar to that which governs gear pumps and could easily be adapted for the purpose. Gear pumps, on the whole, have smaller pumping chambers than vane pumps and would for this reason probably have a lower flow ripple signal. It would however be interesting to see whether design recommendations for vane pumps were similar to those for gear pumps or whether the similarities between the two pumps are merely physical.

REFERENCES

1. **Dickinson, A. L. Edge, K. A. Johnston, D. N.** Measurement and Prediction of Power Steering Vane Pump Fluid Borne Noise. *SAE Noise and Vibrations Conference, NV 2A, 931294.*

2. **Dickinson, A.L. Subramonian, R. Stinebring, D. R.** Investigation of Fluid Flow through a Vane Pump Flow Control Valve. *SAE paper 951113, 1995.*

3. **Drew, J. E., Longmore, D. K., Johnston, D. N.** The Noise Characteristics of Power Steering Systems. *Proc. Instn. Mech. Engrs, part C, 1994.*

4. **Drew, J. E., Longmore, D. K., Johnston, D. N.,** Measurement of the Longitudinal Transmission Characteristics of Fluid-Filled Hose. Systems *Proc. Instn. Mech. Engrs, part I, vol.211, pp219-228, 1997.*

5. **Botti, J. Venizelos, G.** Analysis of the Instability of Wave Propagations in the Steering System's Fluid Lines. Passive Systems of Attenuation (In French) *Vième Congrès International "L'Hydraulique et le Véhicule" Angers, 4 et 5 Mai, 1994.*

6. **Hibi, A. Ibuki, T. Ichikawa T, Yokote H.** Suction Performance of Axial Piston Pump (1st report, Analysis and Fundamental Experiments) *Bull. of the JSME, vol. 20, no 139, pp79, Jan. 1977*

7. **Ibuki, T. Hibi, A. Ichikawa, T. Yokote, H.** Suction Performance of Axial Piston Pump (2nd report, Experimental Results) *Bull. of the JSME, vol. 20, no 145, pp827, Jul. 1977*

8. **Silva, G.** Silent Hydraulic Valves. *SAE, Int. Off-Highway & Powerplant Congress and Exposition, Milwaukee, Wisconsin, paper no 911804, Sept. 1991.*

9. **Numachi, F. Yamabe, M. Oba, R** Cavitation Effect on the Discharge Coefficient of the Sharp Edged Orifice Plate. *ASME J. of Basic Engineering, mar 1960.*

10. **Hayward, A. T. J.** Aeration in Hydraulic Systems - Its Assessment and Control. *Instn. Mech. Engrs, Oil Hydraulics Conf., 1961.*

11. **Plesset, M. S., Hsieh, D.Y.** Theory of Gas Bubble Dynamics in Oscillating Pressure Fields. *The Physics of Fluids, vol. 3, no 6, Nov.-Dec. 1960.*

12. **Sato, K., Kakutani, K.** Measurements of Cavitation Inception. *JSME International Journal, Series B, vol. 37, no2, 1994.*

13. **Holl, J. W., Treaster, A. L.** Cavitation hysteresis *ASME, Applied Mech. Fluid Engineering G. Conf. Cavitation in Fluid Machinery, 1965.*

14. **Schweitzer, P.H. Szebehely, V.G.** Gas Evolution in Liquid and Cavitation *J. of Applied Physics, vol 21, dec. 1950.*

15. **Katakura, H. Tsuji, S. Yamane, R. Fujita, H.** A Research on Air in Oils *JSME, vol 27, no 231, sept. 1984.*

16. **Cha, Y.S.** On the Equilibrium of Cavitation Nuclei in Liquid-Gas Solutions *ASME Journal of Fluids Engineering, vol.103, pp425-431, sept.1981.*

17. **Mori, Y. Hijikata, K. Nagatani, T** Fundamental Study of Bubble Dissolution in Liquid *Int. J. Heat Mass Transfer, vol 20, pp41-50, 1977.*

18. **Tsai, J. Chen, Y** A Generalised Approach on Equilibrium Theory of Cavitation Nuclei in Liquid-Gas Solutions *J. of Fluids Engineering, vol 112, dec 1990.*

19. **Wiggert, D.C. Sundquist, M.J.** The Effect of Gaseous Cavitation on Fluid Transients *Asme, J. of Fluid Engineering, vol 101, pp79-86, mar 1979.*

20. **Lee, I. Kitagawa, A. Takenaka, T** On the Transient Behaviour of Oil Flow under Negative Pressure *Bull. of the JSME, vol 28, no 240, june 1985.*

21. **Epstein, P.S. Plesset, M.S.** On the Stability of Gas Bubbles in Liquid - Gas Solutions *J. of Chemical Physics, vol 18, no 11, nov. 1950.*

22. **Ida, T. Sugiya, T.** Motion of Air Bubbles in Mineral Oils Subject to Sudden Change in Chamber Size (1st Report, Experimental Analysis of Single Spherical Bubbles) *JSME, vol 23, no 181, jul. 1980.*

23. **Rood, E.P.** Review - Mechanisms of Cavitation Inception *J. of Fluids Engineering, vol 113, june 1991.*

24. **Pettersson, M.** Design of Fluid Power Piston Pumps with Special Reference to Noise Reduction *PhD Thesis, Linköping University, Sweden, 1995.*

25. **Wallis, G. B.** One-Dimensional Two-Phase Flow. *McGraw-Hill, 1969.*

26. **Martin, C. S., Padmanabhan, M. Wiggert, D.C.,** Pressure Wave Propagation in Two Phase Bubbly Air - Water Mixtures *2nd Int. Conf. on Pressure Surges, BHRA, 22nd-24th Sept. 1976.*

27. **Nguyen, D. L., Winter, E. R. F., Greiner, M.,** Sonic Velocity in Two-Phase Systems *Int. J. of Multiphase Flow, vol.7, pp311-320, 1981.*

28. **Edge, K. A., Johnston, D. N.** The 'Secondary Source' Method for the Measurement of Pump Pressure Ripple Characteristics. Part 1: Description of Method. *Proc. Instn. Mech. Engrs, part A, 1990.*

29. **Edge, K. A., Johnston, D. N.** The 'Secondary Source' Method for the Measurement of Pump Pressure Ripple Characteristics. Part 2: Experimental Results. *Proc. Instn. Mech. Engrs, part A, 1990.*

30. **Edge, K. A., Johnston, D. N.** A Test Method for Measurement of Pump Fluid Borne Noise Characteristics. *SAE paper 911761, 1991.*

31. **Lau, K. K., Edge, K. A.** Impedance Characteristics of Hydraulic Orifices. *Proc. Instn. Mech. Engrs, part I, vol209, 1995.*

32. **Johnston, D. N., Edge, K. A.** The Impedance Characteristics of Fluid Power Components: Restrictor and Flow Control Valves. *Proc. Instn. Mech. Engrs, part I, vol205, 1991.*

33. **Johnston, D. N., Edge, K. A.** In-situ Measurement of the Wavespeed and Bulk Modulus in Hydraulic Lines. *Proc. Instn. Mech. Engrs, part I, vol205, pp191-197, 1991.*

34. **Johns, P. B. O'Brien, M.** Use of the Transmission Line Modelling (TLM) Method to Solve Non-linear Lumped Networks. *The Radio and Electronic Engineer, vol. 50, no. 1/2, pp59-70, jan/feb 1980.*

35. **Chua, L. O. Lin, P-M.** Computer-Aided Analysis of Electronic Circuits: Algorithms and Computational Techniques *Prentice-Hall, 1975.*

36. **Metzger, G. Vabre, J-P.** Transmission Lines with Pulse Excitation *Academic Press, 1969.*

37. **Stecki, J.S. Davis, D.C.** Fluid Transmission Lines - Distributed Parameter Models. Part 1 - A Review of the State of the Art *Proc. Instn. Mech. Engrs.,part A, vol.200, pp215-228, 1986.*

38. **Stecki, J.S. Davis, D.C.** Fluid Transmission Lines - Distributed Parameter Models. Part 2 - Comparison of Models *Proc. Instn. Mech. Engrs.,part A, vol.200, pp229-236, 1986.*

39. **Goodson, R.E. Leonard, R.G.** A Survey of Modelling Techniques for Fluid Line Transients. *Trans. of the ASME, J. of Basic Engrg, June 1972, pp109-115.*

40. **Edge, K.A.** The Theoretical Prediction of the Impedance of Positive Displacement Pumps. *I.Mech.E. Conf. Quiet Oil Hydraulic Systems, London, oct. 1980.*

41. **Auslander, D.M.** Distributed System Simulation with Delay Line Models. *Trans. ASME, J. of Basic Engrg, vol.90, june 1968, pp195-200.*

42. **Boucher, R.F. Kitsios, E.E.** Simulation of Fluid Network Dynamics by Transmission Line Modelling *Proc. Instn. Mech. Engrs.,part C, vol.200, pp21-29, 1986.*

43. **Brown, F.T.** The Transient Response of Fluid Lines. *ASMI, J. of Basic Engineering, Dec.1962, pp547-553.*

44. **Schönfeld, J.C.** Resistance and Inertia of the Flow of Liquids in a Tube or Open Canal *Applied Scientific Research, A1(2), 1948, pp169-197.*

45. **Zielke, W.** Frequency-Dependent Friction in Transient Pipe Flow *Trans. ASME, J. of Basic Engrg, mar 1968, pp109-115.*

46. **Trikha, A.K.** An Efficient Method for Simulating Frequency-Dependent Friction in Transient Liquid Flow *Trans. ASME, J. of Fluids Engrg, mar 1975, pp97-105.*

47. **Young, F. J.,** Impedance of Tapered Structures. . *J. of the Acoustical Society of America. Vol.35, No.5, part1. 1966. pp841-846.*

48. **Tarantine, F. J., Rouleau, W. T.,** Fluid Pressure Transients in a Tapered Transmission Line. *Trans. of the A.S.M.E. J. of Basic Engrg. March 1967. pp181-190.*

49. **Young, F. J., Young, B. H.,** Impedance of Tapered Structures. *J. of the Acoustical Society of America. Vol.33, No.9. Sept.1961. pp1206-1210.*

50. **Hanselman, D., Littlefield, B.** MATLAB Version 5 User's Guide. *Prentice Hall, 1997.*

51. **Nagata, K.** Reduction of Pressure Fluctuation in a Hydraulic System Including a Vane Pump and Resonator Hoses. *PhD Thesis. Mechanical Engineering, Graduate Division of Science and Technology, Sophia University, Tokyo. Oct1996*

52. **Watton, J. Watkins-Franklin, K.L.** The Transient Pressure Characteristics of a Positive Displacement Vane Pump *Proc. Instn. Mech. Engrs, vol204, part A, 1990.*

53. **Harrison, A. M.** Reduction of Axial Piston Pump Pressure Ripple. *PhD Thesis. University of Bath. 1997.*

54. **Pettersson, M.** Design of Fluid Power Piston Pumps with Special Reference to Noise Reduction. *PhD Thesis. Linköping University, Sweden. 1995.*

55. **McCloy, D. Martin, H. R.** Control of Fluid Power. Analysis and Design. 2nd (Revised) Edition. *Ellis Horwood Ltd. 1980.*

56. **Shampine, L. F., Reichelt, M. W.** The MATLAB ODE Suite. *The Mathworks inc., 24, Prime Park Way, Natick, MA 01760.*

57. **Hanselman, D., Littlefield, B.** MATLAB Version 5 User's Guide. *Prentice Hall, 1997.*

58. **Vaughan, N. D. Johnston, D. N. Edge, K. A.** Numerical Simulation of Fluid Flow in Poppet Valves *Proc. Instn Mech. Engrs, part C, vol.206, pp 119-127, 1992.*

59. **Unruh, D. R.,** Outlet Pressure Ripple Measurement of Positive Displacement Pumps. *Nat. Conf. on Fluid Power, Chicago, 1975.*

60. **Szerlag, S. F.,** Rating Pump Fluid Borne Noise. *SAE paper 750830, 1975.*

61. **McCandlish, D., Edge, K. A. Tilley, D. G.,** Fluid Borne Noise Generated by Positive Displacement Pumps. *I.Mech.E Conf. Quiet Oil Hydraulic Systems, London, nov.1977.*

62. **Edge, K. A., Wing, T.J.,** The Measurement of Fluid Borne Pressure Ripple Characteristics of Hydraulic Components. *Proc. Instn. Mech. Engrs, vol.197B, Nov 1983.*

63. **Bowns, D. E., Edge, K. A.,** The Assessment of Pump Fluid Borne Noise. *I.Mech.E Conf. Quiet Oil Hydraulic Systems, London, nov.1977.*

64. **Johnston, D.N.** Measurement and Prediction of the Fluid Borne Noise Characteristics of Hydraulic Components *PhD Thesis, University of Bath, 1987.*

65. **de Freitas, F. J. T.** The Generation and Transmission of Pressure Ripples in Pump Suction Lines. *PhD Thesis, University of Bath, 1982.*

66. **Edge, K. A. de Freitas, F. J. T.** A Study of Pressure Fluctuations in the Suction Lines of Positive Displacement Pumps *Proc. Instn. Mech. Engrs, part B, vol.199, pp211-217, 1985*

67. **Longmore, D. K.,** The Transmission and Attenuation of Fluid Borne Noise in Hydraulic Hose *I.Mech.E. Conf. Quiet Oil Hydraulic Systems, London, Nov. 1977.*

68. **Longmore, D. K., Schlesinger, A.,** Relative Importance of the Various Vibration Transmitting Mechanisms in Hoses in Typical Hydraulic Systems *Proc. Instn. Mech. Engrs, part I, vol.205, pp105-111, 1991*

69. **BS6335: Part 1: 1990** Methods for Determining Pressure Ripple Levels Generated in Hydraulic Fluid Power Systems and Components. Part 1: Secondary Source Methods for Pumps.

70. **Lecerf, J. P.** La Prévision des Pulsations de Pression dans les Equipments Hydrauliques est une Réalité (in French). *Vième Congrès International, "L'hydraulique et le Véhicule", Angers, 4 et 5 Mai 1994.*

71. **Johnston, D. N.,** Analysis Package for Secondary Source Test Method for Hydraulic Components FBN2: User Guide and Reference Manual Ver. 3.5. *University of Bath, School of Mechanical Engineering, June 1994.*

APPENDIX 1: PARAMETER FILE FOR PUMP1 SIMULATION

GENERAL PARAMETERS

rhoil	8.75E+02	Density of Oil	kg/m^3
bmoil	1.60E+09	Bulk Modulus of Oil	N/m^2
rcons	2.87E+02	Gas Constant	kJ/kgK
tcons	7.70E+01	Temperature	°C
kvisc	3.60E-05	Kinematic Viscosity	m^2/s
ks	1.00E-01	Air Solubility Constant	-

VANE DIMENSIONS

nvanes	10	Number of Vanes	-
vthick	1.26E-03	Vane Thickness	m
vwidth	1.77E-02	Vane Width	m

INLET DIMENSIONS

iodia	1.34E-02	Inlet Orifice to Annulus Diameter	m
iolen	1.00E-02	Inlet Orifice to Annulus Length	m

PUMP ENTRANCE DIMENSIONS

dsport	9.85E-03	Pump Entrance Diameter	m
lsport	1.40E-02	Pump Entrance Length	m

SUPERCHARGE DIMENSIONS

dschge	9.70E-03	Diameter of Supercharge Outflow	m
lschge	5.75E-03	Length of Supercharge Outflow	m

CAM RING DIMENSIONS

diamin	3.71E-02	Diameter of Cam Minimum	m
diamax	diamin+4.72E-03	Diameter of Cam Maximum	m
rotaxl	1.78E-02	Rotating Group Diameter	m
rotdia	3.61E-02	Rotating Group Diameter	m
dacamp	15	Start of Cam Rise	deg
dbcamp	70	End of Cam Rise	deg
dccamp	110	Start of Cam Fall	deg
ddcamp	165	End of Cam Fall	deg

PORT DIMENSIONS

wport	5.38E-03	Width of Port	m
daport	20	suction port leading edge position	deg

dbport	70	suction port trailing edge position	deg
dcport	113	delivery port leading edge position	deg
ddport	165	delivery port trailing edge position	deg
deport	10	length of relief groove	deg
hgroove	1.00E-03	Maximum Height of Relief Groove	m

ANNULUS DIMENSIONS

diann	5.38E-02	Inner Diameter of Annulus	m
doann	6.20E-02	Outer Diameter of Annulus	m
exann	3.00E-03	Eccentricity of Ring to Housing	m
exang	102.5	Angle of Eccentricity from Inlet	deg

APPENDIX 2: PARAMETER FILE FOR PUMP2 SIMULATION

The parameter file for Pump2 is the same as that for Pump1 except for the following:

CAM RING DIMENSIONS

diamin	3.71E-02	Diameter of Cam Minimum	m
diamax	diamin+5.64E-03	Diameter of Cam Maximum	m

APPENDIX 3: PARAMETER FILE FOR PUMP3 SIMULATION

The parameter file for Pump3 is the same as that for Pump1 except for the following:

VANE DIMENSIONS

vthick	1.25E-03	Vane Thickness	m
vwidth	1.64E-02	Vane Width	m

INLET DIMENSIONS

iodia	1.34E-02	Inlet Orifice to Annulus Diameter	m
iolen	1.00E-02	Inlet Orifice to Annulus Length	m

PUMP ENTRANCE DIMENSIONS

dsport	9.85E-03	Pump Entrance Diameter	m
lsport	1.90E-02	Pump Entrance Length	m

SUPERCHARGE DIMENSIONS

dschge	9.59E-03	Diameter of Supercharge Outflow	m
lschge	7.50E-03	Length of Supercharge Outflow	m

CAM RING DIMENSIONS

diamin	4.15E-02	Diameter of Cam Minimum	m
diamax	diamin+4.57E-03	Diameter of Cam Maximum	m
rotaxl	1.64E-02	Rotating Group Diameter	m
rotdia	4.06E-02	Rotating Group Diameter	m

PORT DIMENSIONS

wport	4.35E-03	Width of Port	m

ANNULUS DIMENSIONS

diann	5.80E-02	Inner Diameter of Annulus	m
doann	6.33E-02	Outer Diameter of Annulus	m
exann	0	Eccentricity of Ring to Housing	m
exang	0	Angle of Eccentricity from Inlet	deg